Morphology and Kinematics of Interacting Galaxies: the Spheroidal + Irregular Pairs

Claudia Faye McCain

A thesis submitted for the degree of

Doctor of Philosophy

of The Australian National University

Mount Stromlo and Siding Spring Observatories

January 1997

to my father for his faith,
and to the memory of my mother

Disclaimer

I hereby declare that the work in this thesis is that of the candidate alone, except where indicated in the text.

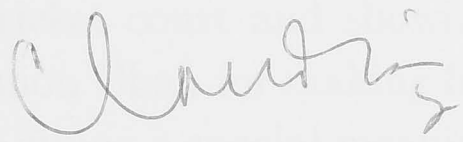

Claudia Faye McCain
January 1997

Acknowledgements

The production of this thesis has been made easier with the help of many, both in professional and personal ways.

I would like to thank Peter Wood and Mike Bessell for the guidance they gave especially during my earlier stay at Mt. Stromlo; to Stuart Ryder, Emmanuel Vassiliadis and Chris Lidman for dragging me to the cricket court and showing me what being a `Roo` –and a `Kiwi`– means. Thanks to Simon Chan for making life at Mt. Stromlo pleasantly bearable, to Dave Fullagar for giving a special meaning to `pit-digging`, to Ron Hola for pointing out what being a blond means when one is dark-haired –and vice-versa, to Ben Stappers for his memorable laughter and naked feet, and to Sungeun Kim for the sharing of life's ups and downs especially during the pingpong matches. Special thanks to Kim Sebo, for his friendship, tireless encouragement and time shared. I am also grateful for the friendship my fellow Indonesians have offered and given during my course in Australia, and to Tom Therik and family for the always-open door. Thanks also to Angelica D'Oliveira-Costa for making the rush to the salad bar at the Forschungsinstitut lively, and to Norbert Langer for pulling me out of the gate of `Erebus` so many times.

I am equally grateful to the pair Maggie Miller and Thelma Johnson, to Jeanette Reagan, to the excellence performed by the technical staff of MSSSO and the computer section, all of whom have many times drawn me out of the mud and showed me where the tools lie.

I thank Ken Freeman, my supervisor, for his patience and his enthusiasm, his guidance and his attention. Thanks to my advisor Peter Quinn for his encouragement and counsel, to Peter MacGregor for many useful advice, and to Agris Kalnajs for the numerous valuable discussions and for pointing out hidden things to me. I also thank the students at Mt. Stromlo for many chats and shared opinions on –quite often– astronomy matters. Additionally I thank the Max-Planck Institut für Astrophysik, Garching, for receiving and bearing me, and Simon White, for the helpful discussions and counsel.

Finally, I would like to acknowledge the financial support I received from AIDAB/Aus-AID and the patience and encouragement shown by Geraldine Cooper.

Abstract

This report gives results of investigations of six interacting galaxy pairs. Each of these pairs consists of a spheroidal and an irregular galaxy, the latter having a morphology that is dominated by its HII regions. I have done CCD photometry and 2–dimensional velocity mapping –based on their ionised gas from longslit spectroscopy– on these galaxies. The major aims are to study the structures and kinematics of the irregular components, and to detect any signatures of cross–fuelling in the early–type members. In one case, radio synthesis data were obtained to map the pair's HI distribution and kinematics as well as the continuum distribution in the 21 cm wavelength.

Optical and near–IR images of these pairs reveal structures inside these galaxies that have not been observed before. It has been found that, unlike those usually observed in interacting and isolated spirals, bar structures are not frequent in these irregular galaxies, but inner spiral structures –contained inside inner disks– appear to be a more common feature. Blue rings are observed in three late–type members. In all the irregular components, the youngest of the blue structures are found to be consistently less than 30 Myr old, independent of the level of interactions. The L_K/L_B values have a small scatter (1.50±0.60), nonetheless the luminosity distributions can differ from the B–band to the K–band due to dust extinction, as is observed in the (optically hidden) nuclei of Arp 147 and Arp 144. Those with high nuclear obscuration are found to have high L_{FIR} as well. Half of the irregular members have a high gas–to–star content; these are the clumpiest galaxies in the study, sugggesting a connection between clumpiness and gas content. In four spheroidal componentss emission line(s) are detected; in three, their integrated colors are comparable to those of the late–type galaxies, all of which are indicative of evolutionary changes due to the interactions with the gaseous companions.

All irregular components show ordered rotation, despite their disorder in their morphology. Those with rings show non–rotational motions in addition to their rotation. Three of the late–type galaxies are found to have low velocity dispersions and low M/L_B compared to isolated spirals. Two others ((Arp 118 and Arp 142) show extremely high internal motions, about 1000 km s^{-1}. Both of these galaxies have rather massive spheroidal companions, but it is not clear whether these massive companions are responsible for the chaos within their irregular components. Although these two galaxies both have these exceptionally large internal motions in their irregular components, I note that their optical emission line spectra are quite different.

For one pair, AM 1806–852 , I also made HI radio synthesis obsservations, and found that the HI kinematics is decoupled from that of the ionised gas. The neu-

tral hydrogen in this system is concentrated around the irregular component, but shell–like structures are seen surrounding the entire system. Its 21–cm continuum emission is also heavily concentrated to the late-type component, with an extension towards and beyond the spheroidal component which I interpret as a signature of infalling matter.

Contents

List of Figures

List of Tables

Chapter 1

Introduction

1.1 Scientific Background

The idea that galaxies interact with neighbouring galaxies and undergo substantial morphological and evolutionary changes is widely accepted now, from observations and from computer simulations alike. Toomre & Toomre (1972, T&T) in their classic paper showed that many impressively extensive structures in interacting galaxies, ie. bridges and tails, can be explained by tidal forces (and projection effects). In their test–particle disk, the severely deformed structures usually reside in the outer parts while the inner regions are almost unchanged. This was further supported by the result of Barnes (1988), who showed that the inclusion of dark haloes will produce a merger sooner, ie. on a timescale of a few rotational periods. In addition, the simulations show that in these interactions, direct orbits favour bisymmetric (m=2) modes and produce extensive tidal distortion, while those with retrograde orbits favour m=1 resonance and result in much less disruptive structures (see, for example, T&T, Hernquist & Quinn, 1989, Hernquist, 1989, and Howard *et al.*, 1993).

Pioneered by Larson & Tinsley (1978), it was shown that interacting galaxies suffer bursts of star formation much more than isolated systems. Kennicutt & Keel (1984) compared spirals with nearby companions and concluded that they show enhancement in nuclear activities, believed to be caused by interactions with the neighbours. Bushouse (1986) found that about 70% of the interacting disks he studied show enhanced star formation activity, whose associated $H\alpha$ emission tends to concentrate towards the nuclear regions. Observations in the infrared further suggest that interacting galaxies show active star formation, with young stars heating the surrounding dust (see Lonsdale *et al.*, 1984, and Joseph & Wright, 1985). Young *et al.* (1986a, b) showed that, in addition to the increased star formation activities, these galaxies also have higher starforming effienciencies.

It was discovered that most interacting pairs exhibit morphological concordance

(Faber & Gallagher, 1979; Noerdlinger, 1979; and Yamagata, 1990), which implies the importance of environmental factors in the evolution of these galaxies. On the other hand, a significant number of interacting pairs –about 30–35%– are observed to be mixed pairs, ie. S+E, which bears on their evolutionary history; however a number of these apparently mixed pairs turn out to be disky pairs, ie. S+S0 (see eg. Sulentic, 1992; Reduzzi & Rampazzo, 1995; and Soares *et al.*, 1995). Zasov & Sulentic (1994) observed star formation enhancement in spiral galaxies of some E+S pairs but others do not show any enhancement at all. No HI deficiency is observed.

Demin *et al.* (1984) in studying paired galaxies observed signatures of interactions in both members in the form of color correlations. This is known as the 'Holmberg effect', which they suggested to be caused by both components in a pair 'synchronising' their chemical abundances due to interactions which further affects their stellar populations. However, the evidence has a large scatter in pairs with S0s as one member and this is believed to be due to S0s not forming a homogenous class of objects. Similar signatures are also later observed by Rampazzo *et al.* (1995) in their study of mixed interacting pairs.

Not all interacting pairs exhibit extensive tidal tails and bridges. In others, the morphology of one component is dominated by largescale irregular and distorted knotty structures. These knotty systems are usually paired with an early-type compact companion which in several examples is clearly disky. The statistics and astrophysical significance of these relatively rare systems are not yet well studied. One might think of these knotty galaxies as a precursor to the amorphous galaxies (see, for example, Hunter, 1984), since several of these galaxies are observed to have nearby companions. Noguchi's (1988b) numerical simulations may be relevant to these systems; he showed that after a few Gyr a violent tidal interaction can produce a galaxy whose stellar component lacks any clear structures such as spiral arms – due to the stabilising effect of the large induced random motions – and ending up with star formation activity in the inner regions.

This thesis is motivated by the wish to study the coexistence of spiral and S0s in interacting pairs concentrating on the S0+knotty-irregular systems described above. In these pairs, the morphology of the irregular component is defined by its distribution of HII regions. In most examples, no regular features like spiral arms or tidal are visible in the irregular component. Nor do most of these irregulars show galactic nuclei. These properties led Freeman & de Vaucouleurs (1974) to suggest that these S0 + (knotty-irregular) systems originate from a single parent disk galaxy that encountered an intergalactic cloud of galactic dimension; the ram pressure of the cloud acting on the interstellar medium of the disk galaxy resulted in a gas–free stripped early type disk galaxy with an irregular companion of gaseous knots. This hypothesis requires the existence of such large intergalactic

clouds, which are now known to be rare (see, for example, Brinks 1993). It seems more likely that these S0+(knotty-irregular) systems were originally two disk galaxies, and the nuclei of the now irregular components are buried amongst the many knots of their HII regions.

If it is correct that these systems originate from pairs of spirals, and that interactions are the cause for this extreme kind of morphological change, then it is intruguing to study what effects the interactions induce on the kinematics of the once–spiral components. The location of the nuclei of the original spirals is also an issue in understanding these systems.

Noguchi's (1988a) self–gravitating models, after being perturbed by another galaxy, resulted in a bar–structure in the center regions of the disk. This tidally–induced bar is found to be stable over a few rotation periods, and acts as an effective mechanism in removing the angular momenta and kinetic energy from the gas clouds, thus resulting in the falling of the clouds into the nucleus and producing (the observed) nuclear starburst activities. This mechanism would suggest that bar structures are more common in interacting galaxies. However, Olson and Kwan (1990) found that a bar is not a necessary prerequisite for interaction–induced nuclear star formation activities. (We note that their adopted rotation curve is much steeper than Noguchi's). They also found, as was further supported by their subsequent study (Olson & Kwan, 1990b), that a stronger interaction produces a more disturbed interstellar medium; as the interaction strength increases, the cloud activity becomes more and more concentrated toward the center of the galaxy. Thus the detection of bar structures and the distribution of the star formation activity within the irregulars are also of interest for this study.

With only a few exceptions, S0s and ellipticals are observed to have no gas and little if any present–day starforming activities. Wardle & Knapp (1986) find that 24% of their sample of 243 S0s are detected in HI; in ellipticals, the HI detection rate was found to be 15%. Their M_{HI}/L_B suggests that gas in these galaxies is of external origin. Mixed pairs are thus interestesting systems to investigate, since hydrodynamical study of interaction–induced star formation and cross–fuelling effects can be made under the simplifying assumption that gas from only one component is involved.

It is not always straightforward to determine whether a galaxy is an S0 or an elliptical, except when it is viewed edge–on (as in Arp 147). In other cases, the judgment depends on the apparent morphology of the early-type component. We chose pairs in which one component shows gaseous irregular knotty structure as described above, and its early–type companion exhibits evidence for a disk component in its outer regions.

We concentrated on the emission–line kinematics of the irregular components, so there is little detailed information from our study about the kinematics of the

early–type component. However, detection of emission lines from the early–type component is of special interest, since this indicates the presence of ionised gas and possibly of the process of 'cross–fuelling' from the gaseous companions.

In summary, the main objects of this thesis are:

- to study the internal kinematics of the gaseous irregular components of our pairs, to determine the amplitude of the disorder motions and to see how much of the original rotation has survived the interaction process

- to study the structure of the irregular components, eg. to detect nuclei and bars that might develop during the interactions

- to study the structures of the S0 companions

- to detect any signatures of cross-fuelling that the S0s might be suffering associated with the interactions

I have chosen six interacting pairs for detailed study: Arp 118, Arp 142, Arp 147, Arp 140, Arp 144, and AM 1806–852 ; the first five come from Arp's Atlas of Peculiar Galaxies (1964), and the last from Arp & Madore's A Catalogue of Southern Peculiar Galaxies and Associations (1987). Table 1.2 gives a brief summary on the interacting pairs chosen. It was apparent from their morphology that the galaxies in each pair are interacting; this was confirmed by their similar redshifts ($\Delta V \lesssim 300$km s^{-1}) measured in this study.

1.2 Thesis Overview

Chapter 2 covers the observational aspects and data reduction performed for this study. Chapters 3, 4, 5 and 6 discuss the objects selected, in order of decreasing morphology disorder: Arp 118 and Arp 142, Arp 147, Arp 140 and Arp 144, and AM 1806–852 . These chapters generally consist of introduction, morphological aspects of the pair, kinematics, and discussion/summary. In the case of AM 1806–852 , the results of HI synthesis observations are also included in the chapter. Chapter 7, discusses the general trend and main conclusions of this study.

Object Name	Other Name	Position (1950.0)	Diameter (′)	m_B	E(arly)/L(ate) Type
Arp 118	N1143	02 52 36.2 –00 22 47	0.9 x 0.8	13.20	E
	N1144	02 52 38.7 –00 23 08	1.1 x 0.7	13.78	L
Arp 140	N0274	00 48 29.8 –07 19 43	1.5 x 1.5	12.80	E
	N0275	00 48 32.7 –07 20 07	1.5 x 1.1	13.16	L
Arp 142	N2936	09 35 08.5 +02 59 11	2.1 x 0.7	14.60	L
	N2937	09 35 09.3 +02 58 22	1.3 x 1.1	13.90	E
Arp 144	N7828	00 03 53.7 –13 41 40	0.9 x 0.5	14.40	L
	N7829	00 03 55.6 –13 41 57	0.7 x 0.7	14.60	E
Arp 147	IC0298	03 08 43.5 +01 07 33	–	–	L
	IC0298B	–	–	–	E
AM 1806-852	N6438	18 05 51.0 –85 25 06	1.6 x 1.3	12.10	E
	N6438A	18 06 18.0 –85 25 18	2.7 x 1.0	12.57	L

Table 1.1: Basic data for the interacting pairs studied in this report.

1.3 References

Arp, C. 1966, *Atlas of Peculiar Galaxies* (Pasadena: California Institute of Technology)

Arp, H.C. and Madore, B.F. 1987, *A Catalogue of Southern Peculiar Galaxies and Association* (Cambridge University Press)

Brinks, E. 1993, in *The Cold Universe*, eds. Montmerle, T., Lada, C. and Tran-Thanh-Van, J., p. 303 (Editions Frontieres: Gif-sur-Yvette)

Bushouse, H.A. 1987, Ap.J. 320, 49

Demin, V., Zasov, A., Dibai, E. and Tomorv, A. 1984, Soviet Astron. 28, 367

Faber, S.M. and Gallagher, J.S. 1979, ARA&A 17, p. 135

Hernquist, L. 1989, Nature, 340, 687

Hernquist, L. and Quinn, P.J. 1989, in *The Epoch of Galaxy Formation*, eds. Frenk, C.S. (Dordrecht: Kluwer Acad. Publ.), p. 427

Howard, S., Keel, W.C., Byrd, G. and Burkey, J. 1993, Ap.J. 417, 502

Kennicut, R.C. Jr. and Keel, W.C. 1984, Ap.J. 279, 5

Noerdlinger, P.D. 1979, Ap.J. 234, 802

Noguchi, M. 1988a, A&A 201, 37

Noguchi, M. 1988b, A&A 203, 259

Reduzzi, L. and Rampazzo, R. 1995, Ap.L. 30, 1

Soares, D.S.L., de Souza, R.E., de Carvalho, R.R. and Couto da Silva, T.C. 1995, A&AS 110, 371

Toomre, A. and Toomre, J. 1972, Ap.J. 178, 623

Wardle, M. and Knapp, G.R. 1986, Ap.J. 91, 23

Yamagata, T. 1990, IAU Coll. 124, p. 25

Young, J.S., Kenny, J.D., Tacconi, L., Claussen, M.J., Huang, Y.-L., Tacconi–Garman, L., Xie, S. and Schloerb, F.P. 1986a, Ap.J. 311, L17

Young, J.S., Schloerb, F.P., Kenney, J.D. and Lord, S.D. 1986b, Ap.J. 304, 443

Zasov, A.V. and Sulentic, J.W. 1994, Ap.J. 430, 179

Chapter 2

Observations and Data Reductions

2.1 Observations

The observations for optical photometry and spectroscopy were done at various telescopes at Siding Spring Observatory. Imaging was performed at the 2.3m and 1m telescopes using a number of CCD detectors for B–, R–, I– and sometimes V–bands, with typical pixel scales of 0.″6 and 0.″37 per pixel, depending on the CCD used. Exposure times range between 200 to 600 seconds, depending on the telescope and filter employed. For AM 1806–852, a few frames of the $H\alpha$ narrow–band were taken as well; these were taken at the 1m telescope.

The K–band images were taken at the 3.9m Anglo–Australian Telescope using IRIS[1], a hybrid infrared array of 128×128 pixel format. We used the Cassegrain focus at f/15, which gives 0.″61 per pixel; due to the size of the array, in some cases only the irregular component could be observed. For this study, the Kn (2.0–2.3 μm) filter was used, which greatly reduces the effect of water vapour at the short wavelength end and thermal emission at the long wavelength end of the filter. All of these frames, optical and near–IR, were gathered between May 1992 to Sept. 1995. In most cases, conditions were photometric during the observing runs.

Longslit spectra were taken at the 2.3m telescope mostly using the Photon Counting Arrays (PCAs) attached to the Double Beam Spectrograph (DBS); in two later occasions a CCD was used instead at the DBS. Each irregular component in each pair was observed in between 6 to 23 position angles (PAs) – depending on the allocated time and angular size of the galaxy – in the red; a few of these were observed in the blue as well, especially to measure the velocity of the spheroidal component. At each PA, the slit was positioned to go across the nucleus of the

[1]the IRIS is manufactured by the Rockwell International Science Center of Thousand Oaks, California

spheroidal component whose continuum peak would later be used as the zero point for registering the velocity map.

For spectroscopy in the red, I used the 1200 G/mm grating, which at λ =7210 Åhas a theoretical dispersion of 36.7 Å/mm. With a scale of 0.″67 per 15μ pixel, this corresponds to about 25 km s^{-1} per pixel and a spectral range of about 450 Å. These observations were aimed at acquiring detailed velocities from the $H\alpha$ and [NII]$\lambda\lambda$ 6548,6584 lines. The spectrograph slit was set to 1.″8 width, which projects to two pixels at the detector. In the blue, I used the 600 G/mm grating, which gives a dispersion of 73.2Å/mm (85.7 km s^{-1}) at λ=3850 Å.

The 21-cm radio observations were made with the Compact Array of the Australia Telescope National Facility (ATNF)[2] for AM 1806–852 only, since this is the only pair in the study south enough to observe with this East–West array. I chose to use configurations 1.5D and 6D (1.5 and 6 km baselines) in order to produce a unique and reasonably unambiguous map, to observe both the extended and smaller structures resulting from the interactions. The data were taken in Aug. 1995 with the 6D array and in Oct. 1995 with the 1.5D array, with the continuum centered at 1344 MHz and HI line at 1409 MHz. For the continuum, there were 13 channels each of 8 MHz width, and for the spectral line 512 channels –which was binned by two– again covering 8 Mhz. The calibrators chosen were 1934-638 for the 6D array, and 1934-638 and 1549-790 for the 1.5D array. An internal interference affected the channel at 1408 MHz; this was 'de-birdied' on-site.

2.2 Data Reduction

2.2.1 Optical Photometry and Imaging

Data reduction for optical images was done using standard routines in the IRAF data reduction package[3]. These images were bias subtracted using (non–preflashed) bias frames. The overscan regions were fitted and then subtracted to remove low level electronic structures. The dark current induced by the detector was negligible so there was no need to correct for this. The flat–field (twilight) images were then combined according to their filter types and normalized; these were used to correct the object images from the large scale response of the detector.

The bias–subtracted and flat–fielded images were then registered using bright but not saturated stars in the neighbourhood. In a number of cases where the

[2]The Australia Telescope is funded by the Commonwealth of Australia for operation as a National Facility managed by CSIRO

[3]IRAF is distributed by the National Optical Astronomy Observatories, which is operated by the Association of Universities for Research in Astronomy, Inc., under contract to the National Science Foundation.

images could not register well, the positions of the bright stars in different frames were cross–correlated to produce better alignment. The typical final alignment is accurate to about 0.1 pixel. These frames were then combined to produce a final image of one observing night. This last procedure also removes cosmic rays by the type of rejection chosen.

To calibrate the photometry, standard stars were used, which were mostly chosen from the the E–region standards of Graham (1982) and from the standard fields of Landolt (1992). Bias subtracted and flat–fielded standard stars frames were normalized to one second exposure times, and used to derive transformations for magnitudes and colors from the observed/instrumental magnitudes and colors, after correction for atmospheric extinction. For the K–band images, the data needed to be first corrected for dark current and bias and then linearised. The reductions are then similar to optical imaging for CCD frames.

The measured photometric transformations were then applied to the objects' observed magnitudes to obtain the magnitudes on the standard system. For the K–band, the color term is negligible (Heisler, private communication), so no color term was introduced into the transformations.

As mentioned earlier, for AM 1806–852 a few $H\alpha$ frames were taken as well. To correct for contribution from the continuum, an R–band image was used: the flux of the spheroidal component in the R image was then normalised to that in the $H\alpha$ image. Here it was assumed that there is negligible contribution from $H\alpha$ emission or absorption in the R-band image of the spheroidal component. I then subtracted the R image from the $H\alpha$ to produce an image of the distribution of $H\alpha$ within the irregular component.

2.2.2 Spectroscopy

The PCA has zero read–out noise and no bias subtractions was necessary. However, corrections for the spectral response and illumination of the PCAs were needed. In addition, the PCAs show small-scale discontinuities in both the spatial and wavelength directions, arising from the fiber coupling between the intensifier and the CCD. To correct for the former, arc lamp lines in each frames were referred to their laboratory wavelength and then traced and corrected for any deviations in the spatial direction. The typical rms for this correction is 0.1 pixel. The coordinate frames were then transformed and applied to the object spectra; in this process the spectra were scrunched and binned in the wavelength axis. The pixel scale resulting from this transformation is about 0.4 Å/pix, which translates to about 18.5 km s^{-1} around $H\alpha$. The resolution is 1 Å at FWHM. Night skylines were fitted and then subtracted from the frame. Unfortunately, nothing much could be done to correct for the discontinuity in the wavelength

direction except to study and judge each emission profile by eye carefully.

In some cases where the signal is weak the spectra were smoothed using a 3×3 Hanning smoothing with a kernel of

$$\begin{pmatrix} 0.17 & 0.25 & 0.17 \\ 0.25 & 0.5 & 0.25 \\ 0.17 & 0.25 & 0.17 \end{pmatrix}$$

This was done in order to gain a higher signal-to-noise ratio, and since the slit width is 1.″8 and the typical seeing is about 2″ no information is lost by this act in the spatial regime.

To measure the redshift of each emission line in each spatial pixel, an artificial 1–dimensional spectrum was used as a template. This template has the emission lines observed in the object spectra but with laboratory wavelengths: in most cases these are $H\alpha$ and [NII]$\lambda\lambda$ 6548, 6584, and sometimes [SII]$\lambda\lambda$ 6716, 6731 and HeI λ6678 as well. The template emission lines are Gaussian with FWHMs similar to that of the PCA's resolution, ie. 1 Å, and each line was given the same weight. The object spectra from each position angle were then Fourier cross–correlated with the template for each spatial row, after continuum subtraction. The errors presented in the velocity slices in the following chapters are actually errors resulted from this process. These are generally larger than cross–correlation for a single line, which, for counts larger than 40, gives an error not more than 7 km s^{-1}. For counts < 10 this error is $\simeq 20$ km s^{-1}.

Often the emission lines have multiple peaks. For this the cross–correlation was done for each peak. If the multiple peaks are blended, these were deblended with the largest weight given to the strongest peak. In some cases deblending was impossible or introduced large uncertainties; these lines were then treated as a single emission.

For the most recent observations, the CCDs replaced the PCAs as detectors at the DBS. Here the frames were first bias–subtracted and flatfielded, and were then further processed similarly to the other longslit spectra as described above.

For the absorption lines in the blue region of the spectrum, the redshifts were measured using spectra of standard stars taken from Maurice *et al.*(1984) as templates. These spectra were scrunched (i.e. wavelength calibrated) to 1–dimensional format before being cross–correlated with the object spectra.

All the data reduction procedure for the spectra was done using the package IRAF as well.

2.2.3 Radio Data

Reduction for the ATCA data was done using the Multichannel Image Reconstruction, Image Analysis and Display (MIRIAD) package (Sault *et al.*, 1995). Bad data were flagged and then after phase correcting the continuum data, data for the secondary calibrators were selected from object data. The primary calibrator data were flux calibrated and, for continuum data, polarisation calibrated. In some cases, the primary calibrator 1934–638 was also used as secondary calibrator. In other cases, the secondary calibrator was flux–calibrated and, in the case of continuum data, polarisation–calibrated using the primary calibrator. The calibration tables were then transferred to the program source. A continuum image was then produced as well as the spectral line cube from the collection of visibility datasets. The final HI cube has a velocity resolution of 6.6 km $s^{-1}$and a half–peak beam width (HPBW) of 7.″5.

The HI radio data obtained for AM 1806–852 show that there is little emission coming from the longer baselines; detections came only from baselines $\lesssim$1000 kλ indicating that the HI emission is not dominated (at the detection level) by small scale structures. This will be further discussed in the chapter on AM 1806–852 .

2.3 Visualisation

To produce 'color' images (eg. (B–R) image), frames with substantially different Point Spread Functions (PSFs) were convolved to match those with larger FWHM. These were again registered as explained earlier, and then divided to produce a grayscale distribution. These 'color' images provide a qualitative visualisation of the color distribution and are a useful way to visualise the dust distribution. A quantitative investigation was reserved for the 1–dimensional surface brighness distributions. A similar procedure was adopted to build composite images, made from the original B, R and I or K images. Here the individual broad–band images were combined: for AM 1806–852 I used the package 'color' in the IRAF package, and for Arp 147 I used the package *it* for producing trichromatic images (Sebastien & Davoust, 1995), which was kindly provided by Emmanuel Davoust.

In order to give an overall view of the distribution of the velocities in each irregular component, the velocity information from all PAs was superimposed on a B or R image. The process was performed after adjusting the pixel scales and registering the positions, using the peak of the continuum of the spheroidal component in the spectrum at each PA and the position of this component in the image. Errors in this registration could come from the differential effects of dust absorption on the spectra and the broad–band images. However I expect that the dust obscuration in the center of the early type components is unlikely to be important in this sense.

The velocities are then presented as 'bubbles' whose colors denote the magnitude of the velocities at each PA. The whole procedure was implemented using the package Advanced Visualisation System (AVS, Currington and Coutant, 1991).

To present the velocity distributions in a two–dimensional contour format, all velocity datapoints from all PAs of each irregular component were translated into rectangular coordinates. For those with multiple values, the datapoints were averaged by weight (according to their errors as resulted from the Fourier cross–correlation fitting). These were then smoothed by method of triangulation which utilises the *conran* F77 library (Quinn, private communication). For AM 1806–852, the program could not handle the chaotic jumps of velocities (see Ch. 6) thus no contour mapping was done for this object.

2.4 References

Currington, I. and Coutant, M. 1991, "AVS - A Flexible Interactive Distributed Environment for Scientific Visualisation Applications", 2nd Eurographics Workshop on Visualization in Scientific Computing

Graham, J.A. 1982, PASP 94, 244

Landolt, A.U. 1992, A.J. 104, 340

Maurice, E., Mayor, M., Benz, W., Andersen, J., Nordstrom, B., Ardebeg, A., Lindgren, H., Imbert, M., Martin, N., and Prevot, L. 1984, A&AS 57, 275

Sault, R.J., Teuben, P.J. and Wright, M.C.H., 1995, "A Retrospective View of Miriad" in Astronomical Data Analysis Software and Systems IV, eds. R. Shaw, H.E. Payne, J.J.E. Hayes, ASP Conf. Ser. 77, p.433

Sebastien, M. and Davoust, E. 1995, Experimental Astronomy v.6, p.223

Chapter 3

Pairs with High Internal Velocities

3.1 Arp 118

3.1.1 Introduction

Arp 118 is a galaxy pair consisting of a distorted spiral (NGC 1144) and a compact spheroidal companion (NGC 1143) separated by $\simeq 40''$. The small velocity difference between the two ($\simeq$ 100–200 km s^{-1}), the highly distorted morphology of the spiral component and the extension of structures from the spiral towards the spheroidal imply that both components are strongly interacting. The irregular component was observed to have very high internal velocities (Tift, 1977, 1982 and Jeske, 1986, hereafter J86) but not until Hippelein (1989) was special attention paid.

Arp 118 is a bright IRAS source and is known to have a very high ratio of far infrared to blue luminosity and a high $S_{100\mu}/S_{60\mu}$ color temperature, indicating a high dust temperature and strong star formation activity (Appleton & Struck-Marcel, 1987). Joseph *et al.* (1984) concluded that infrared activity in interacting pairs is generally associated with one of the components, which in Arp 118 is likely to be the irregular component: IRAS results gave $L_{FIR}=1.2\times10^{11}\ L_{\odot}$. J86 observed a few extranuclear radio sources (in addition to the nuclear source) in NGC 1144 and gave a total HI mass of $\simeq 7.5\times10^{9}\ M_{\odot}$ for the irregular component. Joy & Ghigo (1988) calculated an integrated bolometric luminosity of $2.5\times10^{11}\ L_{\odot}$ for NGC 1144, 80% of which is reradiated in the thermal infrared. They also concluded that much of the 10μm luminosity is emitted from an extranuclear star forming region and that the radio continuum implies recent star forming activity.

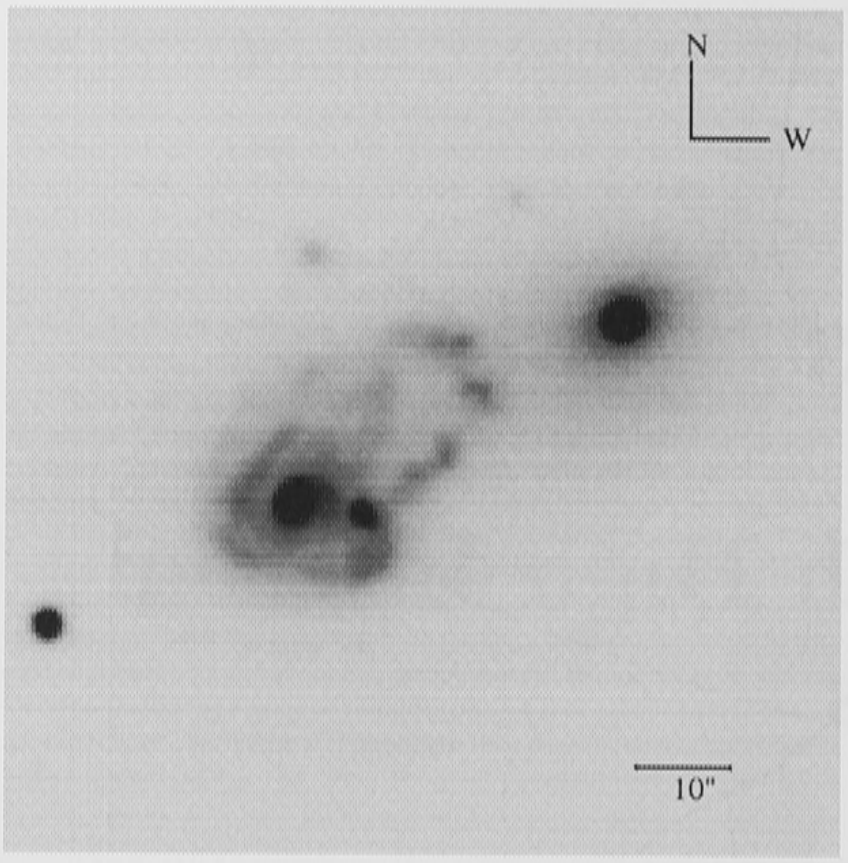

Figure 3.1: B image of Arp 118. All subsequent images have similar orientation unless mentioned otherwise.

3.1.2 Morphology and Photometry of Arp 118

The morphology of the irregular component of Arp 118 is complex (Figs. 3.1, 3.2, 3.3 and 3.4). It shows a knotty loop (relatively smooth in the K–band) that extends towards the spheroidal companion in the NW. Inside this loop there is an apparently distorted disk that also extends towards the NW. On closer inspection this structure turns out to be yet another loop with lower surface brightness in its inner part. The nucleus lies off–center but still inside these structures. Just west of the nucleus there is a luminous blue knot which appears to be at least as bright as the nucleus in the U image of Joy and Ghigo (1988, hereafter J&G88) and is the brightest source in 10μm detected in Arp 118; this source is concluded to be an extranuclear starforming region.

East of the nucleus, and more obvious in the B and R images, a spiral arm structure extends roughly northwards from the nucleus. In this region, $\simeq 4''$ east from the nucleus, J86 observed a radio continuum source; at a higher resolution this is resolved into two radio sources (J&G88). To the south of this feature is another loop structure which might be a part of the NW loop but not as extended, possibly due to projection effects or warping. The R and I images look roughly similar, but in the K–band the eastern arm is not seen and the western knot appears thin; this object is also a radio source (J&G88). The area immediately around the nucleus is surrounded by diffuse matter particularly in the west, bridging the nucleus to the western knot. In the K–band this 'bridge' is curved, resembling a spiral arm that extends from the nucleus towards the western knot.

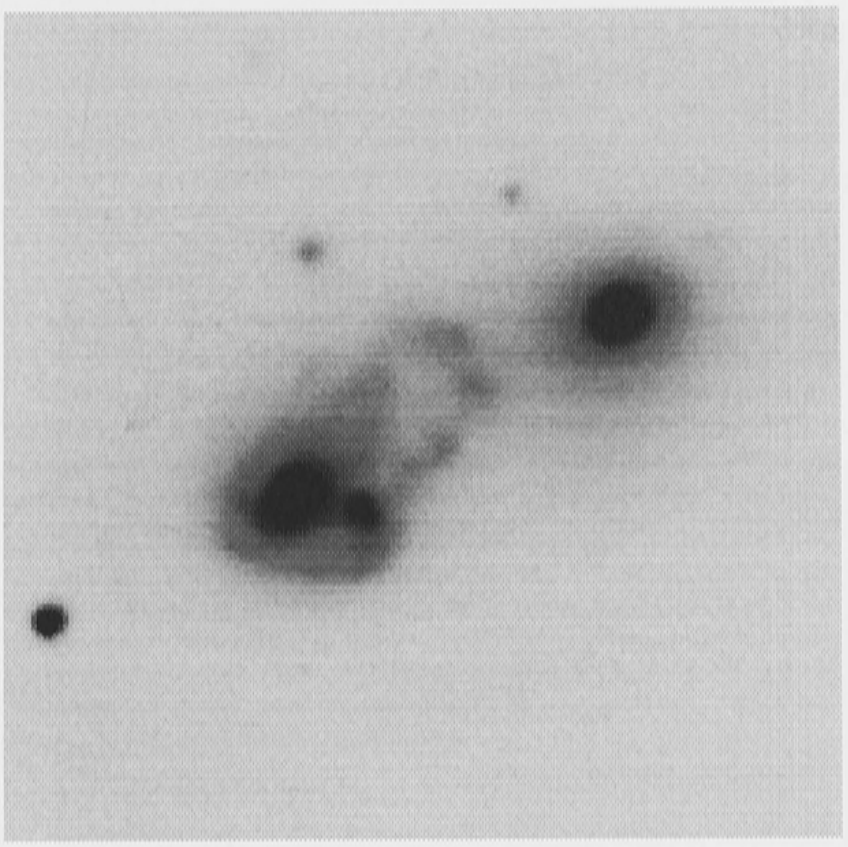

Figure 3.2: R image of Arp 118

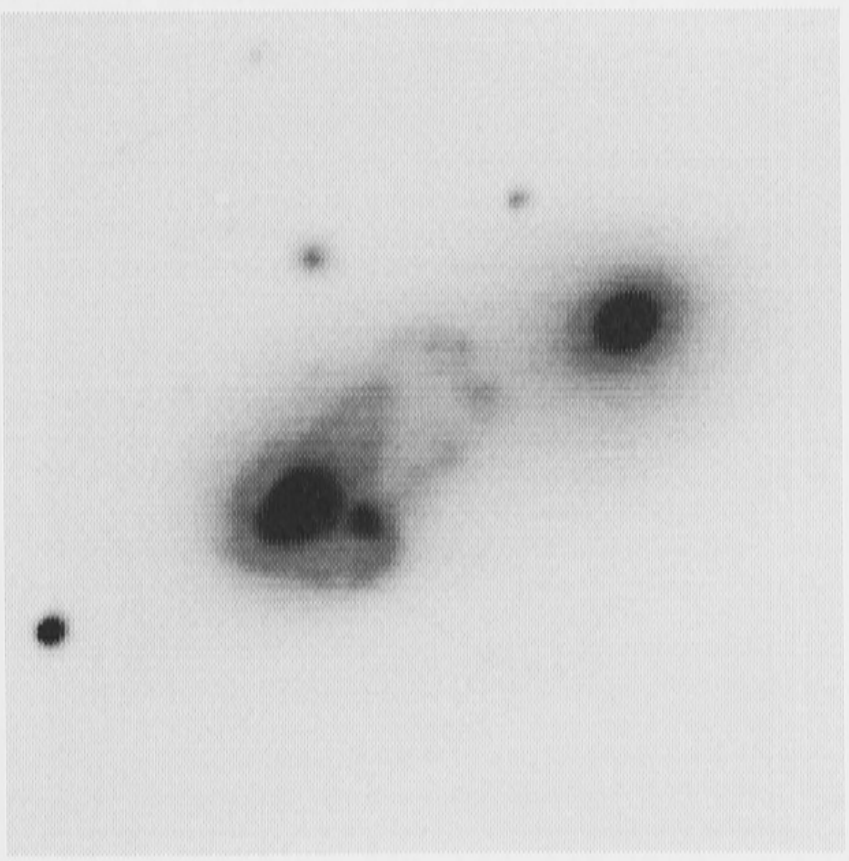

Figure 3.3: I image of Arp 118

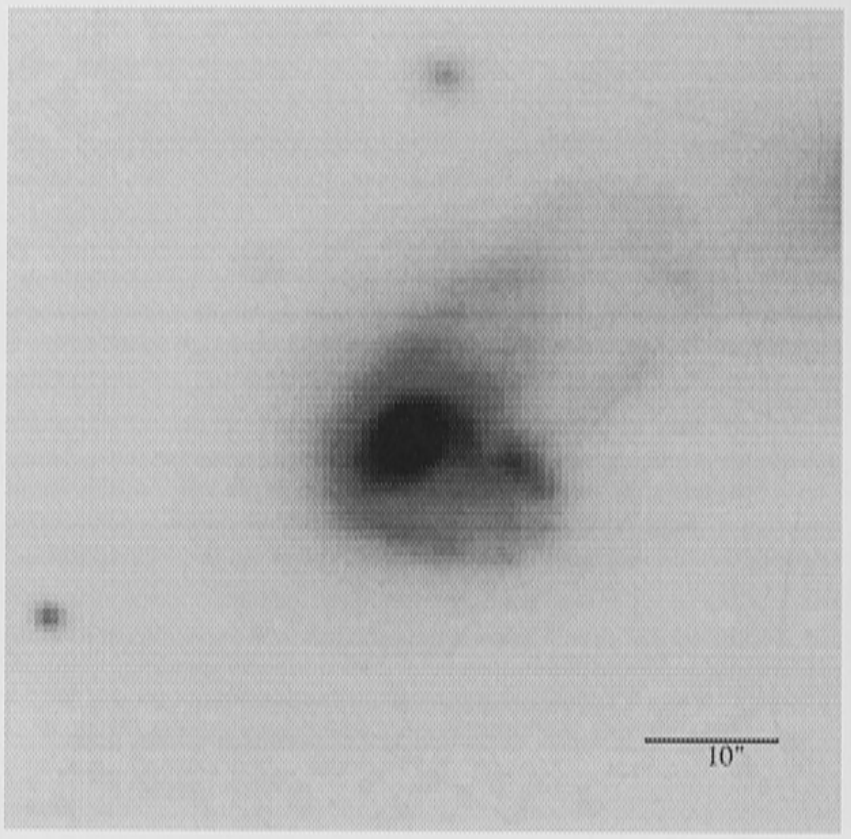

Figure 3.4: K image of Arp 118

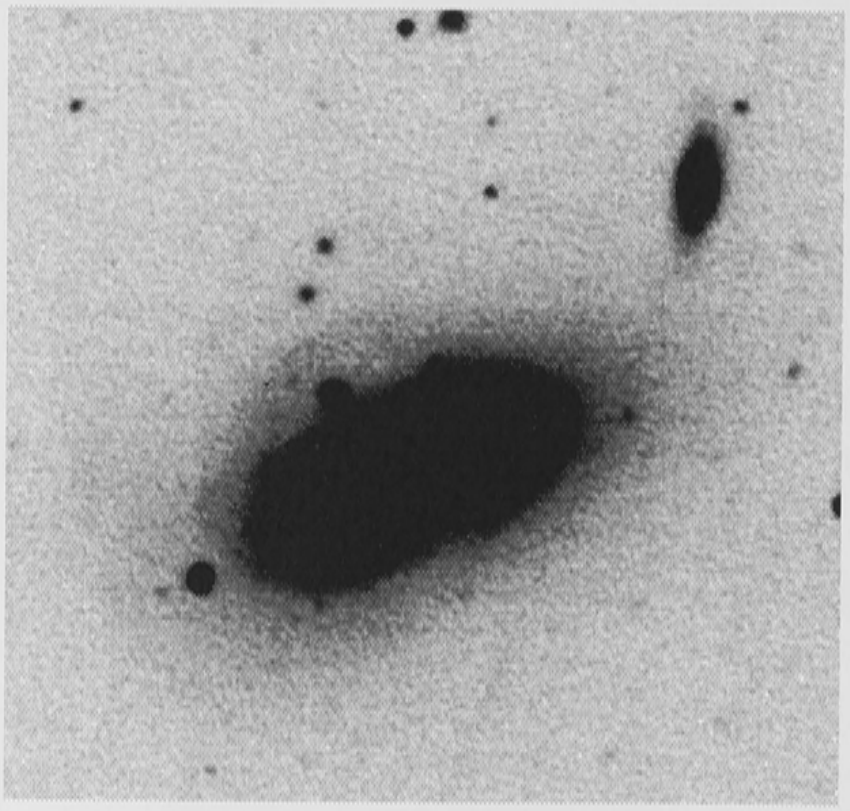

Figure 3.5: R-image of low surface brightness distribution in Arp 118

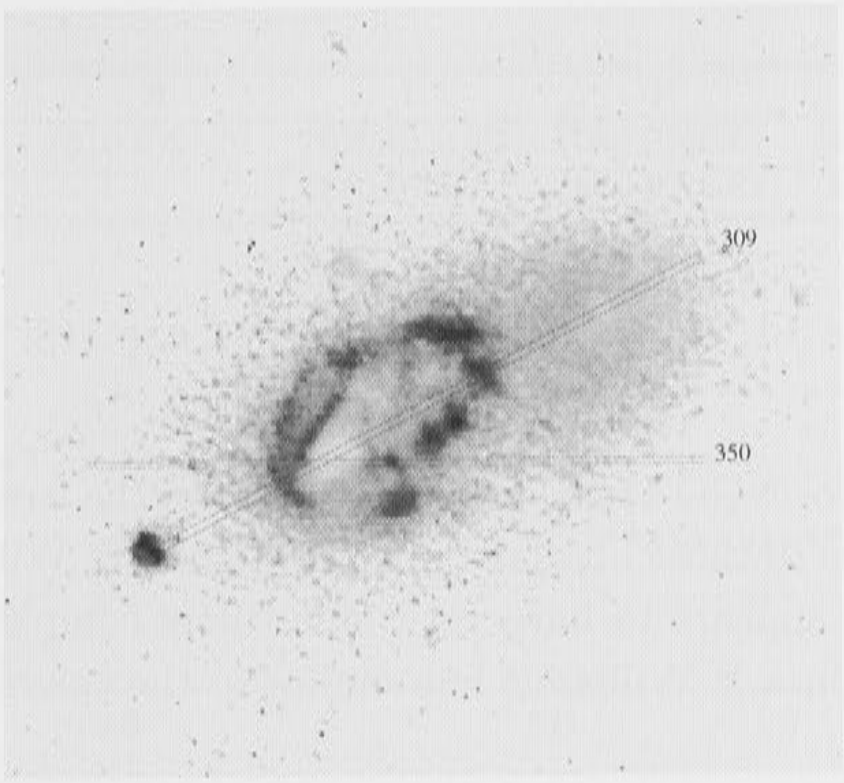

Figure 3.6: (B–R) image of Arp 118. The lines correspond to the positions of a 'slit' described in the next section.

The spheroidal companion lies about 40″ NW from the irregular; at a distance of $\simeq 110$ Mpc, this corresponds to a separation of 23 kpc. The outer isophotes of this component are aligned towards the irregular.

A deep image of Arp 118 shows two faint shells in the NE and eastern parts (Fig. 3.5). This low level luminosity can be traced out to at least 100 kpc. A neighbouring lenticular galaxy lies about 90″ NW from the pair; this galaxy has misaligned inner and outer isophotes. I attempted to measure its redshift but the spectra obtained has not enough S/N to discern any absorption lines; no emissions were detected.

The distribution of dust inside a galaxy can be studied from its (B–R) color distribution, provided the intrinsic color of its stellar population is uniform or smoothly variable. Fig. 3.6 shows (B–R) image of Arp 118: darker regions represent bluer color. One can see a knotty blue ring encircling the nucleus of NGC 1144; note that the part of the ring closer to the companion is bluer and more knotty. Inside the blue ring lies a slighly blue vertical structure. The nucleus itself, lying offset from the center of the ring, displays a red color, which implies dust is accumulated inside this region.

The integrated photometry for Arp 118 is shown in Tab. 3.1; with errors in brackets. No galactic extinction correction is applied henceforth unless mentioned otherwise; for reference, the reddening for Arp 118 is A_B=0.18 mag. Due to the small size of the AAT near-IR array, it was not possible to observe the spheroidal companion of Arp 118 in the near-IR. The K magnitude for NGC 1144 was calculated to be 0.06 Jy. Adopting the relationship derived by Thronson & Greenhouse (1988) for solar neighborhood, the K–luminosity would imply a stellar

Component	B	R	I	K	(B–R)	(B–I)	(B–K)
N1144	14.45(0.024)	13.29(0.010)	13.11(0.010)	10.12(0.015)	1.16	1.35	4.33
N1143	15.22(0.034)	13.97(0.014)	13.90(0.012)	–	1.25	1.32	–

Table 3.1: Integrated photometry of Arp 118.

mass of $\simeq 2\times10^{11}\ M_\odot$ for NGC 1144. While the colors of the irregular component have comparable values to those observed in spirals (Buta & Williams, 1995), the spheroidal companion appears to have very blue colors compared to early-type galaxies observed by Buta & Williams, but similar to the colors of its neighbour NGC 1144.

The surface brightness photometry of the system is shown in Fig. 3.7 and 3.8, corresponding to a slit positions at PA=309° ie. along the major axis, and 350°, ie. crossing the western bright knot; the path of the slit goes roughly from east to west and is shown superimposed on the B–R image. The width of the slit is chosen to be $\simeq 4$ pixel which corresponds to $\simeq 2\farcs5$.

The figures show more structure in B, R and I than at K, as we would expect. The peaks at d$\simeq$ –8″ and d$\simeq$–5″ at PA=309° and 350° respectively correspond to the southern loop and have very blue colors. The flat structure in the colors of the latter is due to the 'slit' going through what appears to be two adjacent spiral arms as can be seen in the (B–R) image. The hump at d=$\simeq$ 8″ (PA=350°) is the western knot, and has colors similar to the southern loop. At d$\simeq$ 24″ (PA=309°), the slit passes the (northern) ring and here the colors get bluer still, reaching B–R$\simeq$ 0.8 mag. Colors this blue can be assigned to a stellar population of the age of about 10^8 yr (Charlot & Bruzual, 1991). The (B–K) color for this part of the ring suggests that it suffers less dust obscuration than the regions closer to the nucleus in the south.

Where the slit goes through the nucleus, the colors become very red, reaching as high as (B–K)$\simeq$ 5.5 mag at its peak. The color distribution is asymmetric about the nucleus: the colors are redder to the east and bluer to the west, and is mostly pronounced in (B–I). This asymmetry suggests inhomogeneous obscuration by dust.

The K–band surface brightness distribution in the disk of NGC 1144 along PA= 309° is not well represented by a conventional bulge–disk decomposition. The surface brightness distribution around NGC 1143 is shown in Fig.3.9, a continuation of Fig.3.7 with the same origin in the absisca. In the R–band the inner regions follow an $r^{1/4}$ law.

The (B–R) color distribution within NGC 1143 is rather flat; in (B–I) a central peak is seen in the innermost few arcsec. The flatness of the color distribution

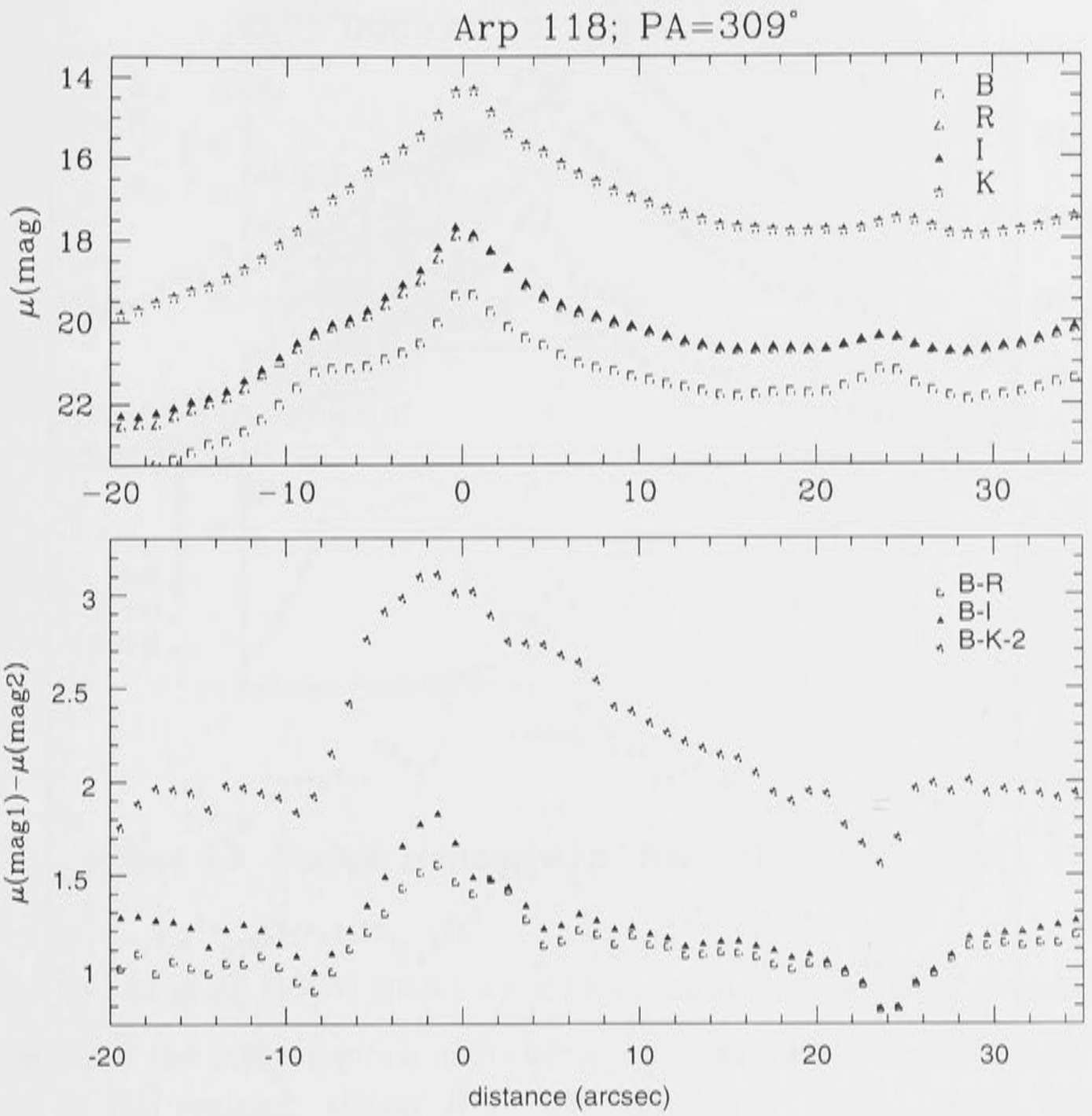

Figure 3.7: Surface photometry of NGC 1144 across the major axis (PA=309°); r=0 corresponds to the peak of the nucleus

is unlike that commonly observed in the central regions of early-type galaxies, and suggests that the nuclear region has suffered relatively recent star formation. There is no evidence for current star formation in this region, since no emission lines are seen in the spectrum of NGC 1143. It seems likely that starforming activity happened in the (recent) past, probably triggered by interactions with NGC 1144. A similar central 'bluing effect' was observed by Rampazzo *et al.* (1995) in some of the mixed interacting pairs they studied, and may be associated with mass transfer (cross-fuelling) from the gaseous component to the early-type component.

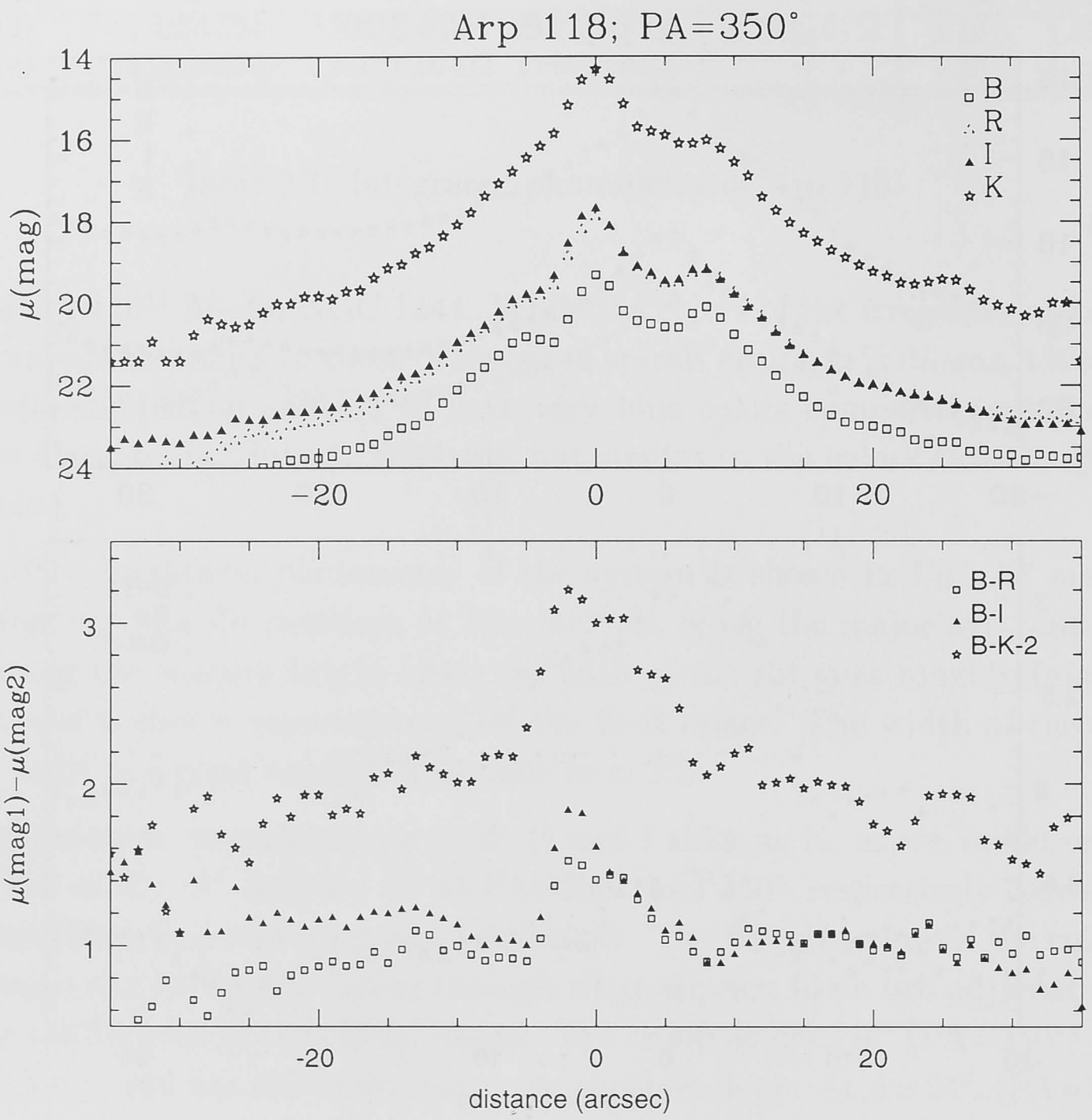

Figure 3.8: Surface photometry of NGC 1144 at PA=350°; r=0 corresponds to the peak of the nucleus.

3.1.3 Spectroscopy

The nucleus of NGC 1144 exhibits emission lines commonly observed in active galaxies. It shows strong [NII]λ6584 relative to $H\alpha$ ($\log([\mathrm{NII}]\lambda6584/H\alpha) \simeq 0.1$) and has the spectral properties of a Type 2 Seyfert galaxy. In addition to the breadth of the emission lines (eg. FWHM([NII]λ6584)$\simeq$ 700 km s^{-1}), they are observed to have multiple peaks, and its [NII]λ 6584 line exhibits a strong double-horned profile often observed in systems with accreting disks. Strong [OIII]$\lambda\lambda$ 4959,5007 lines are observed, which again display split profiles, but no $H\beta$ is detected. From these forbidden lines the heliocentric velocity of the nucleus is calculated to be $\simeq$ 8600 km s^{-1}. The CaII H and K lines give $V_{hel}\simeq$ 9000$\pm$100 km s^{-1} for the stellar component. Veilleux et al. (1996) reported observation of [OII]λ3727, $H\beta$ and [OI]λ6300 in the nucleus of NGC 1144, and the spectrum

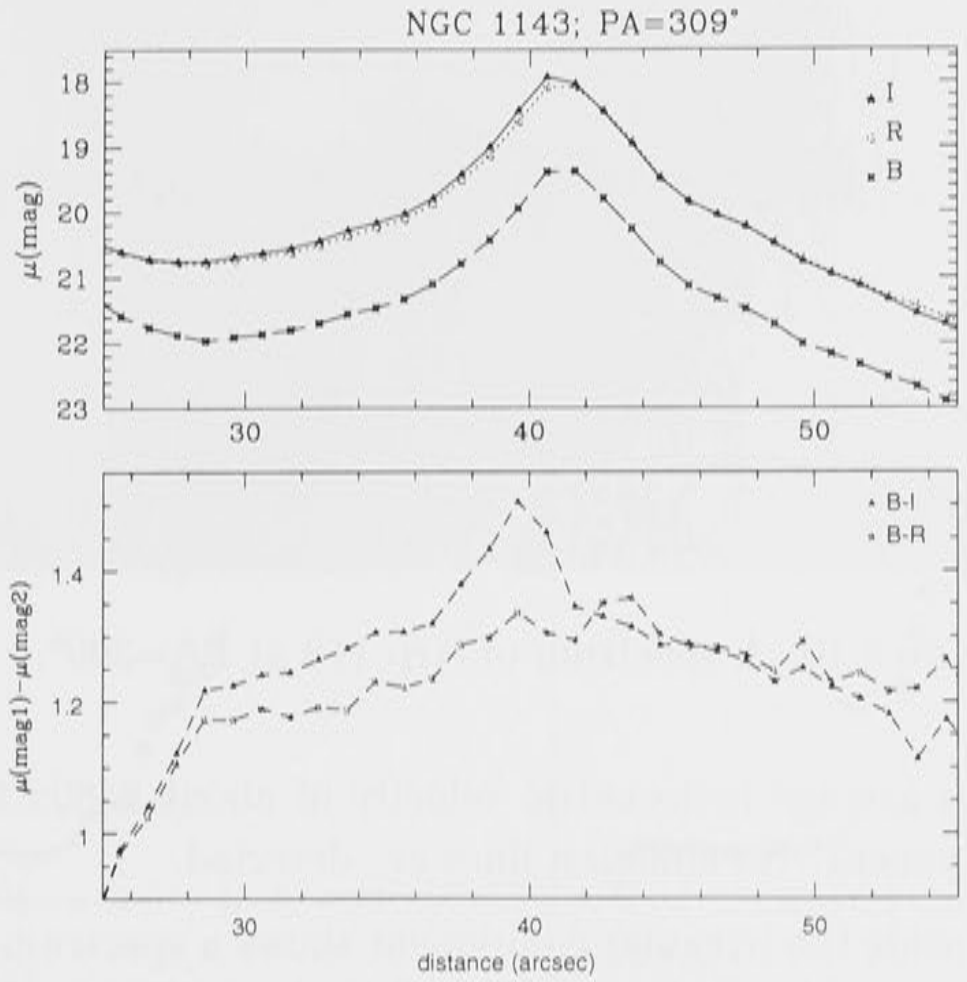

Figure 3.9: Surface photometry of NGC 1143 at PA=350°

obtained by Liu *et al.* (1995) shows a red continuum with a 4000Å break.

The spectra of the outer regions of the irregular components are typical of those observed in HII regions: strong $H\alpha$, accompanied by [NII]$\lambda\lambda$ 6548, 6584 and often [SII]$\lambda\lambda$ 6716, 6731 where the [NII]$\lambda\lambda$ 6548, 6584 to $H\alpha$ ratio in the range 0.3–0.7. These spectra show strong and knotty $H\alpha$emission in the areas where the blue ring lies. Here in these HII regions multiple peaks are again often observed. Between the two components of Arp 118, the spectra exhibit weak continuum emission, implying the existence of a diffuse stellar population in addition to the HII regions.

A spectrum from PA=309° is shown in Fig. 3.10; the spectrum of the spheroidal component lies in the lower part of the image not shown. The emission lines are $H\alpha$ (to the left) and [NII]λ 6583, and the continuum in the center comes from the nucleus of NGC 1144. Note how [NII]λ6583 in the nuclear region is much stronger than $H\alpha$, as commonly found in LINERs/active nuclei. Emission from various parts of NGC 1144 are identified in the figure. Worth mentioning is the sharp slope of the emission lines across the nucleus, and the very large velocity range within the system (about 20Å or 1000 km s^{-1} from one side of the disk to the other). This will be discussed further in the next sections.

The spectra of the spheroidal component show the H and K absorption lines of CaII typical of those observed from an old population; weak $H\alpha$absorption is also

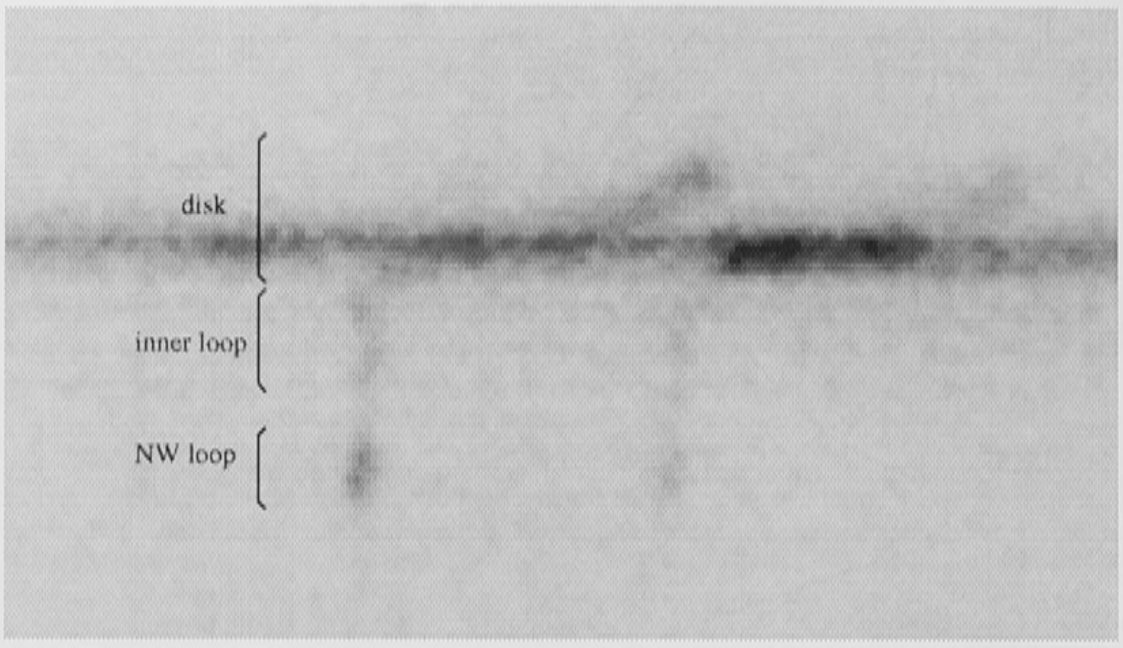

Figure 3.10: A spectrum of Arp 118 at PA=309°.

seen. These give an average heliocentric velocity of about 8480±100 km s^{-1} for the spheroidal component. No emission lines are detected.

The western knot inside the irregular component shows a spectrum typical of HII regions: emission lines of [NII]$\lambda\lambda$ 6548, 6584 , $H\alpha$ and [SII]$\lambda\lambda$ 6716, 6731, with $\log([NII]/H\alpha) \simeq -0.35$. However, these emission lines exhibit an asymmetric wing feature at the blue end of the line profile. The blue knot shows a weak continuum. The line ratios of the area coincidental with the A–source in J&G88's radio map are also typical of HII regions.

3.1.4 $H\alpha$ Kinematics

Spectra were taken at 12 PAs around Arp 118, as shown in Fig. 3.13. The velocity map was constructed from velocities measured from $H\alpha$ and [NII]$\lambda\lambda$ 6548, 6584, and [SII]$\lambda\lambda$ 6716, 6731 if they are strong enough. In most cases, the slit was positioned such that it passes through the nucleus of the spheroidal companion, which provides a precise reference for the slit location. In Figs. 3.11 and 3.12, the origin of the distance is at the nucleus of the spheroidal component, except for two slit position which do not pass through the nucleus of NGC 1143 (these spectra are denoted with an 'x').

The results are shown in Figs. 3.11 and 3.12.

The common feature observed in these longslit spectra is a constant velocity on the edge closer to the spheroidal companion and a steep velocity gradient across the inner disk of the irregular galaxy; this is clearly seen also in Fig. 3.10. Beyond this inner disk, the velocity curves mostly become flat again. The steep gradient, as can be seen in the figures, covers an extremely large range for the internal velocity of a galaxy: about 1200 km s^{-1}. Throughout the inner disk of the irregular component, multiple emission-line peaks are observed. It should be noted, however, that these

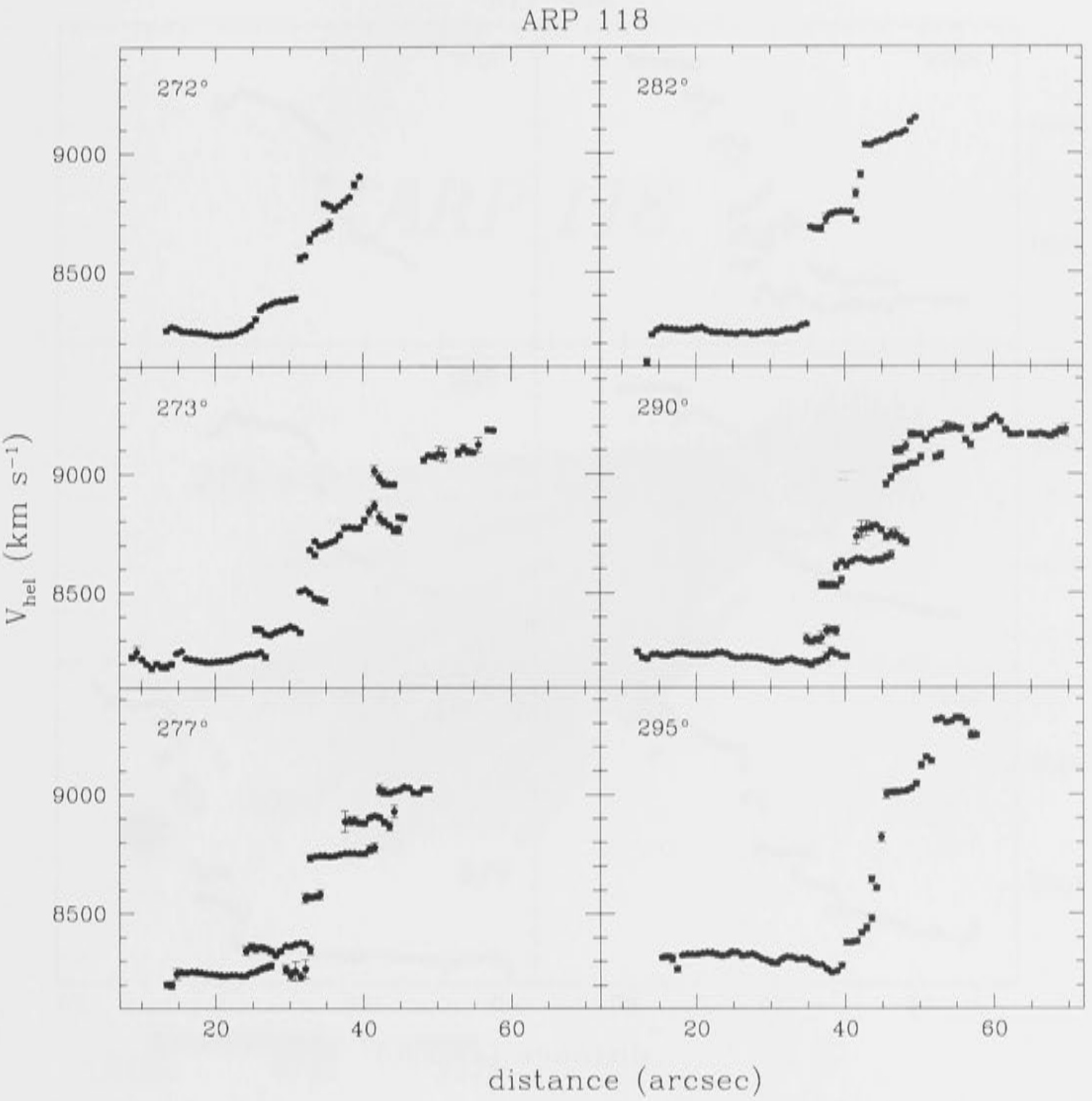

Figure 3.11: Velocities measured from different PAs over NGC 1144. Numbers on the top left corner in each box corresponds to the PA; the errors are cross-correlation errors.

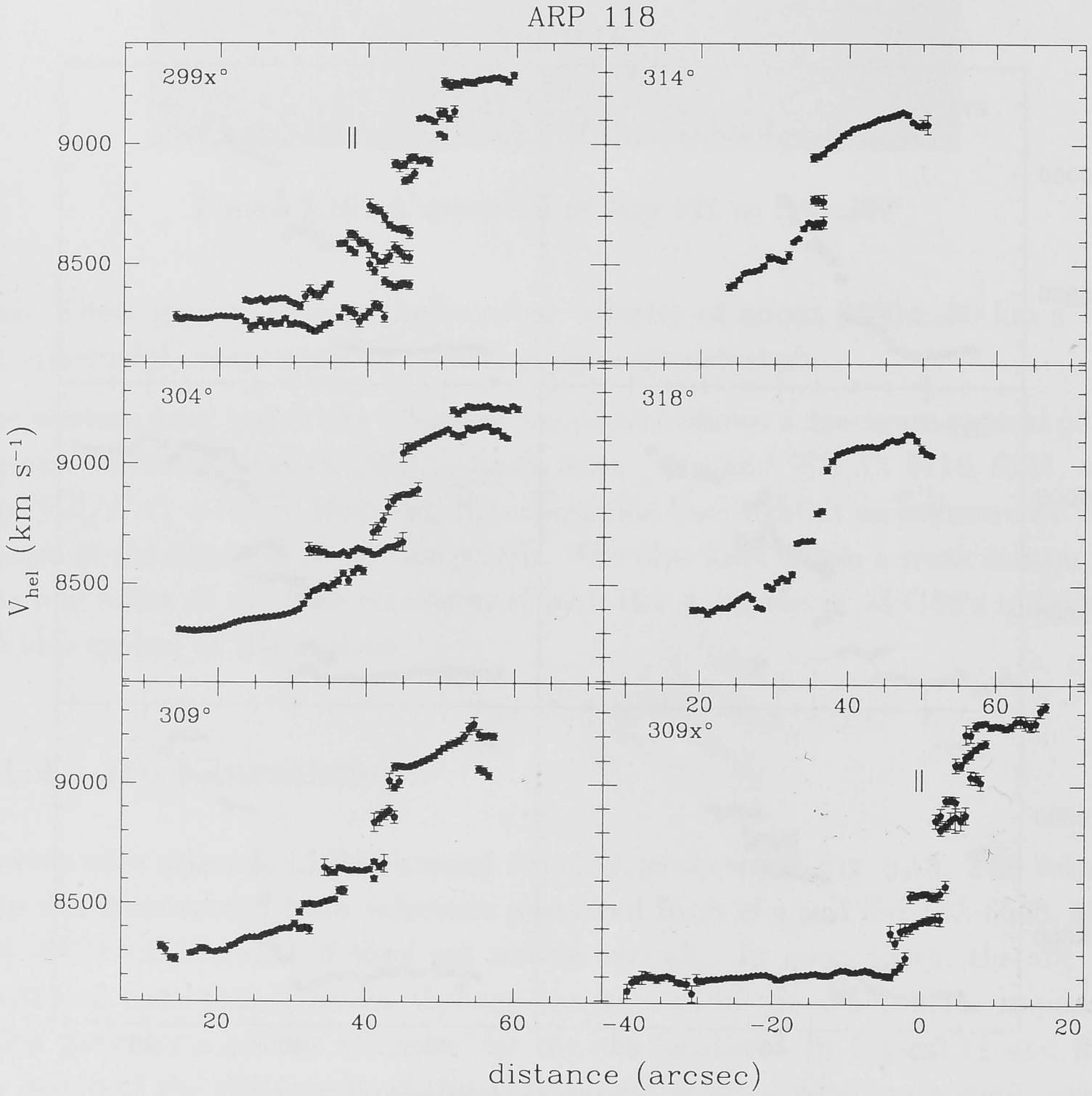

Figure 3.12: Velocities measured from different PAs over NGC 1144. Double-bars denote the location of the continuum of the nucleus; for PA=309x, this is at distance=0. X denotes PAs that go past the nucleus. Others the same as Figs. 3.11

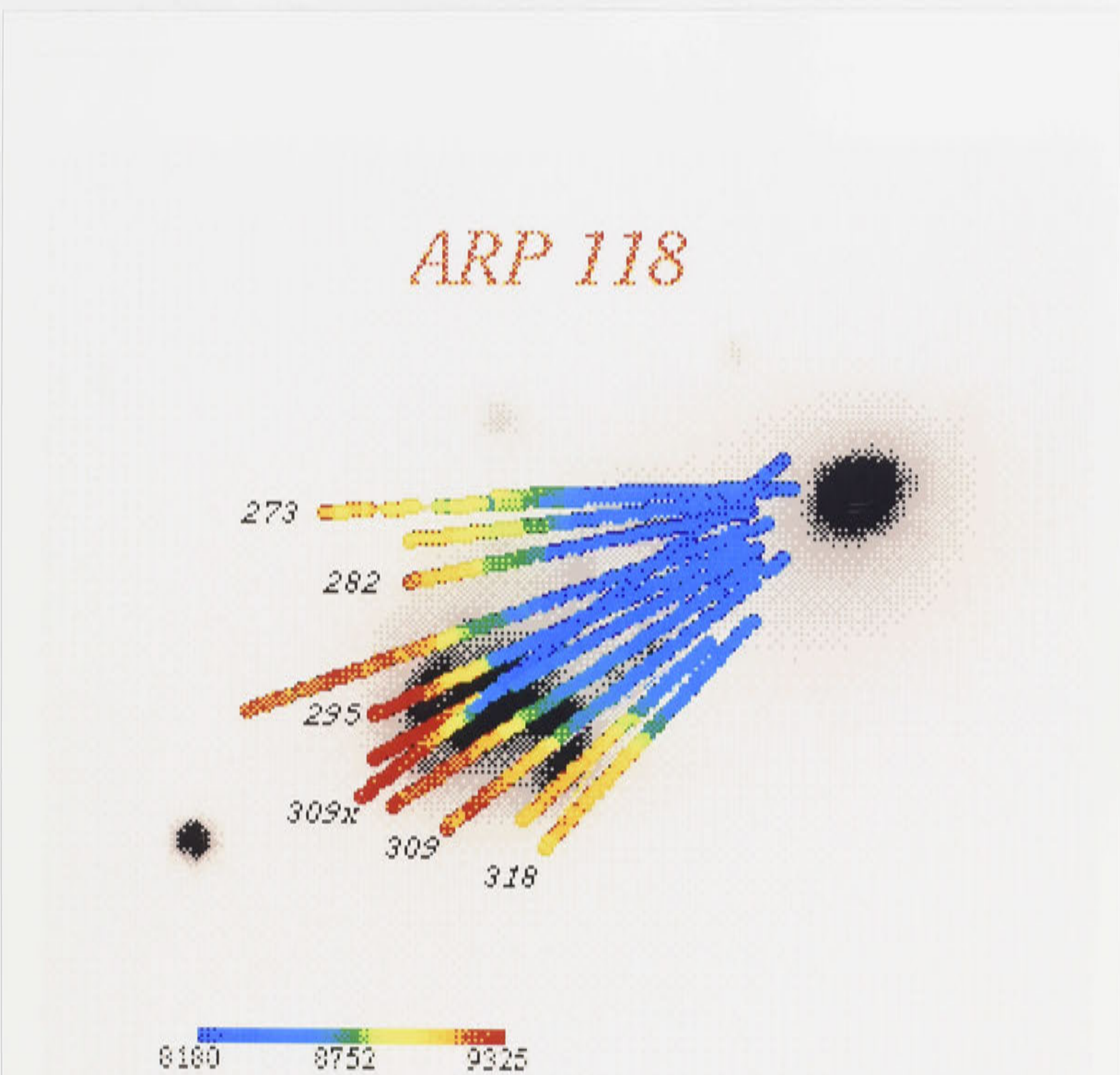

Figure 3.13: Overview of the kinematics inside Arp 118. Colors represent velocities and numbers at the ends are PAs.

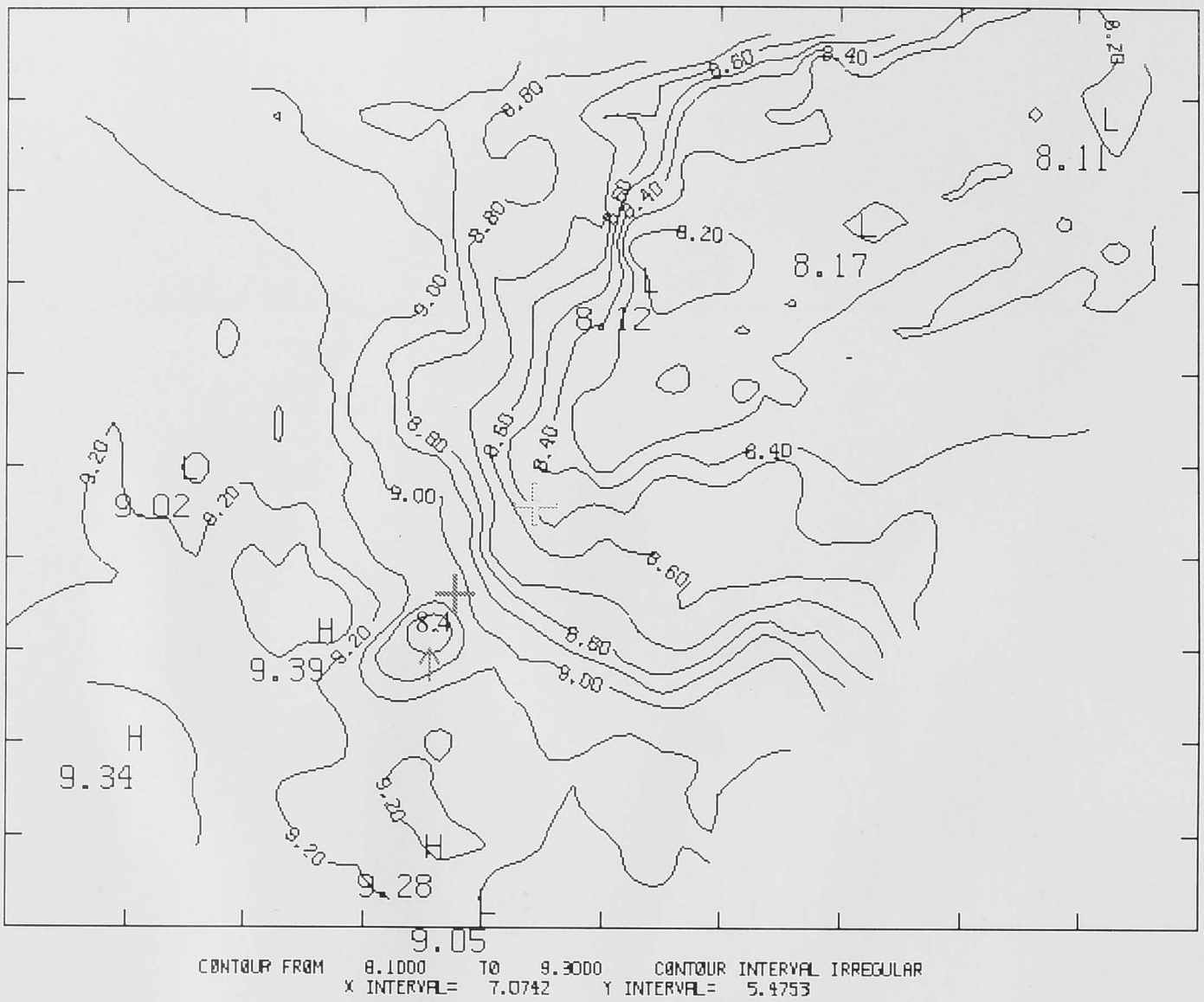

Figure 3.14: Velocity contours of NGC 1144 in units of 1000 km s^{-1}; the cross denotes the position of the nucleus of NGC 1144. Orientation similar to the images.

velocities come mainly from the strong [NII]λ6584 line.

An overview of the kinematics inside Arp 118 is shown in Fig. 3.13, where each line corresponds to the position of the slit and the velocities are color coded. The numbers at the ends are the position angles and in the lower left corner a color legend of the velocities is given. Here multiple velocities have been averaged and the colors have been stretched in the red to give emphasis on the large velocity gradient. The kinematics are superimposed on an R image of the system.

The figure shows a general trend of lower velocities in the NW and higher in the SE along the major axis of NGC 1144, implying that the irregular still experiences significant prdered rotation. The high velocity gradients are distributed mainly over the inner disk in the southern part of the system. The northern loop shows a rather homogeneous velocity distribution; relative to the broad band optical images, the $H\alpha$ emission extends closer to NGC 1143, suggestive of gas streaming towards the spheroidal companion. Otherwise, the emission of $H\alpha$ follows that of the optical distribution.

A velocity contour map of NGC 1144 is shown in Fig. 3.14. The largescale rotation is evident, but there is much velocity distortion: the nucleus is far from equidis-

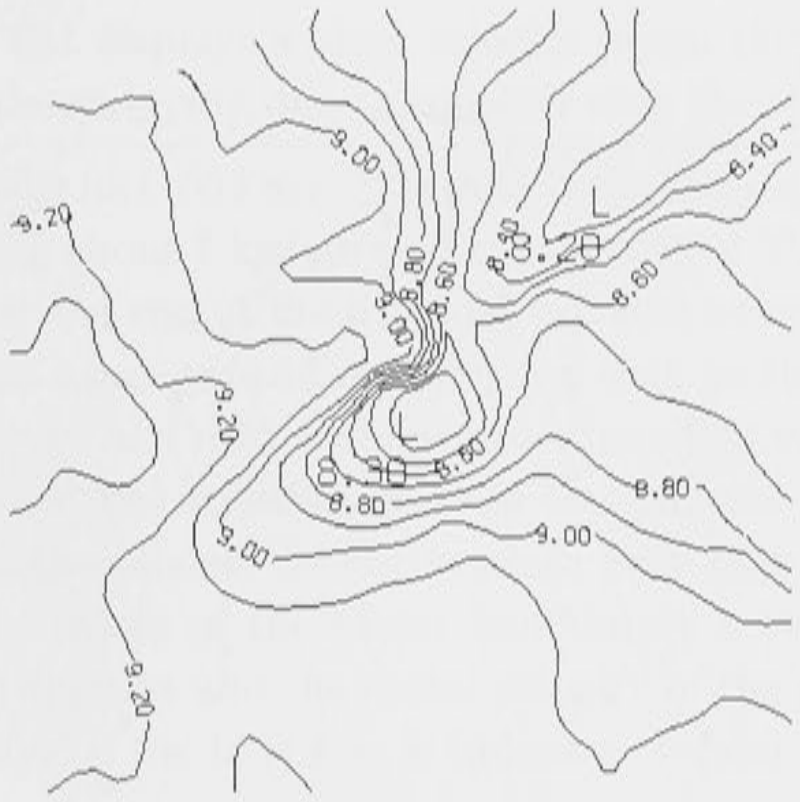

Figure 3.15: Velocity contours around the velocity discontinuity near the nucleus of NGC 1144.

tant from the closed contours, and the kinematic major and minor axes are not perpendicular. Strong non-circular motion is seen in the shapes of the iso-velocity contours. These velocity distortions can be attributed to interactions with the compact companion. A high velocity jump can be seen just next to the high closed velocity contour near the nucleus (arrow in Fig. 3.14). An expanded plot of the velocity contour near the nucleus is shown in Fig. 3.15, where the velocity jump mentioned above is better resolved. The position of this velocity discontinuity lies very near the nucleus, and it covers only a small region: this suggests that the active nucleus might play a role in producing this observed signature.

The blue ring of NGC 1144 displays a remarkably ordered sinusoidal velocity distribution, as can be seen in Fig. 3.16. Here each datapoint denotes a velocity on the ring at a particular position angle θ on the ring; θ=0° is along the major axis of the ring and towards the companion. The run of velocity against θ is well fit by a simple model with a circular ring at an inclination of 55° a rotational velocity of 646±17 km s^{-1} and a radial velocity of (±)51±25 km s^{-1} with a systemic velocity of V_{sys}=8560±9 km s^{-1} . This illustrates again the very large internal velocity scale for NGC 1144. The rotational velocity for this ring is much in excess of the rotational velocity for even the most rapidly rotating spirals.

3.1.5 Discussion

The morphology of Arp 118 is consistent with the outcome from a close but off-axis interaction between a disk and a compact intruder, as shown by Fig. 5 of Toomre (1977); note that in the models the intruder always lies near the minor axis of the ring. However, the velocity gradient inside the irregular component of Arp

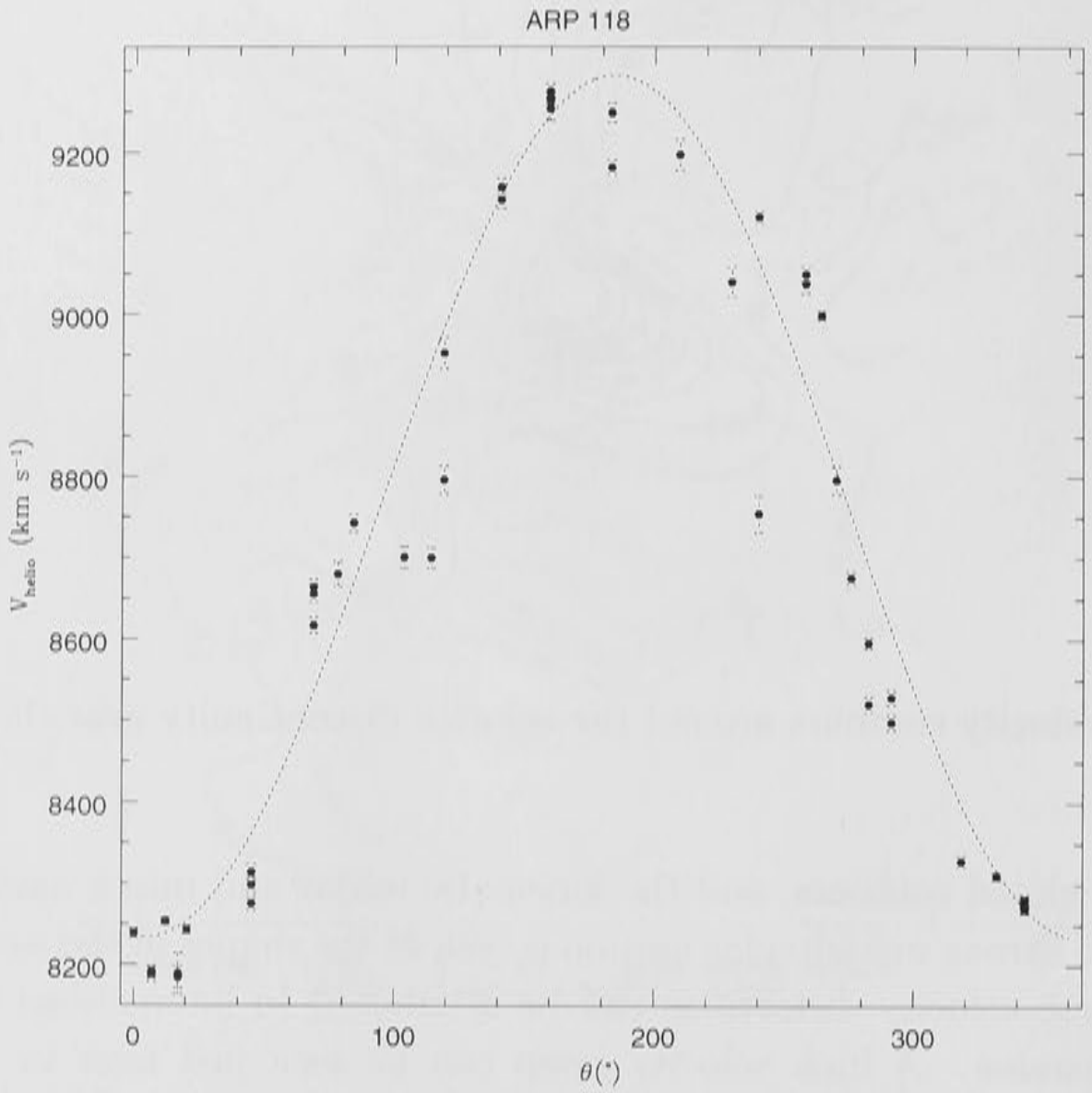

Figure 3.16: Velocity curve of the blue ring of NGC 1144 with position angle on the ring; θ=0°corresponds to the major axis of the ring in the north. The fitting curve is as mentioned in the tex.

118 is extremely large even for (common) interacting galaxies or giant galaxies in dense clusters. From the Tully-Fisher relation, large internal velocity scales are associated with bright galaxies. However in NGC 1144, the large internal motion is not accompanied by an extreme stellar luminosity, although NGC 1144 is relatively bright in the K–band ($\simeq 2\times10^{1}1L_{\odot}$).

The rotational velocity ($\simeq$ 650 km s^{-1}) derived from the velocity curve of the blue ring implies a dynamic mass of $1.2\times10^{1}2$. This gives M/L$\simeq$ 6 interior to the ring, which is large considering the small size of the ring. As a comparison, the largest known rotational velocity for a non–interacting disk galaxy is for the S0/Sa galaxy UGC 12591: its luminosity is L_B=2.1×10^{11} $L_{\odot}$, and its rotational velocity is V_{rot}=506 km s^{-1} (Giovanelli *et al.*, 1989) as measured from optical and radio data. For interacting pairs, Mrk 983, the late-type component of the interacting pair Arp 119, is known to have an extremely large velocity spread as well: 1300 km s^{-1}, contained inside a diameter of about 16 kpc (Marziani *et al.*, 1994). Unlike Arp 118, however, the velocity spread of Mrk 983 does not form a

continuous gradient but displays a large velocity jump; they suggested that this is a consequence of the stripping due to collision with the elliptical companion.

The large velocity range ($\simeq$1100 km s^{-1}) seen in the optical spectra is contained inside a region extending about 7 kpc around the nucleus of NGC 1144; the velocity gradient is steepest at the end of the irregular furthest away from its companion. One might regard this as an expanding disk/ring such as those demonstrated by the models of Gerber *et al.* (1996), where two expanding rings can coexist as a result of a (almost head–on) collision between two galaxies with a mass ratio of about 1:4. However, the models do not produce very high expanding velocities inside the rings. The colors of the bluest knot imply a very young population ($\tau_{ring} \sim$ 30 Myr) but the size and the radial velocity of the ring indicates a kinematic age of $\sim$300 Myr, if the blue ring is indeed a circular expanding structure. Nevertheless, the shape of the longslit emission lines, as shown in Fig. 3.10, strongly suggests asymmetric non-circular motion. This is supported by the 20cm radio map obtained by J86, where the southern loop shows a steep outer contour suggestive of a compressed front. Thus it is likely that radial motion is present and is responsible for the large observed internal motions inside the inner disk. The fact that NGC 1144 has a Seyfert 2 nucleus may also be relevant, since active galaxies are known to cause disturbed kinematics around the nuclear regions (see, for example, Whittle, 1989). I suspect this is what has happened to the kinematics of the immediate surrounding of the nucleus of NGC 1144 (see Fig. 3.15. However, the large spatial extent of the large velocity gradient throughout NGC 1144 might argue against the dynamical importance of an active nucleus. As concluded by Rubin *et al.*(1991) and Reshetnikov (1992), spiral galaxies in interacting systems and galaxy groups tend to have lower –about 75%– rotational velocities compared to isolated spirals (however, see White *et al.*, 1988). This again points to the possibility of NGC 1144 suffering radial motions at the expense of its observed velocity spread.

It has been shown that there also exists a sub-structure in the kinematics of NGC 1144 near the nucleus. The velocity drop is so drastic that it is unlikely due only to the interaction with the spheroidal companion but might be related to the extranuclear radio sources observed by J&G88. Unfortunately no corresponding structure can be observed in the images but it would be interesting to see whether there exists any compact complex of molecular clouds in the vicinity and how these clouds might behave kinematically.

Another question that arises concerning the kinematics of NGC 1144 is what causes the large difference between the (observed) velocity derived from the absorption lines, ie. stellar component, and that from the forbidden lines, ie. the gas: they are $\sim$8600 km s^{-1} and $\sim$9000 km s^{-1} respectively. A decoupling of the stellar kinematics from that of the gas is not uncommon in interacting pairs, yet a

difference of ~400 km s^{-1} is rather large. A study of the stellar kinematics inside this component is needed to understand the dynamics of NGC 1144 better.

Interactions between NGC 1144 and NGC 1143 has apparently caused the central region of the latter to suffer a 'bluing effect' due to recent star formation, presumably due to cross–fuelling by the gaseous component. The extent of the $H\alpha$ emission lines observed has gone as close as ~4 kpc from the center of NGC 1143, giving further proves that gas is being accreted by the spheroidal.

3.2 ARP 142

Arp 142 lies in a poor galaxy cluster designated as MKW 1S (Beers et al., 1984). It consists of a highly distorted irregular with an arc-like tidal feature (NGC 2936) partly encircling a compact spheroidal companion (NGC 2937). It has a rather high L_{FIR}/L_B ($\simeq$0.8) which is indicative of a starburst (Appleton & Struck-Marcel, 1987) but was undetected by IRAS at 12μm and 25μm. The irregular was observed by J86 to have weak (2.3 mJy) 20cm structures similar to the fan–shape observed in the optical. A later observation by Möllenhoff *et al.* (1992) confirmed this finding although the extent is more confined. They also discovered that the inner few arsec of NGC 2936 follow an $r^{1/4}$ profile but the outer regions are more indicative of an exponential disk; the companion is probably an elliptical galaxy.

3.2.1 Morphology and Photometry of Arp 142

The images of Arp 142 in B–, V–, R–, I– and K–bands are shown in Figs. 3.17, 3.18, 3.19, 3.20, and 3.21. The irregular component, NGC 2936, appears to curve from north to west around the spheroidal companion, NGC 2937. Its morphology in B, V, R and I shows a prominent dust lane arching along the irregular component and extending as far as the tidal tail of the irregular in the south. However, the impression is very different in the K–band: the dust lane vanishes and the irregular becomes a well-defined spiral galaxy with a prominent bulge and two distinctive spiral arms extending east and west.

Of the two spiral arms, the northern arm is smooth while the southern arm appears knotty, especially in the B image. The southern arm has two knots that consistently appear in all images: the eastern one almost disapears in I and K images and the western knot one is brightest in K. At low level brightness one can observe a bridge connecting the eastern knot with the spheroidal companion in the south, which suggests that some transfer of mass may be taking place. The apparent tidal tail in the K–image shows an smooth, elongated structure corresponding to the more knotty structures in B and R. The nucleus of NGC 2936 in the K–image appears to be displaced on the immediately-surrounding disk and

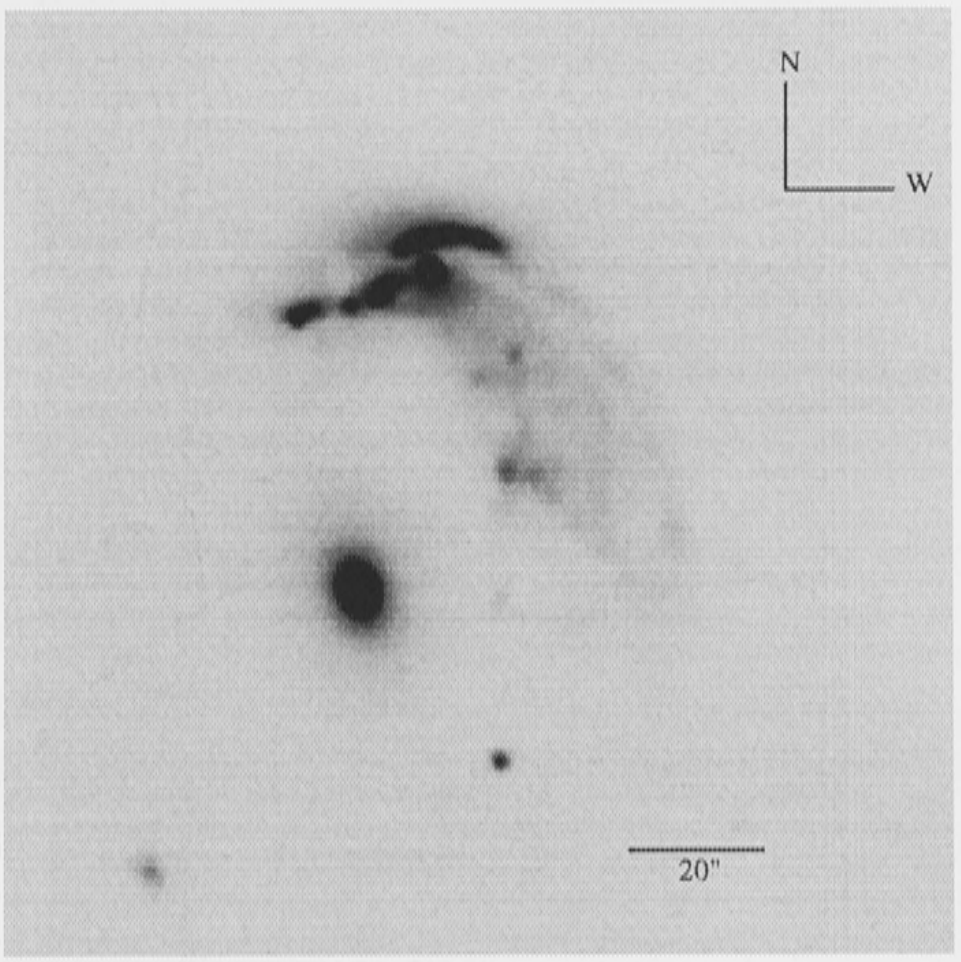

Figure 3.17: B image of Arp 142.

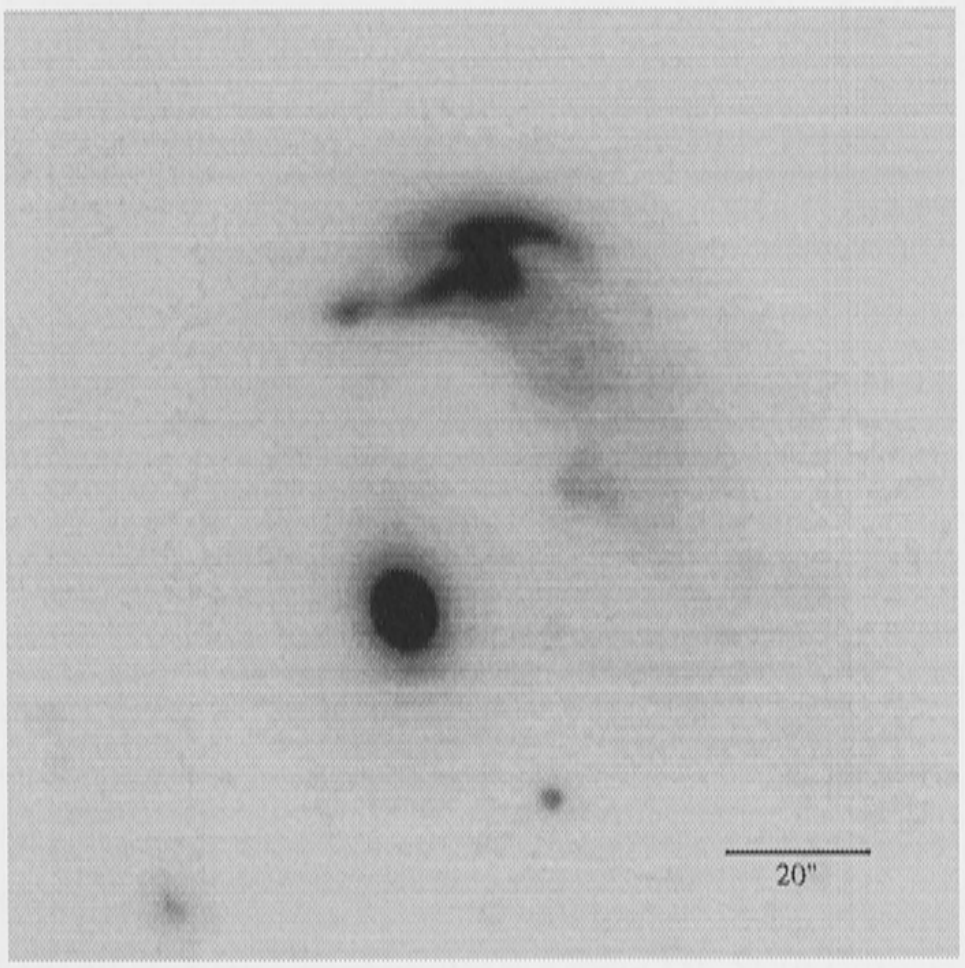

Figure 3.18: V image of Arp 142.

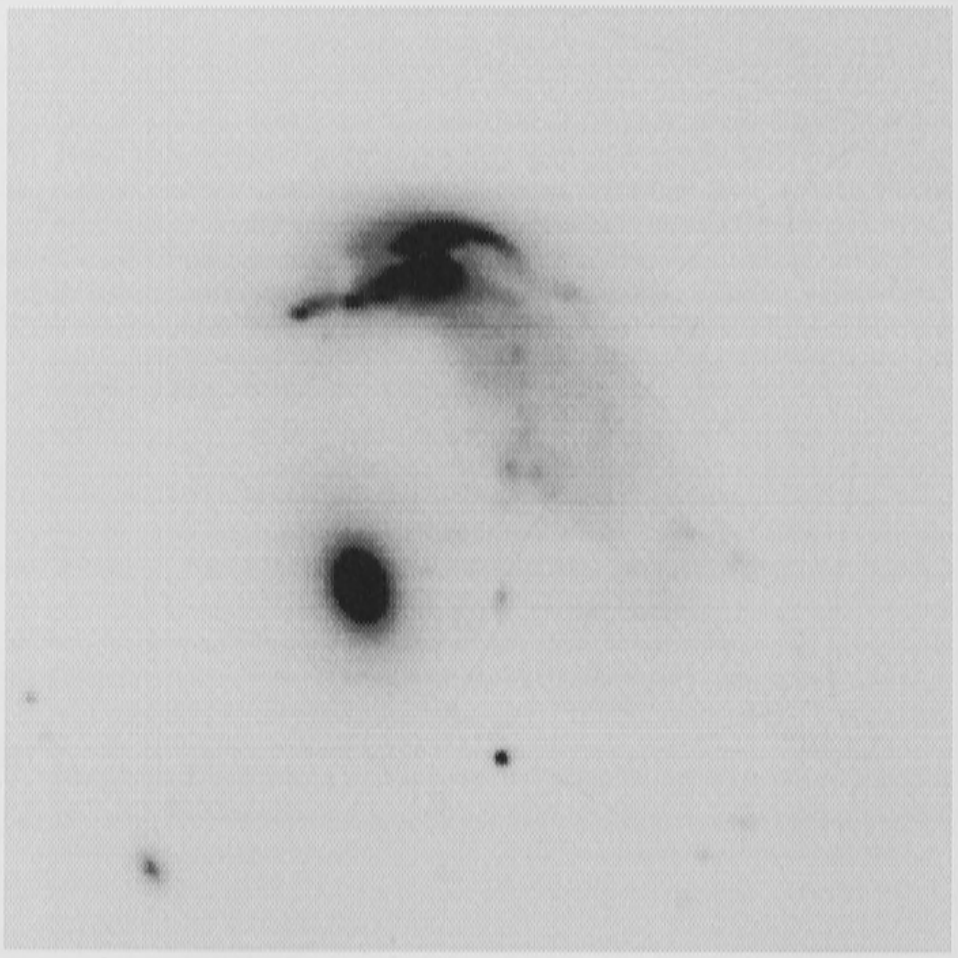

Figure 3.19: R image of Arp 142; scale similar to the B image.

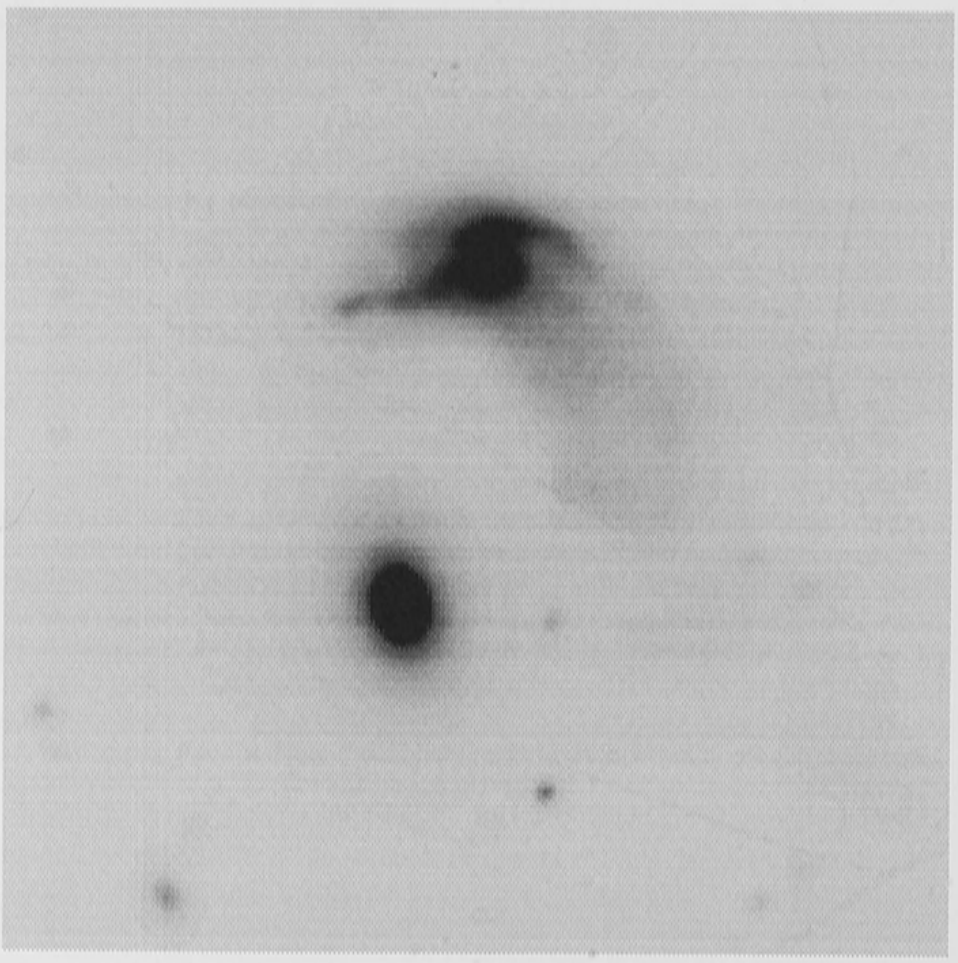

Figure 3.20: I image of Arp 142; scale similar to the V image.

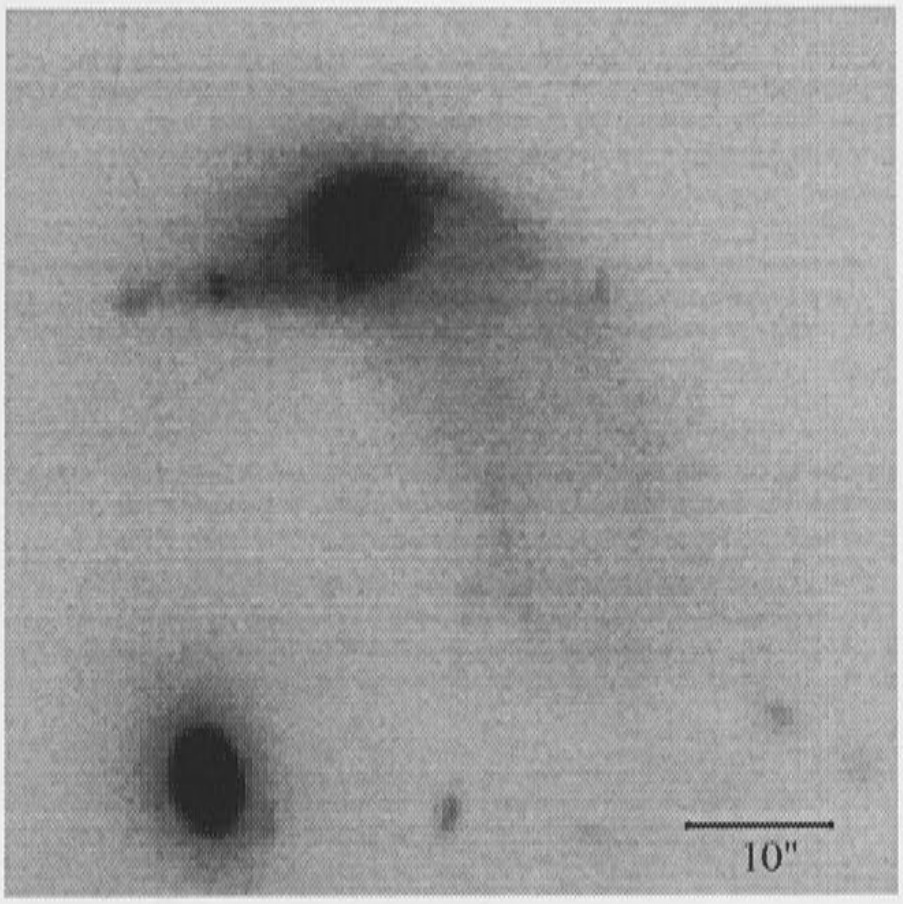

Figure 3.21: K image of Arp 142.

the inner isophotes have a major axis that is almost orthogonal to that of the disk.

The spheroidal companion, NGC 2937, lies roughly south from the irregular component. The separation between the two is $\simeq 50''$, corresponding to about 22 kpc, if a distance of 77 Mpc is adopted. This compact galaxy appears to be disturbed though not severely: its periphery is connected to NGC 2936 in the north and the west, and the isophotes are misaligned. In addition, $\simeq 6''.5$ SE from the center of the spheroidal component there exists a knot structure in the K–band; this is not observed in other passbands, and may be stellar in nature.

About $92''$ NW from the pair lies a jet-like structure partially hidden behind the image of a bright foreground star (see Fig. 3.23). This object on a closer look seems to be a clumpy edge-on galaxy with a brighter knot in the central area presumably to be the bulge. The part that lies south of the foreground obscuring star is fainter. The observable extent of this galaxy is about $61''$. My red spectrum exhibits $H\alpha$ emission from this object, extending to about $50''$ on both sides of the foreground star but stronger and longer at the northern end. Based on the its redshift, the object is at a distance of $\sim$65 Mpc and has a diameter of about 16 kpc for the $H\alpha$ emission and about 20 kpc in the R–band. The velocity spread covers an observed range of 4818–5100 km s^{-1}, this is including the weak split of the $H\alpha$ emission observed in the southern end. We conclude that this structure is not associated with NGC 2936/2937.

The integrated photometry of Arp 142 is shown in Table 3.2; notations as in that for Arp 118. The colors for both the irregular and the spheroidal components are

Component	B	R	I	K	(B–R)	(B–I)	(B–K)
N2936	12.83(0.020)	11.99(0.016)	11.49(0.016)	10.99(0.015)	0.84	1.35	2.11
N2937	13.90(0.028)	12.80(0.018)	12.18(0.018)	10.99(0.016)	1.10	1.72	2.55

Table 3.2: Integrated photometry of Arp 142.

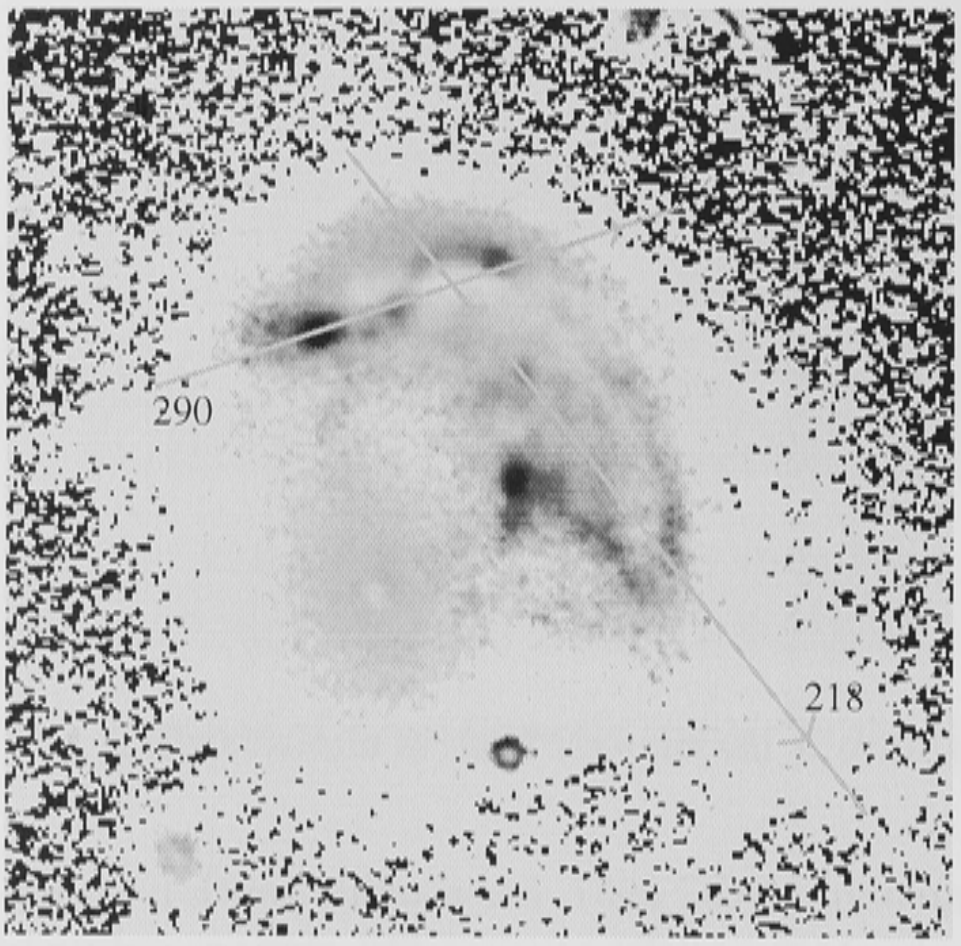

Figure 3.22: (B–R) image of Arp 142. Lines are surface brightness distribution as shown by the next images and arrows indicate the direction of the distributions.

typical of those observed for spirals and early–type galaxies, respectively. The K–magnitudes give stellar masses of 6×10^{10} $M_{\odot}$ for both NGC 2936 and NGC 2937; for the latter, however, this is probably a lower limit since the galaxy lies near the edge of the detector's field. An interaction between two components of comparable mass such as in Arp 142 is expected to disrupt the original morphology of the gaseous disk as soon as the intruder reaches the perigalactic distance, unless the encounter is a retrograde passage (Toomre & Toomre, 1972). Judging from the morphology and kinematics –as will be shown later– of NGC 2936, one can expect that the interaction between both components in Arp 142 is quite recent.

Fig. 3.22 gives the (B–R) image of Arp 142, indicating how dust is distributed inside the irregular component; darker colors correspond to bluer values. The dust distribution is similar to that observed in the B-band but can be observed to extend further south in the tail where it grows wider. The blue spiral arms form an S-shape across the nucleus of the irregular and are fainter in the region where the dust lane crosses. The arms are knotty at both the ends; the eastern

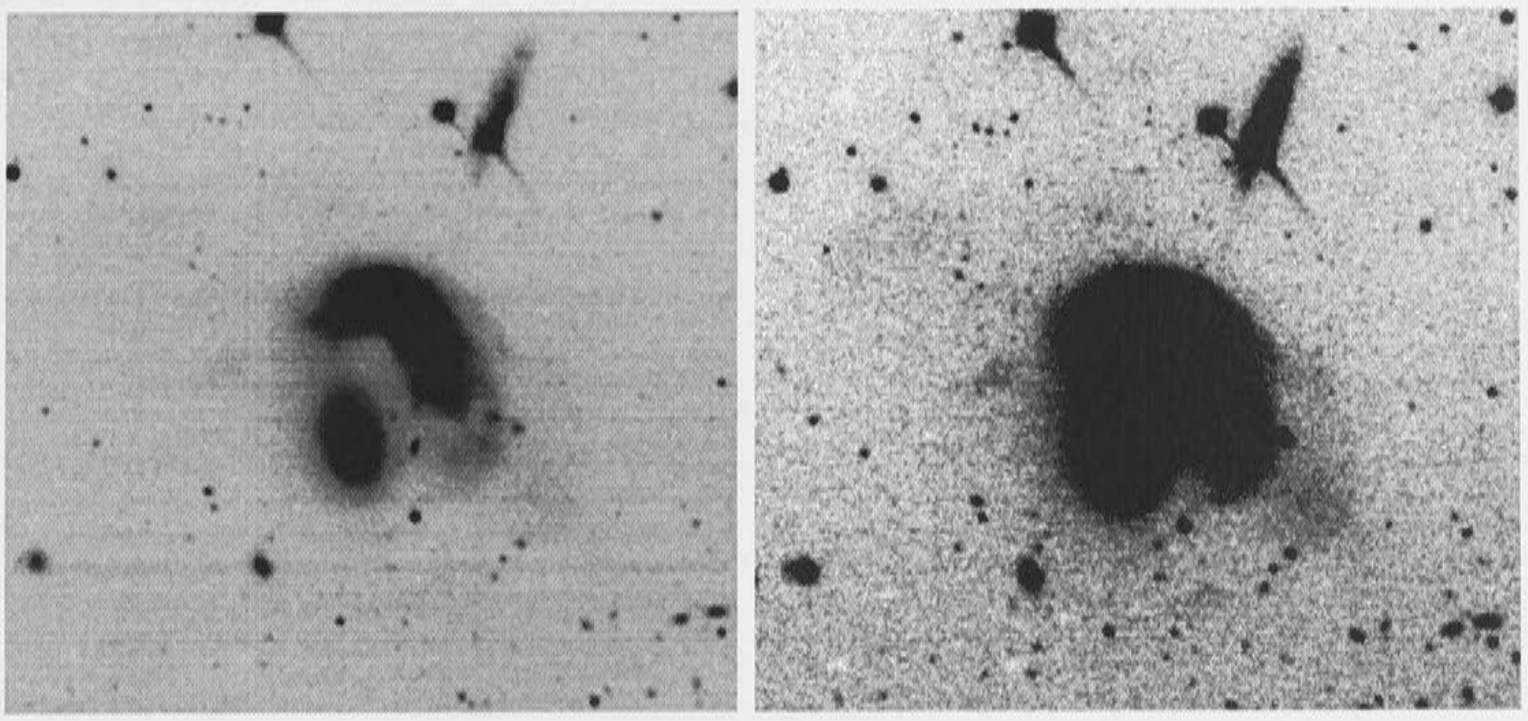

Figure 3.23: Two levels of low surface brightness distribution in Arp 142

knot is observed to peak in the 20 cm radio continuum observed by Möllenhof *et al.* (1992) and, together with the other knot in the tail, is the bluest structure inside Arp 142. It seems likely that a starburst is taking place here. The nucleus itself is heavily obscured and hence hardly obvious in this image. Inside the tidal tail, condensations can be seen, and the bluest one exhibits two jet-like structures pointing towards the southern end of the tail. The SE 'jet' extends further towards the low surface brightness structure seen in Fig. 3.23. A similar feature can be seen extending from the eastern (blue) knot in the eastern spiral arm; its shape gives an impression of a half-cone.

The very low surface brightness distribution of Arp 142 extends from NE to SW but also to the north, as shown in Fig. 3.23 (right). The extent corresponds to a dimension of arcs/shells curving along the tail of the irregular component (Fig. 3.23, left).

Surface photometry of Arp 142 is shown in Figs. 3.24 and 3.25; the PAs are shown superimposed on Fig. 3.22 and the width of the slit used is 4 pixels ($\simeq 2\farcs5$); both PAs go through the nucleus and the dust lane. Due to the non-photometric conditions of the observing runs, only B, R and K magnitudes are shown here.

At PA=218°, the 'slit' starts with the eastern arm north of the nucleus where the (B–R) color experiences a blue dip suggestive of a young population. The dust lane is manifested by the sudden depression in B and R magnitudes just before the peak of the nucleus. Here the (B–K) color rises steeply and becomes very red, reaching 5.6 mag. Note the asymmetric shape of the peak, both in (B–R) and (B–K), as the dust lane passes the northern part of the nucleus. As the slit crosses the tail, the (B–R) color becomes bluer still.

At PA=290°, the first structure encountered is the bright knot in the eastern arm, where it reaches a very blue color of (B–R) $\simeq 0.6$ mag; a color this blue is

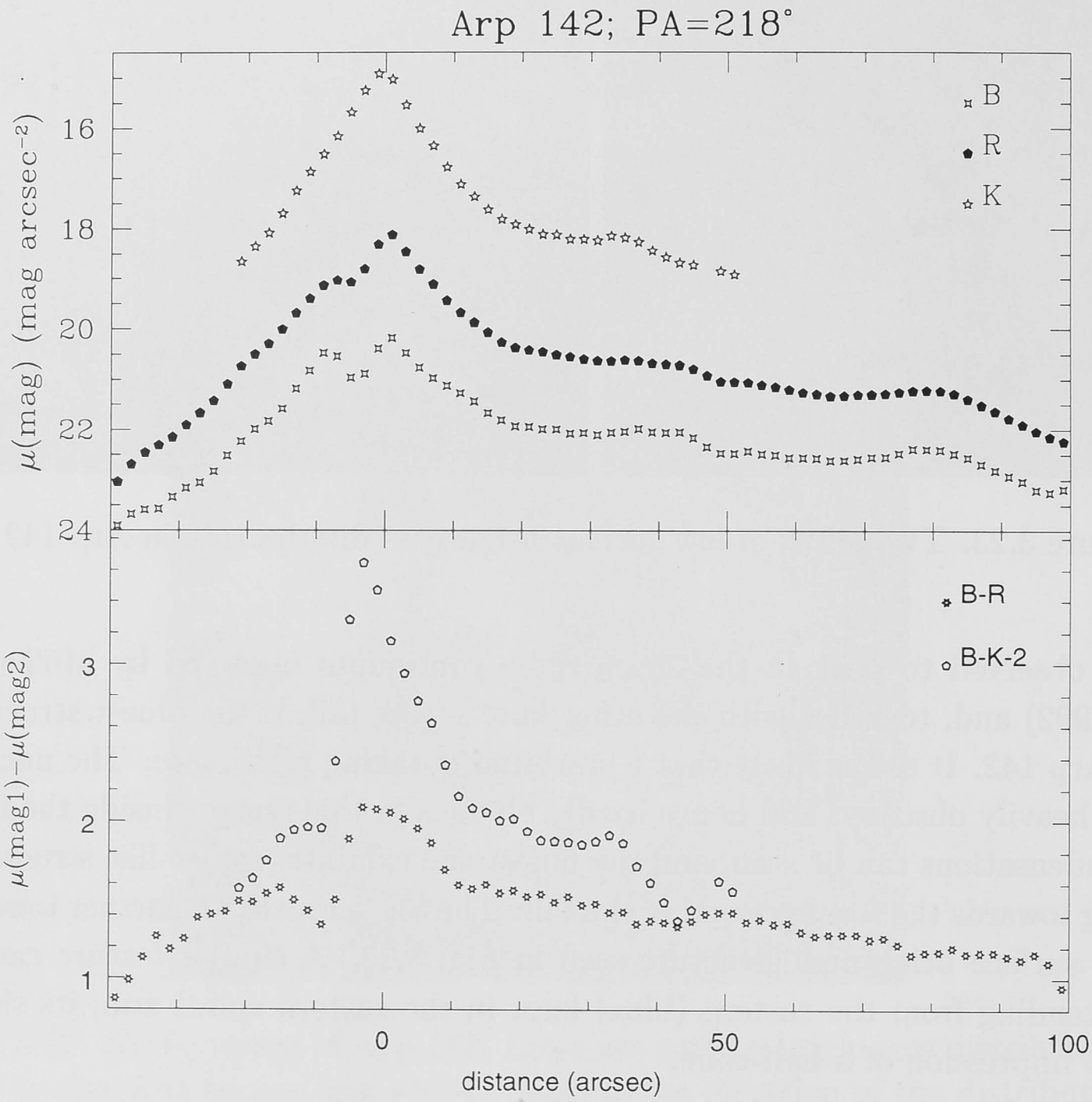

Figure 3.24: Surface photometry of NGC 2936 at PA=218°

expected to come from a very young stellar population. This region is known to be a radio continuum source, and the $H\alpha$ emission is strong and knotty inside this area. The subsequent knots in B and R become redder; this might be due to the stronger effect of dust obscuration closer to the nucleus of the irregular. But this effect, as can be seen in the B–image, is strongest in the western part of the nucleus, where (B–R)$\simeq$ 2.2 mag and (B–K)$\simeq$ 5.5 mag. Here the dust appears to be asymmetrically distributed inside the nucleus. The peak in the K magnitude at d $\simeq$ –14″ corresponds to the bright condensation in the K–image, and, considering the relative position of this knot to the dust lane, might be suffering a significant amount of obscuration in B and R. The nucleus is very red in (B–K), not surprisingly since this region is very dusty in addition to having an old stellar population as commonly observed in galactic bulges.

The inner few arcsec of the surface brightness profile of the irregular in K–band

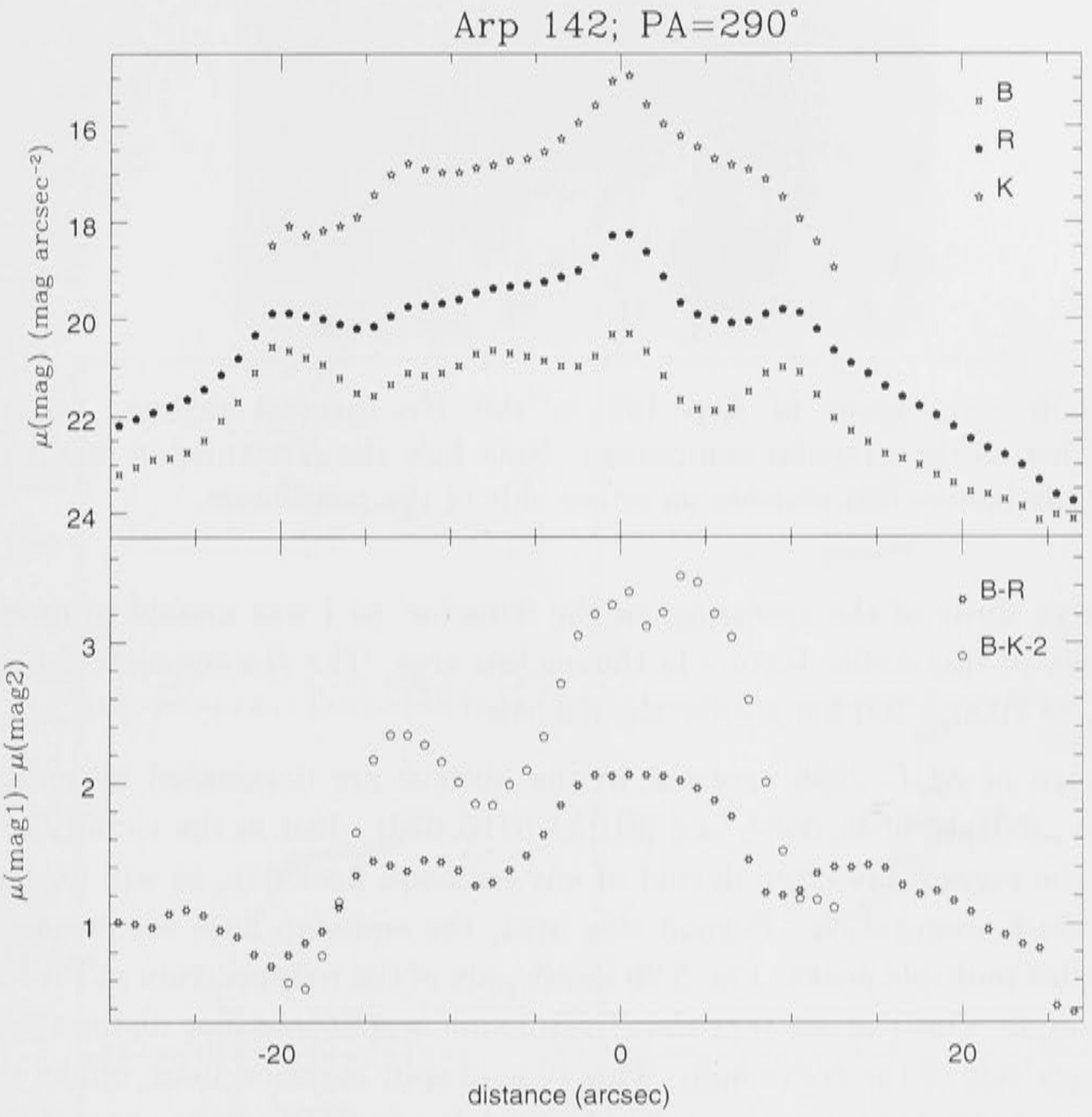

Figure 3.25: Surface photometry of NGC 2936 at PA=290°

follows a de Vaucouleur's law. This is in accordance with the result of Möllenhoff *et al.*(1992). The spheroidal companion, on the other hand, appears to be governed by a weak bulge and a disk.

3.2.2 Spectroscopy

The spectra of NGC 2937 show the CaII K and H lines and the G band as expected from an old stellar population. The average heliocentric velocity given by these lines is 6750 km s^{-1}. No emission lines are detected in the range of 6500-6800Å (rest wavelength) but there is a weak $H\alpha$ in absorption.

The spectra of the nucleus of NGC 2936 exhibit weak $H\alpha$ and [NII]λ 6584 in emission. Here the CaII lines are observed as well. Unfortunately, the refrigeration for the blue detector of the DBS failed at the time of these observations: this failure

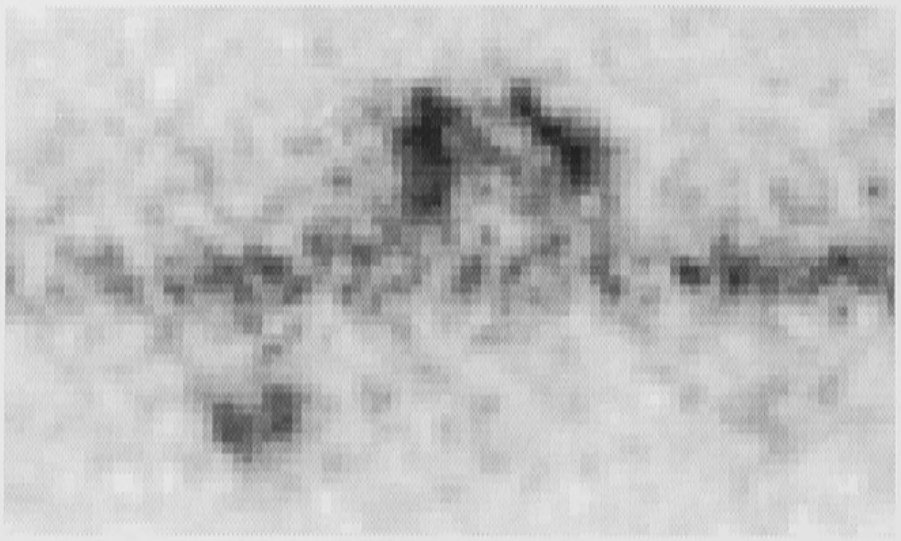

Figure 3.26: Spectrum of Arp 142 in the $H\alpha$ spectral regime, taken at PA=275° across the irregular component. Note how the $H\alpha$ emission line is split into four distinctive components on either side of the continuum.

causes large shifts of the spectrum on the detector, so I was unable to measure the velocity of this stellar feature in the nuclear area. The $H\alpha$ emission line gives $V_{hel,N2936} = 7000 \pm 100$ km s^{-1} for the nucleus.

The spectra of NGC 2936 external to the nucleus are dominated by emission lines: $H\alpha$, [NII]$\lambda\lambda$ 6548, 6584, and [SII]$\lambda\lambda$ 6716, 6731. Just in the vicinity of the nucleus, the regions are often devoid of any emission lines due, as will be shown later, to dust obscuration. Beyond this area, the emission lines are strong and often exhibit multiple peaks. Fig. 3.26 shows part of the red spectrum at PA=275° as an example. One can see that the $H\alpha$ emission is split into four distinct peaks: two on each side of the continuum. This type of split emission lines, unlike those observed in NGC 1144, is commonly observed for ionisation cones projected on an inclined galaxy disk; I will discuss this further in subsequent sections.

3.2.3 $H\alpha$ Kinematics

Longslit spectroscopy from 22 PAs positioned acros Arp 142 is used to study the kinematics of this interacting system; notations are the same as for Arp 118. Figs. 3.27, 3.28, 3.29 and 3.30 show the results of each PA, where heliocentric velocity is plotted agains projected distance in arcsecond; see 3.31 for location of the slit in each PA.

The velocities in the western and southern parts of the irregular (PA=270° to 319°) generally have flat distributions, although here and then multiple peaks begin to appear. Nearer to the spiral structure the velocity distributions become more complicated. For example, starting from PA=334°, the velocity jumps become higher ($\simeq 300$ km s^{-1}). Across the main spiral structure, more coincidental with the distribution of the dust lane in the vicinity of the nucleus, these velocity jumps becomes more extreme ($\simeq 400$ km s^{-1} at PA=303x°). The structure of the

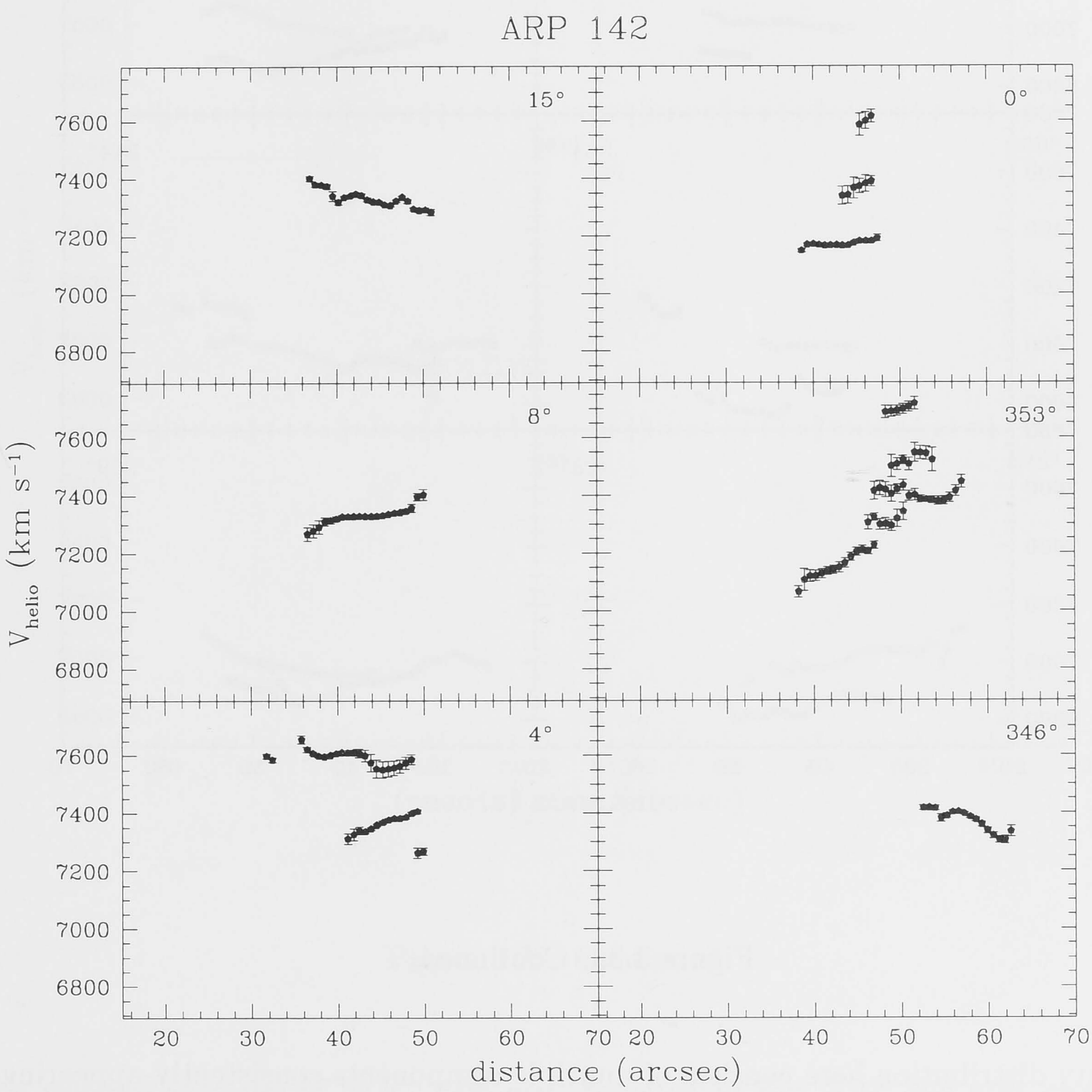

Figure 3.27: Velocities measured from different PAs over NGC 2936. Notations similar to Fig. 3.11

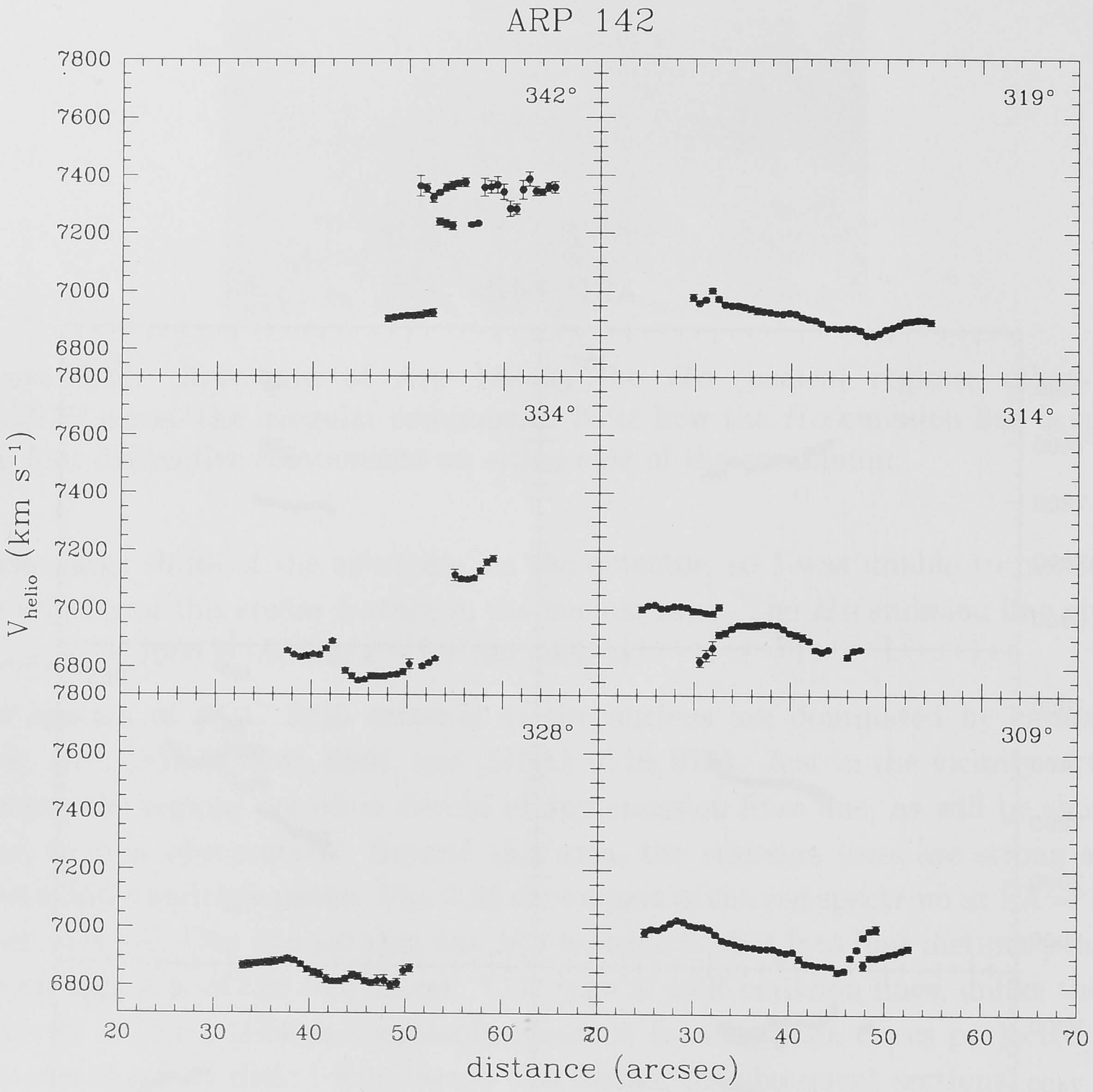

Figure 3.28: Continued.

velocity distribution here consists of multiple components consistently appearing for a certain distance. The largest velocity spread is exhibited by PA=275x°, where $\Delta V \simeq 800$ km s^{-1}. Combining all the PAs, the internal velocity spread of NGC 2936 is 980 km s^{-1}.

As an overview, a kinematic picture superimposed on an R–image is shown in Fig. 3.31. Little or no $H\alpha$ emission is detected in each single–pixel in the nuclear region of NGC 2936, possibly suppressed by dust obscuration. For example, part of PA=261°crosses the strongest dust distribution, hence the lack of emission in that region. This causes inability to obtain velocity information in this region. The tidal tail of the irregular has a fairly uniform velocity distribution, with velocities close to that of the spheroidal companion (~6750 km s^{-1}).

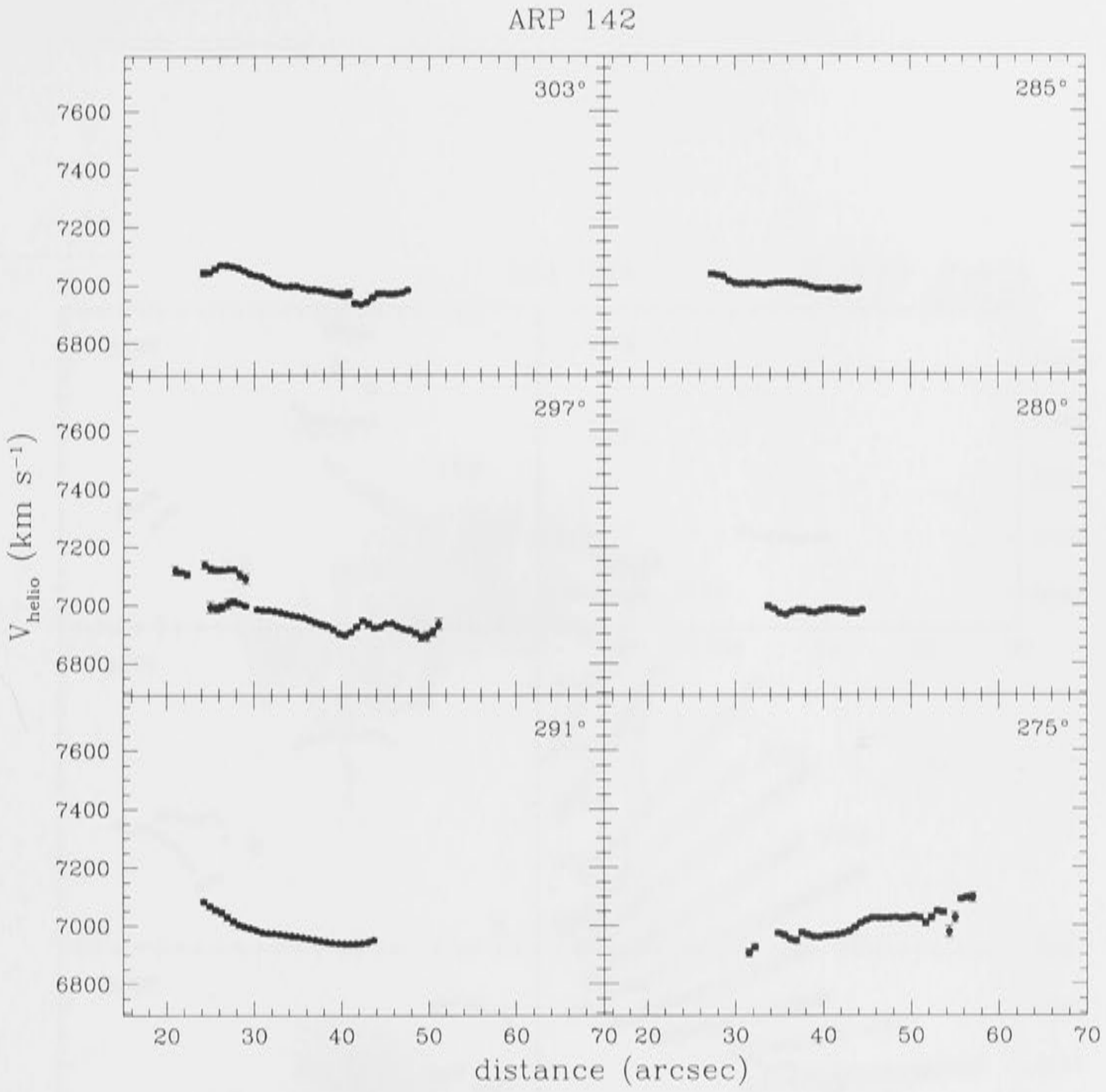

Figure 3.29: Continued

The velocity contours of NGC 2936 are presented in Fig. 3.32; the gray crosses in the north and south represent the approximate positions of the nuclei of the irregular and spheroidal components, respectively. Multiple velocities have been averaged here. Numbers are velocities per thousand of kilometers per second; other notations as in Fig. 3.14 of Arp 118. It is obvious that ordered rotation is still the dominant global kinematic feature in NGC 2936. There are closed isovelocity contours at both ends of the kinematical major axis, which runs roughly from SE to NW. The major and minor kinematic axis are roughly perpendicular, indicating that there is no gross warping. The nucleus of NGC 2936 appears to be displaced from its center of kinematics, away from the companion in velocity. Inside the extended tail, the velocity distribution appears to rise slowly away from the center

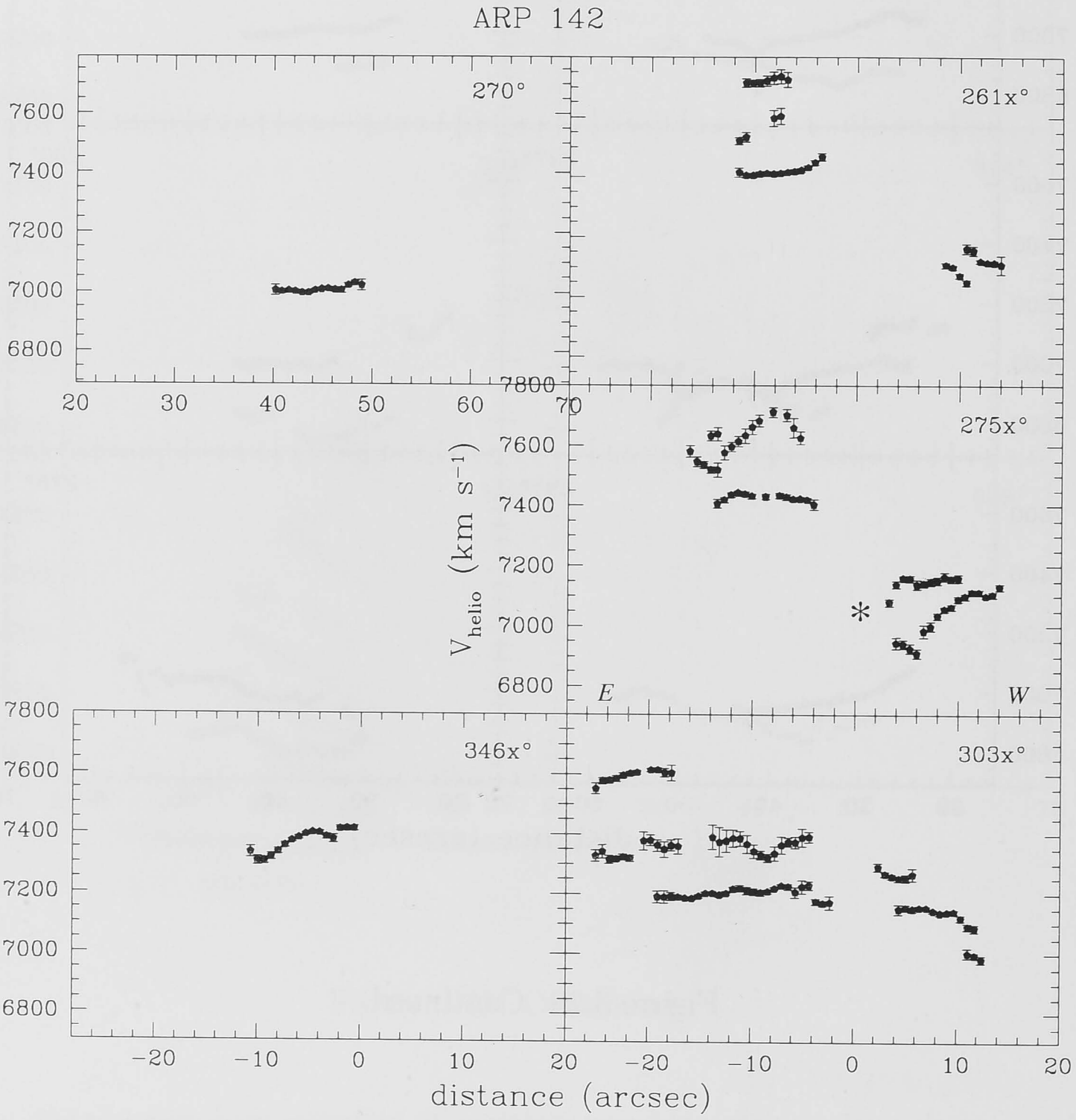

Figure 3.30: Continued, but for PAs that go through the nucleus of NGC 2936. The star in the PA=275x° box denotes the velocity of the nucleus of NGC 1144 measured from its $H\alpha$ emission line.

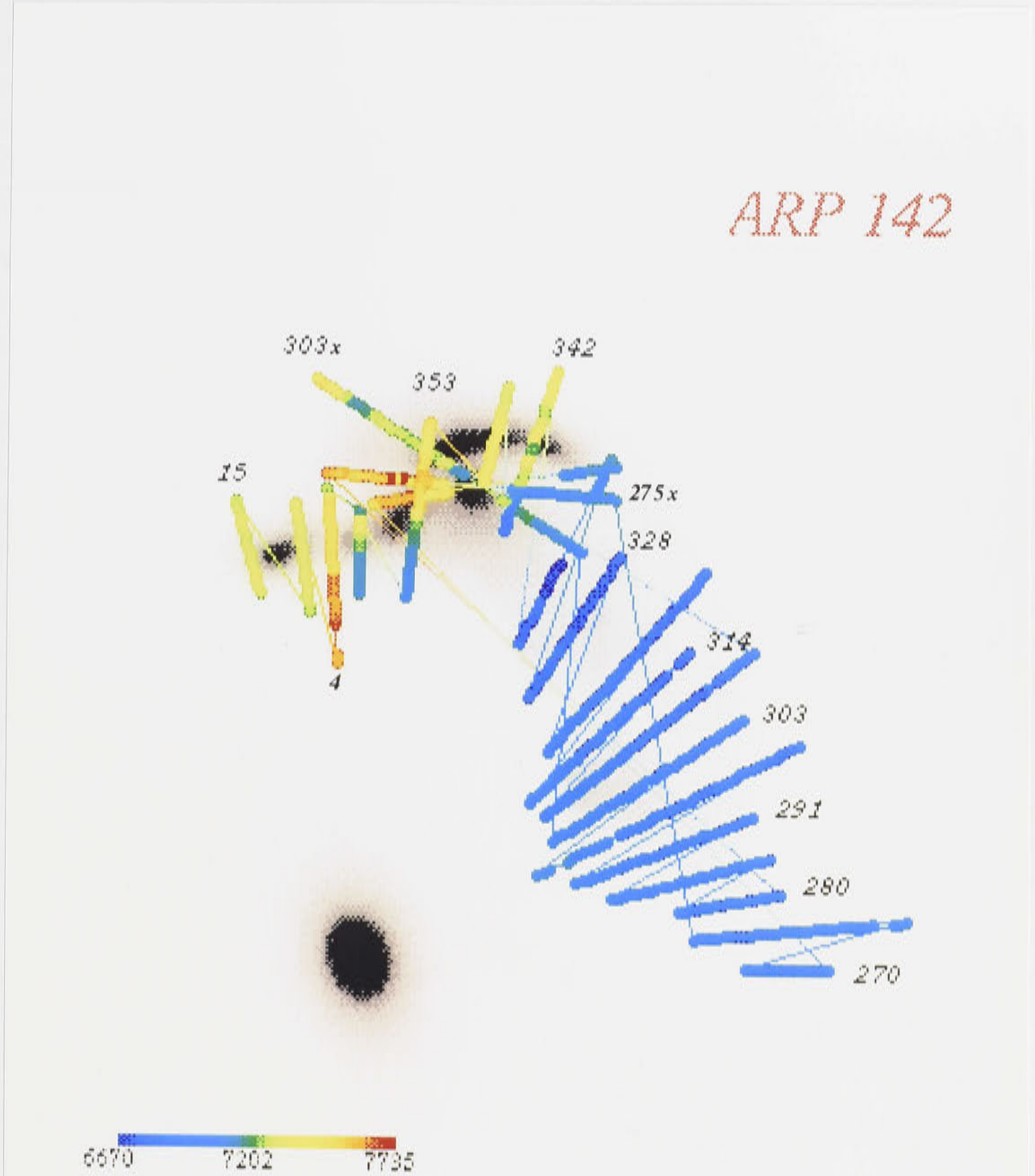

Figure 3.31: Velocity distribution of NGC 2936, superimposed on an R–image

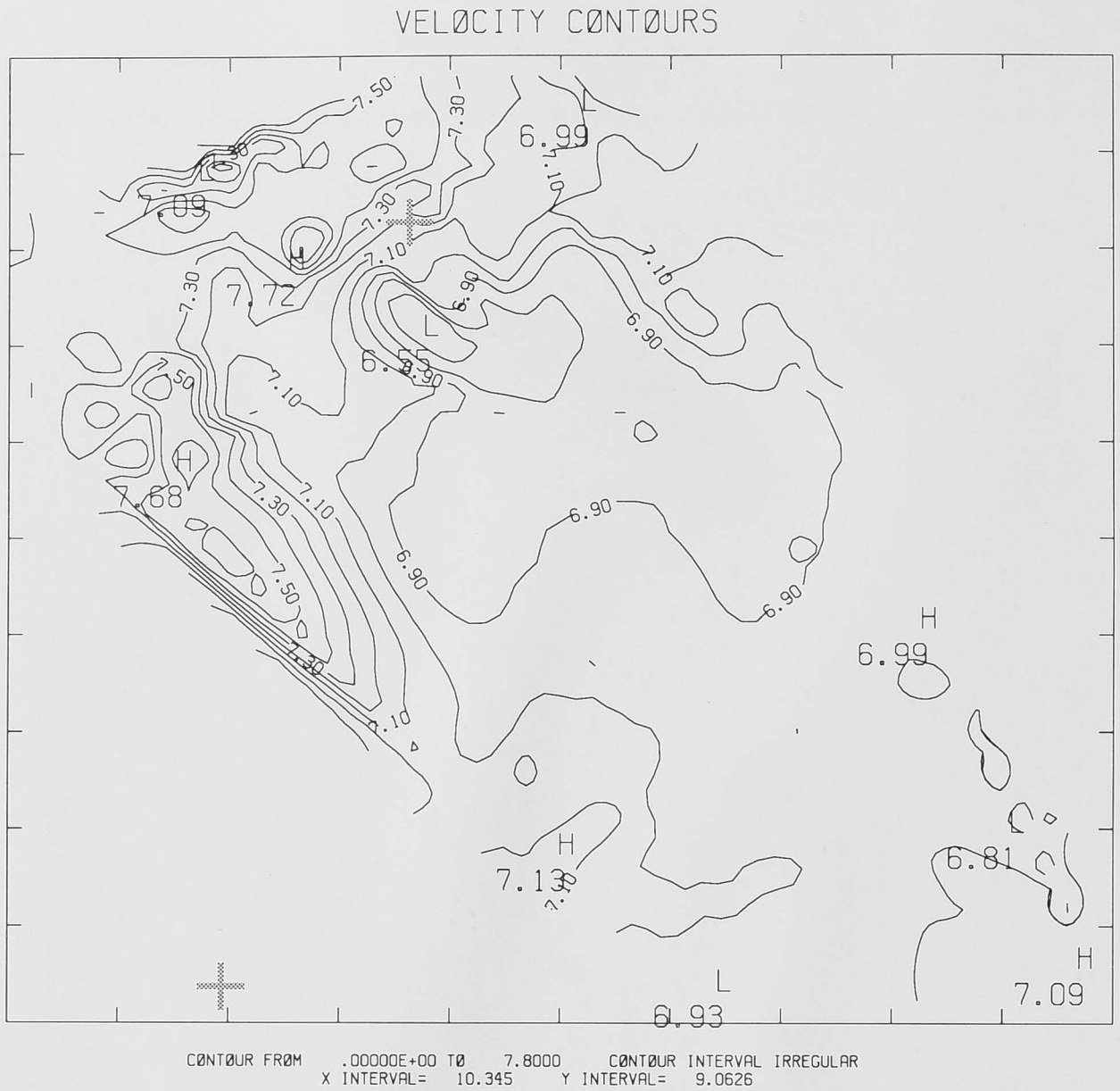

Figure 3.32: Velocity contours of NGC 2936. Numbers are velocities in 1000 km s^{-1} and each consecutive contour has a difference of 100 km s^{-1}. The crosses represent the nucleus of NGC 2936 in the north and NGC 2937 in the south.

of the irregular galaxy until it becomes rather constant at the SW end of the tail.

3.2.4 Discussion

It has been shown that the emission lines coming from regions around the nucleus of the irregular component of Arp 142 exhibit velocity jumps of $\simeq$100-400 km s^{-1}, with a total velocity spread of $\simeq$ 950 km s^{-1}. The structure and kinematics of the irregular, the relative position of the compact companion and the mass ratio implied by both components are suggestive of a recent interaction. This means that it is likely that the original kinematics of the disk galaxy has not been perturbed severely by the interaction, suggesting that the observed kinematics of this galaxy is of intrinsic nature.

Comparing velocity distributions in all PAs, it seems that PA=275x° best represents the kinematic axis of NGC 2936. This PA exhibits two major kinematical structures: a flat and a sinusoidal velocity curve. Separately, the shape of

the higher–velocity curve can be explained by a (gaseous) system consisting of a faster rotating disk embedded in a more slowly rotating disk, such as observed in NGC 3189 inside the Hickson group H44 (Rubin *et al.*, 1991). The lower–velocity curve is of that commonly observed in spirals with flat rotation curves (ΔV $\simeq$300 km s^{-1}). Observing these simultaneously inside a galaxy means that the disks will have to be transparent enough so both velocity patterns can be observed together. On the other hand however, a velocity spread of $\simeq$ 800 km s^{-1} inside a $\simeq$ 6 kpc region –as shown by PA=275x°– is unusually large.

An alternative explanation to the split velocity curve comes from what is often observed in a disk believed to have an (bi–conical) ionisation cone extending at an angle from the disk. The part of the cone closer to the observer will exhibit two different velocities that are both blue–shifted to the systemic velocity of the galaxy. Due to the inclined nature of the disk, the redshifted component of the cone is usually obscured by a torus of accreted material, resulting in a asymmetric split-emission profile. The extent of these cones, such as that observed in NGC 5252 (Tsvetanov *et al.*, 1989), can reach as far as ~30 kpc.

If the high velocity spreads inside NGC 2936 are caused by a (possibly biconical) ionisation cone, then one would expect the cone to go roughly east–west, as shown by the orientation of the largest velocity gradient, and by the orientation of the dust lane inside the spiral. What appears in the (B–R) image of NGC 2936 (Fig. 3.22), where a half–cone is suggested at the edge of the eastern arm, supports this scheme as well. Since dust is thicker in the western region, one can also expect emission from this part to be more obscured, as is observed in the longslit spectra going through the nucleus. If this is true, then the eastern lobe of the cone will be inclined toward the observer. As a consequence, the velocities here will be blueshifted from the velocity of the nucleus if there is outflow motions, or redshifted if the radial motions are negative, and vice versa inside the western lobe of the cone. Then according to this scheme, NGC 2936 will have inflow motions. However, ionisation cones are normally observed inside host galaxies with active nuclei, as indicated by their emission line ratios and lines observed. This does not seem to be the case for NGC 2936, where no broadline emission is observed inside/around the nucleus and away from the nucleus the [NII]λ 6584 to $H\alpha$ ratios are more typical of those observed in HII regions. Inside the nucleus this ratio is difficult to measure due to the weakness of the emission lines, but [NII]λ 6584 does not appear to be stronger than $H\alpha$.

3.3 Simulating the Velocity Jumps

The isovelocity contours of NGC 1144 and NGC 2936 exhibit local extra–nuclear velocity jumps of the order of $\simeq$300–500 km s^{-1} ; in the nuclear regions, these are

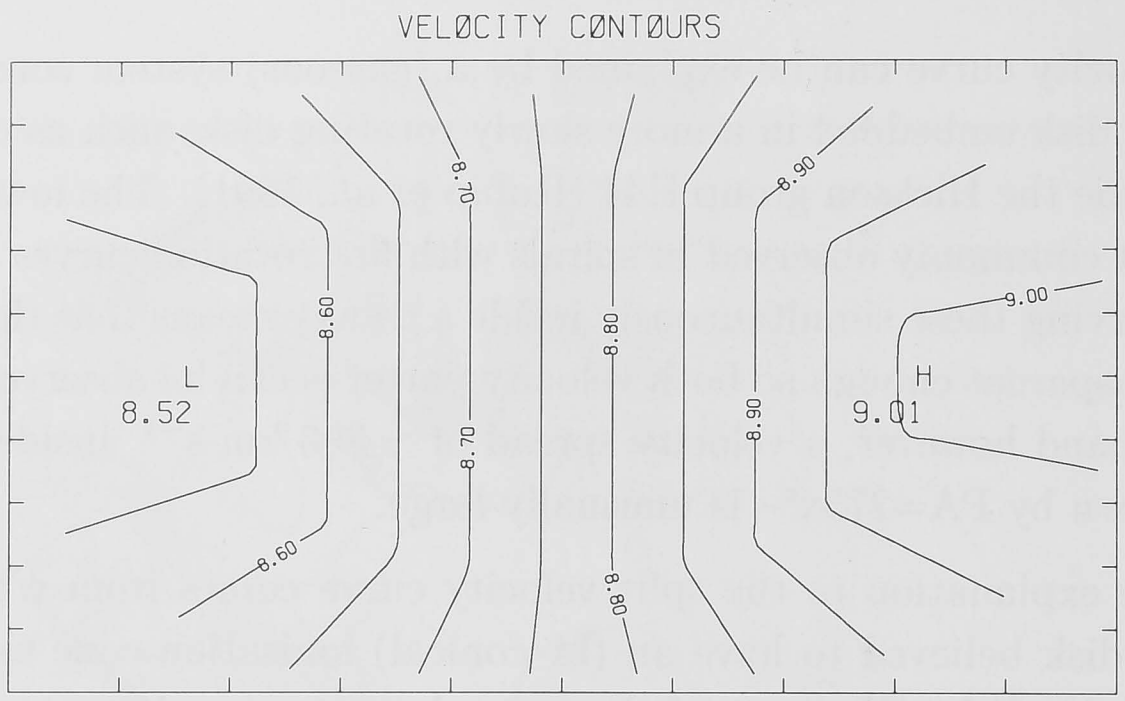

Figure 3.33: Simulated isovelocity contours for an inclined rotating disk with no point mass; L and H denote the low and high extrema of the velocities, respectively, and numbers are velocities in thousands of km s^{-1}. Positions where each isocontour bends are where the velocity pattern change from linear (inner) to constant (outer), at $r{=}2h$. Here, as in the next figure, the inclination is 55°.

about 1000 km s^{-1} (see Figs. 3.14 and 3.32). In order to (try to) understand the nature of this phenomenon, I have attempted a simple simulation to produce a similar effect. This approach is based on the idea that a concentration of mass can alter locally the galaxy's smooth velocity distribution, namely that governed by the galaxy rotation. One can think of this concentration of mass as a complex of molecular clouds, as indeed often observed inside spiral galaxies especially those interacting ones. Thus in this model, velocities contributed by these molecular clouds, treated as one point mass, ie. Keplerian, are basically superimposed on the global rotational motions.

3.3.1 The Model

I started with a 2-dimensional rotating disk, with a radial rotational velocity law

$$V_{rot} = \begin{cases} V_\circ + (V_{max}/2h)\, r & \text{for } r \leq 2h \\ V_{max} & \text{for } 2h < r \leq r_{max} \end{cases} \tag{3.1}$$

where h is a scalelength defining where the rotation becomes flat, V_{max} is the rotational velocity of the flat part of the rotation curve, and r is the distance from the center of the disk. The values of h and r_{max} were chosen to be 2.5 kpc and 8 kpc, respectively; V_{max} is adopted to be 300 km s^{-1}, typical for a galaxy as massive as NGC 1144.

Next I calculate the effect of the softened 'point mass', which has a mass and a radius such that

$$V_{pm} = \begin{cases} (G\, m_{pm}/r_{pm})^{1/2} & \text{for } r' \leq r_{pm} \\ (G\, m_{pm}/r')^{1/2} & \text{for } r' > r_{pm} \end{cases} \tag{3.2}$$

where pm denotes the 'point mass', r' is the distance from the center of the mass, and G is the gravitation constant.

The two velocity fields, rotational and point mass, were combined and corrected for inclination. The velocity field was then smoothed and mapped using the same procedure as that done to the velocity data resulted from longslit spectroscopy. The observer's viewing angle is adopted to be 0° with respect to the lines of nodes. Fig. 3.33 shows the velocity contours for an inclined disk without any point mass.

3.3.2 Results

The smaller and the more massive the point source is, the more strongly it contributes to the local velocity distribution. In addition to these, the apparent velocity jump is also strongly affected by the location of the point source relative to the observer. Figs. 3.34a, 3.34b and 3.34c show the resultant velocity contours with three different point source positions; other parameters –radius, mass and inclination, which was chosen to be 55°– are the same. The adopted value of r_{pm} is 100 pc. Here the velocity jump becomes larger as the point source gets closer to the center of the disk; placing the source in the center of the disk resulted in a much larger velocity jump (Fig. 3.34d): in this scheme, it is about 1000 km s^{-1}.

A point source as massive as 10^{10} $M_\odot$ with a softening radius as small as 100 pc is needed to produce a velocity jump of $\simeq$250 km s^{-1} *on* the disk; Fig. 3.34 shows the velocity field for these values. By itself, the point mass gives a maximum velocity of $\simeq$ 660 km s^{-1}. Molecular cloud complexes with mass and radius of this order are known. For example, IC 694, one component of the interacting pair Arp 299, is observed to have a concentration of molecular clouds with a mass of M_{H_2}=3.9×10^9 $M_\odot$, within a radius of $\simeq$ 250 pc (Sargent & Scoville, 1991). Arp 220, an ultraluminous IR galaxy, is observed to have M_{H_2}=2.5×10^{10} $M_\odot$inside a radius of 315 pc (Scoville *et al.*, 1991). In both cases, however, the complexes are contained inside the nuclear regions. The extra–nuclear H_2 complexes –as are also observed in Arp 299 and Arp 220– are usually observed to have radii larger than 300 pc.

As mentioned earlier and shown by the figure, placing the cloud complex in the center of the disk produces a high velocity jump: about 1000 km s^{-1} for M_{ps}=1×10^{10} $M_\odot$ and r_{ps}=100 pc. This is about what is observed inside the nuclear regions of NGC 1144 and NGC 2936. Applying the mass and radius observed in the molecular complex in Arp 220, with an adopted inclination of 45°, I obtained a central velocity jump of about 900 km s^{-1}. It is thus encouraging to

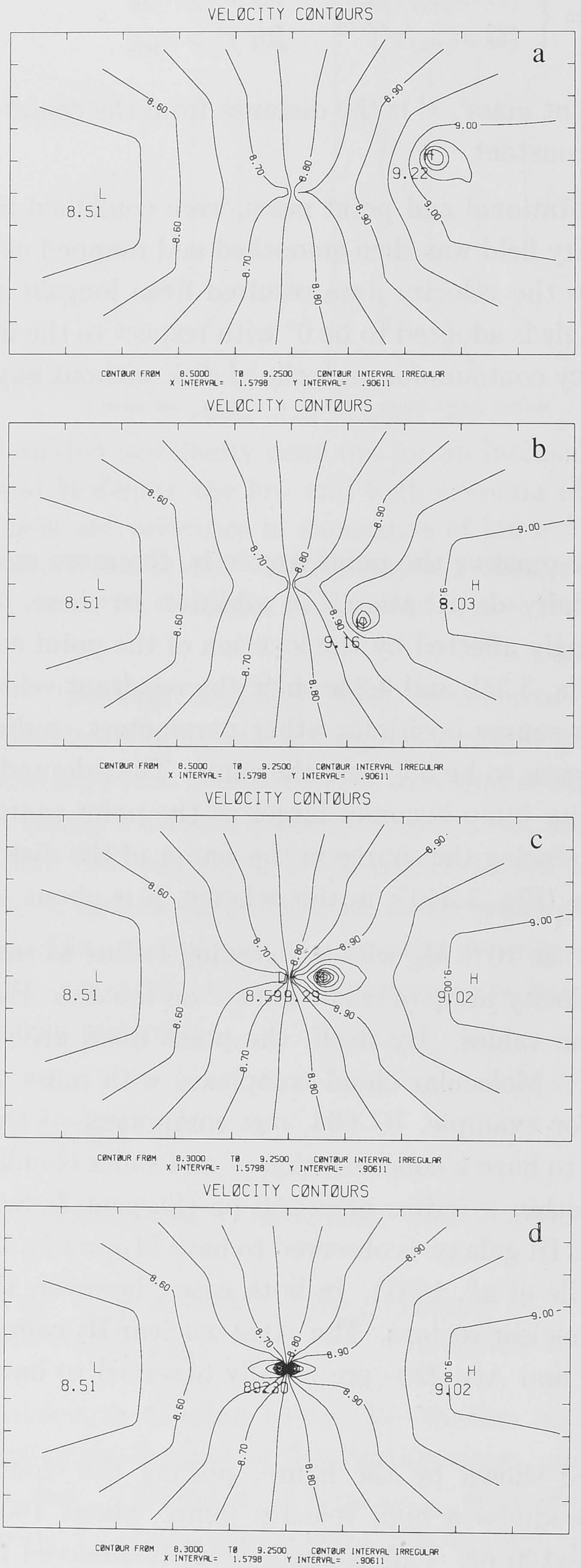

Figure 3.34: Results of simulating a velocity jump for different positions of the point mass; notations are similar to the previous figure.

discover that in addition to the mass, the velocity dispersion of molecular clouds in Arp 220 is observed to reach as high as 900 km s^{-1} at FWZP (Solomon *et al.*, 1990).

To summarise, adding a 'point mass' cannot produce the observed velocity jumps in the disks of NGC 1144 and NGC 2936 unless extreme parameters are used. However, positioning this 'point mass' in the center can reproduce this behaviour, such as that observed in a number of starburst galaxies (and in the central regions of NGC 1144 and NGC 2936). It is thus important to observe Arp 118 and Arp 142 in C0, to study their molecular cloud contents and their kinematics, and compare these to those of the gas.

3.4 Conclusions

Both interacting pairs Arp 118 and Arp 142 show very high internal motions inside the irregular components. The shapes of the longslit emission lines exhibit different structures: a steep, continuous feature for NGC 1144, and a split profile for NGC 2936. These might imply that the nature of the large velocity spreads are different in each irregular component. The split profile that is observed in the latter is commonly found in galaxies with ionisation cones, which are hosted by active nuclei, yet the line ratios and emission lines observed inside NGC 2936 do not support this scheme. On the other hand, NGC 1144 has a Seyfert 2 nucleus, whish is often observed to cause large velocity dispersions inside and in the vicinity of the nucleus. However, in the case of NGC 1144, the velocity gradient is spatially very extensive to have been caused by an active nucleus alone. Additionally, the line ratios characteristic of active nuclei are only seen in the nuclear region of NGC 1144.

It is worth comparing the cases of Arp 118 and Arp 142 with Arp 119, also an irregular+spheroidal pair. Marziani *et al.*(1994) observed the irregular component of Arp 119, Mrk 984, to have a velocity spread of ~1300 km s^{-1}. Unlike NGC 1144, whose largest velocity spread has a rather continuous structure across the nucleus and extends across the major axis of the irregular, in Mrk 984 the spread is caused by multiple velocities such as observed in NGC 2936, and goes across the minor axis of the spiral. Both the irregular components of Arp 118 and Arp 119 have signatures of active nuclei as observed by their line ratios; however in Mrk 984 the characteristic emission lines extend to more than 16 kpc.

The irregular component of Arp 118 exhibits a blue ring structure extending towards the spheroidal component. If it is an expanding ring, then the age implied is $\simeq 300$ Myrs and $M_{dyn} \simeq 1.2 \times 10^{12}\ M_{\odot}$. But the bluest (B–R) and (B–K) colors give an age of a few million years for a single burst population is assumed (Leitherer & Heckman, 1995). In NGC 2936, a connected-pair of spiral arms appears

instead, with two condensations sitting at the edges and the bluest (eastern) knot implied a young underlying population as well. In both systems the nuclei are heavily reddened ((B–K)$\sim$5–6 mag) and suffer asymmetric obscuration.

In both systems, the extended structures have velocities that gradually become similar to the velocities of the early type companions, suggesting material being pulled in by the companions. In Arp 118, this is supported by the extent of the $H\alpha$ emission lines, which stretches close toward the spheroidal component. The extension of the low level surface brightness distribution in both pairs is parallel to the rotational axis of the irregular components suggestive of matter being expelled due to the kinematics of the systems. The extent of these structures have a dimension of the order of $\sim$100 kpc.

Dynamical models are needed to study how interactions can produce high internal motions confined inside one component. For Arp 118 and Arp 142, kinematics of the stellar, molecular and HI components are important to study how other building–blocks are behaving inside these hot systems. Narrow line images (eg. [OIII]) of NGC 2936 is needed as well to be sure of the existence and the extent of an ionisation cone.

The simple simulation performed here is able to reproduce the velocity jumps observed inside the nuclear regions of NGC 1144 and NGC 2936. However, a similar reproduction requires implementation of unrealistic parameters in the mass and dimension of the point mass, ie. the molecular cloud complex.

3.5 References

Appleton, P.N. and Struck-Marcell, C. 1987, Ap.J. 312, 566

Demin, V., Zasov, A., Dibai, E. and Tomorv, A. 1984, Soviet Astron. 28, 367

Gerber, R.A., Lamb, S.A. and Balsara, D.S. 1996, MNRAS 278, 345

Giovanelli, R., Haynes, M.P., Rubin, V.C. and Ford, W.K. 1986, ApJ. 301, L7

Jeske, N. 1986, Ph.D. thesis, University of California at Berkeley

Joseph, R.D., Meikle, W.P.S., Robertson, N.A., Wright, G.S. 1984, MNRAS 209, 111

Joy, M. and Ghigo, F.D. 1988, Ap.J. 332, 179

Korneef, J. 1983, A&A 128, 84

Leitherer, C. and Heckman, T.M. 1995, ApJ.S. 96, 9

Liu, C.T and Kennicutt, R.C. Jr. 1995, ApJ.S. 100, 325

Marziani, P., Keel, W.C., Dultzin-Hacyan, D., Sulentic, J.W. 1994, Ap.J. 435, 668

Möllenhof, C., Hummel, and Bender, R. 1992, A&A 255, 35

Rampazzo, R., Reduzzi, L., Sulentic, J.W. and Madejski, R. 1995, A&ASS 110, 131

Rubin, V.C., Hunter, D.A. and Ford Jr., W.K. 1991, ApJ.S. 76, 153

Sargent, A.I and Scoville, N.Z. 1991, Ap.J. 366, L1

Scoville, N.Z., Sargent, A.I., Sanders, D.B. and Soifer, B.T. 1991, Ap.J. 366, L5

Solomon, P.M, Radford, S.J.E. and Downes, D. 1990, Ap.J. 348, L53

Thronson & Greenhouse. 1988, Ap.J. 327, 671

Tift, W.G. 1977, Ap.J. 211, 377

Tift, W.G. 1982, Ap.J.S. 50, 319

Toomre, A. 1978, in IAU Symposium 79: The Large Scale Structure of the Universe, ed. M.S. Longair and J. Einasto (Dordrecht: Holland), p. 109

Tsvetanov, Z., Tadhunter, C., Pérez, E. and Ganzález–Delgado, R. 1989, in Proceedings of ESO Workshop on "Extranuclear Activity in Galaxies", Garching, 16–18 May 1989, eds. E.J.A. Meurs and R.A.E. Fosbury (ESO: Germany), p. 19

Veilleux, S., Kim, D.-C., Sanders, D.B., Mazzarella, J.M, and Soifer, B.T. 1995, ApJ.S. 98, 171

White, S.D.M., Tully, R.B. and Davis, M. 1988, Ap.J. 333, L45

Chapter 4

The Ring Galaxy Arp 147

4.1 Introduction

Ring galaxies have become classic objects to study from both theoretical and observational points of view. They are believed to be a product of near head-on collisions, and their symmmetry, simplicity and distinctive morphology have attracted both schools to model and observe. These galaxies are generally knotty with one or more companions nearby. From his observations of 40 ring galaxies, Thompson (1977) found that the frequency of these objects drops dramatically inside clusters. It seems that ring galaxies are rare and mainly occur in regions of low galactic density. Athanassoula & Bosma (1985) estimated the frequency of ring galaxies to be about 0.02 to 0.2% of the spirals.

A handful of ring galaxies were studied by Theys & Spiegel (1976), and one of the general trends they discovered, which then fueled subsequent theoretical efforts, was that the companion seems to lie preferentially near the minor axis of the ring. Other conclusions were that the rings have similar colors to those of Magellanic irregulars, and there are indications that these rings have significant expansion velocities.

Their second paper (1977) was an attempt to model these objects. Their first N-body simulation of a head-on collision using hot stellar and gaseous components was hardly successful in producing rings. The second more simplified model, however, resulted in the collision knocking out the target nucleus, producing a collection of rings that expand and subsequently crowd together. Lynds & Toomre (1976) and Toomre (1978) gave a clearer picture on what actually happens during and after the collision: as the intruder plunges through the target disk, the stars experience a brief pull which causes the disk to contract. When the intruder exits, the system rebounds strongly, forming an outward propagation of a transient high amplitude density wave. Numerical experiments show that this wave is essentially kinematic and not due to self-gravity. Later attempts to model ring galaxies

employ dissipative gas/hydrodynamics to produce a more detailed picture of the formation of ring galaxies (see, for example, Appleton & Struck-Marcel, 1987; Struck-Marcel & Lotan, 1990; Struck-Marcel & Higdon, 1993; Gerber *et al.*, 1992 and 1996).

Many ring galaxies are observed to exhibit enhanced star formation (Larson & Tinsley, 1978); the bright knots on the ring are generally very blue, implying recent star formation activity. Appleton & Struck-Marcel (1987), from their optical and far-infrared observations, have argued that a number of rings are undergoing star formation at the starburst level.

One type of ring galaxies is what Theys & Spiegel (1976) classified as RE: an empty ring with an apparent lack of a nucleus. The 'missing nucleus' has raised a variety of theories: Freeman & de Vaucouleurs (1974) suggested that the companion, which is often a gasless elliptical or SO galaxy, might be the former nucleus of a gaseous disk, swept out by an intergalactic cloud of galactic dimension. Theys & Spiegel (1977) tried to remove the nucleus of the target galaxy sufficiently far from the disk to produce the morphology but found this difficult to achieve. More recent authors have suggested that the nucleus might actually be one of the knots that build up the ring (Huang & Stewart, 1988; Gerber *et al.*, 1992).

Arp 147 is a pair of galaxies consisting of an empty ring (IC 0298) and a compact SO companion (IC 0298B) located near the former's minor axis. Theys & Spiegel (1976) first studied this ring system in detail. They observed strong [OII]λ3727 emission from both the ring and the spheroidal components. Using this [OII] line, they built a kinematic scheme for the ring of Arp 147. They found that the velocity gradient inside the ring is about 160 km s^{-1}, and, based on the position angle of the maximum gradient lying so close to the minor axis, proposed that the ring has a significant expansion (or contraction) velocity.

Ghigo *et al.*(1983) performed X-ray observations on Arp 147 with the Einstein Observatory but did not detect it; an upper luminosity limit was calculated to be 42.9 ± 0.7 ergs s^{-1}. Jeske (1986) observed Arp 147 in HI and found that the spectral profile exhibits triple-peaked feature that can be deconvolved into two peaks corresponding to the ring and a third corresponding to the spheroidal companion. The dip between the first two peaks never reaches zero intensity, as was also observed in the Cartwheel galaxy, which led him to conclude that the HI distribution is not as concentrated as the optical matter. He calculated that 75% of the HI is associated with the ring, and the rest with the companion, which means that the companion has a relatively large amount of gas for an SO galaxy. The total HI mass was calculated to be $5.2 \times 10^9 M_\odot$.

Schultz *et al.* (1991) obtained IUE low-dispersion spectra of an area corresponding to the brightest optical knot of the ring of Arp 147. It shows a continuum with no evidence of other spectral features. From this they concluded that the brightest

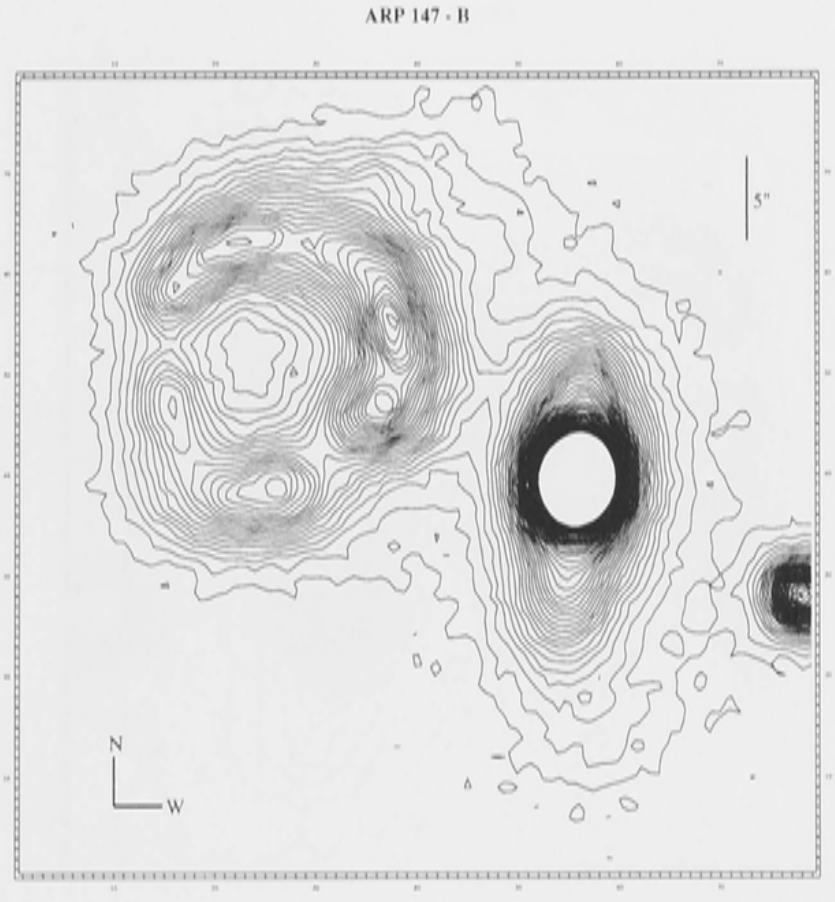

Figure 4.1: B contours of Arp 147

Component	B	R	I	K	(B – R)	(B – I)	(B – K)
S0	16.16(0.048)	14.78(0.019)	14.12(0.017)	11.77(0.015)	1.38	2.03	4.39
ring	15.82(0.040)	14.63(0.018)	14.21(0.018)	12.47(0.015)	1.19	1.61	3.35

Table 4.1: Integrated photometry of ring and S0 components

knot in the ring is actually the remnant of the pre-collision nucleus, although they did not specify in which bandpass image this brightest knot was identified. A K–band image of Arp 147 was taken by Majewski and Hereld (1991) but was not presented. They reported that the ring of Arp 147 shows 'a strong peak where its optical images show a conspicuous paucity of light'. Unfortunately no further investigation on this was published.

Horellou *et al.*(1995) observed a collection of ring galaxies including Arp 147 in CO. They could not detect Arp 147 in CO(2-1) but their observation in CO(1-0), which is of low S/N, gives an estimated H_2 mass of $2.2\times\ 10^9\,M_\odot$ for Arp 147. The mean velocity of the ring was observed to be $V_{hel} = 9665$ km s^{-1} with velocity dispersion of 191 km s^{-1}.

4.2 Morphology

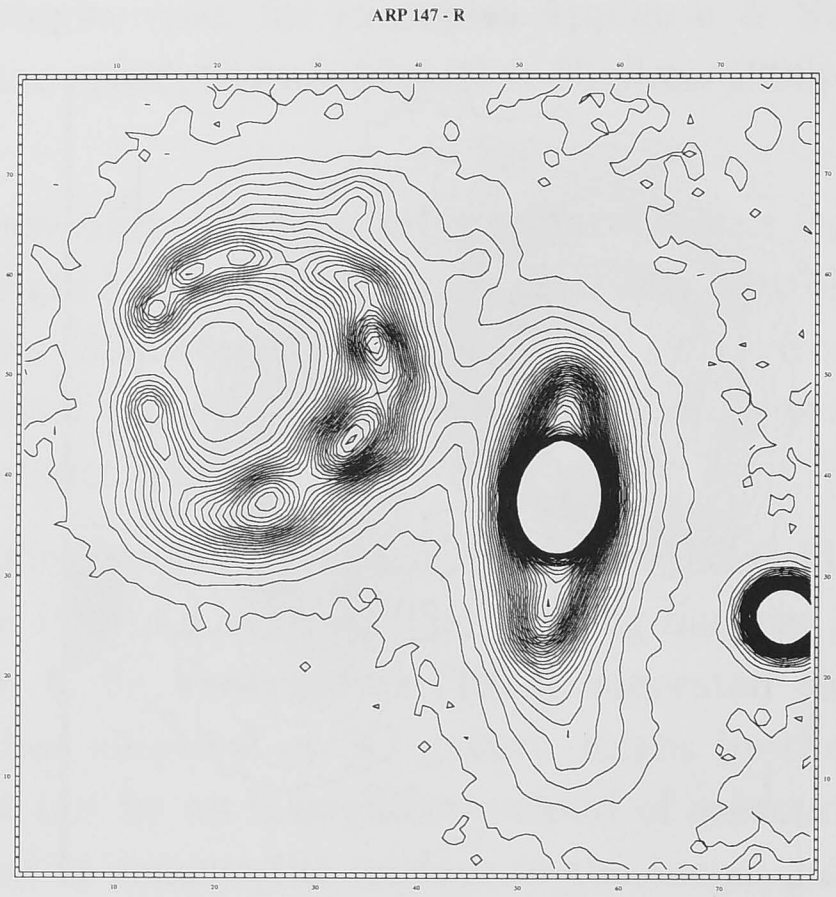

Figure 4.2: R contours of Arp 147

Table 4.1 presents integrated photometry of Arp 147, not corrected for galactic reddening (A_B=0.23 mag). Fig. 4.1, 4.2, 4.3, and 4.4 show contour plots of B, R, I and K images of Arp 147; in these figures, north is up and west is right. My integrated photometry of the pair is presented in Table 4.1. The numbers in brackets are the errors of the measurement. The composite image of Arp 147 is shown in Fig. 1.5; the R and K images have been convolved so to match the point spread function of the B image. The blue, green and red colors correspond to B, R and K passbands respectively, but the scale is stretched to emphasize the red feature.

Our spectroscopy give a systemic velocity of 9630 $\mathrm{km\,s^{-1}}$ for the ring; this corrresponds to a distance of 128 Mpc ($\mathrm{H_\circ = 75\,km\,s^{-1}}$). At this distance, the size of the ring is about 9 kpc in diameter, and the separation between the centers of the two components is about 13 kpc.

4.2.1 Of the Companion

The companion of Arp 147 is an edge-on S0 galaxy with an asymmetric disk. The nucleus appears to be slightly displaced to the north, and its major axis is misaligned from the disk. The disk itself is distorted in the inner southern part, pointing slightly towards west, but in the outer southern part it bends away from the ring producing a 'flare' structure. These features are most obvious in the K and R images where the seeing is best, and it is suggestive that these are due to

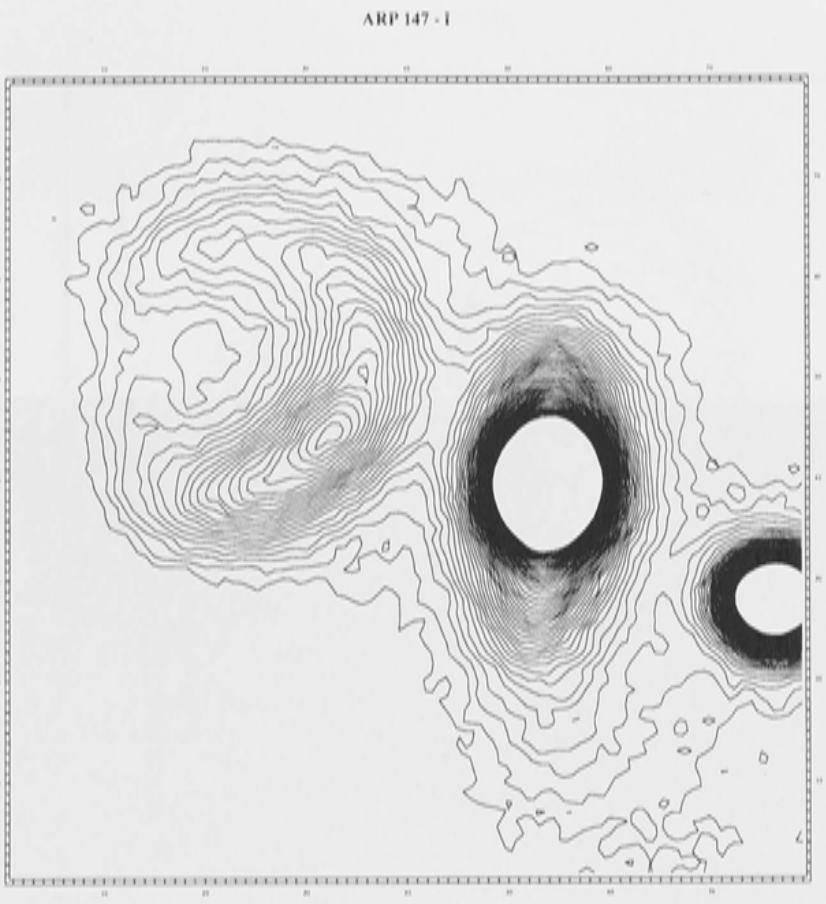

Figure 4.3: I contours of Arp 147

the encounter that produced the ring.

The integrated colors of the spheroidal component are typical of those observed in S0 galaxies although it is slightly bluer in (B–R). But the colors of the outer (tidal) tail, the 'flare', are especially red, (B–K)$\sim$5 mag, redder than the integrated colors of the spheroidal but surprisingly comparable to the colors of the 'red knot' which I shall discuss in the subsequent sections.

The surface brightness profile of IC 0296B along its major axis in the K–band can be fitted with a two–component (bulge and disk) profile. Fig. 4.6 (upper) shows results of fitting a disk (D) and a bulge (B) along the major axis of the spheroidal companion in the K–band; radius=0 corresponds to the center of the galaxy. The two–component profile is designated as D+B; dots represent the observed brightness distribution. However, a part of the disk displays a wing structure that cannot be fitted with any conventional profile; this appears to be related to the distortion inside the disk as can be observed in the images.

The middle and lower parts of Fig. 4.6 show the change of ellipticity and isophotal twisting inside IC 0298B as a function of distance from the center. The ellipticity changes gradually until it is rather constant beyond r=8″, where the existence of the disk component is established. The level of twisting inside the S0 is low in the inner part then stays constant at r> 4″.

As mentioned earlier, Theys and Spiegel (1976) found strong [OII]λ3727 emission line coming from the companion. Jeske (1986) observed that 25% of the total HI

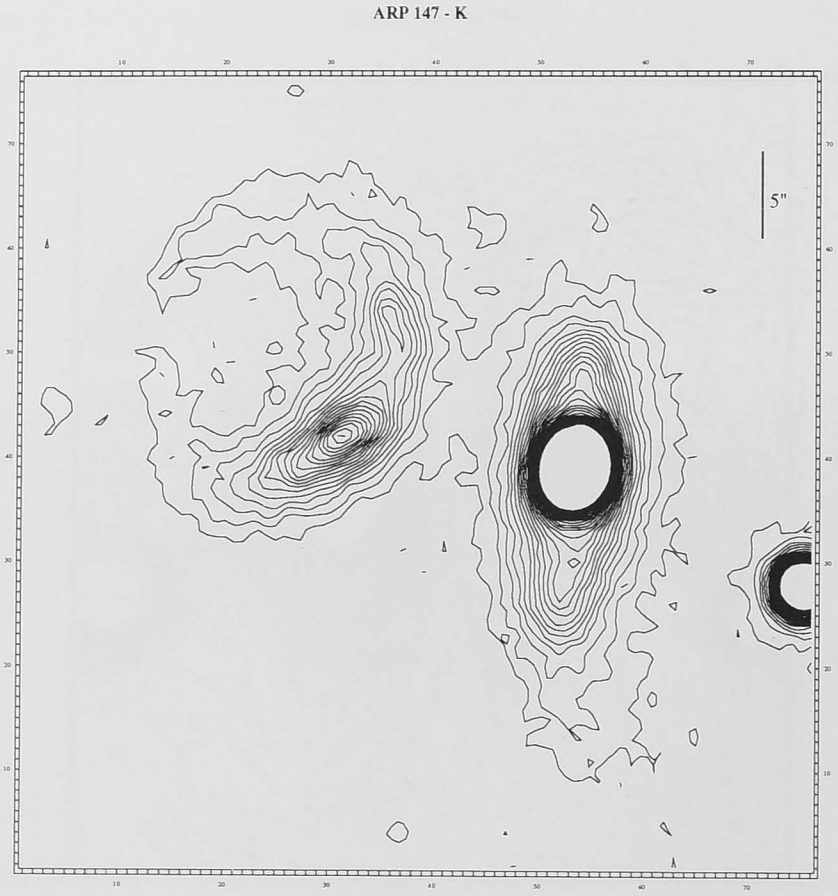

Figure 4.4: K contours of Arp 147

is emitted by this object, which corresponds to $\sim 1.3 \times 10^9 M_\odot$. He concluded that the companion has not lost its gas and that the lack of emission lines from other parts than the nucleus is caused by lack of emission mechanisms rather than by lack of gas. Our red spectrum of the spheroidal component shows a signature of shocks typical of active galaxies: it has a broad hump with a strong [NII]λ6584 emission line, with an [NII]λ6584 to $H\alpha$ ratio of about 1.2. This is consistent with Jeske's radio result which indicates that the emission is nonthermal in origin, with a spectral index of –0.8.

Based on its $H\alpha$ and [NII] $\lambda\lambda$6548,6584 lines, I derived a heliocentric velocity of 9412 ± 12 km s^{-1} for this spheroidal component.

4.2.2 Of the Ring

The B and R images of Arp 147 show an almost complete ring which consists of arcs and knots as can be seen in Fig. 4.1 and 4.2. At two positions the ring breaks completely. Possibly due to its better seeing, the R image displays more well defined knots but otherwise is in good agreement with structures in the B image. This implies that the same source is contributing to both passbands, most likely to be $H\alpha$ in the R–band emitted by the young population residing in the ring. On the north-east outer edge of the ring there exist two knotty features which, as I shall show later, have the highest velocities in the system. The ring is thicker on the eastern side, closer to the companion.

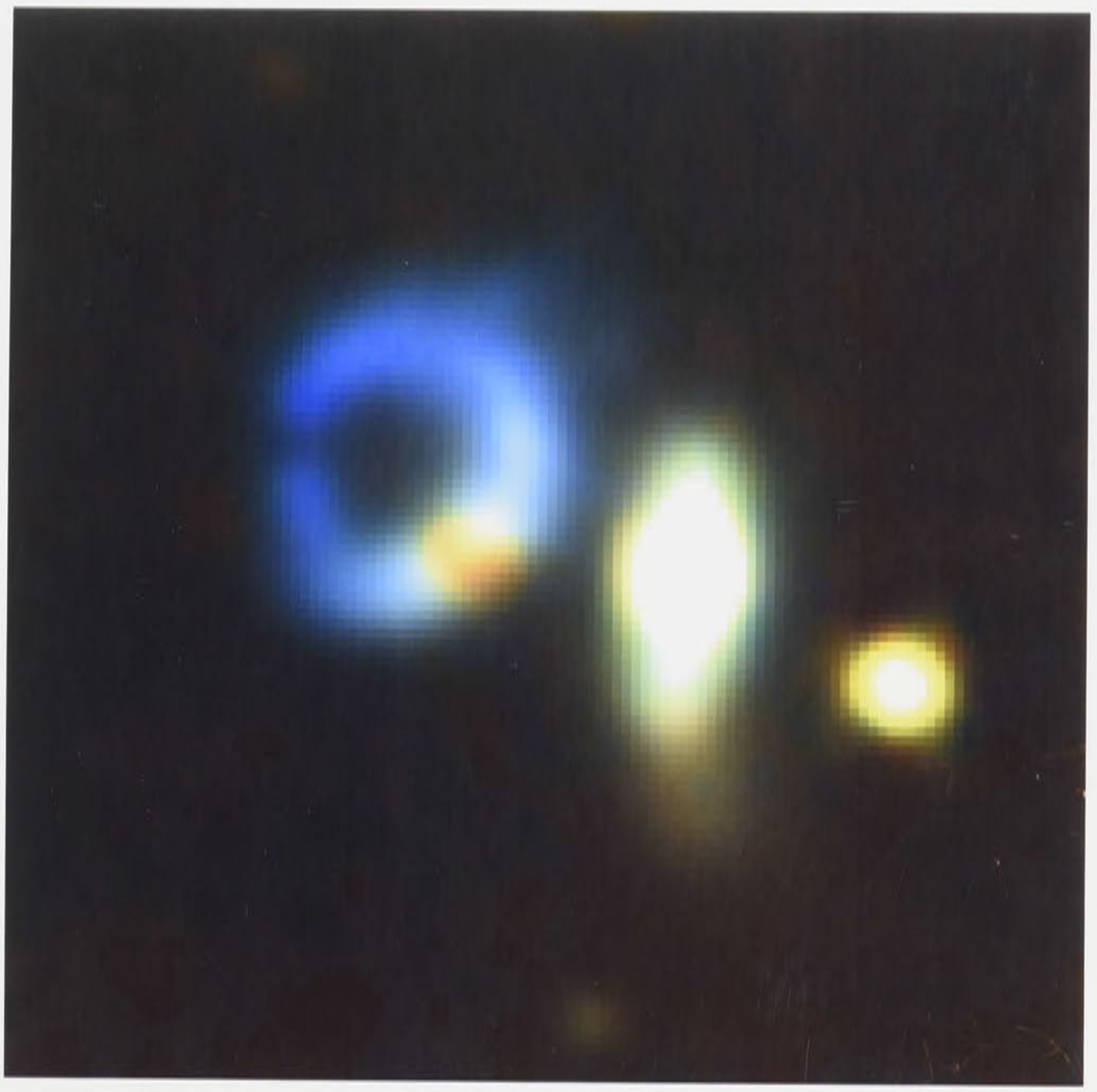

Figure 4.5: Composite image of Arp 147. Blue, green and red correspond to B, R and K passbands; the red color is stretched so as to emphasise the red knot.

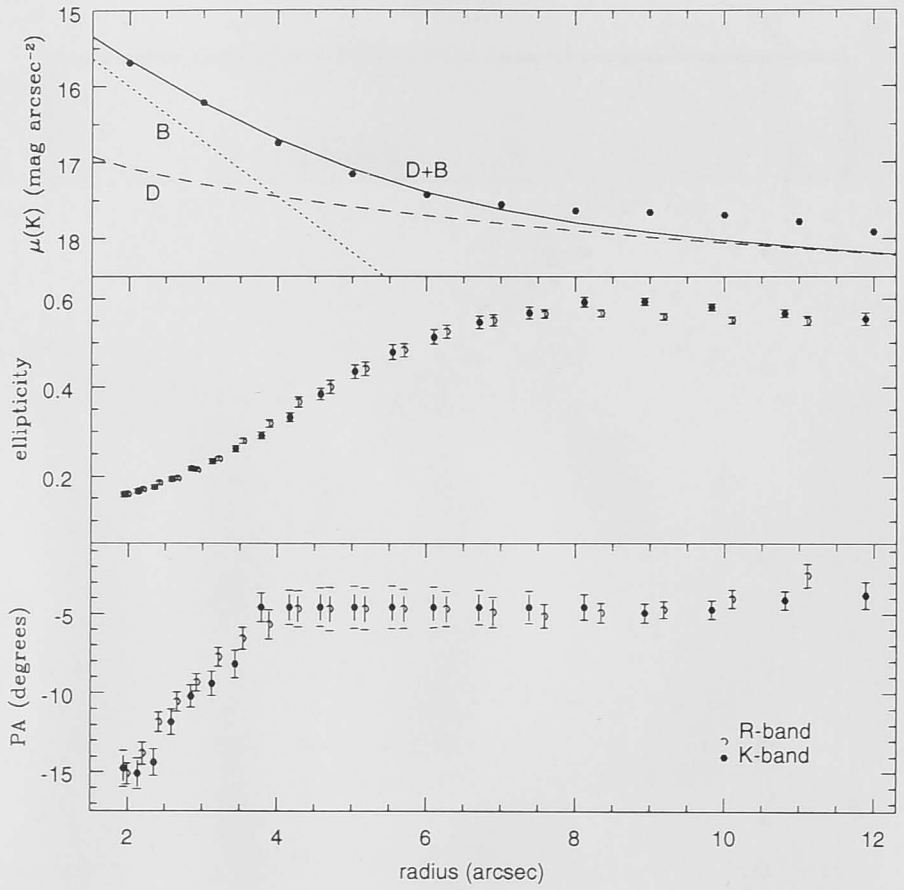

Figure 4.6: Surface brightness distribution along major axis (upper), ellipticity (middle) and twisting (lower) of IC 0298B as a function of distance from the nucleus. Filled and empty dots are K– and R–band data, respectively. Results of fitting a bulge (B) and a disk (D) is shown in the upper panel as a solid line (D+B).

The K and I images of the ring are generally consistent with each other, showing a well defined arc on the east which fades away towards the west, although the I ring extends further forming a more complete ring. The brightest knot is seen roughly at the same position, that is, where the minimum surface brightness occurs in the B and R images. And since this knot is very bright in K, and has a very red (B–K) color, as will be evident later, I shall refer to this structure as 'the red knot.'

There is also a second less luminous knot that appears in K but not resolved in I, again possibly due to worse seeing. This second knot lies roughly northwestwards from the nucleus: it is thin and elongated and its straightness almost 'cuts' through the ring. This knot has its counterpart in B and R images, although it appears better defined in the latter.

Results of simulations (Gerber *et al.*, 1996) predict that the stellar ring as shown in the K-band image will be thicker than the gas/blue ring. This is probably due to the small random velocities of the gas before the collision. Majewski and Hereld's (1992) results support this: they found that (generally) the K–band images of ring galaxies show thicker rings than the optical ones. We are unable to confirm this. On the contrary, our K-band image of Arp 147 shows a thinner ring compared to that in the R-band, except around the area where the light is dominated by the

red knot. This K-band ring is also rounder than the optical ones.

The integrated colors of the ring of Arp 147 (Table 4.1) are comparable to those observed in, for example, later type spirals observed by de Jong (1994), although the intrinsic scatter in his sample is large. The red spectra of the ring shows emission lines of $H\alpha$, [NII] $\lambda\lambda$6548,6584 and [SII] $\lambda\lambda$6716,6731, with [NII]λ6584/$H\alpha$ values typical of those observed in HII regions.

Azimuthal Profile of the Ring

In order to study the ring further, I have plotted the surface brightness in each band against position angle, where PA = 0° lies to the north from the center of the ring and increases to the east. The thickness of the ring is defined by the morphology in the B image, with its center measured as half the distance between peaks of the flux in the ring. The fluxes inside the ring were averaged radially, binned into 3° bins in azimuth, and transformed into surface brightness using the transformations derived from standard stars.

The result is shown in Fig.4.7. As can also be seen in the images, the surface brightness variations in B are similar to those in R: both have dips at PA $\simeq -140°$ and $\simeq 70°$, which correspond to the brightness depletion in the images. While the general trend is similar for K and I, μ_K has a flat zone at $-40°$ to 40° before it rises quickly and peaks at $\simeq -120°$; this happens slightly earlier, at PA $\simeq -140°$ for μ_I. Another interesting feature is that the K and I peaks are also shifted from those of the B and R dips.

The color changes with PA are shown in the bottom panel; the high level of noise at PA$\simeq$60° to 100° is due to the low surface brightness in K in this region. As expected, the red knot is very red in (B–K), reaching a maximum of about 5 mag. The trend is similar although not as strong and is confined to a smaller PA range for (B–I). In (B–R), however, this extremum almost disappears: the profile appears rather flat. The ring itself, excluding the red knot, has blue colors, comparable to those of late– to irregular–type spiral galaxies. The (B–R) color is especially blue on the northern part of the ring, around PA=–60° to 80°.

To investigate the contribution of $H\alpha$ to the R-band image, I have measured the equivalent width (EW) of the $H\alpha$ emission lines –based on my spectroscopic data– in the ring, and found that the western part of the ring has EW$\simeq$200 Å, reaching $\simeq$300 Å on the extreme, as compared to EW$\simeq$100 Å in the eastern region. This means that in the R image, the contribution from $H\alpha$ emission can reach to about 15–20%, which translates to a brightening of about 0.15–0.2 mag in R. Since the ring is already blue in (B–R), this further emphasises that the ring has a very young population.

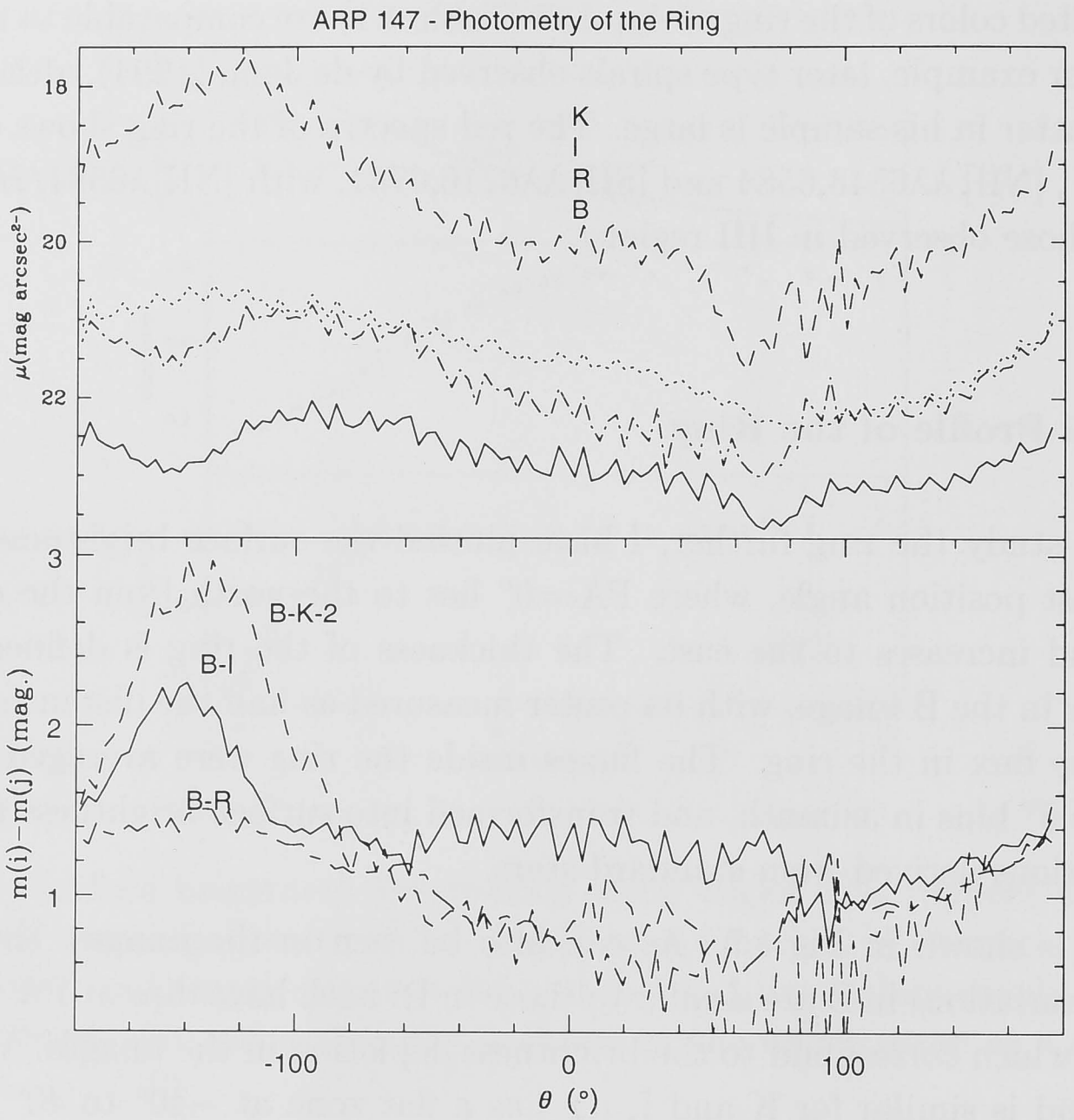

Figure 4.7: Azimuthal surface brightness photometry of the ring

Radial Profile of the Ring

I have also measured how the surface brightness and colors change with radius of the ring. For this I have chosen a position angle that goes from the peak of μ_K (the red knot) through the center across to the other side of the ring, which is at PA=60° on the ring. This is shown in Fig. 4.8. The datapoints are averaged values of a 'slit' with a width of 3 lines corresponding to $\simeq$ 1.8 arcsec.

As in Fig. 4.7, the top diagram of the figure shows the surface brightness distribution while the lower diagram shows the color changes across the ring: the first peak at d$\simeq$ –14″ corresponds to the north-eastern side of the ring; the second at d$\simeq$ 0″ is the red knot.

Some of the features here are similar to those already discussed in the previous section so will not be repeated. Some other points are worth mentioning. First, while the red knot has brighter K and I surface brightness than the rest of ring, in B and R it is similar to the ring. Second, the surface brightness of the central

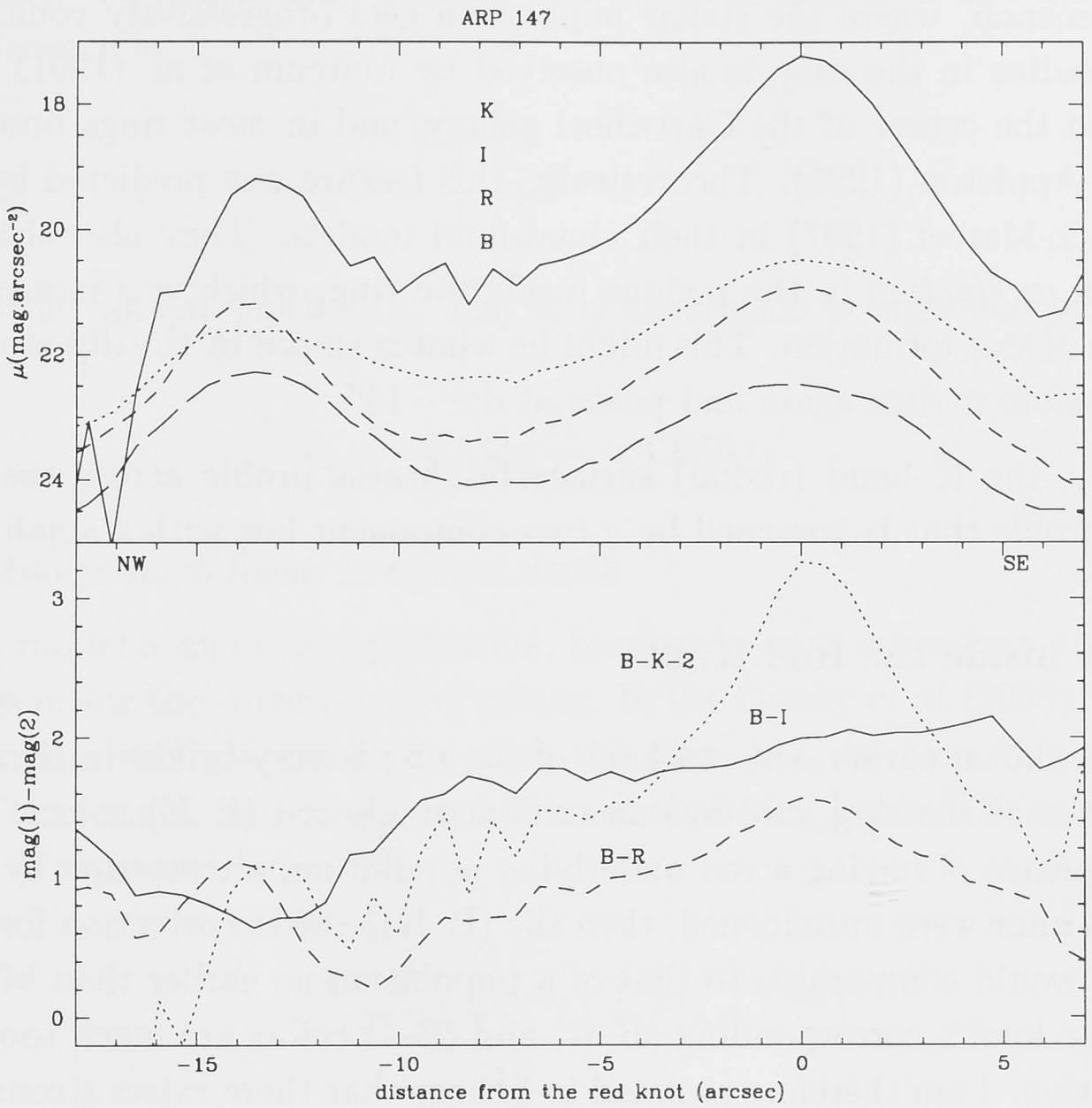

Figure 4.8: Radial surface brightness photometry of the ring

part of the ring ($-10'' \lesssim d \lesssim -5''$) never vanishes in any of the passbands. There is luminous matter inside the ring. Simulations show that, while the propagating expanding wave sweeps almost all of the gas in the disk radially, forming a well defined ring, the disk stars react less. This results in a more diffuse stellar ring where some amount of stars are left behind on the disk (see, eg., Gerber *et al.*, 1996).

Thirdly, there is a hint of gradual shifts in the radial position of the peaks of the ring between K, B and R. This is most obvious in K and R. Also, while μ_K declines rapidly to the NW and is lost in the background at d$\simeq$–16″, μ_B and μ_R decline more gradually and extend further out on the leading edge of the ring. This suggests that the gaseous ring is larger than the stellar ring. Similarly, the peak of (B–R) in the ring occurs further out than the peaks of (B–K) and (B–I), suggestive of the *progressive star formation* where the stellar population gets progressively younger with increasing radius in a ring galaxy. This is thought to be due to the expanding wave in the ring that compresses gas as it goes outward

causing star formation after the encounter on the leading edge of the ring.

This phenomenon, where the stellar population gets progressively younger with increasing radius in the ring, is also observed by Marcum *et al.* (1991) between the ring and the center of the Cartwheel galaxy, and in most rings observed by Marston & Appleton (1995). Theoretically, this feature was predicted by Appleton & Struck-Marcel (1987) in their cloud-fluid models. They also observed in their results *rarefaction* in the regions inside the ring, which was interpreted as suppression of star formation. This might be what is shown by the dip at d$\simeq -11''$ in (B–R), before it rises again and peaks at d$\simeq -14''$.

Additionally, the K–band (radial) surface brightness profile across the nucleus exhibits a profile that is governed by a two–component law with a small bulge.

Extinction inside the Red Knot

As has been shown earlier, the red knot of the ring is very bright in K compared to other parts of the ring, and has an outstandingly red (B–K) color. This can be a consequence of having a red underlying population, obscuration by dust, or both. If the knot were unreddened, then the $(B–K)_\circ$ –after correction for galactic extinction– would comparable to that of a population no earlier than M2 giants. However, the knot's corresponding (B–R) and (B–I) colors are much too blue for this population. I am therefore inclined to believe that there exists a considerable amount of dust obscuring the red knot in the shorter wavelengths.

A reddened underlying population dominated by late G-giants seems to give a more plausible explanation to the observed colors. For example if I choose a typical KO giant to represent the underlying population, with $(B\text{-}K)_\circ \simeq 3.0$, then the color excess

$$E(B-K) = (B-K)_{red\ knot,obs.} - (B-K)_{K0III} \tag{4.1}$$

in the red can be calculated. Also:

$$E(B-K) = A_B - A_K \tag{4.2}$$

In order to calculate the amount of obscuration inside the red knot,the next step is to derive E(B–V) from E(B–K): E(B–V) is related to the column density of diffuse interstellar HI by (Bohlin *et al.*(1979)),

$$\langle N(HI)/E(B-V)\rangle \simeq 5\times 10^{21}\,\mathrm{atom\,cm^{-2}\,mag^{-1}} \tag{4.3}$$

Rieke & Lebofsky (1985) measured the interstellar extinction law based on stars in the direction of the Galactic center. This can be used directly in the Screen

model, where the obscuring material lies between the observer and the objects. In this model, the relationship between the observed flux at λ and the intrinsic flux of the source is:

$$\frac{I_\lambda}{I_\circ} = e^{-\tau_\lambda} \tag{4.4}$$

where τ_λ is the optical depth at λ. The total absorption is expressed by:

$$A_\lambda = -2.5 \log \frac{I_\lambda}{I_\circ} = 1.086\, \tau_\lambda \tag{4.5}$$

Thus the absorption is linear in optical depth.

The Screen model is an oversimplification, because in most situations, the obscuring dust lies inside the corresponding galaxy. In the Disney *et al.* (1989) Sandwich model, the dust and gas are mixed with the stars but, because they are more dissipative than stars, they sink into a thinner obscuring layer. The extinction in this model is expressed by:

$$\frac{I_\lambda}{I_\circ} = \frac{1-\zeta}{2}(1 + e^{-\tau_\lambda}) + \frac{\zeta}{\tau}(1 + e^{-\tau_\lambda}) \tag{4.6}$$

where ζ is the relative thickness of the gas/dust slab compared to that of the stars.

To calculate the total absorption A_B, I use the ratio given by Rieke & Lebofsky (1985),where $A_K \approx 0.085\ A_B$. This gives:

$$A_B = \frac{(B-K)_{obs} - (B-K)_\circ}{0.915} \tag{4.7}$$

The next step is to calculate τ_B using (4.5) and (4.6). I have chosen $\zeta = 0.8$ (ie. the dust scaleheight is slightly thinner than the stars) almost arbritarily; the red knot seems very dusty, which favours high values of ζ, yet it is unlikely that the dust and stars are totally mixed. Once τ_B is obtained, again using the result of Rieke & Lebofsky (1985) but this time for their optical depth ratio (which depends more on the nature of the dust/grain than the model used), τ_V can be derived. This is then transformed into A_V using (4.6) and gives the E(B–V) distribution from the (B–K) values inside the red knot.

The results are shown in Fig. 4.9. The top panel is a replica of Fig. 4.7 but only showing the B and K surface brightness distribution, except the horizontal axis has been transformed into angular distance from the peak of the red knot in the K-band; it roughly goes from south to north on the ring. The middle panel is the

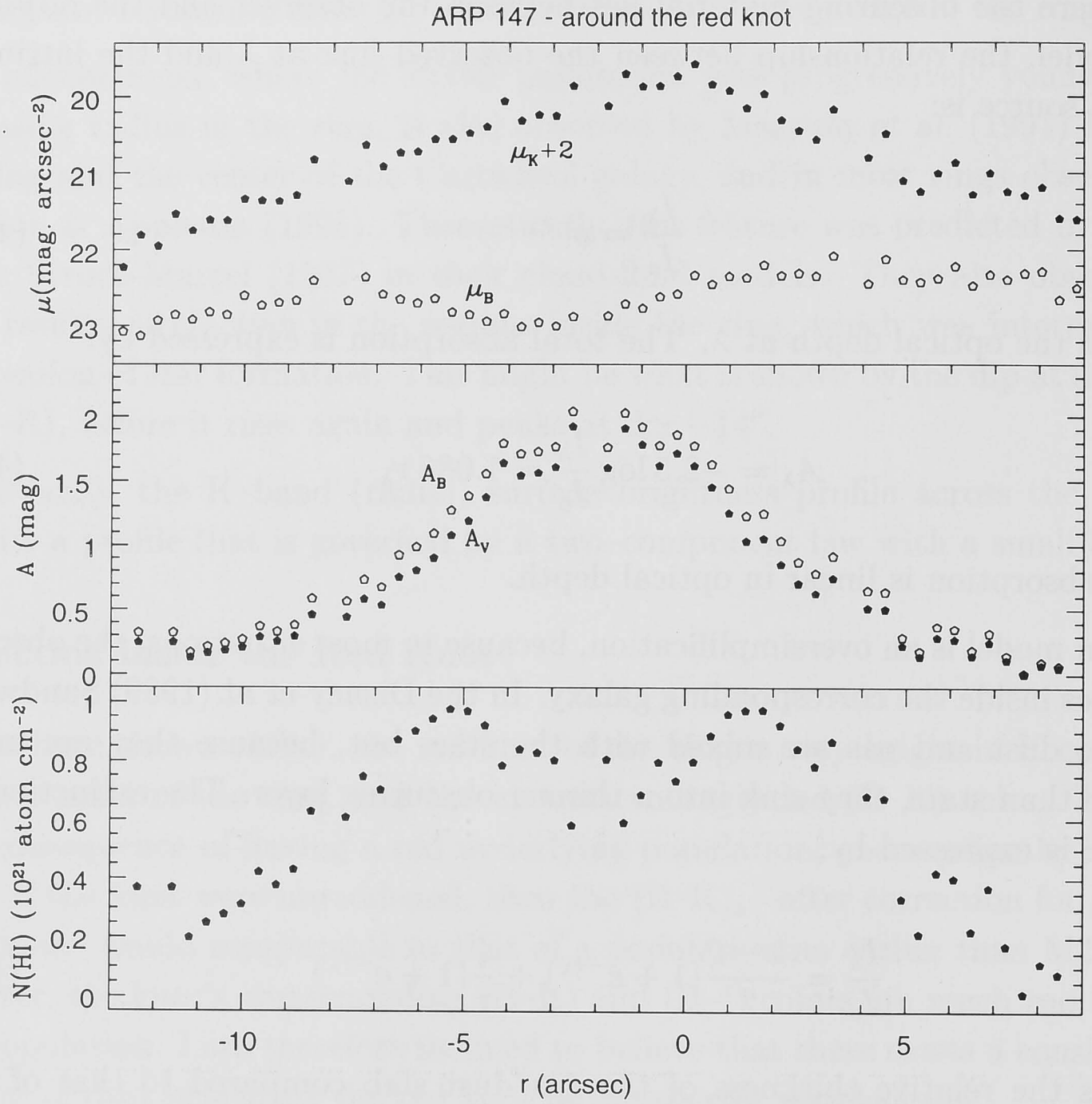

Figure 4.9: Dust distribution around the Red Knot of Arp 147

total absorption A_B and A_V. Note that the peaks of the absorption lie between the minimum dip in μ_B and the maximum of μ_K.

The bottom panel is the distribution of obscuring dust expressed as the surface density of HI. It is interesting to note that the heaviest obscurations lies offset from both the extrema of B and K. This discrepancy between the peak of K and the peaks of the obscurations is indicative of the circular motion of the ring relative to the red knot, presuming that it goes clockwise north to east over the ring. This might also explain the noisy distribution of gas/dust between both peaks: a consequence of a 'smoothing' effect produced by the rotation.

Unfortunately most simulations of ring galaxies are concentrated on the radial motion of the ring. Gerber *et al.* (1992), however, depicted the rotational effect in more detail. In their model of Arp 147, the highest density of the disk stars exists between two local maxima of the gas distribution, with one peak –related to the 'first peak' in this observation– closer to the stars density peak. Their second gas density peak, however, seems less strong than the first one, while my observations

indicate that they have comparable density. In their calculation the gas density in these maxima is about 1×10^{22} atom cm^{-2}, about a factor of ten more than observed in the ring of Arp 147.

4.3 Kinematics

Results from longslit observations of the ring, based on $H\alpha$ and [NII] emission lines and taken over seven position angles (PAs), are shown in Fig. 4.10. It should be noted here that the PAs, unlike those discussed in the morphology section, are centered on the spheroidal component's nucleus; PA $= 0°$ is to the north and increases to the east as usual.

The general kinematics of the ring is represented by PA $= 283°$ and $296°$, which show the most extreme velocity diference – about 150 km s^{-1} – across the minor axis of the ring (PA $\simeq 296°$). Note that there is an area where there is no emission coming from the center of the ring; those that are emitted from inside the ring I believe are mostly caused by the effect of seeing, which is typically $2''$ to $3''$. As the slit proceeds away from the minor axis, intersecting the ring more tangentially, the velocity 'jump' becomes smaller. At PA $= 307°$ the previously declining trend in velocities changes sign, and at PA $= 328°$, right at the outer (tangential) edge of the ring, the velocity reaches its maximum of about 9800 km s^{-1}. These high velocities in both PAs morphologically correspond to the outer knots of the ring mentioned in the previous section and might be another body of gas moving with different velocities than that on the ring.

The emission lines also show clear multiple peaks at PA $= 270°$, $307°$ and $328°$. In PA $= 307°$, the higher velocities might correspond to gas associated with PA $= 317°$ and $328°$, while the lower velocities are part of the ring.

Another interesting feature is a drop in velocities at the outer edge of the spectra at PA $= 283°$ and $296°$ and, with only one datapoint, at PA $= 317°$. Although there are only a few data points here, and the emission line strength is weak compared to others, I have no reason to doubt their reality.

The overall picture of the kinematics of the ring, superimposed on a B-image, is shown in Fig. 1.10. In this picture, velocities with multiple peaks were averaged with weights based on the linestrength. It can be seen that there are at least two superimposed major trends of velocities on the ring. The first goes roughly from west to east, the second from south to north then curves towards east. I suspect that this comes from a combination of rotational and expansion velocities.

To calculate the rotational and radial velocities of the ring, I have firstly fit an ellipse to the ring in the B image. Based on this ellipse I then chose datapoints lying on the ellipse and measured each datapoint's position angle ϕ; here $\phi = 0°$ is on

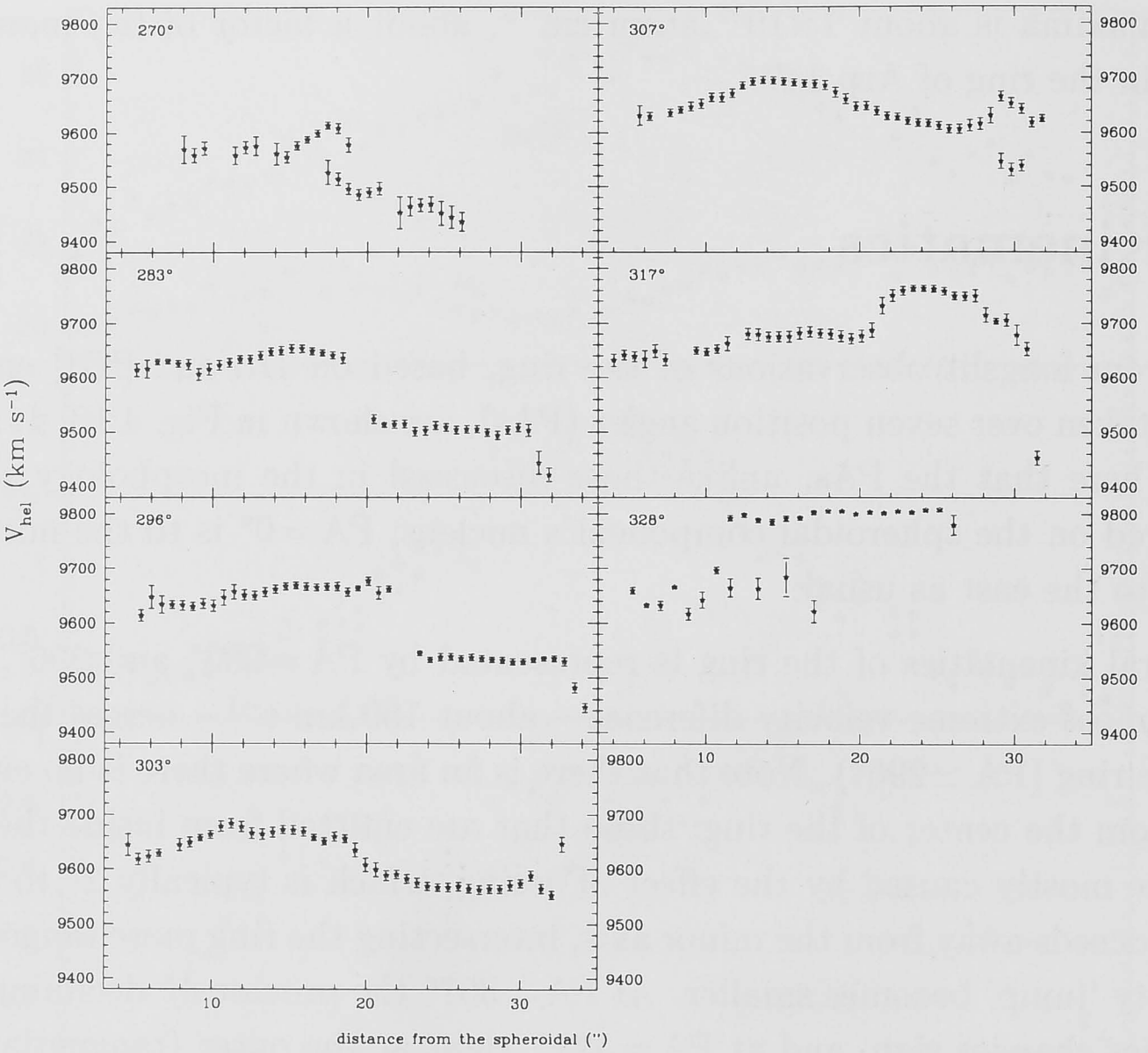

Figure 4.10: Observed heliocentric velocities on the ring of Arp 147

the line from the center of the ring to the north and ϕ increases counterclockwise. For inclination i of the ring,

$\tan\theta = \tan\phi \cdot \sec i$

where θ is the position angle in the plane of the galaxy. The observed (heliocentric) velocities were then fitted to the equation:

$$V_{obs} = V_{syst} + \sin i\ (V_{rad}\ \sin\theta\ +\ V_{rot}\ \cos\theta) \tag{4.8}$$

with V_{obs} the observed velocity, V_{syst} the systemic velocity of the ring, V_{rad} the expansion (or contraction) velocity, and V_{rot} is the rotational velocity of the ring;V_{rad} and V_{rot} are assumed constant on the ring. For this ring I have adopted an inclination of 30° based on the ratio of major to minor axis, assuming that it is intrinsically circular.

The data and their fitted sinusoidal curve is shown in Fig. 4.12. The best fit gives:

$V_{syst} = (9629 \pm 9)$ km s^{-1}

$V_{rad} =$ (-58 $\pm$ 14) km s^{-1}

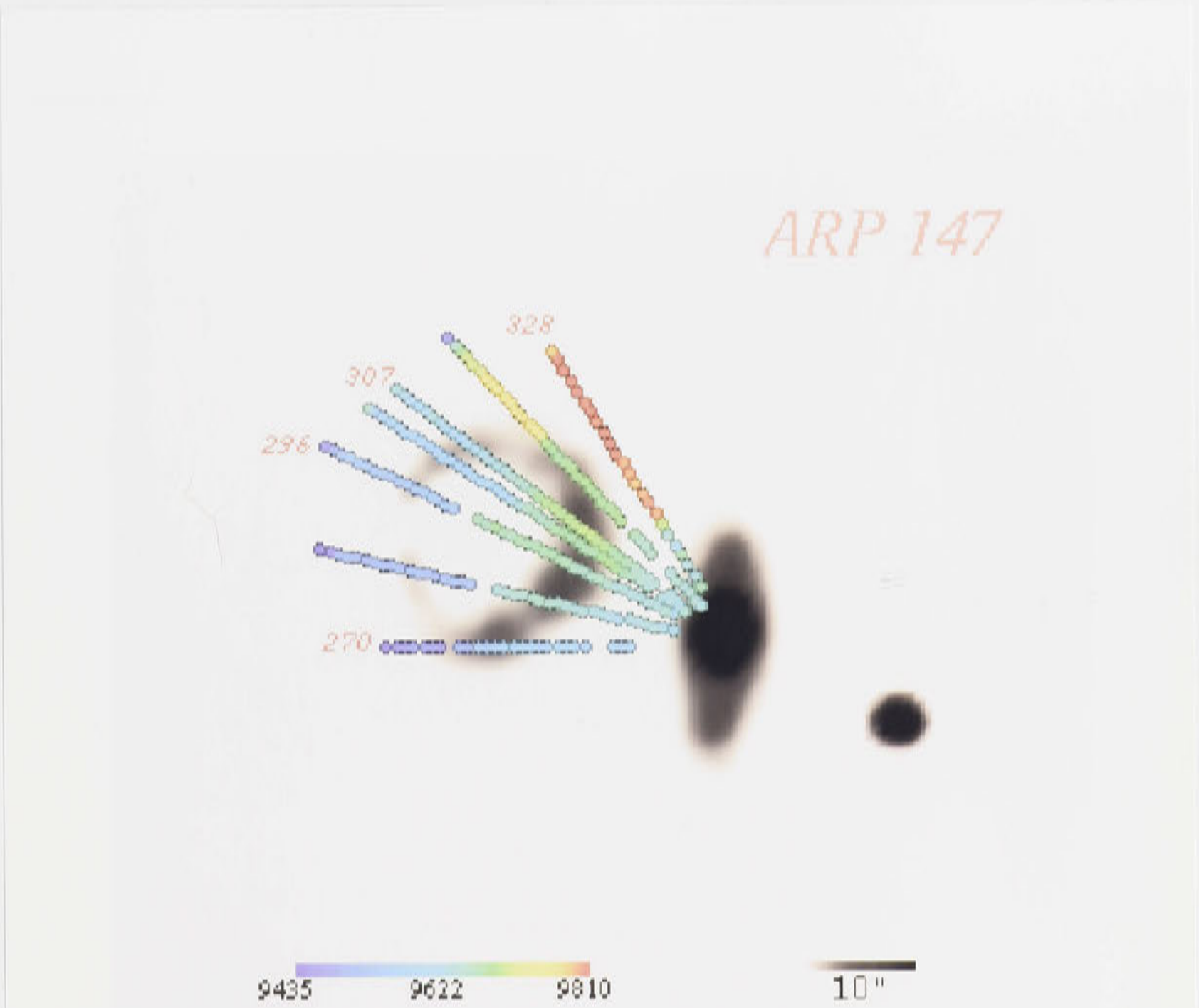

Figure 4.11: Velocity distribution of Arp 147 overlaid on an optical image. The numbers at the ends of the slit positions are the position angle.

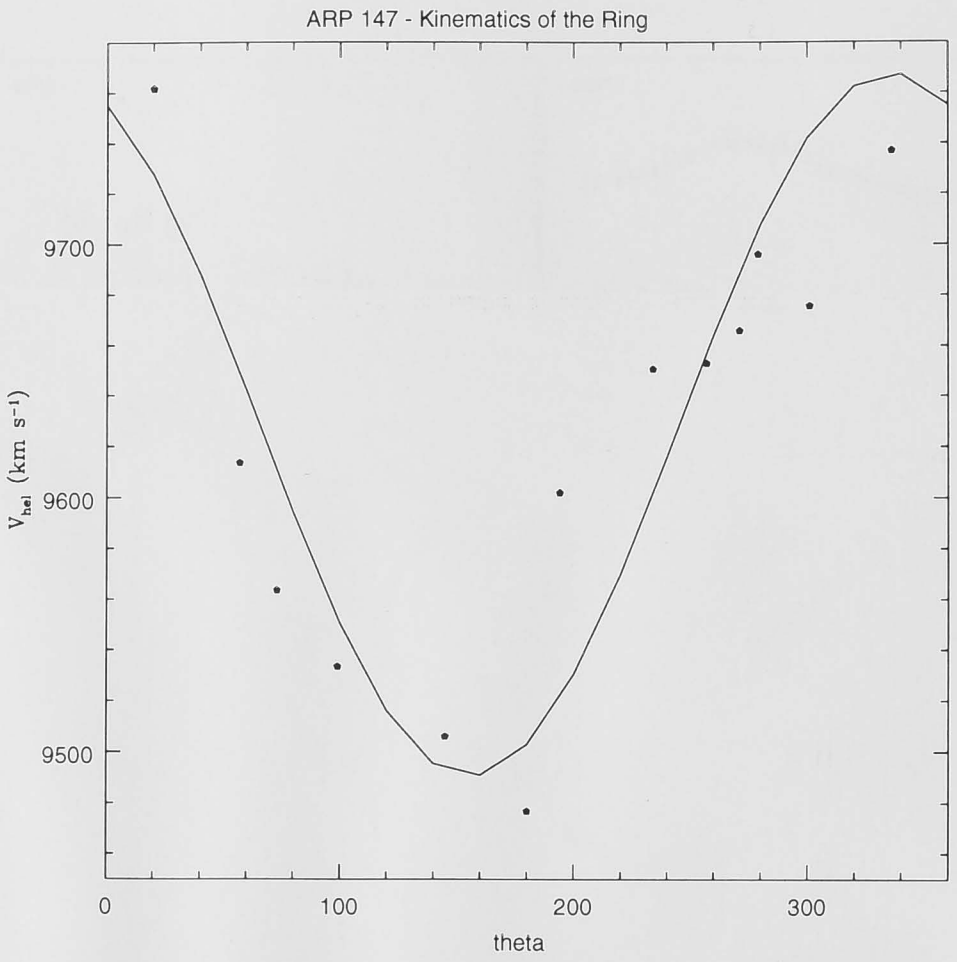

Figure 4.12: Data and fitted curve for rotational and radial velocities of the ring of Arp 147

$V_{rot} = (126 \pm 16)$ km s^{-1}

The negative value of V_{rad} does not mean that the ring is contracting, but simply that one cannot tell whether the ring is contracting or expanding unless one knows which side of the ring is receding/approaching. If we accept Gerber *et al.*'s prediction (1992), that the eastern part of the ring is receding, then this will mean that the ring is expanding (at a velocity of 58 km s^{-1}).

Unfortunately we do not have velocity information for the red knot. The closest we have is at PA = 283° where the slit slices just at the outer edge of the knot. This position corresponds to $\theta \simeq 200°$ in Fig. 4.12. Nevertheless the velocity here deviates significantly from the fitting curve which might imply that the red knot has affected its motion. Excluding this datapoint gives a similar solution:

$V_{syst} = (9624 \pm 10)$ km s^{-1}

$V_{rad} = (-56 \pm 15)$ km s^{-1}

$V_{rot} = (135 \pm 15)$ km s^{-1}

4.4 Masses

Since the major contribution of the total mass comes from the old stellar population which dominates at K, I have used the K–band magnitudes to estimate the

masses of the components of Arp 147. I have measured that $K_{ring} = 12.47 \pm 0.015$ mag and $K_{SO} = 11.77 \pm 0.015$ mag which, using the transformation given by Korneef (1983), corresponds to $F_{K,ring} = 6.84$ mJy and $F_{K,SO} = 13.03$ mJy. Employing Thronson and Greenhouse's relationship (1988) based on the observed stellar population in the solar neighborhood, for near-infrared mass-to-light-ratio, I have, for Arp 147:

$M_{old\,pop.,ring} = 2.9 \times 10^{10} M_{\odot}$

$M_{old\,pop.,SO} = 5.5 \times 10^{10} M_{\odot}$

This gives a total luminous (K-band) mass of

$M_{old\,pop.,tot} \simeq 8.4 \times 10^{10} M_{\odot}$

Rough dynamical estimates of the masses follow from assuming that the ring of Arp 147 is circular, and that the circular motion is Keplerian. Then:

$$M_{dyn.,ring} = \frac{V_{circ}^2 \cdot r}{G} \tag{4.9}$$

V_{circ} is the circular velocity of the ring, and r is the radius. This is a poor assumption, since the ring of Arp 147 has a significant expansion velocity. Eq. (4.9) gives $M_{dyn.,ring} = 1.7 \times 10^{10} M_{\odot}$. This dynamical mass of the ring is not inconsistent with that derived from the K-band luminosity.

If, instead, I assume that both IC 298 and IC 298B are in a bound system, then

$$M_{dyn.,tot.} = \frac{\Delta V^2 \cdot d}{G} \tag{4.10}$$

where ΔV is the velocity difference of both components, and d is their separation. For Arp 147, ΔV is $220\,\mathrm{km\,s^{-1}}$ and d is about 13 kpc, which gives $M_{dyn.,tot} = 1.5 \times 10^{11} M_{\odot}$. Since the orbital parameters (eg. inclination, eccentricity, phase) of the system are unknown, this dynamical mass is only a lower limit to the total mass of the system.

To estimate the kinematic age of the ring, I assume that the ring's expansion velocity is constant with time. This is not correct, since the expanding wave will decelerate during its expansion. This will give a lower limit to the ring's age:

$$\tau_{ring} = \frac{r_{ring}}{V_{rad}} \tag{4.11}$$

which is $\sim 7 \times 10^7$ yr. If, as in Lynds & Toomre's model (1976), the collision path is perpendicular to the disk of the target galaxy, assuming it is a circular ring, the age of the system is:

$$\tau_{sys.} = \frac{d}{\Delta V} \cot i \; yr \tag{4.12}$$

where i is the inclination of the ring. This gives $\tau_{sys} = 1 \times 10^8$ yr. Again these two estimates are roughly consistent.

Another estimate of the age of the ring can be derived from its colors. The blue colors of the ring suggest that it is dominated by a blue, young population. Additionally, it is now a well–established belief that ring galaxies are products of near–head–on encounters. It may then be appropriate to use the evolutionary synthesis models by Leitherer & Heckman (1995) for starbursts. The (B–R) color of the bluest structure in the ring of Arp 147 indicates that it has an age of log(t)$\simeq$6.8 for a burst with abundance of one to two times the solar abundance. A continuous star formation rate gives a slightly older age estimate, log(t)$\simeq$6.9, but the (B–K) color of the ring is much too red compared to that of the models, even after correcting it for the estimated contribution from the strong nebular lines (about 30% in early phases according to Leitherer & Heckman). Population synthesis models by Charlot & Bruzual (1991) give similar conclusions for a single burst scenario. Thus the (color) age of the ring of Arp 147 is about 6×10^6 yr, much younger than the ages derived kinematically and dynamically. It thus appears that the ring of Arp 147 has suffered a recent burst of star formation.

4.5 Discussion

4.5.1 Comparing Notes

Gerber *et al.* (1993) made numerical models of Arp 147-type ring galaxies. Their simulation uses an exponential disk of gas (SPH) and stars, surrounded by a spherical stellar halo. For the gasless intruder, an elliptical galaxy, they use a spherical distribution of stars. Their computation models a collision between two equal-mass galaxies, with the impact point slightly offset from the disk's center and almost perpendicular to the disk. Some of their main results are:

- the nucleus of the disk is knocked out of the plane of the disk such that, due to orientation, it lies in front of the ring, thus obscuring the corresponding part of the ring behind it
- the projected kinematics shows a velocity gradient highest (receding) at the north-east part of the ring and lowest (approaching) at the south-east part; this is a consequence of the ring's rotational and expansion motions
- the brightest knot in the ring in a B-image is predicted to be the true nucleus of the disk galaxy

The kinematics I have measured for Arp 147 qualitatively agrees with what Gerber *et al.* have calculated, ie. where the extreme velocities occur on the ring as discussed in the section on kinematics above. Quantitatively, my observations give values for rotational and expansion velocities: 126 and 58 km s^{-1}, compared to the predicted 140 and 150 km s^{-1}. My derived expansion velocity is considerably different from that obtained by Jeske (1986): his estimate is 135 km s^{-1} (and 137 km s^{-1} for the rotational velocity). No error was given, but we note that his highest spectral resolution is about 8 Å while it is not more than 2 Å for the observations reported in this chapter.

One additional comment: there is clear indications that the ionised gas is present external to the ring and between both components, as can be seen in Fig. 4.11. The extent of the ionised gas is almost twice the radius of the stellar ring.

4.5.2 The Red Knot

The red knot shows strong indications that it is the nucleus of the former disk galaxy. Jeske (1986) found that the strongest radio continuum emission is coincidental with where the optical ring breaks, ie. where the red knot lies; here the spectral index is steeper. He also observed lack of optical emission lines there and concluded that the source is hidden behind obscuring material.

As has been shown in the figures, while the rest of the ring is relatively blue, the red knot has an extremely red (B–K) color, reaching up to about 5 mag. This knot is much redder than the other knots in the ring, and can probably be explained by the effect of dust in the underlying populations.

Does the nucleus lie in the background, embedded in, or in the foreground of the ring? The azimuthal K (and I) surface brightness distribution on the ring has a profile that peaks smoothly along the ring, giving the impression that it is an integral part of the ring. The position of the nucleus, which lies inside the (largest) gap between two knots as observed in the B and R images also favours the idea that the nucleus is embedded inside the ring. Thus, the apparent observation supports the view that the nucleus is indeed immersed in the ring itself.

4.5.3 The Masses

The indication from the K-band photometry that the companion is twice as massive as the ring makes comparison with dynamical models more difficult. Most models invoke small intruders. Gerber *et al.*(1996) in their N-body/hydrodynamical simulations model how rings will form from collisions with different mass ratios between the 'intruder', a somewhat gasless compact galaxy, and the 'target', a gaseous exponential disk with a halo. They used mass ratios of 1:1, 1:4 and 1:10.

The highest mass ratio (1:1) gives some significantly different results from the others: by 80 Myr, the stellar ring has become much more dispersed while the gaseous ring peaks and is sharp. By 100 Myr, due to the more dissipative nature of the gas, the gaseous ring has lagged behind and is thus contained inside the stellar ring. In addition, the disk galaxy is disturbed: it is significantly warped out of its planar pre-existing structure, resulting in a complex flow of material near the ring. These effects are not observed in the other simulations.

It has been shown earlier that the K–band ring of Arp 147 is slightly smaller and thinner than the R–band ring. These observations are in disagreement with what the models predict. Marston & Appleton (1995) observed a similar trend in the ring galaxies they studied: all implies a larger gaseous (ie. $H\alpha$) ring compared to the K–band ring. A possible explanation for these discrepancies is that the pre-collision disk is an HI-rich, low surface brightness galaxy with insignificant stellar content. The gas propagation due to the interaction induces the first star formation inside the disk; the K-band ring is actually a by-product of the star formation thus contains a predominantly young stellar population.

An interaction with a more massive companion might create a single, relatively short lived ring. It is anticipated that this ring can be quite bright since most of the disk has been transformed into a ring (Gerber, private communication).

Also, we recall that the mass is derived for the components of Arp 147 from the K–luminosity and an assumption about the stellar population. For a galaxy that has just recently experienced a starburst, as seems likely for Arp 147, the core-helium burning stars can contribute significantly to the K–band. According to Bruzual & Charlot (1996), the $(M/L)_K$ is about 0.2–0.6 for an age of 0.1 Gyr, depending on the model used. If this is the case, then the K–luminous mass of the ring could be overestimated by a factor of 1.7–5.

Another option to consider is that there might be another companion whose head-on collision has produced the ring of Arp 147, despite the fact that IC 0298B, the nearby companion, has a similiar redshift and a rather distorted disk. There is a spiral galaxy with unknown redshift about 2.5 arcmin southwest from Arp 147. However, I cannot identify any potential compact third object in the vicinity of the pair, though it is conceivable that this object is so compact that it is almost indistinguishable from other point sources.

If our mass estimates are correct, then further investigations are needed on how a head-on collision -or any type of collision- with a mass ratio of 2:1 or even higher will produce a sharp, well defined ring.

4.6 Summary

The knots in the ring of Arp 147 are relatively young objects except for one very red knot which is very prominent in the K-band image. This red knot is suspected to be the true nucleus of the original disk galaxy and appears to be embedded in the ring, rather than projected on the ring. The obscuring dust and gas inside the red knot is calculated to be about $0.8\times\ 10^{21}$ atom cm^{-2}. The companion is significantly distorted due to the interaction.

The ring is rotating and expanding with about half the rotational velocity, and has a kinematic age of about 7×10^7 yr. It exhibits luminous matter inside and ionised gas outside the ring. The mass of the ring is found to be half that of the companion.

4.7 Reference

Appleton, P.N. & Struck-Marcel, C. 1987, Ap. J. 318, 103

Athanassoula, E. & Bosma, A. 1985, ARA&A 23, 147

Bohlin, R.C., Savage, B.D., Drake, J.F. 1978, Ap.J. 1978, 224, 132

Bruzual, G.A. and Charlot, S. 1997, Ap.J. in prep.

Disney, M., Davies, J., Phillips, S. 1989, MNRAS 239, 939

de Jong, R.S. 1995, A&A, in prep.

Freeman, K.C., de Vaucouleurs, G. 1974, AP. J. 194, 569

Gerber, R.A., Lamb, S.A., Balsara, D.S. 1992, Ap.J. 399, L51

Gerber, R.A., Lamb, S.A., Balsara, D.S. 1996, MNRAS 278, 345

Ghigo, F.D., Wardle, J.F.C., Cohen, N.L. 1983, AJ 88, 1587

Horellou, C., Casoli, F., Combes, F., Dupraz, C., 1995, A&A 303, 361

Huang, S. & Stewa4t, P. 1988, A&A 197, 14

Jeske, N.A. 1986, PhD. Thesis, University of California, Berkeley

Koornneef, J. 1983, A&A 128, 84

Larson, R.B., & Tinsley, B.M. 1978, Ap. J. 227, 756

Leitherer, C. and Heckman, T.M. 1995, Ap.J. Suppl. Ser.

Lynds, R. & Toomre, A. 1976, Ap. J., 209, 382

Majewski, S.R & Hereld, M. 1991, BAAS, 178th Meeting, p. 1032

Marcum, P.M., Appleton, P.N., Higdon, J., 1991, BAAS 23, 1390

Marston & Appleton, P.N. 1995, AJ 109, 1002

Rieke, G.H., Lebofsky, M.J. 1985, Ap. J. 90, 900

Schultz, A.B., Spight, L.D., ROdrigue, M., Colegrove, P.T., DiSanti, M.A., 1991, BAAS, 178th Meeting, p. 953

Struck-Marcel, C. & Lotan, P. 1990, Ap. J. 358, 99

Theys, J.C., & Spiegel, E.A. 1976, Ap. J. 208, 650

Theys, J.C. & Spiegel, E.A., 1977, Ap. J., 212, 616

Thompson, L.A. 1977, Ap. J. 211, 684

Thronson, H.A. and Greenhouse, M.A. 1988, Ap. J. 327, 671

Veilleux, S., Cecil, G., Bland-Hawthorn, J., Tully, R.B., Filippenko, A.V., and Sargent, W.L.W. 1994. Ap.J. 433, 48

Toomre, A. 1978, in The Large Scale Structure of the Universe, IAU Symp.No. 79, eds. M. Longair, J.Einasto, p. 109. Dordrecht, Reidel.

Chapter 5

The Highly Disrupted Pairs

5.1 Arp 140

5.1.1 Introduction

Arp 140, or VV81, is an interacting pair consisting of a distorted spiral, NGC 275, and an S0 galaxy, NGC 274. At a distance of ~23 Mpc, the separation between both components is ~5.5 kpc (50″), and the total extent of the system is ~13 kpc. Compared to the systems studied in this report, Arp 140 has a rather small dimension.

The HI spectral profile of Arp 140 observed by Peterson & Shostak (1974) shows an asymmetric double-peaked feature commonly observed in strongly interacting pairs, with a velocity separation of ~150 km s^{-1}. The total HI mass implied by the profile was calculated to be 3.3×10^9 $M_\odot$. Hodge & Kennicut (1983) detected HII regions in both components.

5.1.2 Morphology

The first five subsequent figures show images of Arp 140 at different wavelengths. Due to the small field of view of the near–IR detector, however, NGC 274 was not observed in the K–band.

The irregular component shows a few knots scattered around a central concentration; the knots are embedded inside and connected by diffuse matter which form a distorted 'M' shape. This structure sits on a yet more diffuse distribution, forming the whole configuration of NGC 275. In the B–band (Fig. 5.1), the central knot appears to be dim compared to others but this gradually changes towards longer wavelengths: in the I (Fig. 5.4) and K (Fig. 5.5) images, this central feature becomes the brightest structure inside the irregular component, and I conclude that

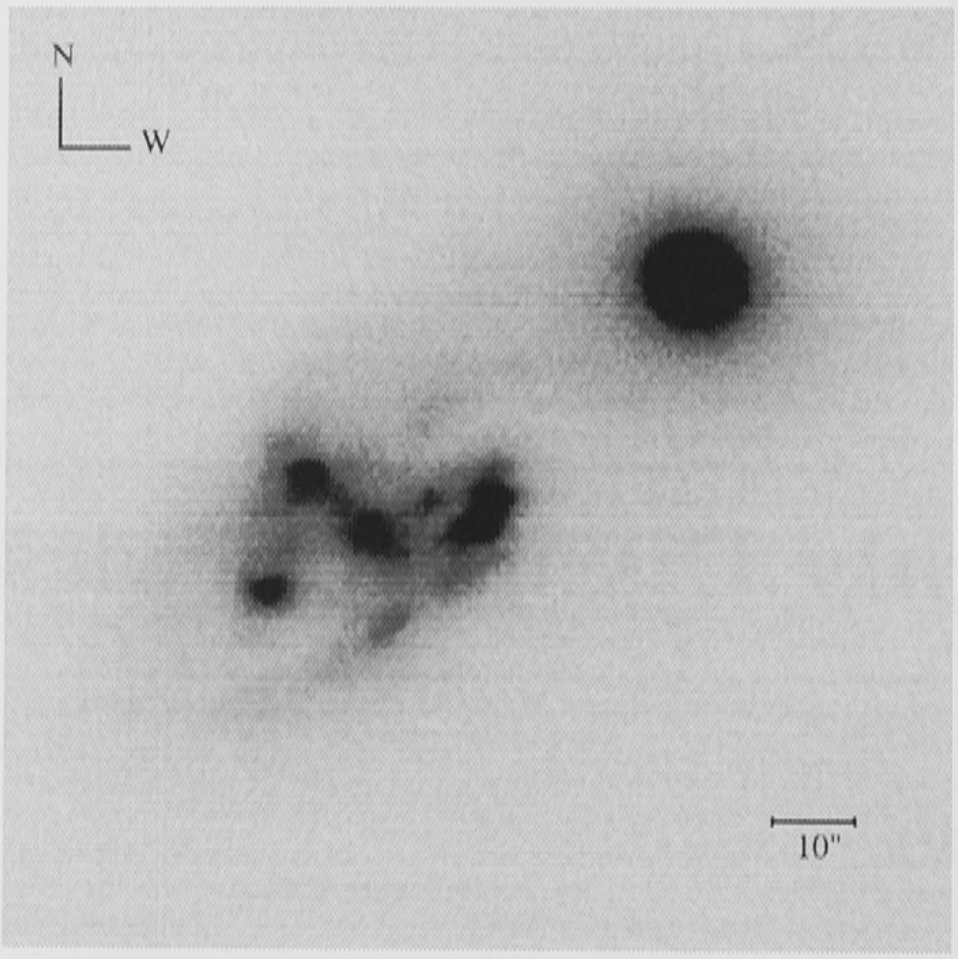

Figure 5.1: B image of Arp 140. The scale is indicated by the bar in the lower right corner; subsequent V, R and I images have similar scale. All images have similar orientation.

it is the true nucleus of NGC 275. However in the K image this nucleus is rather distorted in the NE part and a faint plume emerges northwardly. In the B–, V– (Fig. 5.2) and R–bands (Fig. 5.3), the brightest structure lies $\sim 15''$ westwards from the central nucleus instead and is observed to emit strong $H\alpha$ lines. This consists of two knots and is likely to be an HII region complex; the southern knot of this pair is very dim compared to the other one in the K–band.

The nucleus itself lies on an extended bar-like structure, with a NE–SW extent of about $15''$. This 'bar' coincides with the minor axis of the irregular component and becomes more diffuse towards longer wavelengths; it is also a blue structure, as it becomes diffuse in longer wavelengths. In the R–, I– and K–bands, the 'M' shape of NGC 275 becomes more diffuse.

About $50''$ to the NW lies the companion, NGC 274. Its diffuse envelope suggests that it is an S0 galaxy seen almost face–on. Its outer isocontours are slightly distorted and misaligned and the nuclear region is rather elliptical. Clumps of red material can be seen around this component in the longwavelengths; it is not clear, however, whether these are physically connected to the NGC 274 or are foreground objects instead. A faint jet–like feature emerges from the periphery of the spheroidal component towards the irregular, where it is nearly met by another (diffuse) feature extending from the latter, an indication that interaction is taking place between the two components.

Table 5.1 presents integrated photometry of Arp 140 and of knots inside the

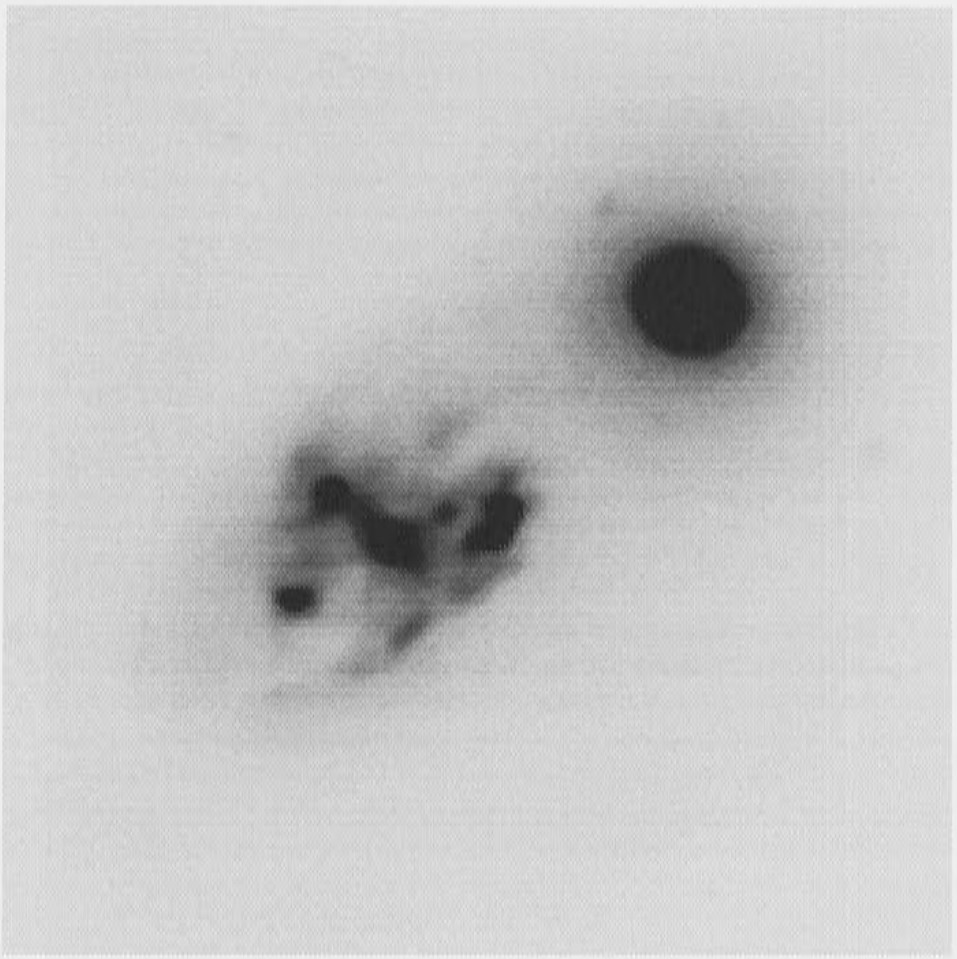

Figure 5.2: V image of Arp 140.

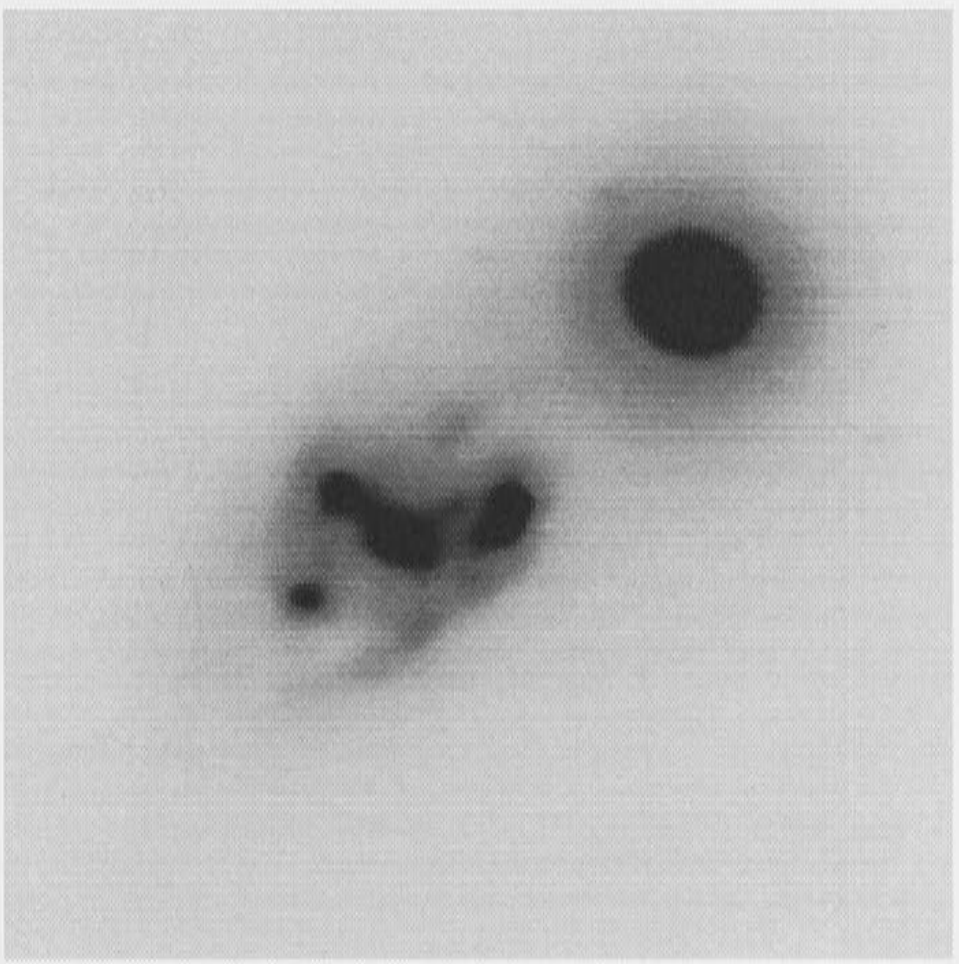

Figure 5.3: R image of Arp 140.

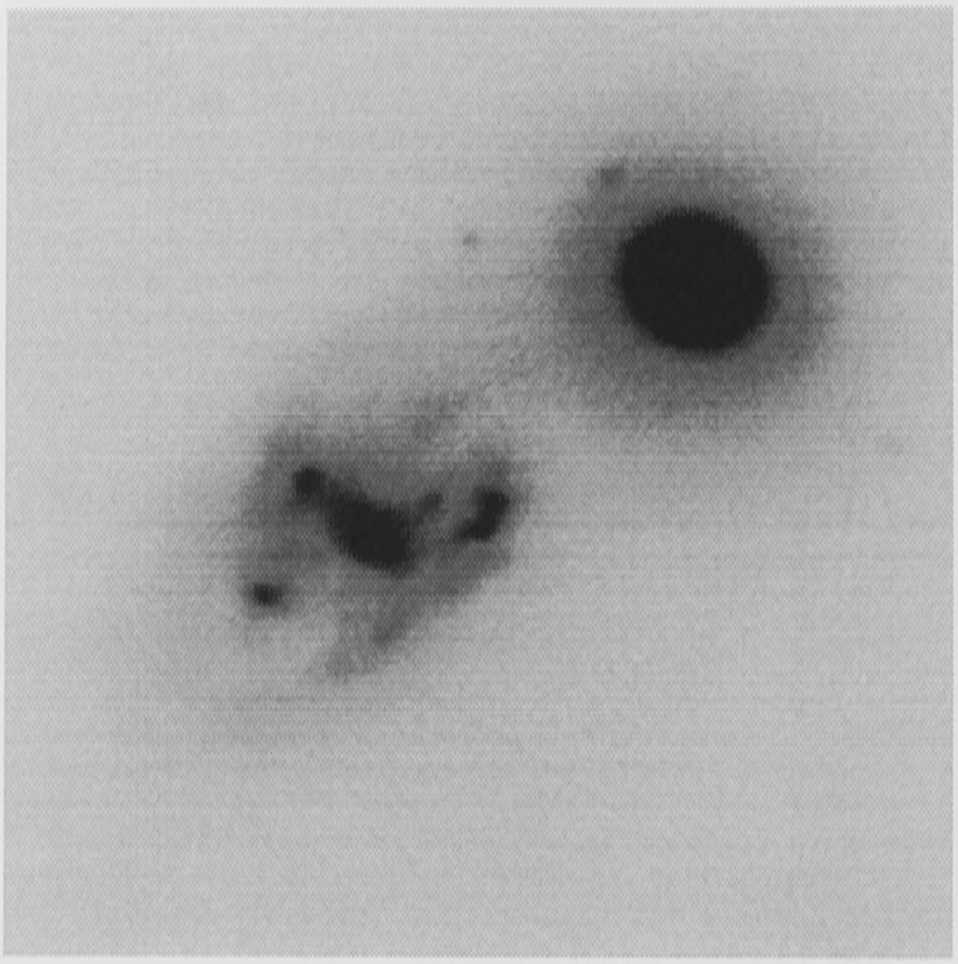

Figure 5.4: I image of Arp 140.

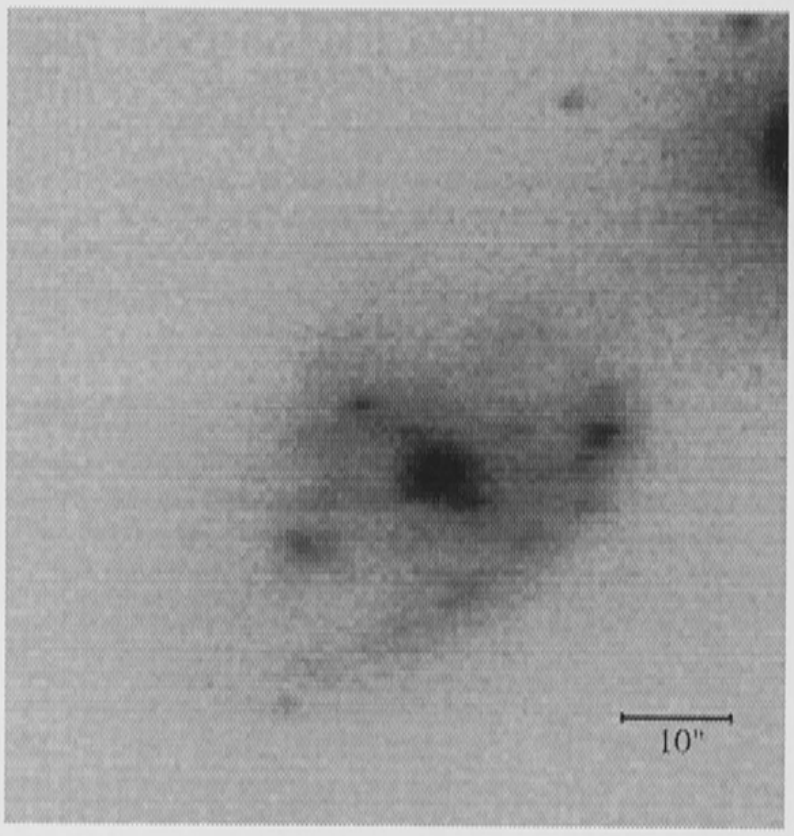

Figure 5.5: K image of Arp 140.

Component	B	I	K	(B–I)	(B–K)
N0274	13.24(0.08)	10.75(0.04)	—	2.49	—
N0275	13.00(0.08)	10.71(0.04)	10.10(0.02)	2.29	2.90
#1	16.88(0.22)	15.03(0.10)	14.33(0.04)	1.85	2.55
#2	16.81(0.22)	15.08(0.10)	13.95(0.04)	1.73	2.86
#3	16.01(0.15)	14.35(0.06)	13.90(0.04)	1.67	2.12
#4(n)	17.04(0.24)	15.02(0.10)	13.52(0.04)	2.02	3.52
#5	17.93(0.36)	16.05(0.16)	14.73(0.08)	1.89	3.20
#6	17.93(0.35)	15.87(0.14)	14.62(0.08)	1.70	3.31
#7	17.76(0.32)	15.41(0.12)	14.10(0.04)	2.35	3.66

Table 5.1: Integrated photometry of Arp 140; n denotes the nucleus of the irregular component.

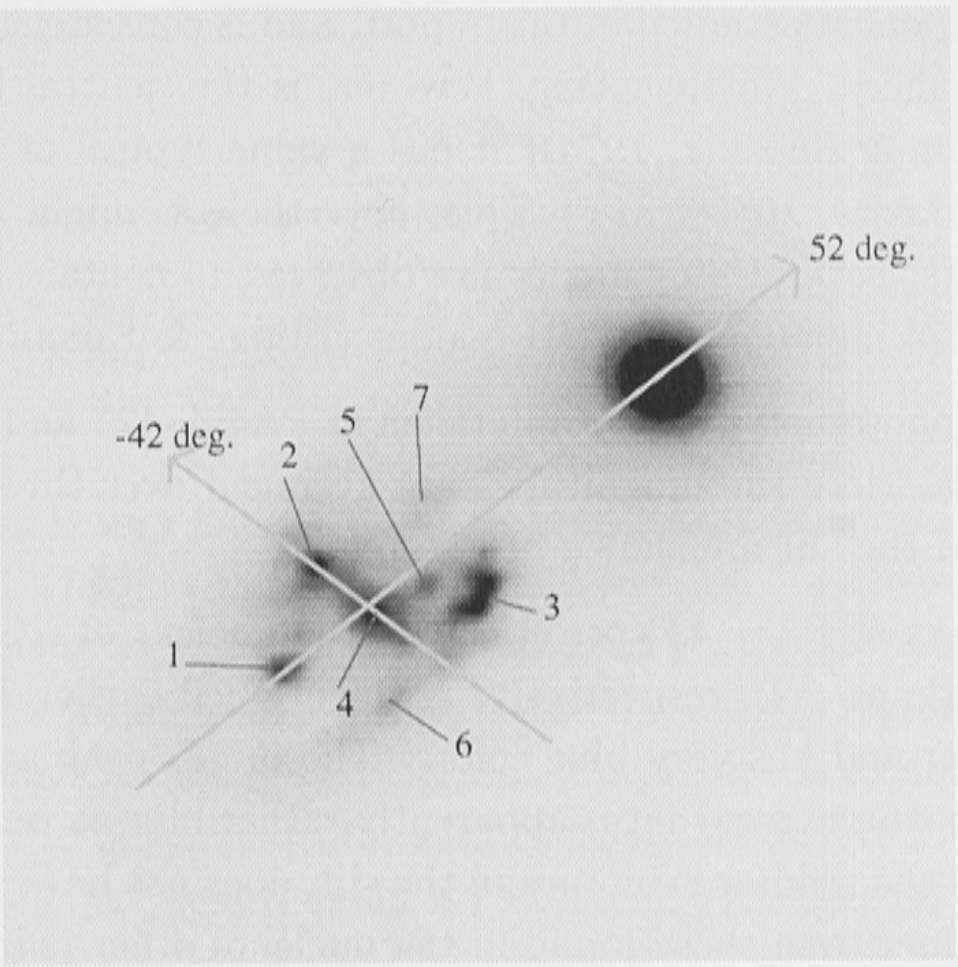

Figure 5.6: V image of Arp 140 with measured knots denoted. The lines correspond to the 'slit' position angles of the measured surface brightness photometry and the arrows show their directions as presented in Figs. 5.7 and 5.8.

irregular component; for designated structures refer to Fig. 5.6. Due to non-photometric conditions, no magnitudes can be calculated from the V– and R–bands; the larger errors in the B magnitudes are due to the less sensitive detector used. No extinction correction, Galactic nor local, is applied.

The table shows that, even including Galactic extinction correction ($\Delta m_B = 0.21$ mag), NGC 275 has very blue colors, particularly in (B–K). Exceptions are the nucleus (knot #4) and knot #7: for the first, it is common to observe redder colors in galaxy nuclei. The latter is the 'bridge' connecting the irregular with the spheroidal component mentioned earlier and, judging from its redder color, might be obscured by dust; despite its diffuse appearance, this object is observed to emit a knotty $H\alpha$ profile. It appears that the knots tend to have bluer colors compared to more extended structures, although the scatter is high due to the errors in the B magnitudes. The bluest knot (#3) is consistent with colors of an underlying stellar population of a few 10^7 yr old based on an instantaneous burst model (Charlot & Bruzual, 1991).

The K–band total luminosity of NGC 275 is calculated to be 60.6 mJy, which, using the transformation derived by Thronson & Greenhouse (1988) for mass distribution in the solar neighborhood, gives a total mass of 8.1×10^9 $M_\odot$ for the irregular's old stellar population. This value is marginally small compared to other irregular components studied in this report, and is consistent with the small dimension of the galaxy. Worth noting, however, is the neutral hydrogen mass of Arp 140 (Peterson & Shostak, 1974): it has a value typical of those observed in normal spiral galaxies, 10^{9-10} $M_\odot$. This, nevertheless, might be contributed by both components: several S0 galaxies are observed to contain gas, and gas is observed in NGC 274 in the form of HII regions (Hodge & Kennicut, 1983).

Surface brightness photometry of Arp 140 taken at PA= $-42°$ and $52°$ are shown in Figs. 5.7 and 5.8. Here the magnitudes are averaged over three rows ($\sim1.8''$) and the locations of the slit are shown in Fig. 5.6.

The two major peaks at PA=$-42°$correspond to the nucleus of NGC 275 and the northeastern knot (knot #2), respectively. As mentioned earlier, in the B image the latter is brighter and has very blue colors. The minor peak at d=$-12''$ is the outer edge of the southern arm that is apparently rather blue as well. The nucleus itself, although it is the reddest structure in the slit, does not have very red colors: they are 1-2 mag bluer than those found in the nuclei of other pairs studied here. This might indicate that there exists little dust inside the nuclear region.

At PA=$52°$, the knot #1 is again brighter in B than the nucleus. Here it is the bluest structure in the plot, having (B–I)$\sim$0.9 mag ((B–I)$_\circ$ $\sim$0.75 mag) and (B–K)$\sim$2.2 ((B–K)$_\circ$ $\sim$2.1), again indicative of an underlying population not older than 30 Myr. At d$\sim20''$, the colors display a peak, corresponding to the faint diffuse structure north of knot #3 as observed in the K–band.

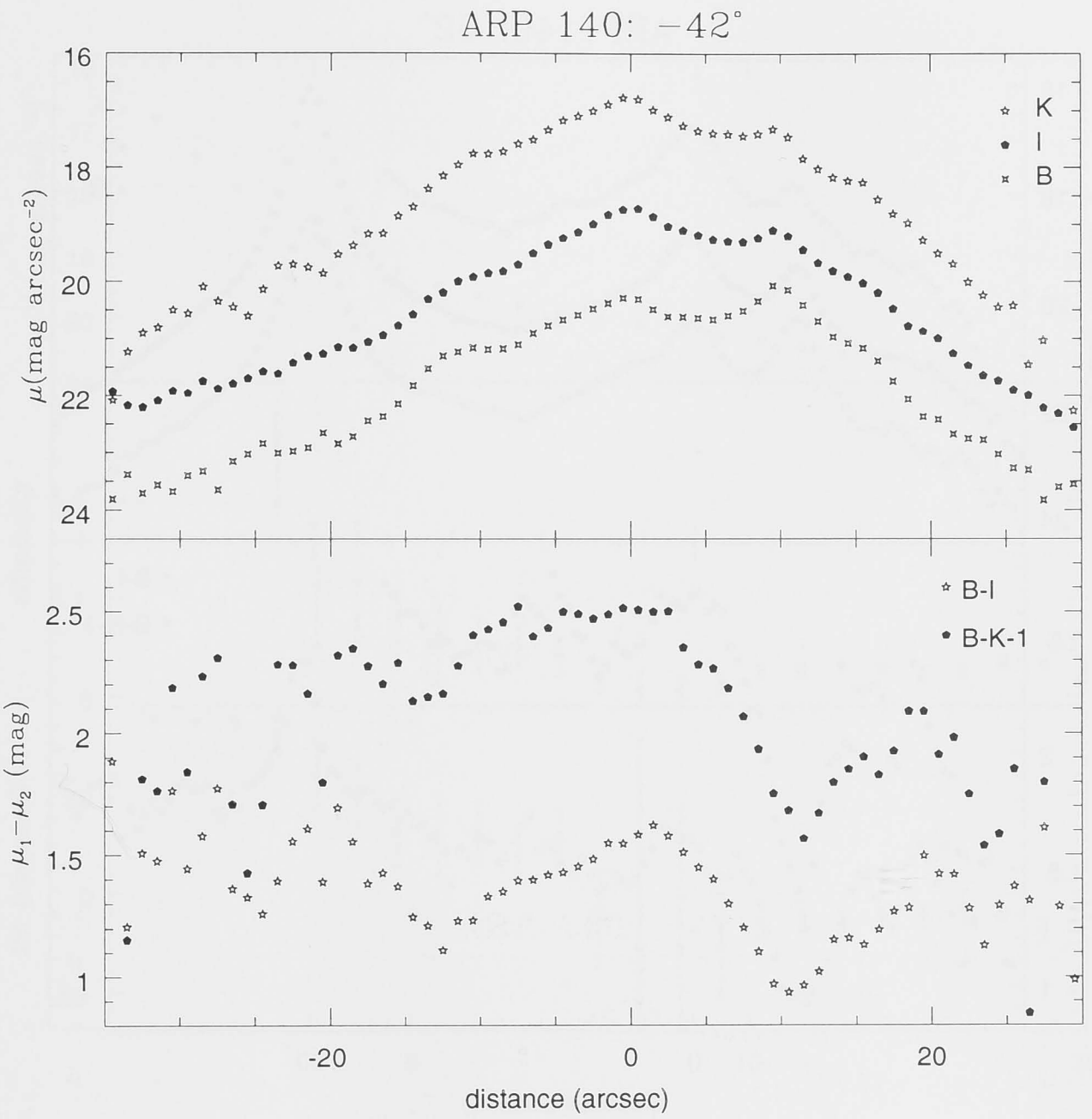

Figure 5.7: Surface photometry of Arp 140 at PA=–42°; d=0° denotes where the nucleus of NGC 275 lies.

The nuclear region is very flat in (B–K): in both PAs, the color difference does not exceed ∼0.2 mag, which is unusual for nuclear regions. As a comparison, all other irregular components in pairs that are observed in the K–band in this project show a (B–K) color gradient of 1-2 mag inside the nuclear regions alone, reaching a value of 4–5 mag. At PA=–42°, the flat-top feature is asymmetric about the nucleus but seems to be coincidental with the central bar. At PA=52°, the extent of the feature is smaller, which again is consistent with the 'slit' crossing the bar almost diagonally.

A color gradient inside a galaxy can be a) a radial change in stellar population distribution, and b) a radial variation in reddening due to dust extinction. De Jong (1996) argued that the most plausible explanation for color gradients in spiral galaxies comes from stellar population differences. If the bar is a recent phenomena, as suggested by its morphology in different passbands, it seems likely that the flat structure is caused by a low population gradient. In addition, the

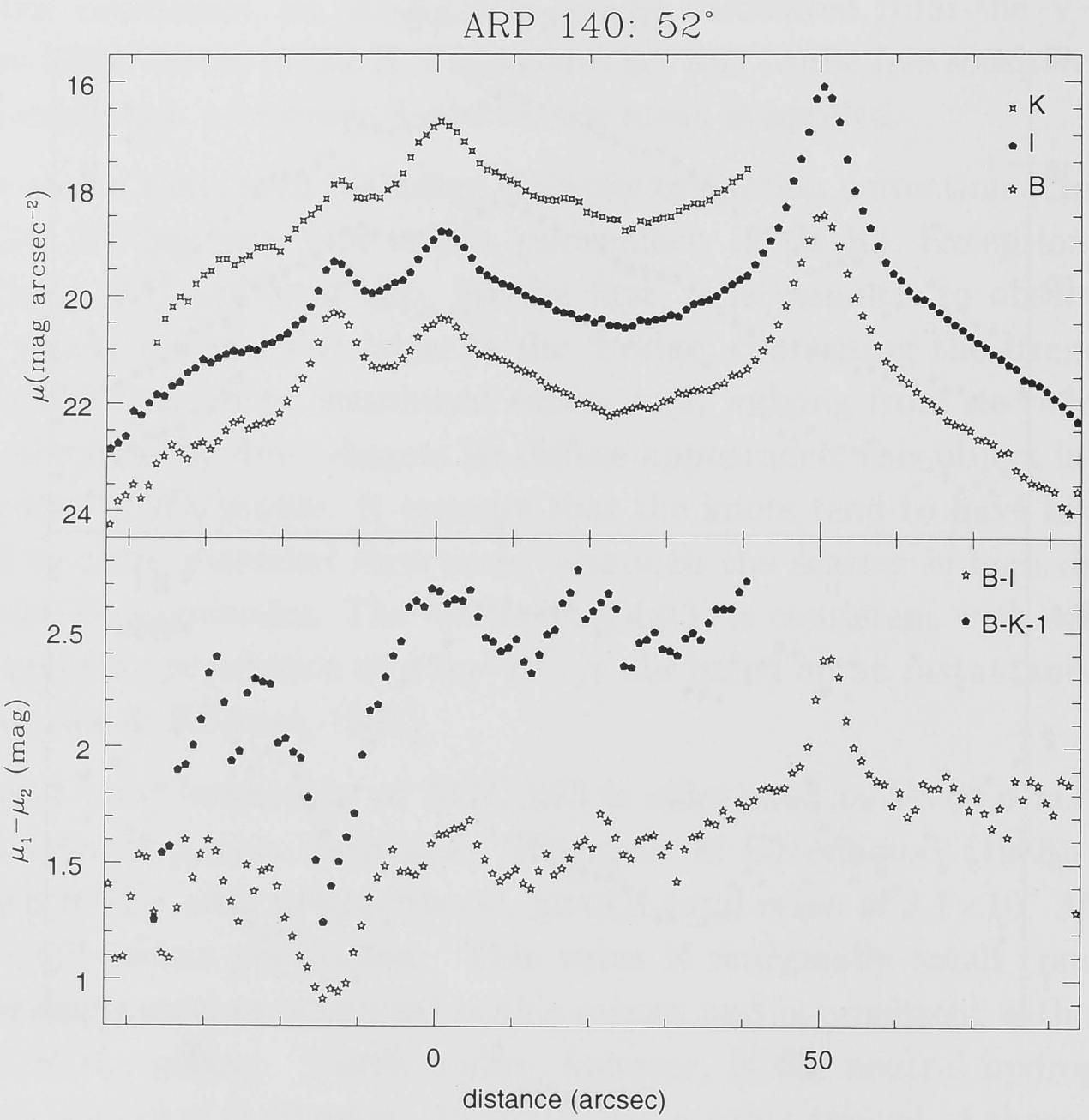

Figure 5.8: Surface photometry of Arp 140 at PA=52°; notations are the same as in Fig. 5.7.

low values of (B–K) are evidence of little dust within the bar.

The (one–dimensional) surface brightness profile of NGC 275 along its minor (ie. bar) and major axis follows an exponential law, despite its disrupted appearance. The spheroidal companion also follows an exponential: as the morphology shows, NGC 274 is a disky system (Fig. 5.9, upper). The ellipticity and twisting profiles of the spheroidal companion are also plotted in the middle and lower panels of Fig. 5.9, respectively. The small ellipticity of the disk in the outer region implies that the NGC 275 is seen face–on. With the twisting that is not oriented towards the irregular galaxy, it is suggestive that the galaxy is not heavily disturbed due to interactions.

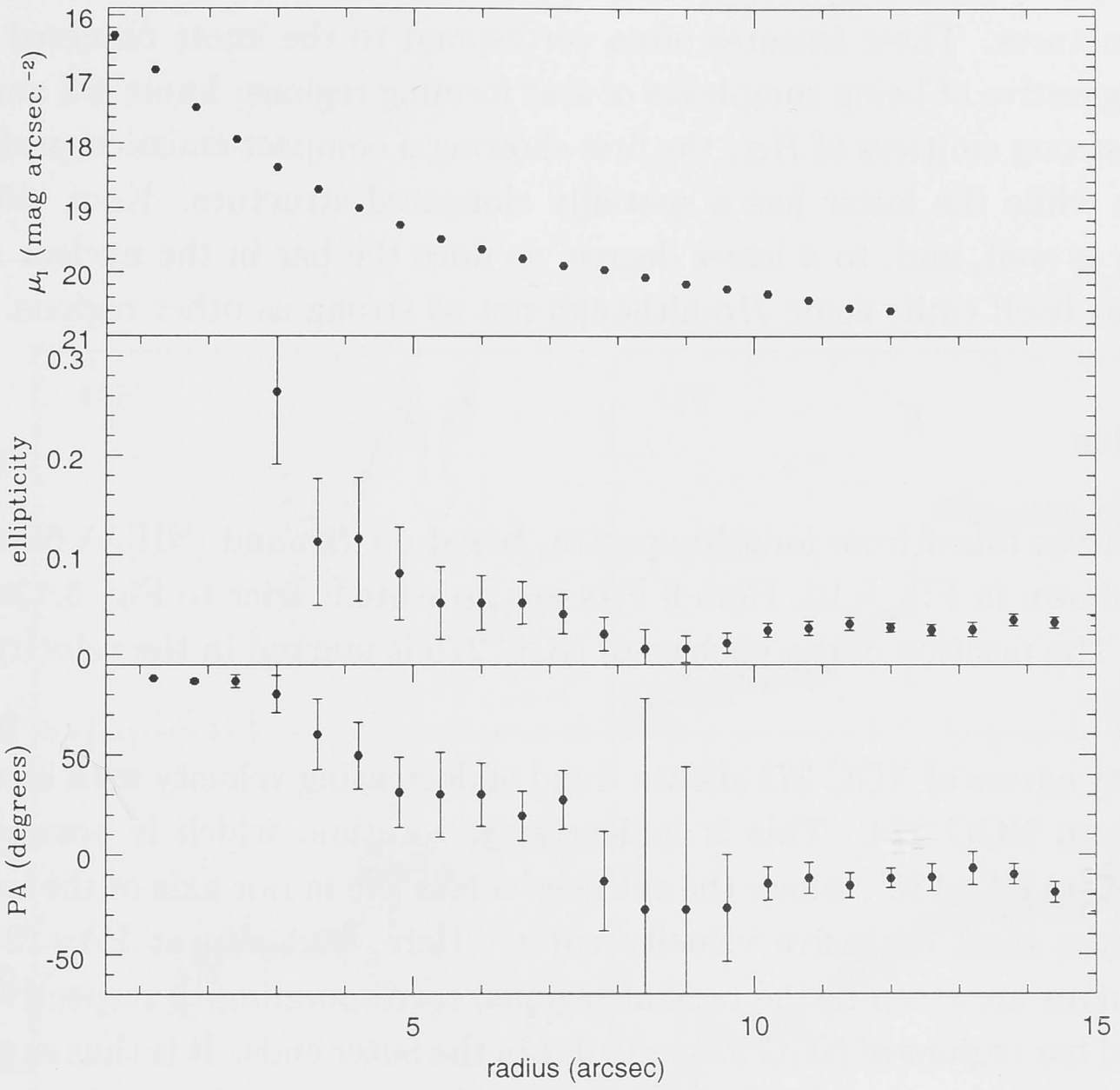

Figure 5.9: Luminosity profile in I–band (upper), ellipticity (middle) and orientation of major axis (lower) of NGC 274 as a function of distance from the center.

5.1.3 Spectroscopy

The spectra of NGC 274 are observed to exhibit the H and K lines, G bands and Balmer lines in absorption. In the red, [NII]$\lambda\lambda$ 6548Å,6583Å are also seen, accompanied by a broad absorption profile of $H\alpha$. This nuclear [NII] emission and $H\alpha$ absorption lines are sometimes observed in spheroidal components of interacting pairs, and are thought to be a signature of interaction (Rubin *et al.*, 1991). The lines give an average heliocentric velocity of about 1720±50 km s^{-1}. The irregular component is rich in emission lines: Hζ, Hδ, Hγ, Hβ, $H\alpha$ [OIII]$\lambda\lambda$ 4959,5007, [NII]$\lambda\lambda$ 6548,6583, HeI λ 6678 and [SII]$\lambda\lambda$ 6716,6731. The line ratios of some of these lines imply that NGC 275 is rich in HII regions, which agrees with the conclusion of Keel *et al.* (1985) that the galaxy has an emission class of an HII region. Nevertheless much less $H\alpha$ emission is observed to come from the nuclear region. The heliocentric velocity derived from these emission lines for

NGC 275 is measured to be about 1850±50 km s^{-1}.

The longslit $H\alpha$ (emission) line profiles of NGC 275 are strong and mostly have knotty structures. These features often correspond to the knots observed in the images, suggestive of being complexes of star forming regions: knots #2 and 3 are especially strong emitters of $H\alpha$, the first showing a compact emission profile and is stronger while the latter has a spatially elongated structure. Knot #5 emits strong $H\alpha$ as well, and, to a lesser degree, so does the bar in the nuclear region. The nucleus itself emits some $H\alpha$ although not as strong as other regions.

Kinematics

Velocity curves taken from longslit spectra, based on $H\alpha$ and [NII]$\lambda\lambda$ 6548, 6584 lines, are shown in Fig. 5.10. Here 6 PAs are presented; refer to Fig. 5.12 for slit positions. The position of the nucleus of NGC 275 is marked in the velocity curve for PA=130°.

The velocity curves of NGC 275 show a trend of decreasing velocity with increasing distance from NGC 274. This is indicative of rotation, which is possibly best represented by PA=130°, where the slit goes across the major axis of the irregular and gives the most extensive velocity curve. Here, and also at PA=124°, the velocity curves are steep in the central regions, corresponding to respectively the nuclear and bar regions of NGC 274, and flat in the outer ends. It is thus suggestive that the rotational axis of NGC 275 goes roughly along its minor axis, as will be discussed more later. The total velocity spread is ∼250 km s^{-1}. The flat velocity structure at PA=118°, d=50″–60″ corresponds to knot #2, while the large scatter at d=40″–50″ is due to the weak emission in that region.

Although NGC 275 has a definite signature of rotation, it is clear that the interactions with NGC 274 have disturbed its original kinematics. Signs of dynamical distortions are observed not only in the outer edges of the velocity curves, but also near the central region of the irregular component.

The ends of the velocity curves nearer to NGC 274 show declines in velocities, becoming closer to the velocity of the S0 galaxy. The further ends exhibit a larger scatter of velocities compared to the those emitted by the central region. The steep velocity gradient (ΔV∼120 km s^{-1}) at PA=310°, which is contained inside the nuclear region (d=45″–55″) is followed by 'humps' that mark the edges of the bar. The velocity dips at d=62″ and 40″ correspond to the positions of knots #1 and #5 respectively. These are clear signs of strong interactions, as the inner part of an interacting galaxy will be the last to suffer kinematic disturbances (see Barnes, 1992).

Velocity contour and distribution of NGC 275 are shown in Figs. 5.11 and 5.12, respectively, with the latter being superimposed on an R image of Arp 140. Again,

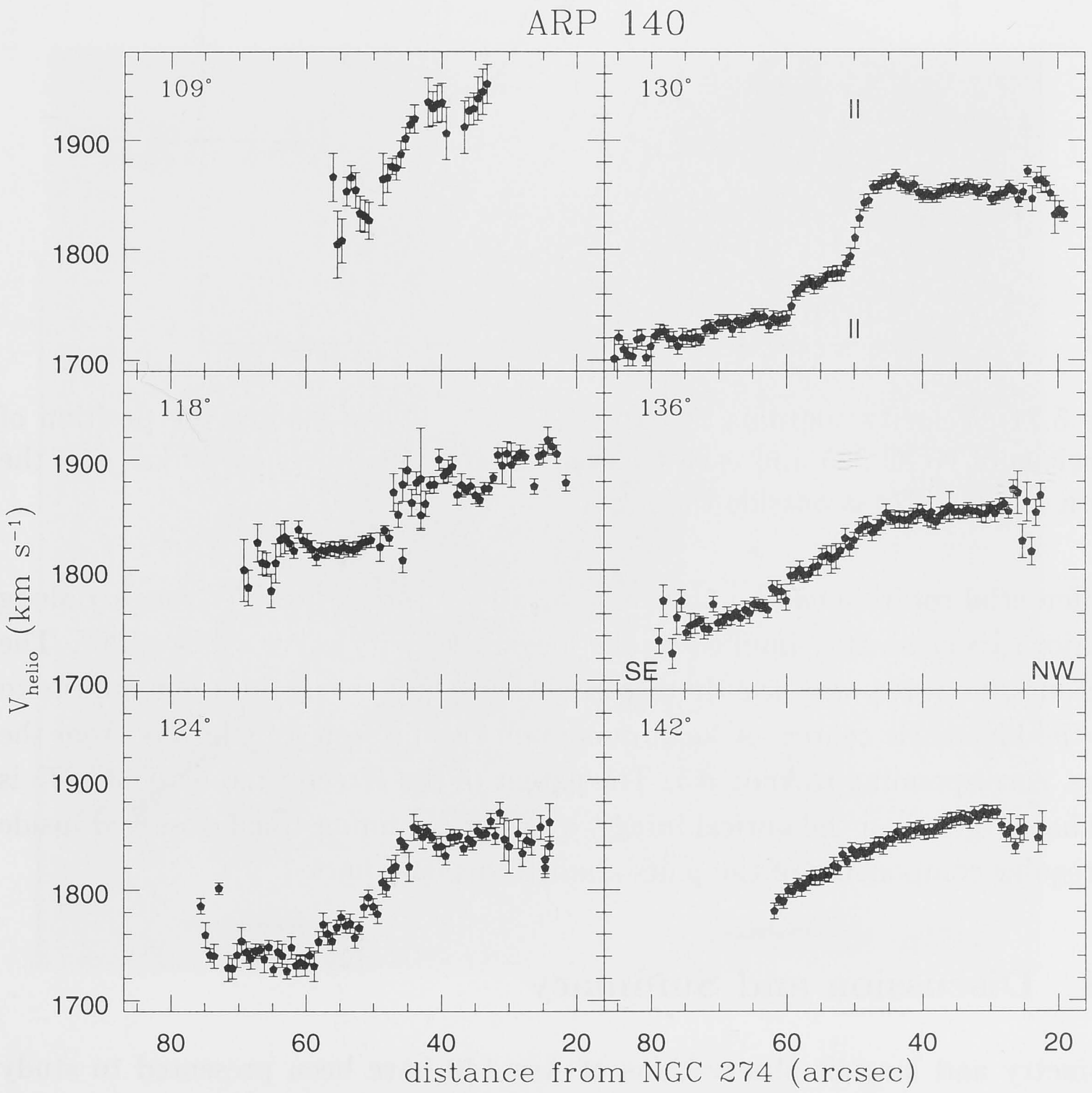

Figure 5.10: Velocity curves of NGC 275 plotted with distance from the spheroidal companion. At PA= 130° the position of the nucleus of the irregular is marked.

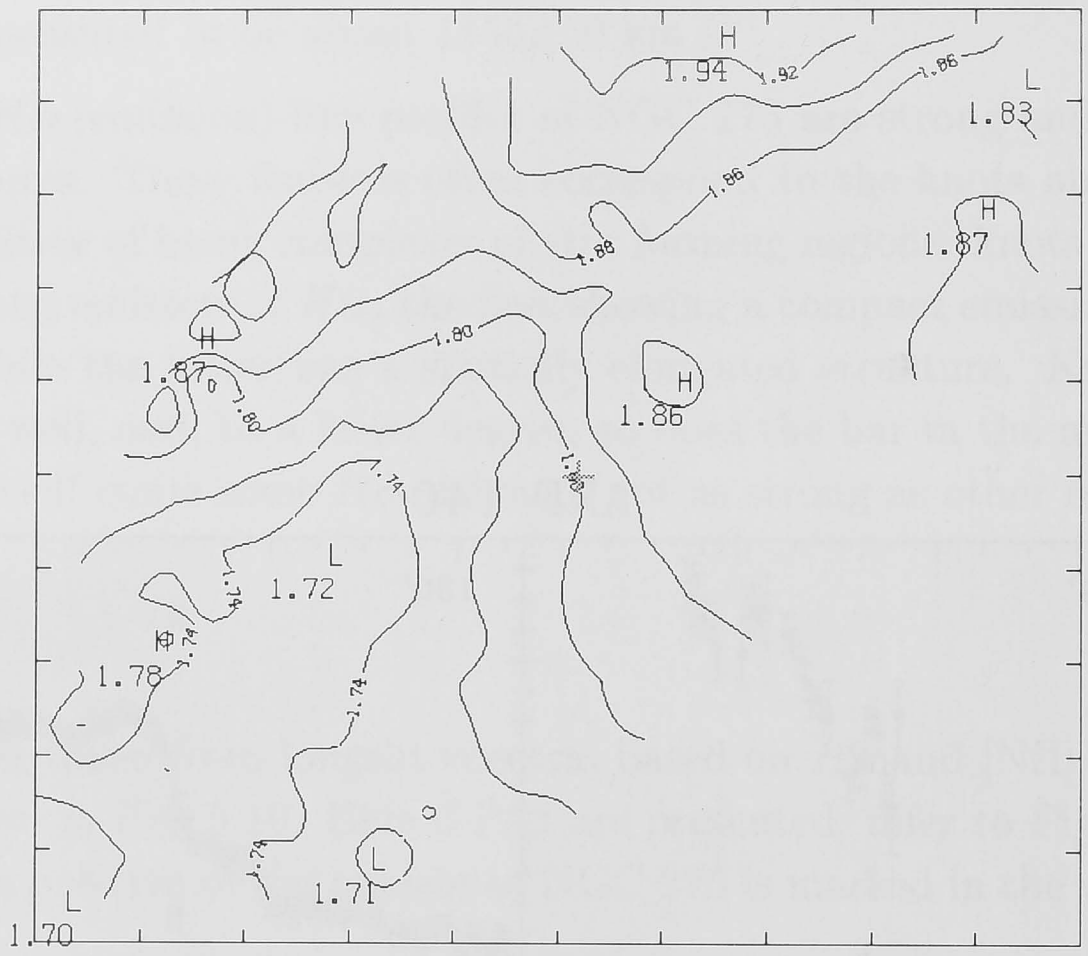

Figure 5.11: Velocity contours of Arp NGC 275. Cross denotes the position of the nucleus of NGC 275 and each consecutive contour differs by 30 km s^{-1}; the position of NGC 274 is outside the frame.

the differential rotation can be observed to extend from SE to NW roughly along the major axis as already implied by the longslit velocity curve at PA=130°. The isocontours, however, are heavily distorted, and the nucleus does not appear to lie on the kinematic center. A local maximum can be seen a little NW from the nucleus, corresponding to knot #5. The extent of the $H\alpha$ emitted by NGC 275 is somewhat larger than the optical image, a rather ccommon trend observed inside the irregular components of the pairs studied in this report.

5.1.4 Discussion and Summary

Photometry and longslit observations of Arp 140 have been presented to study the structure and kinematics of the system. The morphology of NGC 275 exhibits many knots but no strong tidal features can be observed inside the pair. Based on Keel's criteria (1991) for interacting pairs, the kinematics and morphology of Arp 140 are consistent with those caused by a retrograde encounter. This is further supported by models which show that a retrograde passage causes little damage to the global structure of the disk galaxy (Toomre & Toomre, 1978), favouring production of rich, small-scale internal structures instead of extended, thin tidal features (Howard *et al.*, 1993). It is unclear from the models, however, how this type of encounter affects the kinematics of the irregular component.

A bar is observed in the central region of NGC 274; its major axis runs along

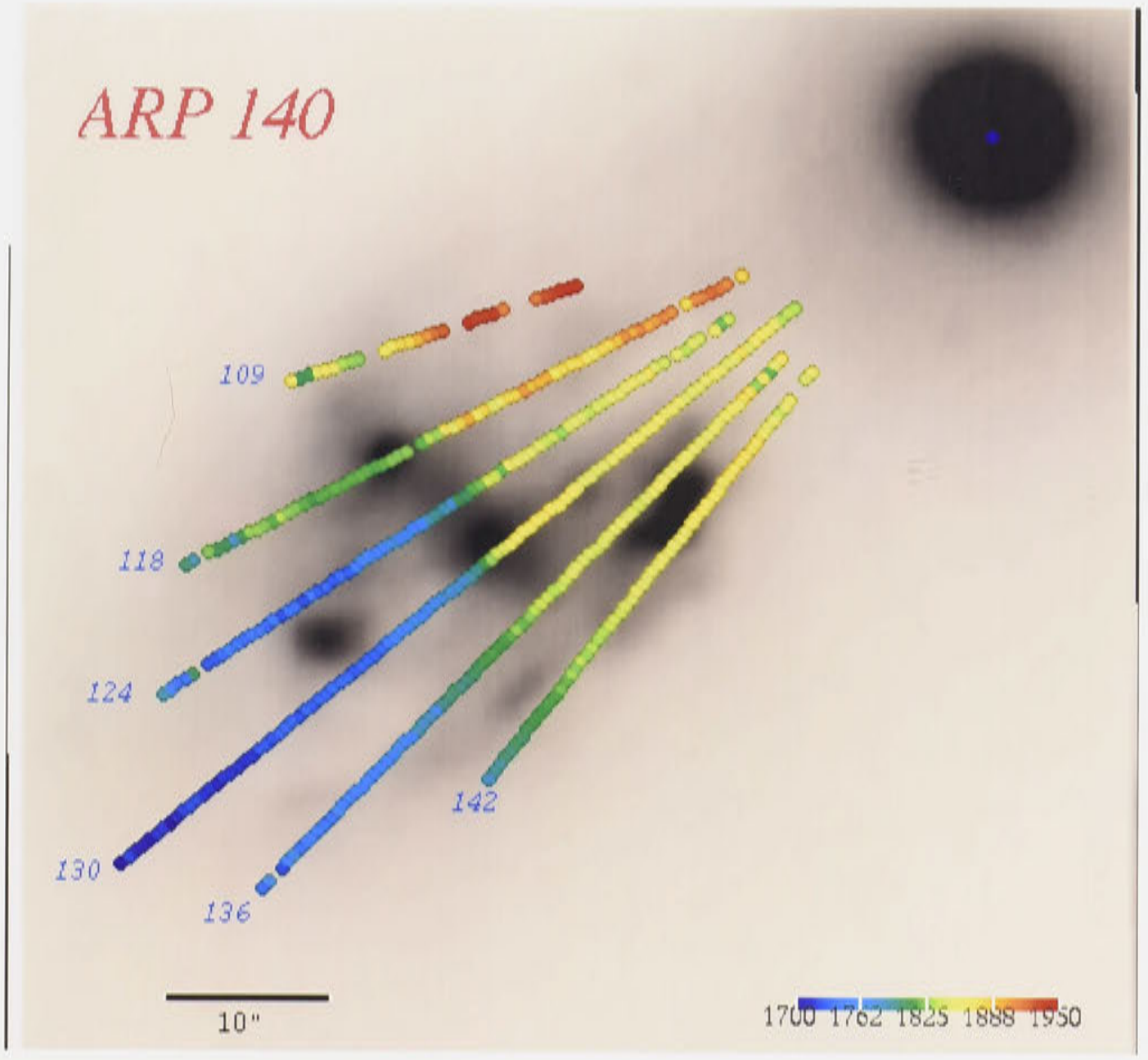

Figure 5.12: Velocity map of NGC 275 overlaid on an R–image of the system.

the minor axis of the disk galaxy. This bar appears to be well–defined in the B and V images but is otherwise diffuse in other passbands. The flat topped (B–K) color structure along the bar and its low values are suggestive of a low population gradient with little dust.

It is believed that bars are fragile structures, and are prone to being dissolved and become bulges (Barnes & Hernquist, 1995; Norman *et al.*, 1996; but see also Miller, 1995). If this is true, then the bar of NGC 274 is likely to be formed due to interactions with NGC 275 and is not a pre–collision phenomenon. The more diffuse morphology in the longer wavelengths represents the (old) stellar distribution that is likely to be structurally disky instead of bulge–like, but more detailed surface brightness analysis is needed to confirm this. The bar does not appear to have large velocity spreads along its major axis. More longslit spectroscopy along the bar is needed to understand the kinematics of both the stellar and gaseous components of this structure.

The knots are found to have very blue colors, implying very young stellar populations with little dust within NGC 275. Observations by Sofue *et al.* (1993) show that Arp 140 has a high L_{FIR}/L_{CO} compared to those of normal galaxies, which support the notion that Arp 140 has an enhanced activity of star formation induced by interactions but not necessarily a large amount of dust. The latter is also implied by the low content of dust ($L_{FIR} \simeq 5\times10^9\ L_\odot$) as shown by the IRAS result, and low L_{FIR}/L_B ($\simeq$0.3) for both components.

The color of the spheroidal component is typical of those observed in early type galaxies, so no 'Holmberg effect', where colors of each galaxy member in an interacting pair are correlated, is detected in NGC 274. Nevertheless, NGC 274 is suspected to have gone recent star forming activities, as exhibited by its blue (B–V) color and by the detection of HII regions by Hodge & Kennicut (1983). My data show that $H\alpha$ (spectral) emission is observed only 2 kpc from the center of NGC 274, with velocities dropping towards the velocity of this component. [NII]λ 6583 is observed in the spheroidal component. Additionally, a thin bridge-structure connecting it to the companion is also observed, all of which are indications of NGC 274 experiencing mass–transfer from its closest neighbour.

The result of longslit observations show that rotation is the major feature in the kinematics of NGC 275; this is very likely inherited from the original kinematics of the pre-collision disk. Nevertheless, the outer edges of the velocity distribution show signatures of disturbances due to the interactions with NGC 274. The very central region (diameter$\sim$10″) of NGC 275, however, appears to still retain its original, smooth rotational motion. But slightly external to this region, kinematic distortions are observed, and these seem to coincide with neighboring knots. These are either indications that the local features are induced by self-gravity which has produced its own local kinematics, or they are 'hiccups' in the global–resulting

kinematics which further induce concentrations of matter, ie. knots, in the local regions.

As has been mentioned earlier, the HI mass found for Arp 140 by Peterson & Shostak (1974) was calculated to be 3.3×10^9 $M_\odot$. Relating this with the stellar mass derived from the K–band luminosity, the neutral gas comprises about 25% of the stellar mass. This is a large fraction compared to other spiral galaxies which typically has an HI to stellar mass ratio of not more than $\simeq$10%. Noguchi & Shlosman (1993), in their numerical simulation on the stability of a two–component (gas and star) disk, found that a significant amount of gas, ie. 20% of the stellar mass, gives a dramatic change in the dynamical behaviour of a disk galaxy; the gas becomes locally unstable due to self–gravity and transforms into massive clumps. It is thus attractive to apply this scheme on NGC 274, considering the morphology and HI to stellar mass ratio of this galaxy. Unfortunately, their model suggests that a bar does not develop in this scheme, which is what is observed in NGC 274.

An alternative (supplementary) explanation to this discrepancy might lie in the orbital nature of the interactions in Arp 140. As indicated earlier, Arp 140 might be experiencing a retrograde encounter. This type of encounter is believed –and proven by simulations (see, eg., Howard *et al.*, 19–)– to preserve the morphology of the galaxies (compared to direct encounters). If NGC 274 had had an oval/bar structure prior to the encounter with NGC 275, as quite commonly observed in isolated spirals, then it might have survived the retrograde encounter until present time.

5.2 Arp 144

5.2.1 Introduction

Arp 144 has a more disrupted morphology than Arp 140. Classified as a ring galaxy firstly by Freeman & de Vaucouleurs (1974) due to the irregular's morphology, it has two components: NGC 7828 and NGC 7829. The first is a heavily distorted and knotty spiral with what seems to be tidal features extending from the central region. The companion is rather compact yet is not free from tidal distortions caused by the interactions. They are separated by a distance of 30″, which translates to 11 kpc if a distance of 77 Mpc is adopted. Together, the luminous part of both components extends over ∼40 kpc.

The system of Arp 144 was observed to have a very large envelope of neutral hydrogen, which extends to about 200 kpc at the longest and contains a total mass of 7.5×10^9 $M_\odot$ (Higdon, 1988). The longest extension is coincidental with the orientation of the configuration in the optical but there also exists a structure

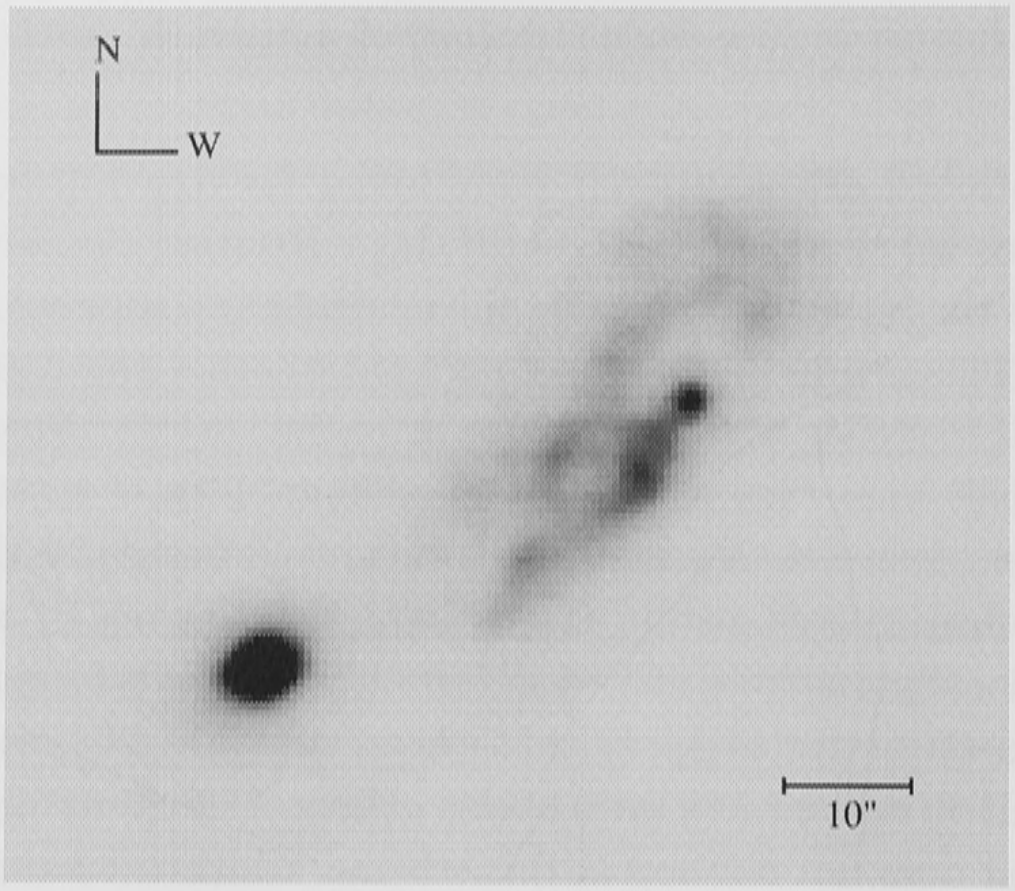

Figure 5.13: B image of Arp 144.

that stretches roughly perpendicular to this in the west. This led Higdon to conclude that the morphology is caused by an interaction of a gigantic intergalactic cloud with a spiral, as proposed by Freeman & de Vaucouleurs (1974). But Joy *et al.* (1988) argued against this by showing that both components of Arp 144 do have concentrations of old star populations, as shown by its K–band image. Then Smith & Higdon (1994), in order to study tidal tails of merging galaxies, tried without success to detect the plumes of Arp 144 in CO(1–0). The central region, however, was observed to have V_{CO} =5770 km $s^{-1}$and $M(H_2)$=6.8×10^9 $M_\odot$.

5.2.2 Morphology

The irregular component of Arp 144 is very disturbed (figs. 5.13, 5.14, 5.15 and 5.16). In the NW there is an arc which is knotty at places and in the outer edge, detached from it, lies a few feathery structures.At one end this arc is connected to the central region (discussed below) while at the other it is detached from any structure. Inside this arc a bright knot sits with what seems to be a bridge connecting it to the central structures of NGC 7828; this knot, as can be seen, is brighter in the blue image. In the SE, a sharp structure points almost SE and approximately north of it a more diffuse feature extends towards the spheroidal component. All these outer structures appear to be smoother in the K–band.

In the B image, the central region of NGC 7828 gives the impression of an asymmetric and diffuse ring which exhibits some condensations at a few regions *on* the ring, the strongest lying in the western part. The central part of the ring seems to be devoid of any bright source in the blue, but this changes in the longer wave-

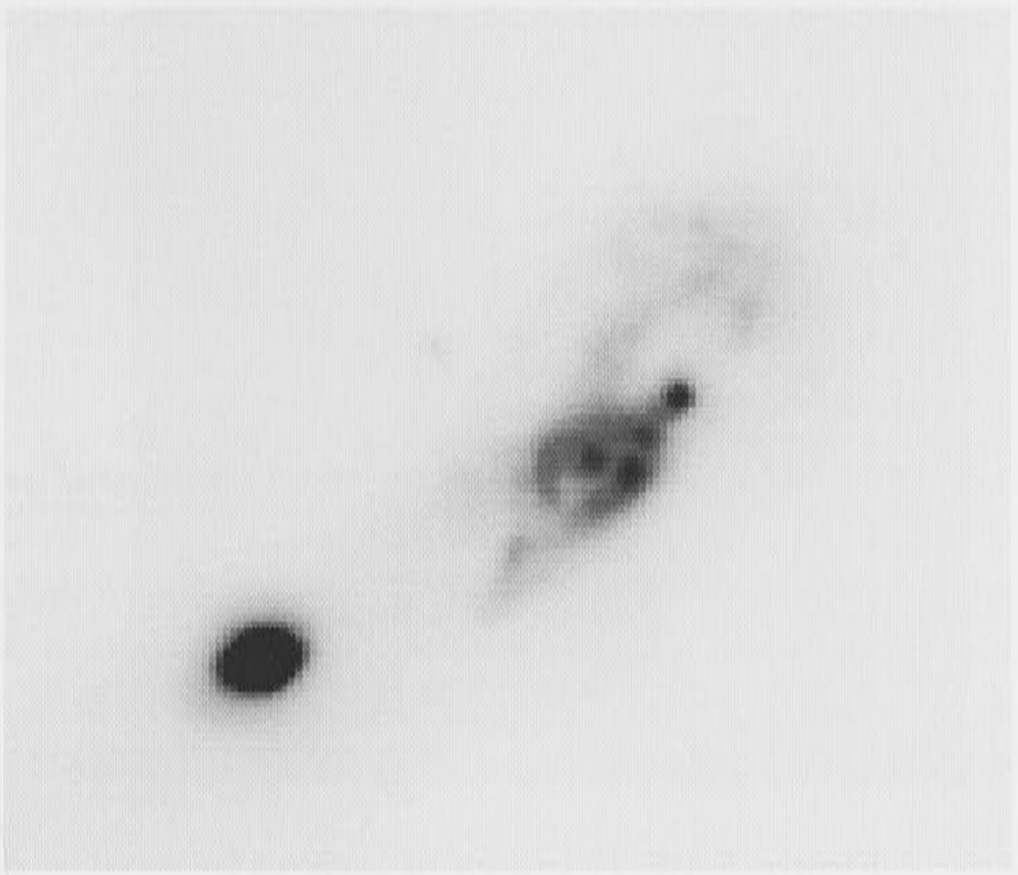

Figure 5.14: R image of Arp 144.

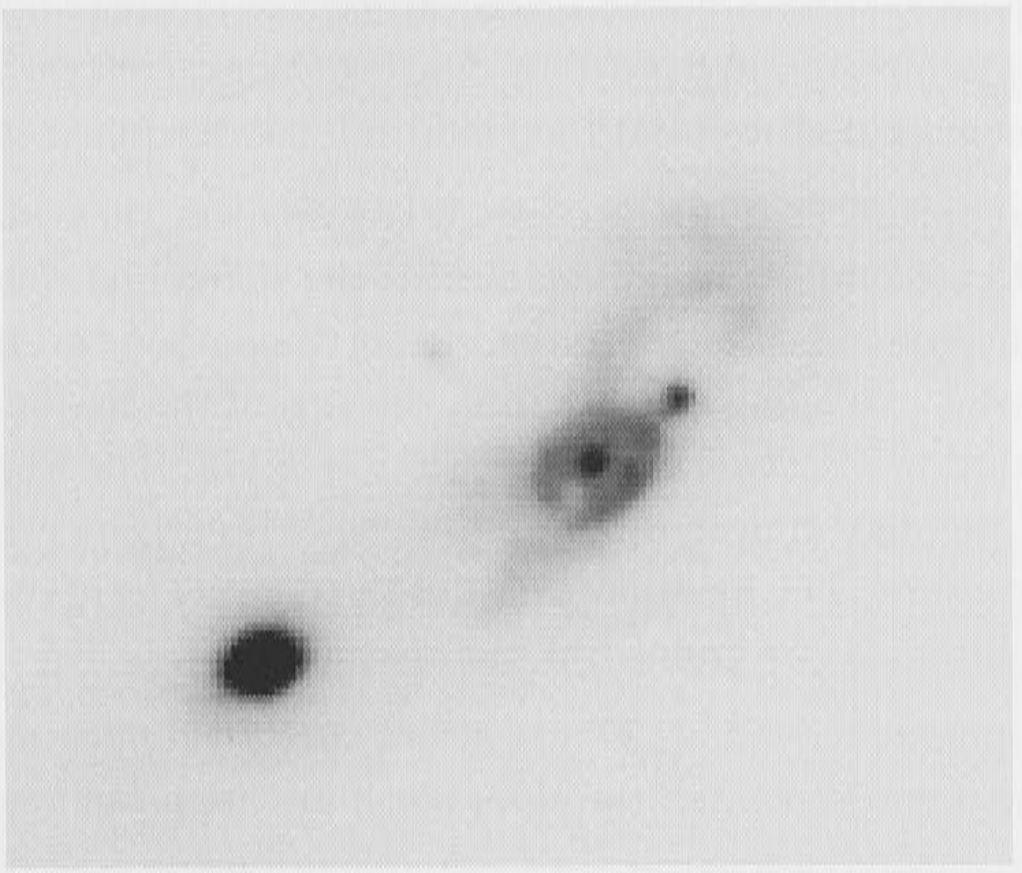

Figure 5.15: I image of Arp 144.

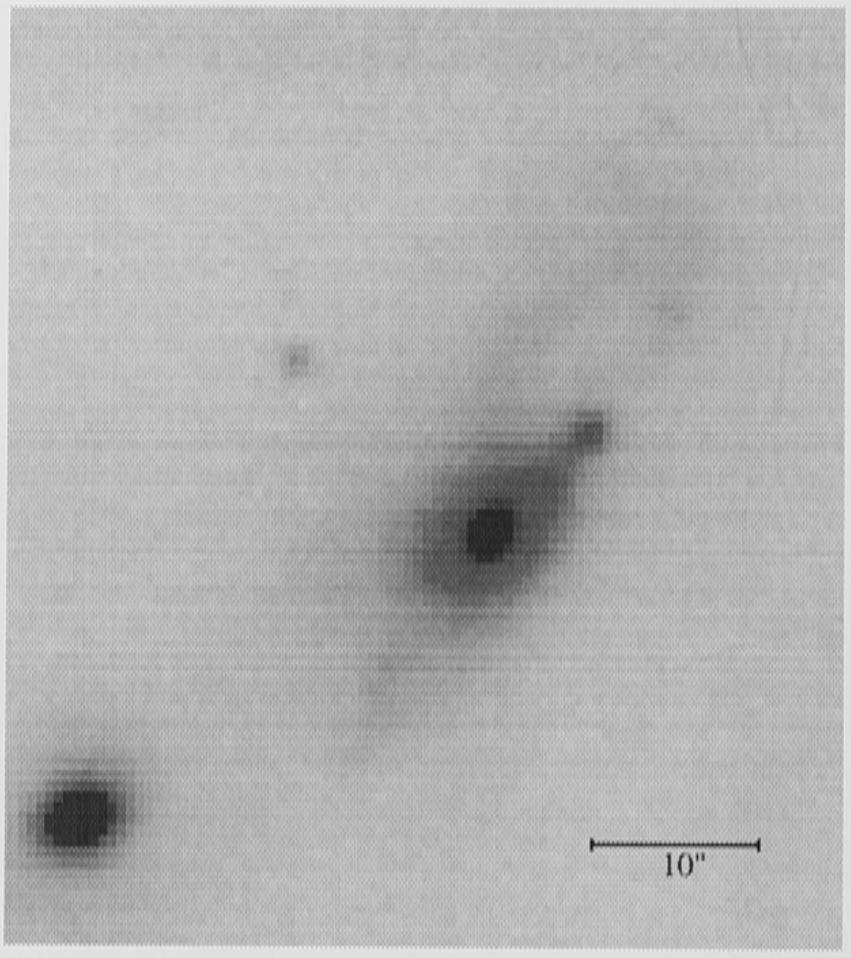

Figure 5.16: K image of Arp 144.

lengths: a weak pointsource is seen in the R image, and becomes brighter in the I-band image and then more so in the K image. It seems that this central object is the nucleus of the irregular component suffering severe obscuration by dust at the shorter wavelengths. The ring becomes better defined in the R– and I–bands, yet still asymmetric and is broken in two places. Its SW (broken) part seems to be attached to the pointed structure mentioned earlier, the morphology is suggestive of the latter being a foreground feature to the ring. What condensations exist in the B image become brighter in R but then fade in I and disappear in the K–band.

The ring also disappears in the K image. What appears then is an elongated disk-like feature whose major axis points towards the spheroidal companion. This disk appears to be wider in the southeastern part and there are indications of two weak spiral arms extending roughly from the tips of the major axis but then each bends westward and eastward, as shown in Fig. 5.17a. The isophotes toward the inner part of the disk appear to be misaligned (Fig. 5.17b), where they also exhibit a boxy structure. The innermost part of the nucleus seems especially boxy although the resolution is constrained by the seeing.

The spheroidal companion, NGC 7829, has also a distorted appearance. Its major axis is oriented roughly NW-SE but the outer isophotes are misaligned to the inner ones. Faint diffuse matter surrounds this component: to the NW it connects the spheroidal companion to NGC 7928, in the SE it flares out to 30″–40″. We note that the northern edge of this flare structure is almost collinear with the northern end of the irregular component, as can be seen in Fig. 5.18. On a lower surface brightness level, a faint halo can be seen surrounding especially the northern part

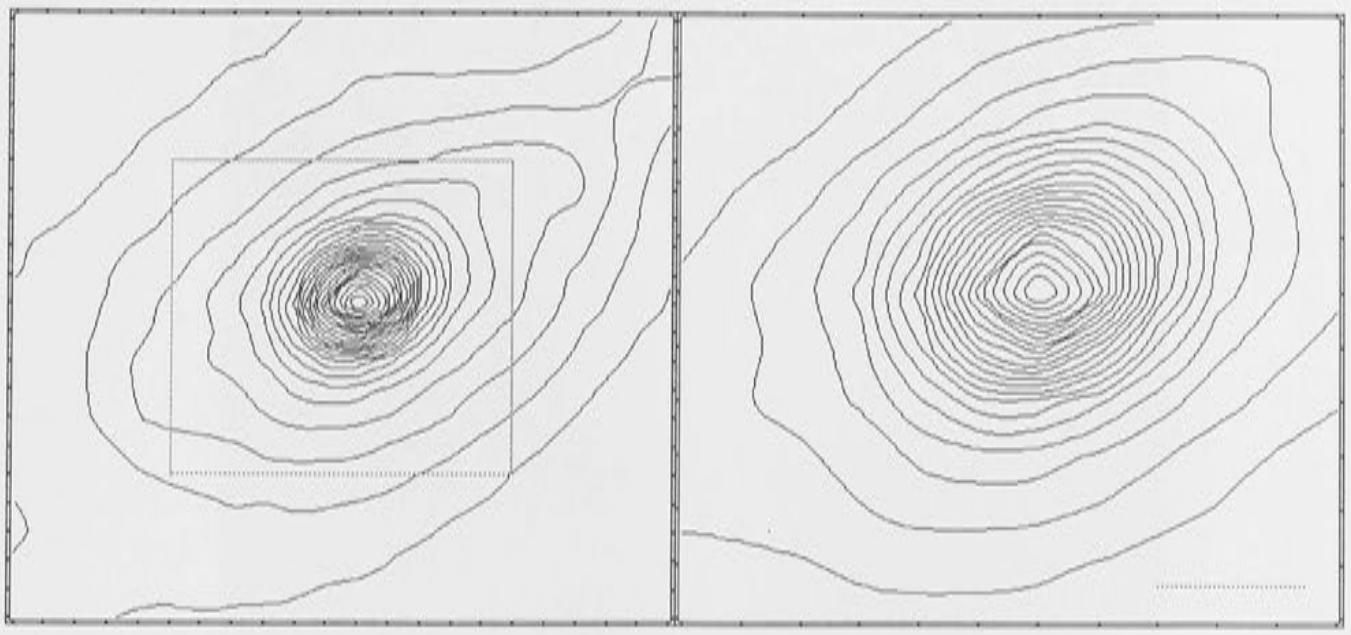

Figure 5.17: Isophotes of the inner region of NGC 7828 in the K–band. The left figure has a dimension of $12.8'' \times 12.9''$ while the figure on the right side is $6.7'' \times 6.7''$. The box inside the left figure is similar to that of the right and the bar in the lower right corner corresponds to the seeing of the observing run.

of NGC 7829.

Higdon (1988), in studying the distribution of neutral hydrogen in Arp 144 (as shown in Fig. 5.19, with Higdon's kind permission), noted that the HI structures have no corresponding tidal tails visible on the Palomar Sky Survey image. As can be seen in Fig. 5.18, the northern tip of the irregular component exhibit a faint extension towards the west, a structure that is also observed in Higdon's HI map. Other than this, I agree with Higdon that, unlike in the HI, no optical structure can be observed extending from NGC 7828 towards the west, nor is there any tidal structure that corresponds to the very extended features observed in HI.

In the neighborhood of the system, about $250''$ to the SW, lies Arp 51, a rather distorted face-on spiral galaxy with a dimension of about $34'' \times 27''$. In the NE, about $150''$ away, lies a compact galaxy whose nature is unknown and is not listed in the IPAC database.

The (B–R) image of Arp 144 is shown in Fig. 5.20; here redder colors are represented by darker grayscale. It can be seen that most of the structures inside the irregular component are rather blue compared to the spheroidal, which is expected from a spiral galaxy. The bluest object in the system appears to be the knot NW of the ring, knot #1 in Fig. 5.21. The spurs in the outer regions and a part of the arc are rather blue as well. A (red) dustlane emerges, almost connecting both components, extending SE-NW halfway across the irregular component. The peripheral region of the spheroidal closer to the irregular galaxy is slightly redder than that the other side, which can be understood as the accumulation of dust between the components due to their interactions. The nucleus itself is the reddest structure inside the system, redder than the SO galaxy.

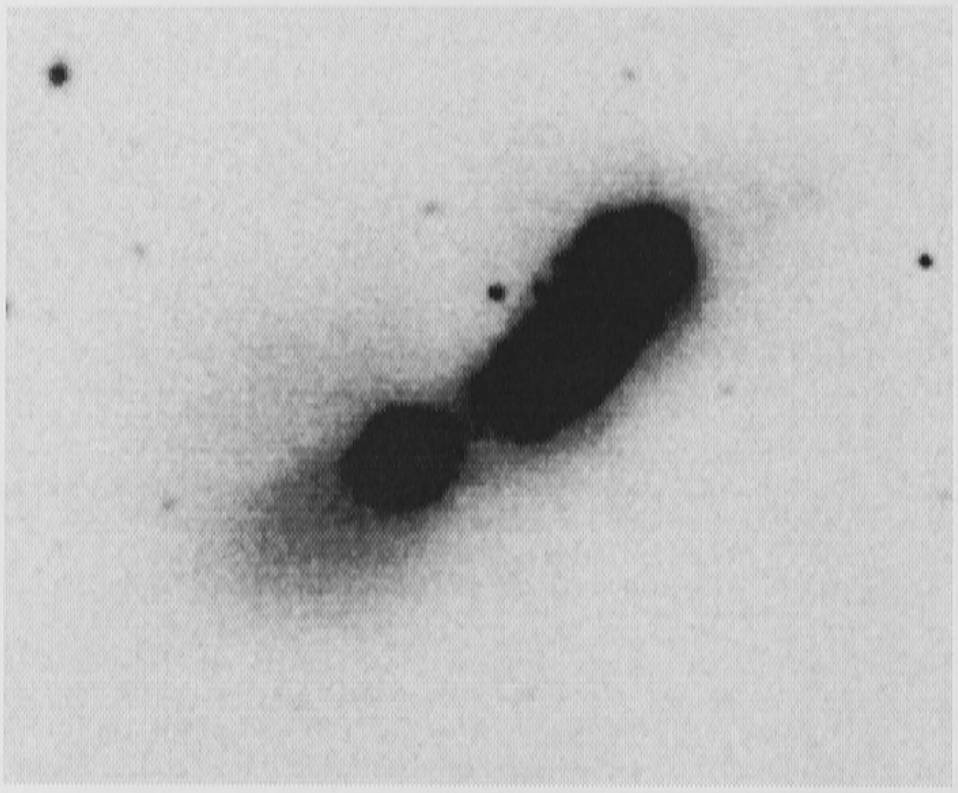

Figure 5.18: Low surface brightness R–image of Arp 144.

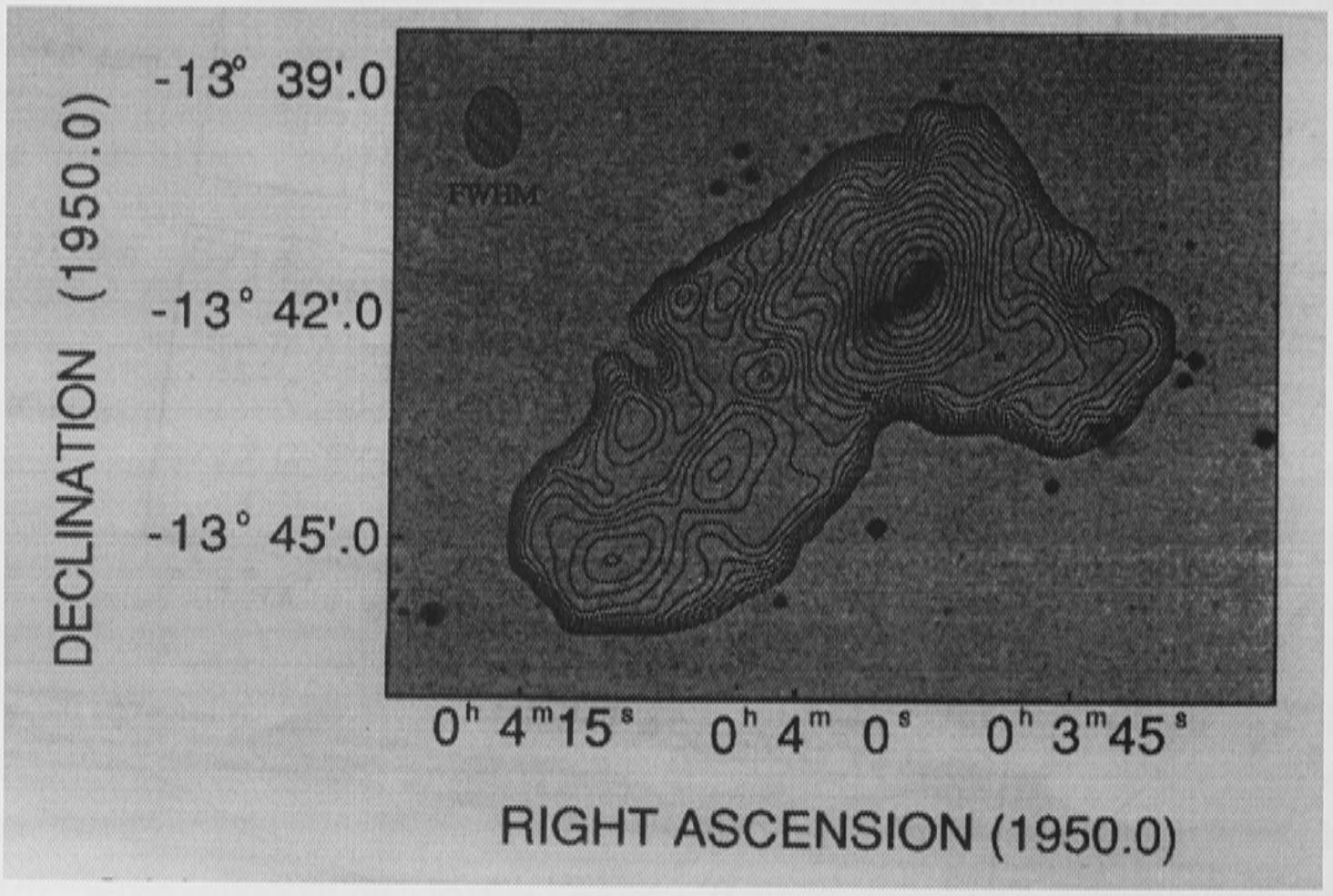

Figure 5.19: HI distribution of Arp 144 (Higdon, 1988).

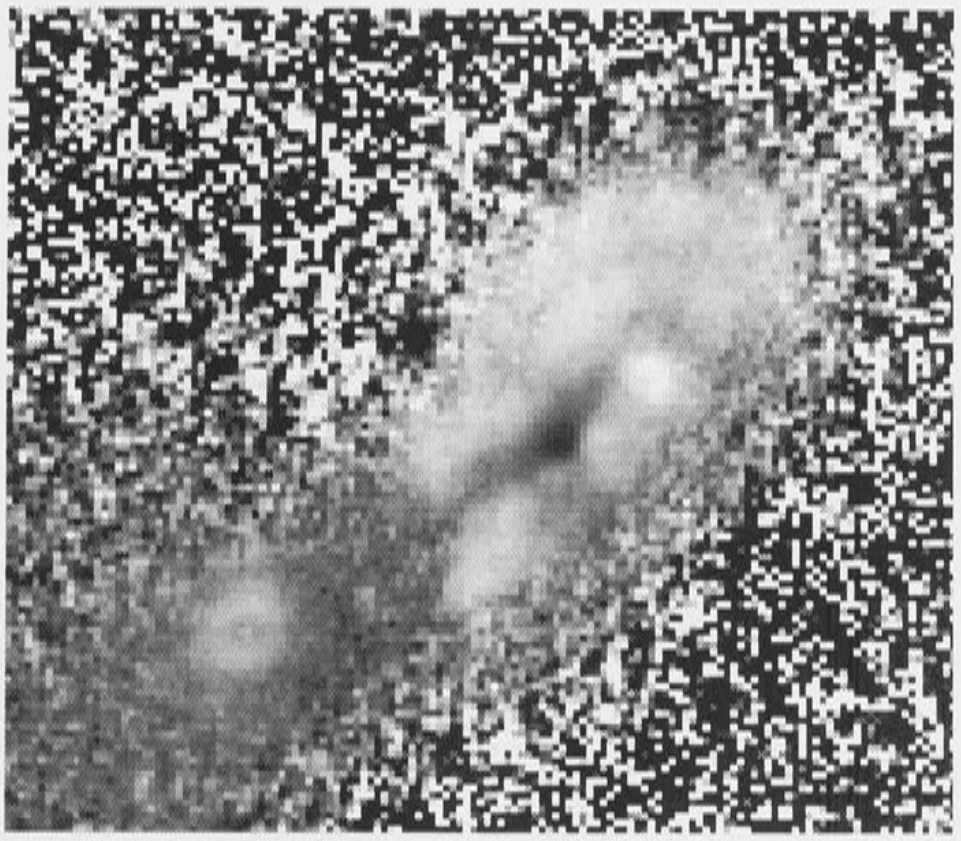

Figure 5.20: B–R image of Arp 144 showing dust distribution inside the irregular component.

Integrated photometry for Arp 144 and for knots inside the irregular component is given in Table 5.2. Note that in the K–band image NGC 7829 lies rather on the edge of the field of view of the array, hence the upper and lower limits for the K–magnitude and (B–K) color. In a number of cases the structure of the knots are rather fuzzy in the K–band, unabling the magnitudes to be measured.

Despite its relatively blue integrated (B–R) color, NGC 7828 has a red (B–K) value implying the existence of a large amount of dust inside the galaxy. This seems to be concentrated around the nuclear region (knot #8), where (B–K) reaches $\sim$5 mag. The other knots are rather blue, but knot #1 is especially blue, suggestive of having a young population with an age between 10^7 to 10^8 yr if an instantaneous burst is assumed (Charlot & Bruzual, 1991). Here the $H\alpha$ line is very strong, which implies the existence of OB stars.

The K–band fluxes of Arp 144 are calculated to be 34.4 mJy for NGC 7828 and <17.4 mJy for NGC 7829. Using similar transformation as that used for Arp 140, these fluxes translate to 5.3×10^{10} $M_\odot$ and $>2.7\times10^{10}$ for NGC 7828/29. These values put Arp 144 as a pair with a rather high luminous mass compared to other pairs studied here.

Surface brightness distributions of NGC 7828 are shown in Fig. 5.22, taken across the irregular component at PA=38° (see Fig. 5.21). The first structure encountered is the pointed feature in the SE (d$\simeq$–15″ to $\simeq$7″): it has very blue colors indicative of a young underlying stellar population. Beyond this the magnitudes become slightly dimmer, before they rises again as the 'slit' goes past the south-eastern part of the inner ring (d$\simeq$–5″).

Component	B	R	I	K	(B–R)	(B–I)	(B–K)
N7828	15.04(0.02)	13.81(0.02)	12.98(0.02)	10.72(0.01)	1.23	2.06	4.32
N7829	14.760(0.02)	13.49(0.02)	13.02(0.02)	<11.45(0.01)	1.23	1.74	>3.31
#1	17.75(0.08)	16.92(0.08)	16.40(0.08)	14.84(0.09)	0.83	1.34	2.91
#2	18.61(0.12)	17.47(0.10)	16.93(0.10)	—	1.14	1.68	–
#3	17.66(0.08)	16.47(0.06)	15.98(0.06)	—	1.19	1.68	–
#4	18.70(0.14)	17.59(0.10)	17.22(0.14)	16.34(0.14)	1.11	1.48	2.36
#5	18.80(0.14)	17.78(0.12)	17.26(0.14)	15.65(0.10)	1.02	1.53	3.15
#6	18.86(0.16)	17.76(0.12)	17.27(0.14)	16.32(0.15)	1.09	1.58	2.54
#7	19.24(0.18)	18.17(0.14)	17.75(0.18)	—	1.07	1.48	—
#8(n)	17.79(0.20)	16.50(0.06)	15.95(0.06)	12.80(0.03)	1.29	1.84	4.98

Table 5.2: Integrated photometry of Arp 144. Refer to Fig. 5.21 for designated knots. Note limits for the K–band magnitude and (B–K) color.

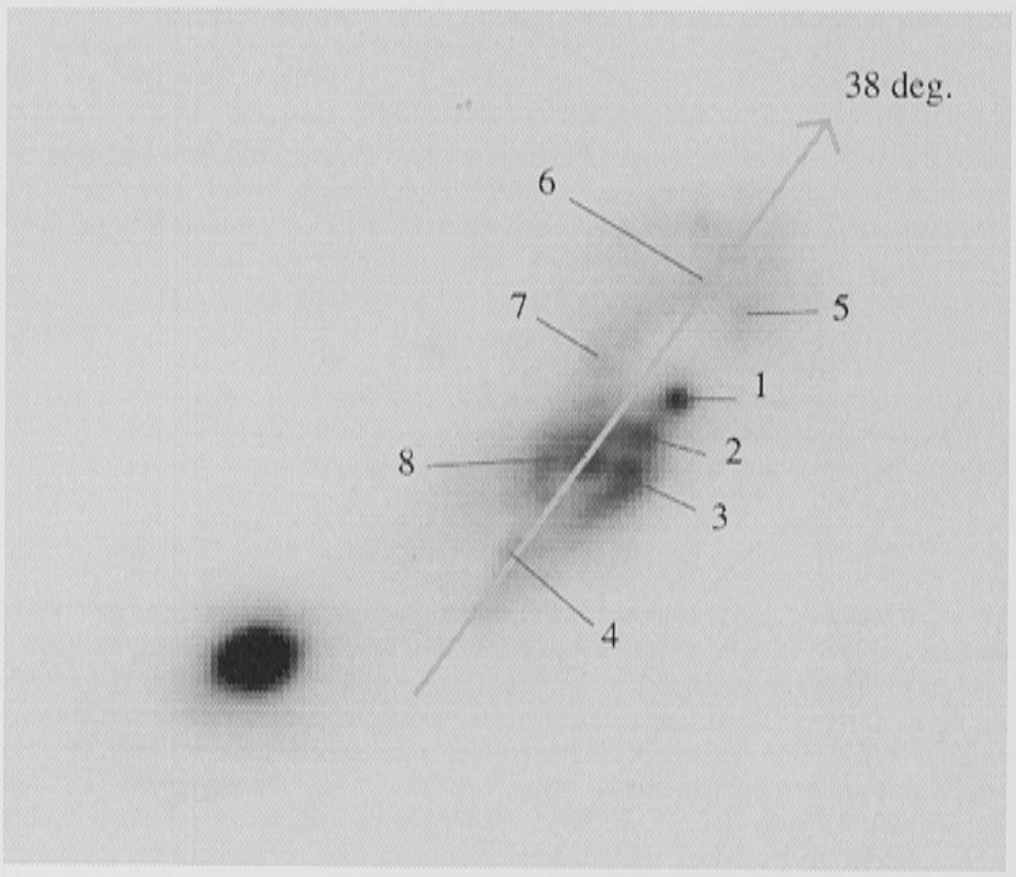

Figure 5.21: Knots numbers and slit PAs referred in the text on a R image of Arp 144.

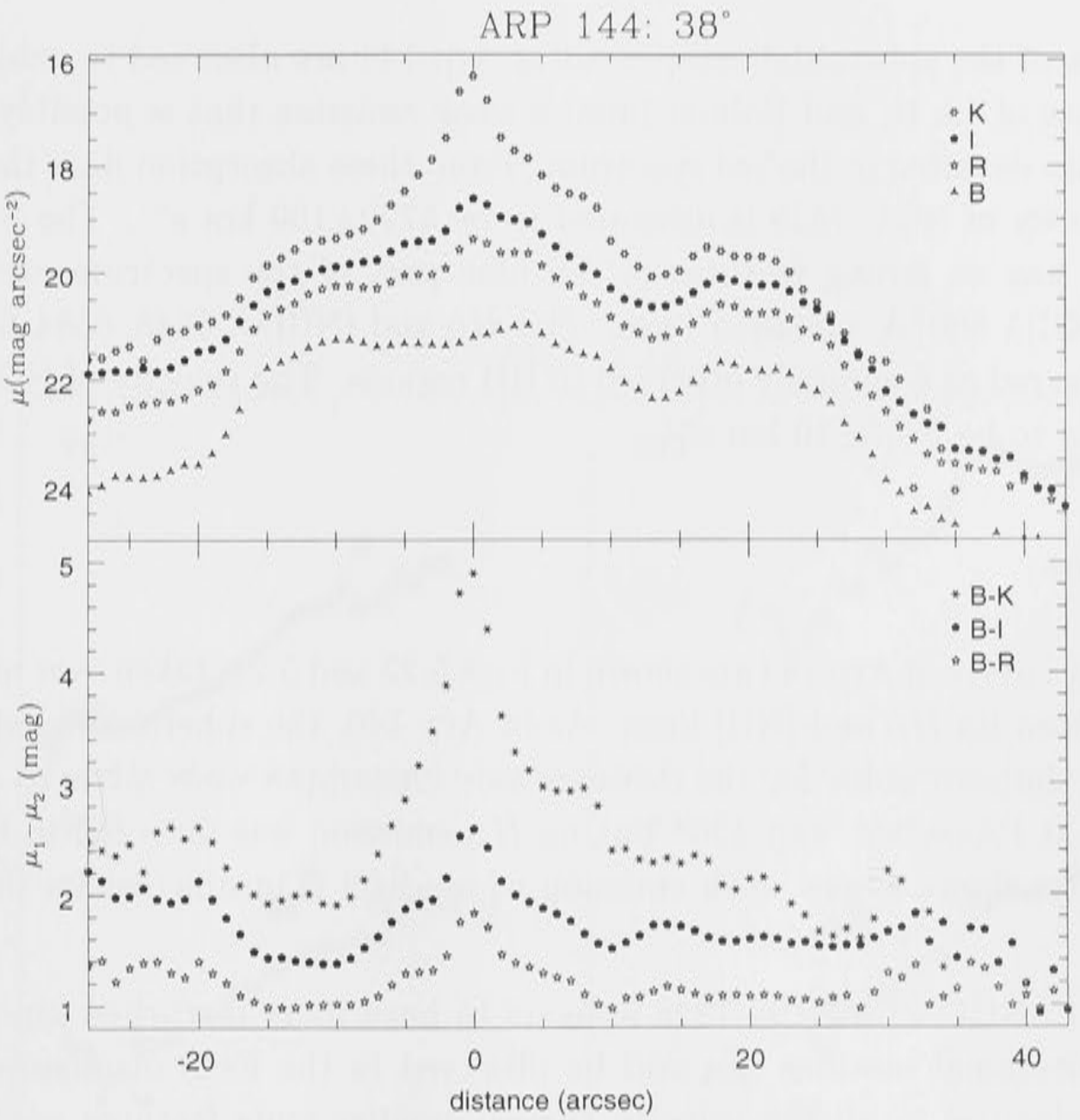

Figure 5.22: Surface photometry of NGC 7828 at PA=38°.

Inside the ring the brightness remains rather flat in the B–band, while in the R and I bands it peaks at the small nucleus. In K, however, the magnitudes rise then decline smoothly until it reaches the other end of the inner disk (or inner ring, in other passbands). Here the (B–K) colors become extreme, reaching to ∼5 mag strongly suggests a large amount of dust residing inside this region. The flat (B–K) structure at d≃4″–9″connects the outer part of the ring to the (southeastern) inner region of the arc. The dip in colors at d=10″ is contributed by the bright knot #1, whose colors are also very blue similar to those shown by the pointy structure. At d≃17″, the slit passes the inner part of the arc and here the colors are slightly bluer. The 'spurs' on the outer edge of the arc have the bluest (B–K) color in this PA.

A fit of NGC 7829 along its major and minor axis reveals a (R–band) surface brightness profile following an $R^{1/4}$ law, despite the heavy distortion this galaxy displays in its morphology.

5.2.3 Spectroscopy

The spectra of the spheroidal component of Arp 144 are observed to exhibit absorption lines of Ca II, and Balmer lines; a weak emission that is possibly [NII]λ 6583Å is also detected in the red spectrum. From these absorption lines the heliocentric velocity of NGC 7829 is measured to be 5720±100 km s^{-1}. The irregular component has no strong features in the blue part of the spectrum except for $H\beta$ and [OIII]λ 5007Å emission lines. The $H\alpha$ and [NII]$\lambda\lambda$ 6548, 6584 lines are strong in the red as commonly observed in HII regions. The velocity of NGC 7828 is calculated to be 5755±10 km s^{-1}.

Kinematics

The velocity curves of Arp 144 are shown in Figs.5.23 and 5.24, taken over nine PAs measured from its $H\alpha$ and [NII] lines. As in Arp 140, the spheroidal component is taken as the zero point for the distance axis. Attempts were made to observe NGC 7828 at PAs=285° and 336° but no $H\alpha$ emission was detected in the first and the latter shows a very weak emission whose S/N is insufficient for deducing velocities.

Compared to NGC 275, NGC 7828 appears to have more disturbed kinematics: although rotational motions can still be observed in the form of monotonically changing velocities in all the velocity curves, smaller scale features are present in most PAs. On the further ends from the spheroidal component, these local features are sometimes coincidental with the northern arc and spur–structures. For example, at PA=307°, 309° and 311°, the rise in velocities around d$\simeq$45″ are correlated with the position of the arc. Nevertheless, unlike in NGC 275, the knots around and inside the inner ring do not seem to display any velocity glitches, as can be seen, for example, at d=35″ at PA=297°. The velocities nearer to the spheroidal companion have values closer to that of this component. In and around the ring region, multiple velocities can be observed, again indicating matter moving with different velocities due to the interactions. Except for PAs=307°and 311°, this happens at the ring region itself, but more on this will be discussed later. The total velocity spread observed inside NGC 7828 is about 450 km s^{-1}, which is a typical number for a spiral galaxy. The slow slopes of the velocity slices in the inner region, eg. PA=302°22″$\lesssim$distance$\gtrsim$, go linear with radius, implying a solid body rotation.

The velocity contours of NGC 7828 are yet more complicated (Fig. 5.25). A few velocity extrema can be seen here, but it is likely that the maximum contour at V_{max}=5950 km s^{-1} is not part of the global kinematics but more of a local velocity feature. If this is the case, then, the general trend of the kinematics is lower velocities in the SE and higher in the NW, as seen in the velocity curves.

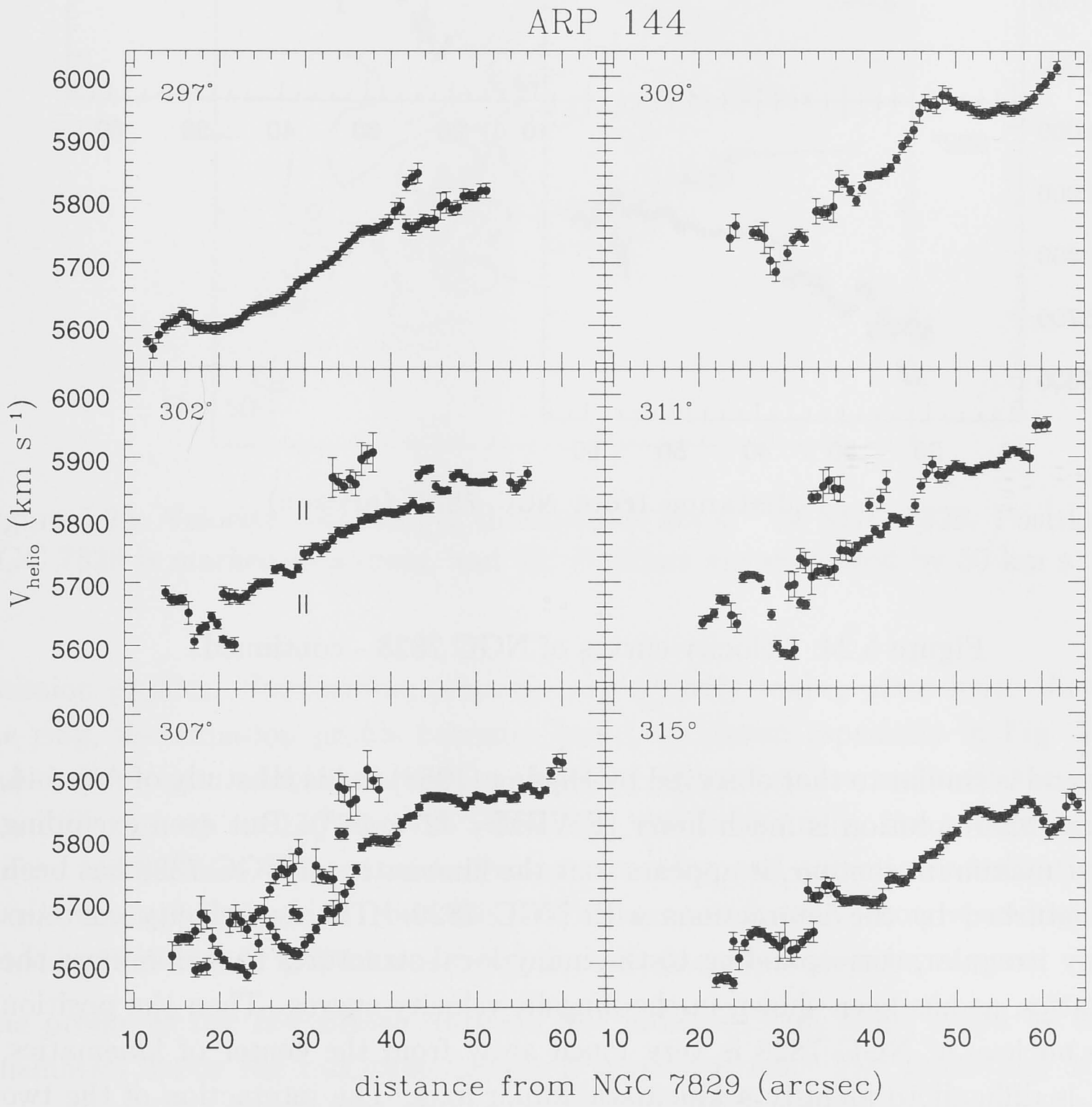

Figure 5.23: Velocity curves of NGC 7828. Position of NGC 7828 is marked at PA=302°.

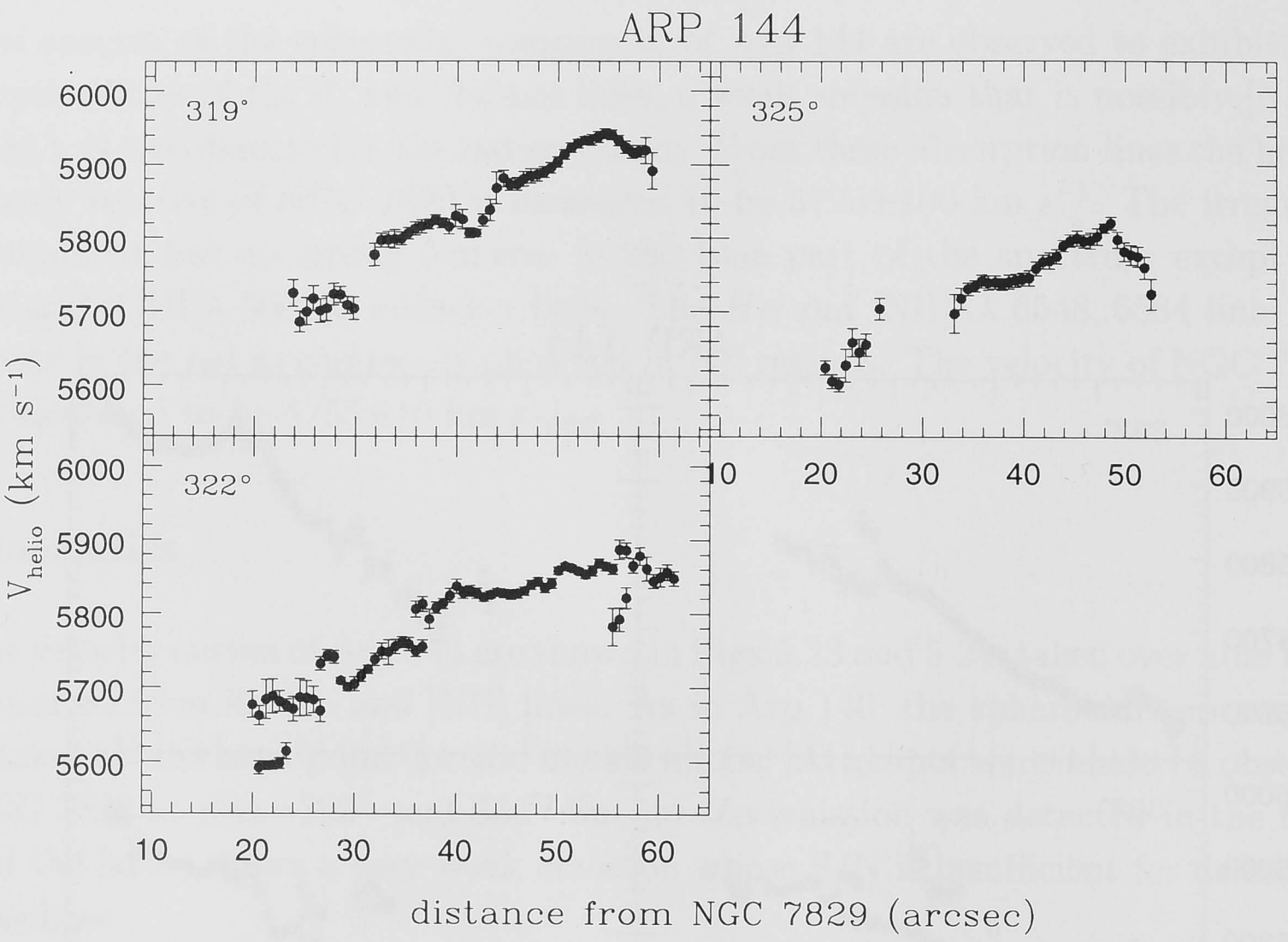

Figure 5.24: Velocity curves of NGC 7828 - continued.

This trend is similar to that observed by Higdon (1988) in his HI study of Arp 144, although his resolution is much lower (FWHM= 42″× 58″). But even excluding the first maximum contour, it appears that the kinematics of NGC 7828 has been very disturbed by the interactions with NGC 7829. The iso-velocity contours are very irregular, corresponding to the many local structures that dominate the kinematics, as has been shown in the longslit velocity curves. Then the position of the nucleus of NGC 7828 is very much away from the center of kinematics, and it is difficult to identify a kinematic minor axis. The interaction of the two components of Arp 144 appears to be well advanced, with even the most internal parts of the irregular having been severely damaged dynamically.

The velocity spread is shown in Fig. 5.26, where the distribution of regions with detected $H\alpha$ emission lines can also be seen. At some places no $H\alpha$ is detected. The $H\alpha$ emission is detected as close as $\sim$8″ (3 kpc) away from NGC 7829, with similar velocities, again implying matter being accreted by the S0 companion.

Fig. 5.27 shows the $H\alpha$ longslit emission profiles of three PAs that go through the ring of NGC 7828. The differential rotational velocity can be observed especially in the outer region, where it is rather flat in velocity and and shows strong knotty

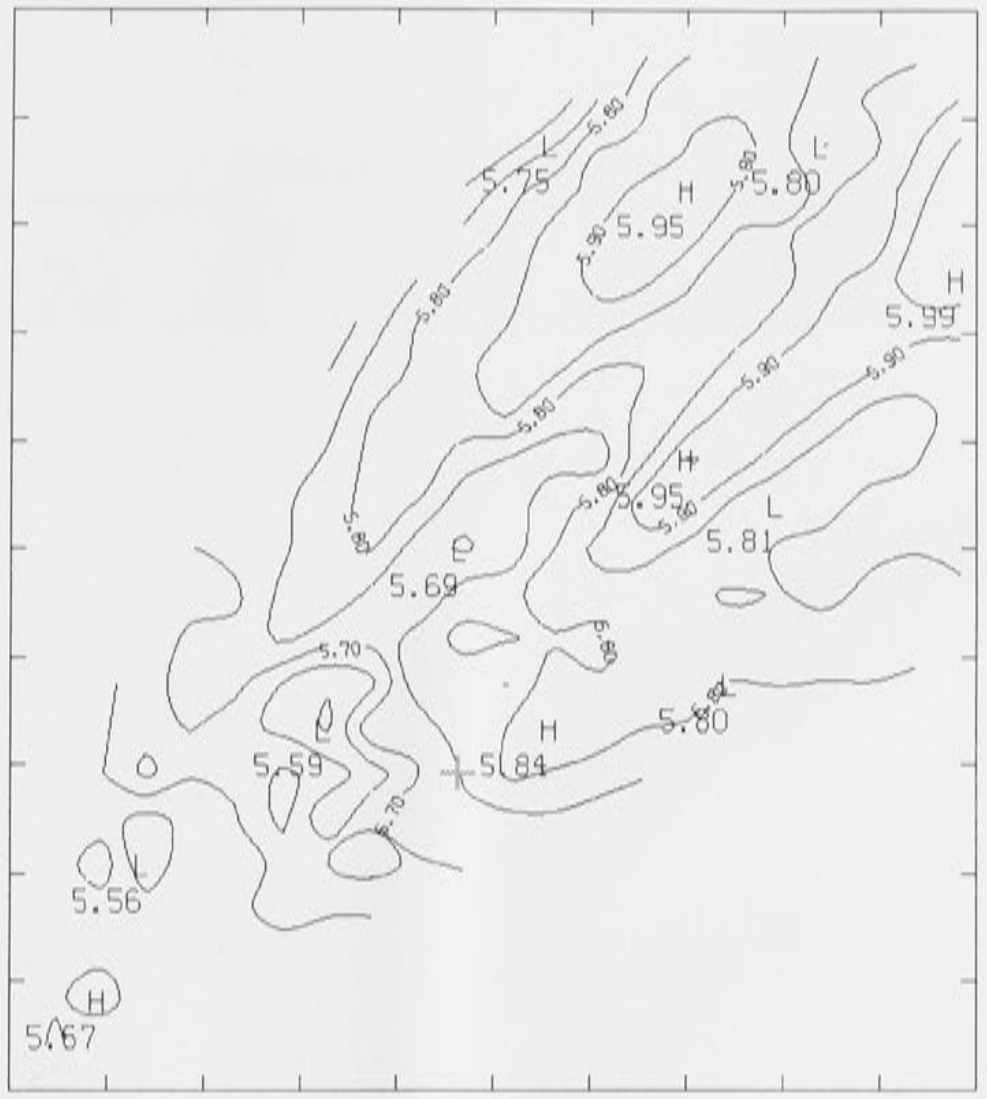

Figure 5.25: Velocity contours, in thousand of km s^{-1} of NGC 7828. Position of NGC 7828 is marked as a cross, and the contours are separated by 50 km s^{-1}.

emission profiles. Starforming processes are actively taking place here. Just on the ring, the emission profile becomes broad, as shown especially in Fig. 5.27b and c. Here split velocities are often observed when they are resolved: the peaks can differ by up to 150 km s^{-1}. However, inside the ring, the profile is very diffuse, sometimes without any obvious structure and sometimes indicative of (weak) multiple velocities. Here the FWHM can reach $\simeq$6Å –corresponding to a spread of velocity of $\simeq$270 km s^{-1}– while it is about half in outer regions.

The profile of the $H\alpha$ diffuse emission line indicates that there might be other kinematics inside the ring than merely a rotational one. The thickening of the inner part of the profile and the detection of (some) multiple-peaks in the inner regions are suggestive of non-circular motion. An expanding ring will produce a feature that has double-valued velocities at smaller radii and a single one at the largest radius, known as the 'oval-shape' (see review by Oort, 1977), and are commonly observed in CO in the central regions of galaxy.

In Fig. 5.27 I have overlaid an ellipse over the diffuse emission profiles to study if any conclusion can be drawn. It appears that, although the signature is not particularly strong, it is indicative that the inner ring is suffering an expansion kinematics. At PA=297° the observed velocities are blueshifted and vice versa at PA=307°. At PA=302°, where the slit goes past the central part of the ring, the

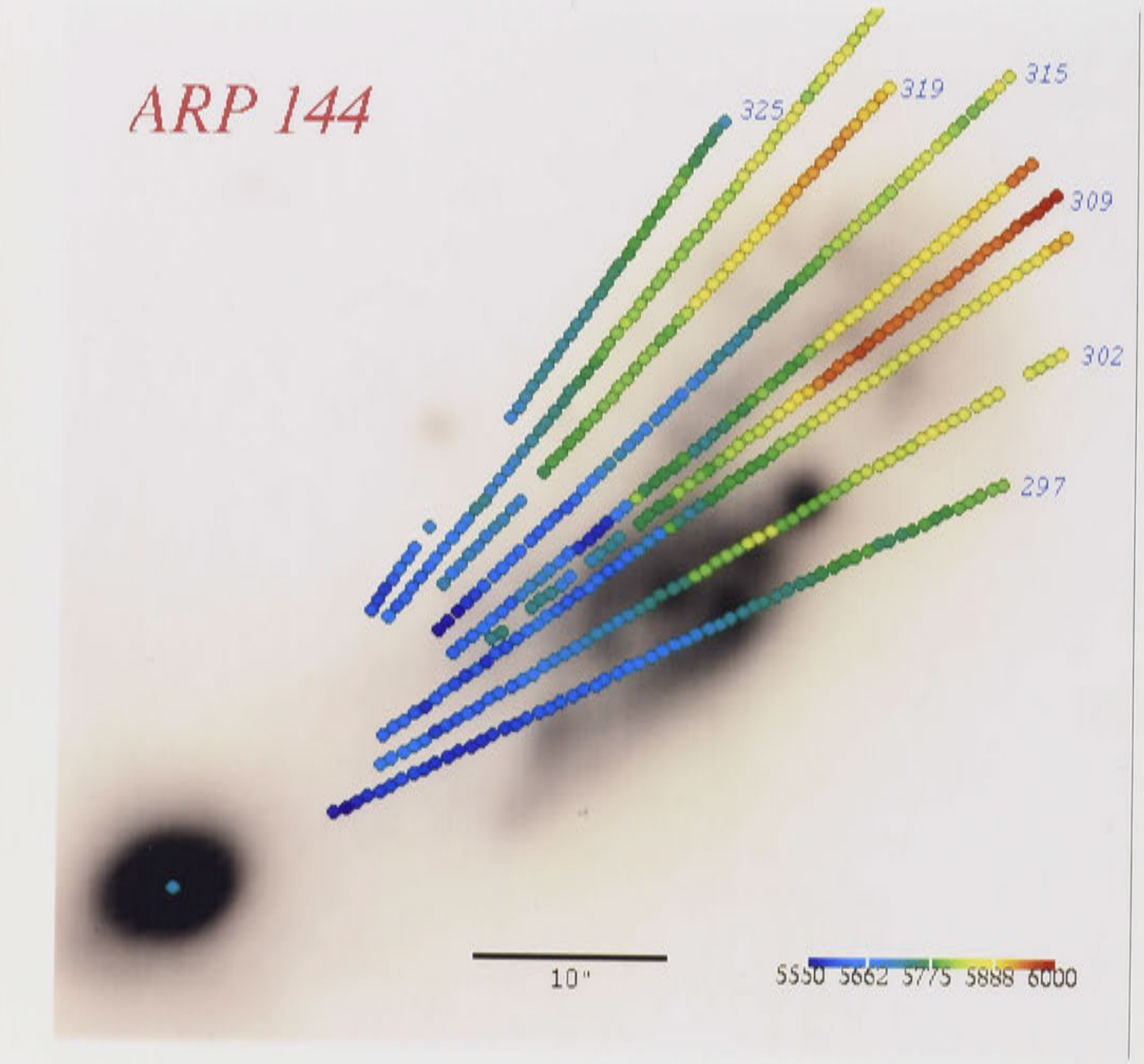

Figure 5.26: Velocity spread inside NGC 7828 overlaid on an R–band image. Each number at the end of each slit position designates the PA, the scale is indicated in the lower left corner, and the colors representing the velocities are shown in the legend in the lower right corner

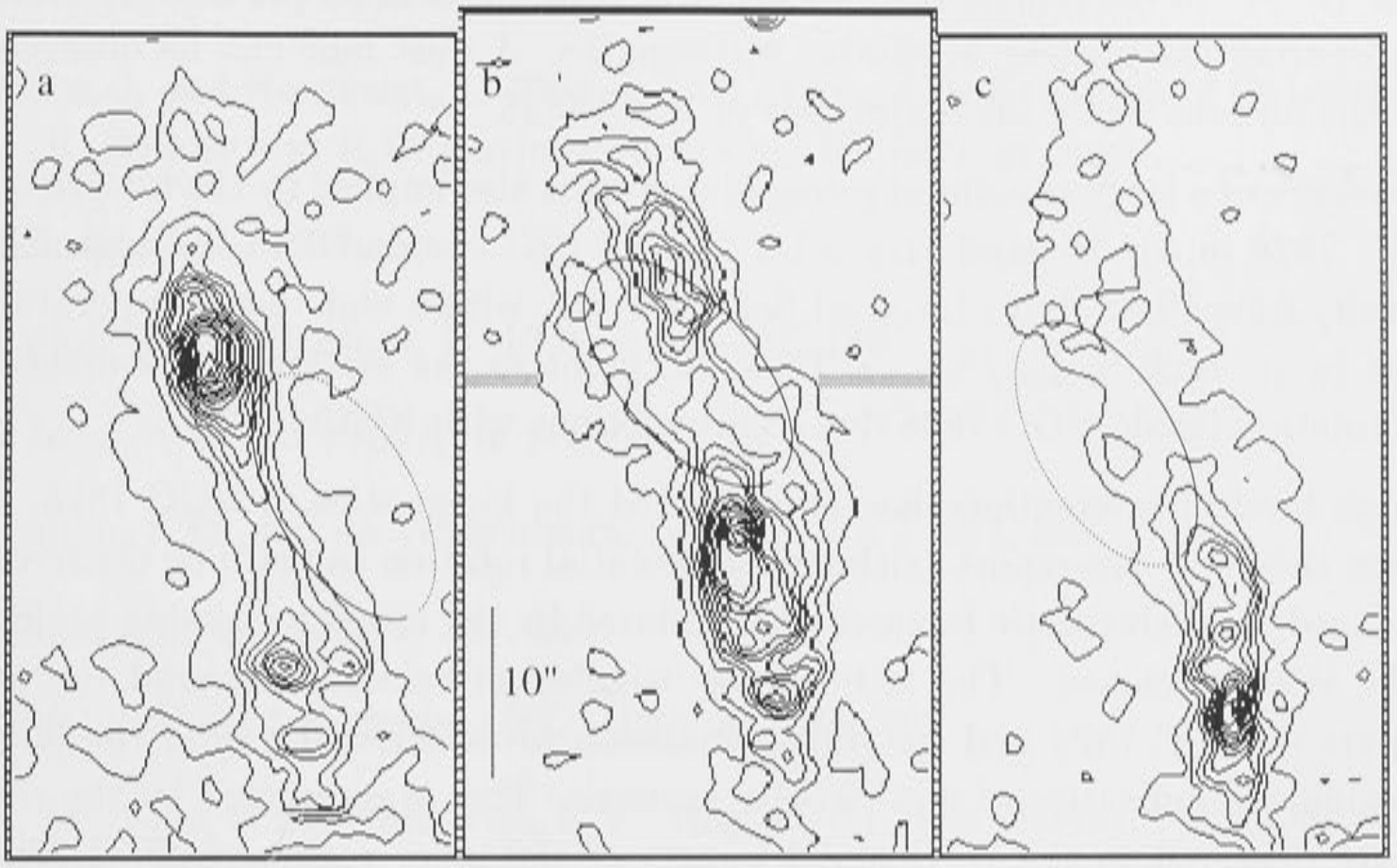

Figure 5.27: $H\alpha$ profiles taken from PAs=297°, 302° and 307° implying non-circular motions inside the inner ring of NGC 7828. The ellipse in each profile traces the suspected oval velocity patterns; each figure has the same scale both in wavelength (x–axis) and spatially (y–axis).

ellipse fits better although a better fit should be done provided the stronger signal can be obtained. A deeper longslit spectra is needed to derive a more conclusive result. A two-dimensional spectral study of the central part of NGC 7828 in C0 and a higher resolution HI observation will be essential to learn more about the kinematics of NGC 7828.

5.2.4 Discussion and Summary

Multi–wavelength observations of Arp 144 show that the system has undergone strong interactions which have distorted the original morphology of both components but mostly affecting the gaseous member, NGC 7828. The resulting general structure is comparable to that simulated by Toomre & Toomre (1978) for a direct parabolic passage of an equal mass intruder at 2–3$\times 10^8$ yrs after perigalactic encounter (see their Fig.2). Although missing in details of hydrodynamic phenomena (eg. the inner ring and certain fragmentations), their result shows a feathery arm on the further end and two streams of material toward the companion, as well as some accreted material on the outer end of the spheroidal, as observed in NGC 7828/29.

The photometry of NGC 7828 shows that the galaxy has very blue colors except for the nuclear region; the bluest structure implies underlying population age of no later 10^8 yr. In the central region sits a blue ring whose inner part is very dusty thus obscuring the nucleus at shorter wavelengths. A dust lane can be observed across the nucleus along the major axis of NGC 7828.

The presence of a large amount of young blue stars is also implied by the luminosity of NGC 7828 in the B–band: $L_B \simeq 1.5\text{–}2\times10^{10}\ L_\odot$, compared to the high FIR luminosity from IRAS data: $L_{FIR} \simeq 1.5\text{–}2\times10^{10}\ L_\odot$, with a high dust temperature implied by its high $S_{100\mu m}/S_{60\mu m}$. These all point to the existence of enhanced star formation inside NGC 7828 due to interactions with NGC 7829.

The high level of interactions has also affected the kinematics of NGC 7828, as has been shown in this report: although differential rotation can still be observed, pronounced local kinematic features are exhibited by the longslit emission profiles and the velocity curves. The latter show 'wiggles' of velocities around the arc and spurs of NGC 7828 and the diffuse emission profiles coming from the inner ring region are indicative of non-circular motions. This is supported by the ring structure observed in the B, R and I images of the inner region of NGC 7828, whose dimension is comparable to that of the diffuse $H\alpha$ profile emitted from the same region.

It has been shown that the interactions go the other way as well: the spheroidal component is also (strongly) disturbed. In addition to the tidal distortion it is suffering, NGC 7829 also exhibits blue colors often observed in (mixed) interacting pairs, believed to have been caused by recent star forming activities. This is supported by the detection –although weak– of emission lines from the nuclear region of NGC 7829.

5.3 References

Barnes, J. and Hernquist, L. 1992, ARA&A 30, 705

Barnes, J. and Hernquist, L. 1995, in IAU Symp. 171, Evolution of Galaxies, ed. R. Bender and R.D. Davies (Dordrecht: Kluwer), in press

Bushouse, H.A. 1987, Ap.J. 320, 49

Charlot, S. and Bruzual, G. 1991, Ap.J. 367, 126

De Jong, R.S. 1996, A&A, in press

Freeman, K.C. and de Voucouleurs, G. 1974, Ap.J. 194, 569.

Higdon, J.L. 1988, Ap.J. 326, 146

Hodge, P.W. and Kennicut, R.C. 1983, A.J. 88, 296

Joy, M., Ellis, H.B., Tollestrup, E.V., Higdon, J.L, and Harvey, P.M. 1988, Ap.J. 330, L29

Keel, W.C., Kennicut, R.C., Jr., Hummel, E., van der Hulst, J.M. 1985, A.J. 90, 708

Laurikanen, E. 1990, A&A 232, 323

Laurikanen, E. and Moles, M. 1989, Ap.J. 345, 176

Miller, 1995, in IAU Colloq. 157, Conf. Summary, Barred Galaxies, ed. R. Buta, B.C. Elmegreen, and D.A. Crocker (Dordrecht, Kluwer), in press

Norman, C.A., Sellwood, J.A. and Hasan, H. 1996, Ap.J. 462, 114

Oort, J. 1977, ARA&A 15, 295

Peterson, S.D. and Shostak, G.S. 1974, A.J. 79, 767

Rubin, V.C., Hunter, D.A. and Ford Jr., W.K. 1991, Ap.J.Suppl.Ser. 76, 153

Smith, B. and Higdon, J.L. 1994, A.J. 108, 405

Sofue, Y., Wakamatsu, K., Taniguchi, Y. and Nakai, N. 1993, Pub. Astr. Soc. Japan, 45, 43

Chapter 6

The Merging Pair AM1806-852

6.1 Introduction

AM 1806–852 is an interacting pair consisting of an early type (NGC 6438, or NW component) galaxy and a very disrupted companion (NGC 6438A, or SE component). Sersíc (1966) found evidence for large velocity differences inside the system, with peaks at 6300, 4300 and 2680 km s^{-1}. However, Burbidge & Burbidge (1971) did not observe this and concluded that both components actually have similar heliocentric velocity, which is about 2400 km s^{-1}. Subsequent results by various authors do not observe the large velocity differences as well, but they vary in terms of what the velocities of both components are (see, for example, Sadler & Sharp, 1984 or Sekiguchi & Wolstencroft, 1992).

The angular separation between the components is about 0.5 arcmin, which corresponds to about 5 kpc if a distance of 33 Mpc is used ($H_\circ$= 75 km s^{-1} Mpc^{-1}). The irregular component extends over about 85″ or 14 kpc. AM 1806–852 lies within a loose group of 3 galaxies designated as LGG #417 (Garcia, 1993).

The NW component is not detected by IRAS, but NGC 6438A is an IRAS source, classified as 'normal' by Rush *et al.* (1993) in their extended 12μ galaxy sample. The information obtained from IPAC gives f(12μm)=0.25 Jy, f(25μm)=0.27 Jy, f(60μm)=2.7 Jy and f(100μm)=7.4 Jy.

6.2 Optical Observations

6.2.1 Morphology

The ratio of the size of the irregular and the separation of both components of AM 1806–852 suggests that that this system is a merger in progress; Fig. 6.1,

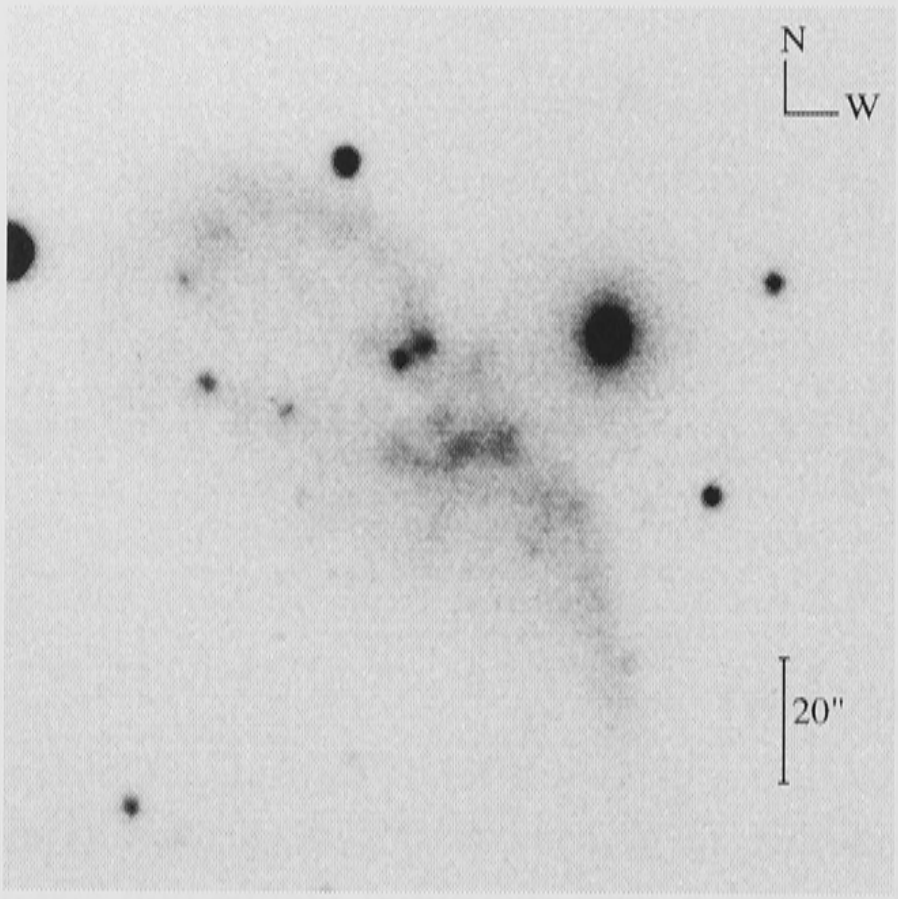

Figure 6.1: B image of AM 1806–852

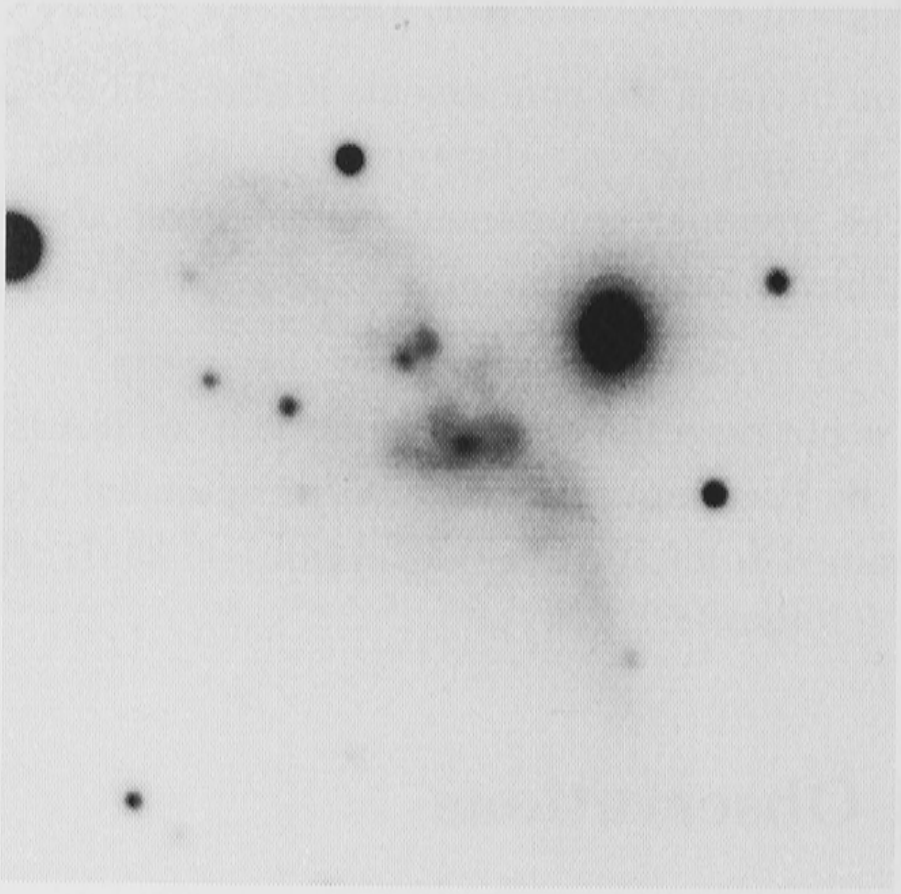

Figure 6.2: V image of AM 1806–852

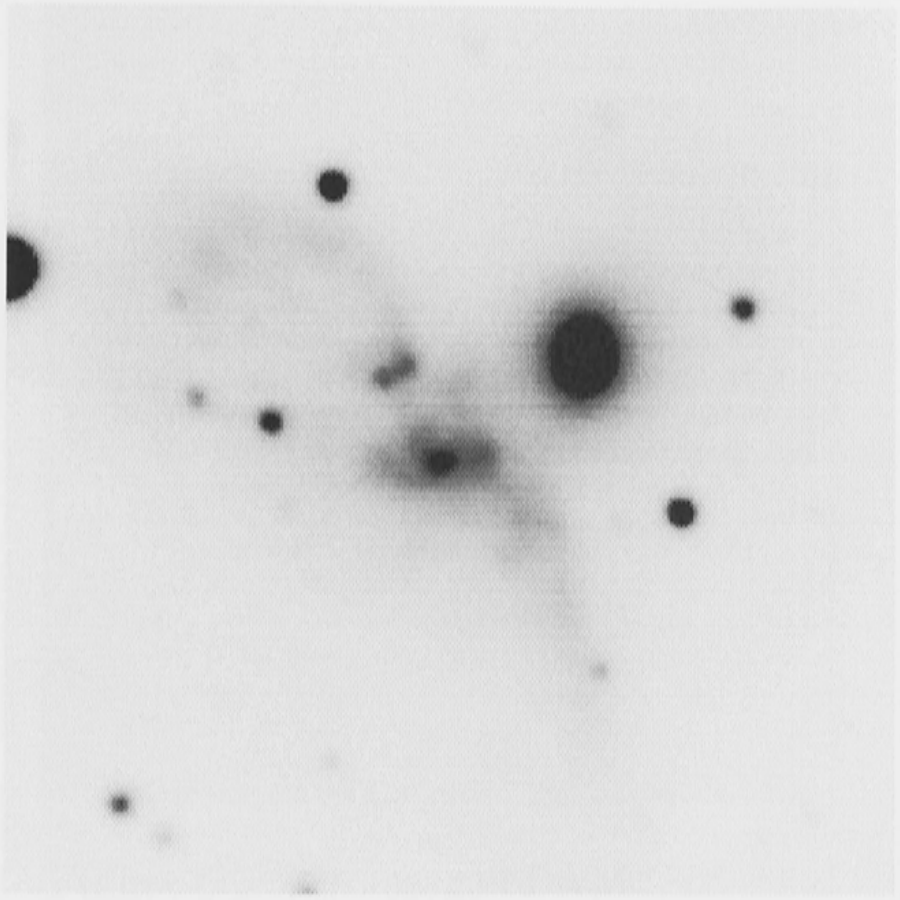

Figure 6.3: R image of AM 1806–852

6.2, 6.3 and 6.4 show respectively B, V, I and R images of AM 1806–852 . The irregular component consists of two major tidal structures extending south and NE. The southern arm starts with a diffuse structure closer to the inner disk then fades until it flares out in the south. While it is rather diffuse in the east, this arm has a sharp edge in the west suggestive of a leading compression front. The northeastern arm is a loop which seems to originate from two bright point sources north of the nucleus. This loop has knotty structures and there are faint 'spoke' features inside the loop. As in the southern arm, this loop has sharp outer edges in the west but diffuse in the other directions.

In the core of the irregular, there is a nucleus within an apparent inner disk. This nucleus is rather small and faint compared to the whole structure, suggesting that the pre-collision galaxy might be a late type spiral. The inner disk shows at least two arm-like structures; the third in the west might be another arm, or a somewhat diffuse and elongated knot which shows up prominently in the V–band. Donzelli & Espíndola (1996, hereafter D&E) refer to both this third arm and to the nucleus as the 'decentered nucleus' of the irregular. Slightly north to the inner disk, there is a partly detached structure, accompanied by another similar but fainter structure on the opposite side of the disk in the south.

There are a few foreground stars in the irregular component, some of which are very red, but the two point sources almost north from the inner disk is physically related to the system, as will be shown later. The brightness of these knots surpasses that of the nucleus in the B image, and I will refer to them as the 'blue knots'. These blue regions were concluded to be a nucleus of a third component inside the interacting system by D&E. They also observe these knots to be brighter

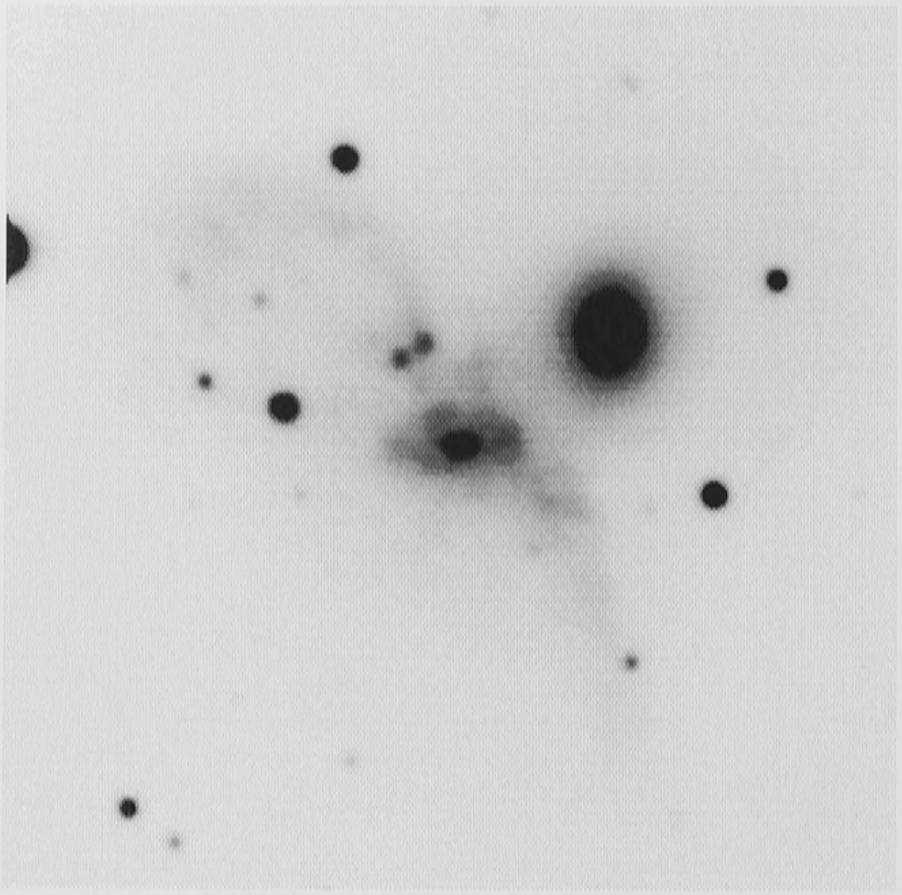

Figure 6.4: I image of AM 1806–852

than the nucleus in V but my V image does not confirm this. Around these knots there is diffuse matter which, as mentioned earlier, seems to connect to the northeastern arm.

Fig. 6.5 shows the $H\alpha$ image of the pair, corrected for continuum emission using the I band and scaled assuming that the spheroidal component has negligible amount of $H\alpha$ emission, after convolution to give both images similar PSF. Due to the non-photometric night, I was unable to calibrate the flux with those of standard stars.

One can see that the $H\alpha$ image is dominated by two concentrations of $H\alpha$ emission. The northern one corresponds to the blue knots although more extended in the west compared to the diffuse matter around the knots seen in other passbands. The second $H\alpha$ knot coincides with the nucleus of the inner disk though its orientation is tilted. These are presumably regions of active star formation.

The spheroidal component, NGC 6438, might be an elliptical or a (face-on) S0. Rampazzo & Sulentic (1992) in their survey of isolated E/S pairs concluded that NGC 6438 does not have any trend of diskiness, neither does it show any signature of boxiness. They did find, however, that this component exhibit isophotal twisting, presumably due to the violent encounter with the irregular. D&E made Similar conclusions about the spheroidal component's isophotes.

The B, R and I composite image of AM 1806–852 is shown in Fig. 6.6: blue, green and red represent B, R and I passbands respectively. As can be seen, the general structure of the irregular is dominated by blue, while the nucleus and its immediate surroundings and the spheroidal component are rather red.

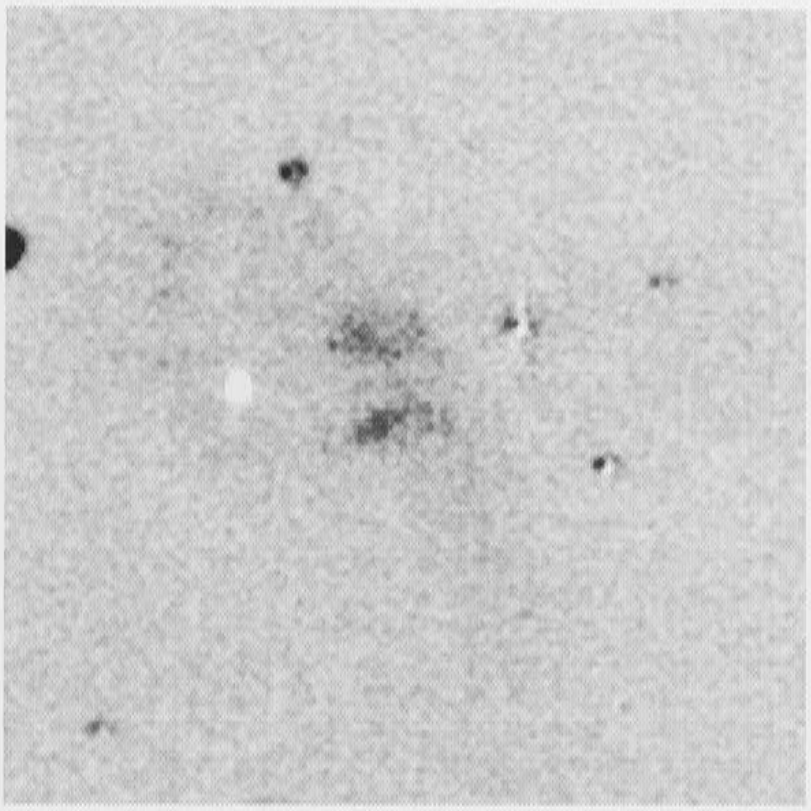

Figure 6.5: $H\alpha$ image of AM 1806–852

Component	B	V	R	I	(B–V)	(B–R)	(B–I)
Irr.	12.83(0.020)	11.99(0.016)	11.49(0.016)	10.72(0.015)	0.84	1.35	2.11
S0	13.90(0.028)	12.80(0.018)	12.18(0.018)	11.34(0.016)	1.10	1.72	2.55
1	14.83(0.040)	13.96(0.024)	13.38(0.025)	12.57(0.021)	0.86	1.44	2.26
2	17.48(0.135)	17.08(0.061)	16.64(0.066)	15.96(0.051)	0.40	0.84	1.51
3	17.43(0.132)	16.95(0.057)	16.51(0.062)	15.87(0.049)	0.47	0.91	1.56
4	16.06(0.071)	15.28(0.026)	14.80(0.028)	14.06(0.021)	0.79	1.26	2.55

Table 6.1: Integrated photometry of AM 1806–852 . Refer to Fig. 6.7 for the numbers

The integrated magnitudes and colors for AM 1806–852 are shown in Table 6.1; numbers in brackets are the photometric errors. The CCD used here is not particularly sensitive in the blue, hence the larger errors in B. The knots corresponding to those in the first column are shown in Fig. 6.7.

One can see that the spheroidal component has rather red colors compared to typical E/S0 galaxies, see, for example, results by Buta & Williams (1995) in their survey of bright galaxies. This could be due to obscuration by dust produced and spread during the interaction, which is a common phenomenon inside interacting pairs.

The integrated colors of the irregular companion are comparable to colors of early type spirals. Component #1, which is the inner disk including the nucleus, has rather red colors, as commonly observed in galactic nuclei. Knots #2 and #3 are bluer and, as has been shown earlier, are surrounded by $H\alpha$ emission. Knot #4, which is just SW from the inner disk, shows intermediate colors. These indicate a mixed population: an older population appears to co-exist with active star

Figure 6.6: Composite B, R and I image of AM 1806–852 represented, respectively, by blue, green and red colors.

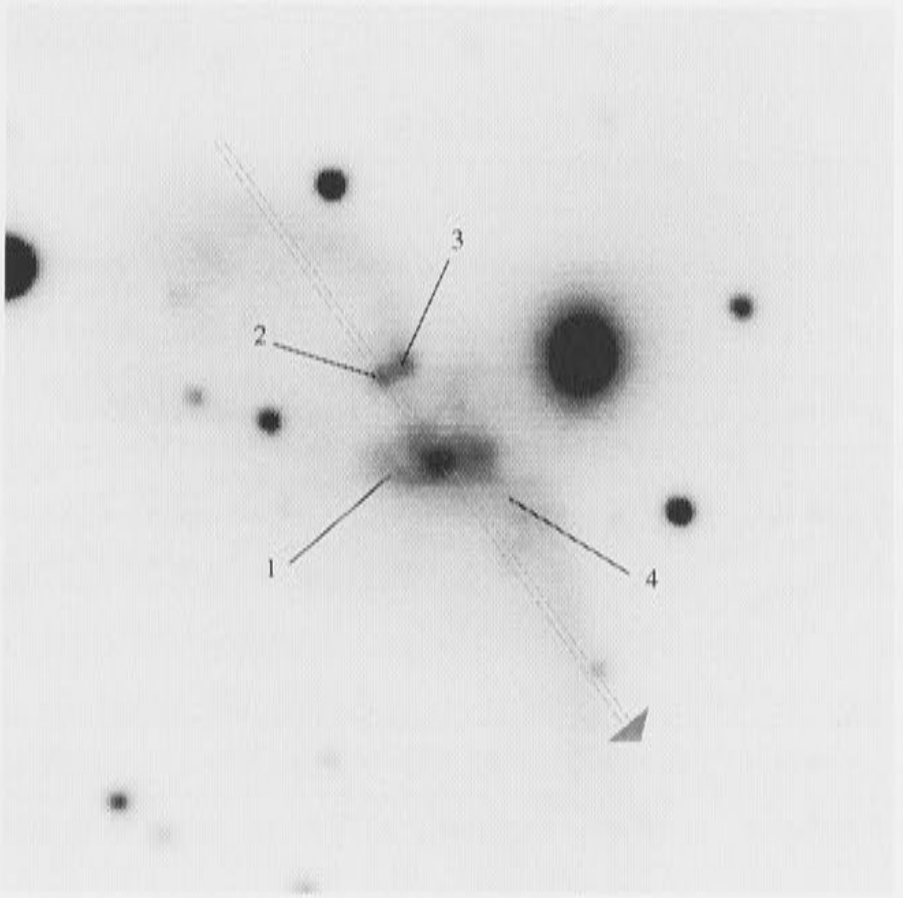

Figure 6.7: R image of AM 1806–852 with numbers corresponding those shown in Table 6.1. The straight line corresponds to PA=55° and the arrow shows the path of the slit in Fig.6.8

formation, as indicated by the amount of $H\alpha$ emission seen in Fig. 6.5. But this is common enough in spirals and irregular systems.

Surface photometry at PA=55° is presented in Fig. 6.8, where the position angle connects the nucleus of the irregular component with the first blue knot (see Fig. 6.5 for the slit position). The top panel shows the surface brightness of the irregular component in B, V, R and I wavelengths while the bottom one displays the colors.

The surface brightness (upper) plot starts at the outer edge of the NE loop. The surface brightness drops inside the northeastern loop, then rises again nearing the blue knot at d$\simeq$–17″; note that in B this peak is less bright than the blue knot. At d$\simeq$–5″, the northern arm of the inner disk produces a shoulder which is more prominent in B and V before the surface brightness peaks again at the nucleus of the irregular component. A similar but weaker feature appears again at d$\simeq$7″. The (nearly) symmetric structure suggests an inner (blue) ring around the nucleus but images with better resolution are needed to confirm this. The diffuse structure inside the southern arm manifests itself at d$\simeq$20″, before it fades away as the tail of the southern arm beyond d$\simeq$40″. The peak at d$\simeq$40″is contributed by the red foreground star seen in the composite image.

The colors of the outer regions of NGC 6438A are mostly quite blue, with (B–V) reaching as low as $\sim$0.2 mag, indicating a young population in these regions. The northeastern loop and the blue knot show particularly low values of all three

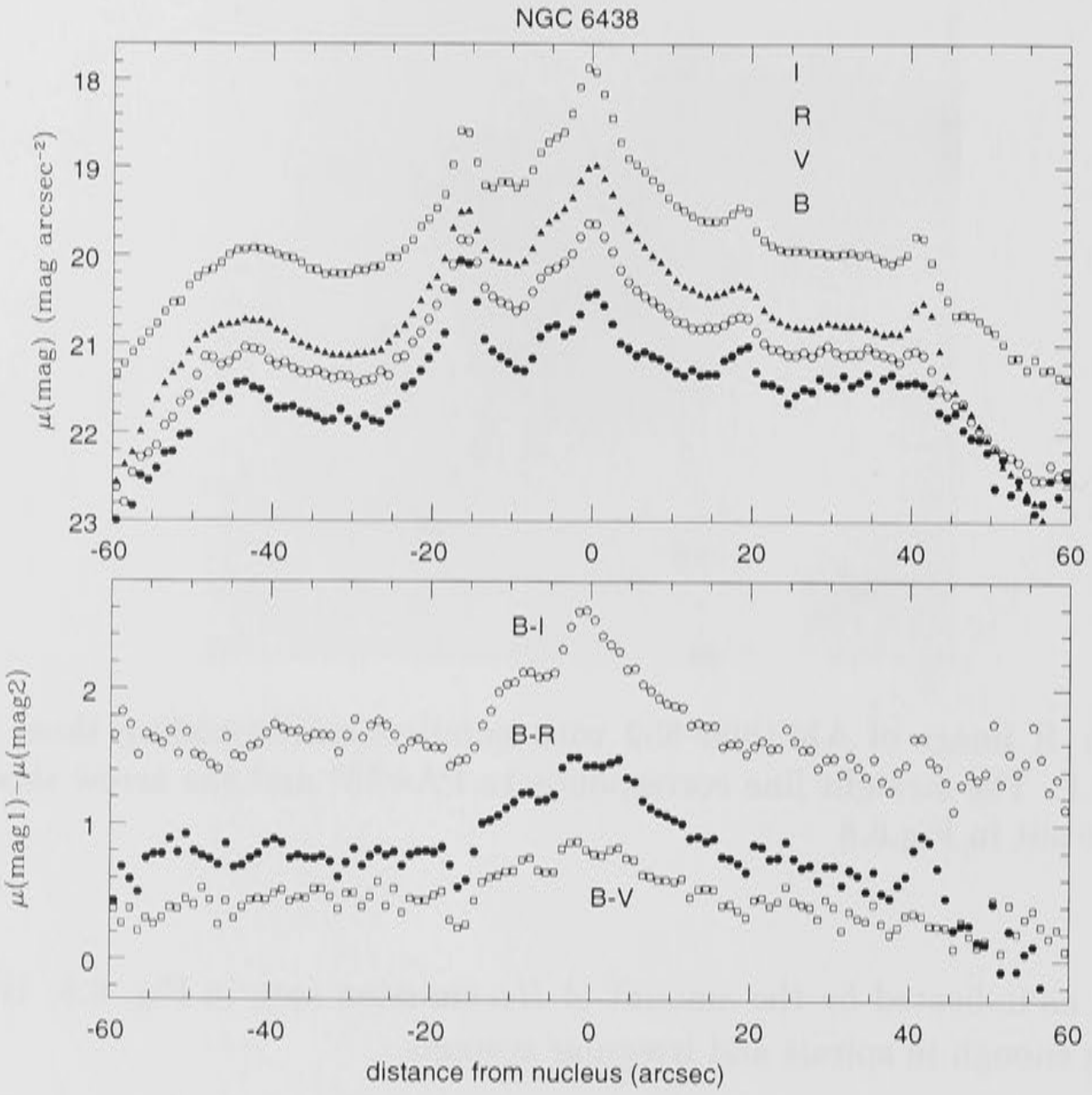

Figure 6.8: Surface photometry of AM 1806–852 at PA=55; distance=0 is the nucleus of the irregular component.

colors. The suspected blue ring shows a dip in colors at d$\simeq$–5″and at d$\simeq$7″. The nuclear region of NGC 6438A shows a plateau in (B–V) and (B–R), but is clearly peaked in (B–I): this structure in the colors is probably associated with recent star formation and dust in the nuclear regions. Beyond the nucleus the colors become steadily bluer to the outer end of the southern arm.

The surface brightness profile of the inner disk of the irregular across its major axis can be fitted well with a two–component (bulge + disk) profile. NGC 6438 itself, on the other hand, appears to follow an $R^{1/4}$ law, suggesting that it is indeed an elliptical system.

6.2.2 Spectroscopy

General Trends

The irregular component of AM 1806–852 shows strong $H\alpha$and [NII] $\lambda\lambda$6548, 6584 emission from its HII regions and also from the nucleus, suggesting that there is active star formation in the nuclear region, consistent with the $H\alpha$ narrow–band image. The spectra in 12 position angles are used to build velocity map of AM 1806–852 which will be discussed in the next section. The spheroidal component shows broad $H\alpha$ absorption and [NII]λ6584 emission, the latter being typical for elliptical and SO galaxies in compact groups (Rubin *et al.*, 1991). De Mello *et al.* (1996), in their population synthesis study of this early type galaxy showed that the dominant population is old and metal deficient ($[Z/Z_{\odot}]_{max}$=–0.5) but a significant flux fraction at 5870Å comes from a younger stellar component (age $\lesssim 5\times10^8$ yr).

Our blue spectra are weak. Hβ is seen in absorption in the spectrum of the spheroidal component and also, weakly, in the spectrum of the blue knots. We have adopted heliocentric velocities of 2470 and 2485 km s^{-1} for the spheroidal component and the nucleus of the irregular components respectively. For the blue knots, our data give 2635 km s^{-1}for the $H\alpha$ velocity. This is similar to that observed by D&E: 2628 km s^{-1} for the blue knots.

$H\alpha$ Kinematics

Longslit spectra of AM 1806–852 were taken at 12 PAs across the irregular component. The nucleus of the spheroidal component provides the zero point of the distance along the slit. The velocity map was constructed using velocities from $H\alpha$ and [NII] $\lambda\lambda$6548, 6584, and are shown in Fig. 6.9 and 6.10.

The largest velocity gradient is seen at PA=95°and 110°, reaching about 270 km s^{-1}. If one smoothes the local features, then the velocity slice at PA=95° has the appearance of a flat velocity curve with a steep gradient in the center; however, this slice does not go through the nucleus of NGC 6438A but the blue knot, as can be seen in Fig. 6.2.2 The slit passes through the nucleus at PA=129°. Here the velocity distribution is very asymmetric, with the continuum of the nucleus lying in the flat regime of the velocity spread. A similar result was obtained by D&E from their spectrum at PA=90°.

Multiple velocity components can again be seen in some PA's. The total velocity spread observed inside the irregular component from my spectra is lower than that observed by Burbidge & Burbidge (1966): they found an internal velocity difference of 350 km s^{-1}extending throughout the longest extension in the irregular at PA=47°.

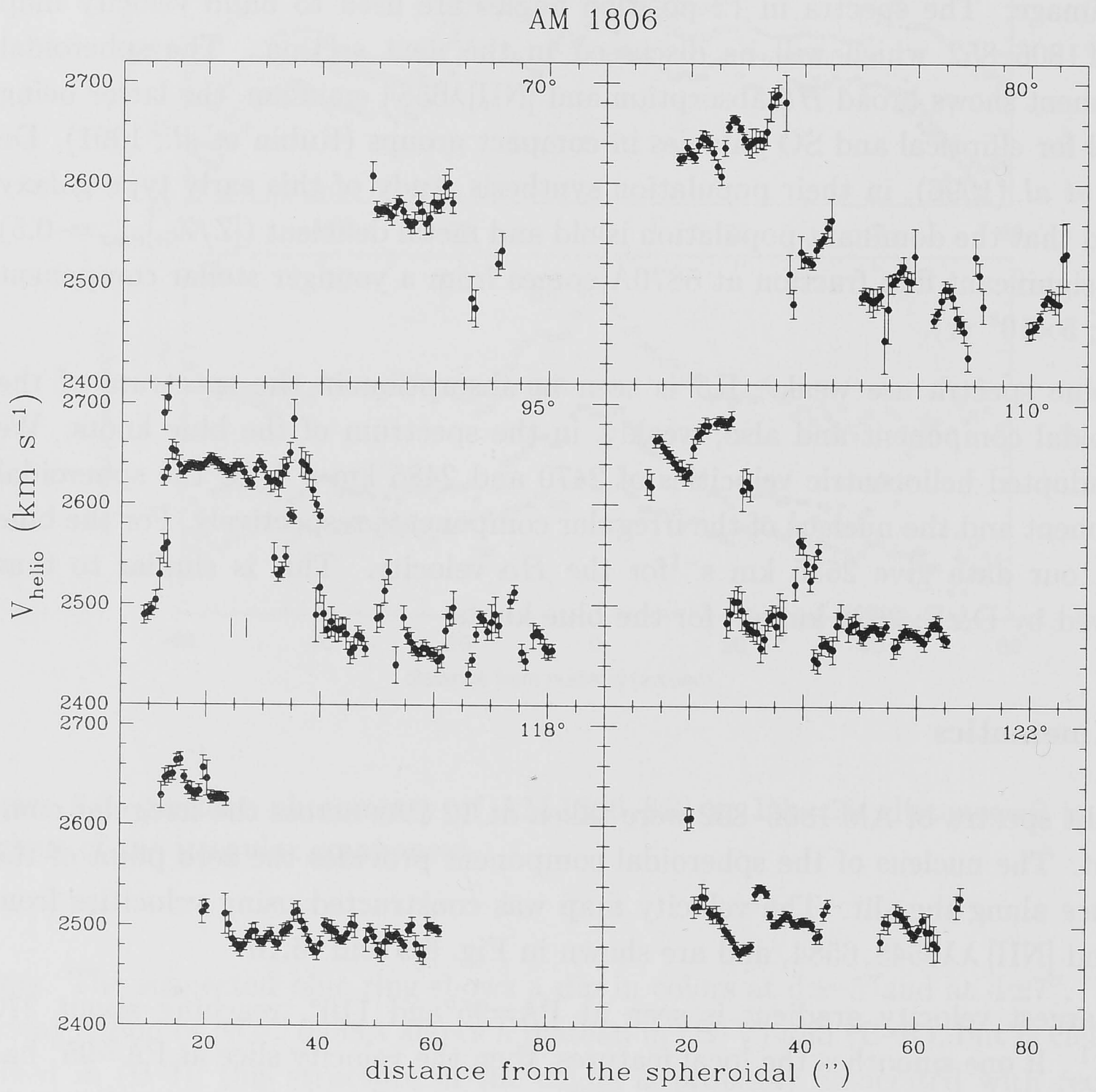

Figure 6.9: Longslit velocity maps of AM 1806–852 . Numbers on the upper right corners are position angles. The double-vertical lines at PA=95° show the location of the blue knots.

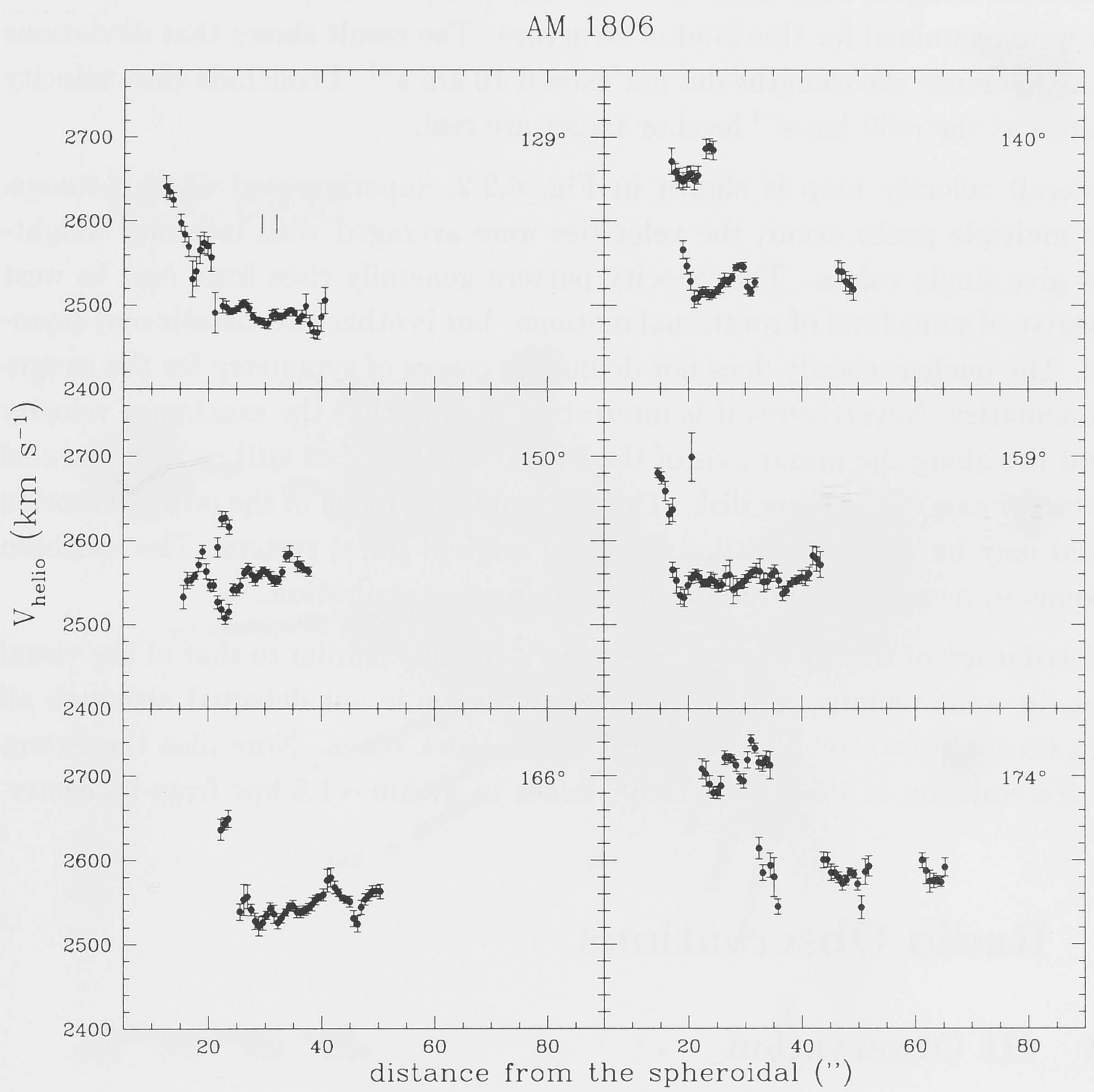

Figure 6.10: Longslit velocity maps of AM 1806–852 . Numbers on the upper right corners are position angles. The double-vertical lines at PA=129° show the location of the blue knots.

The velocity distributions along the slits in each PA seem irregular, exhibiting scatter from about 30 km s^{-1} to 80 km s^{-1}. It was first suspected that this might be instrumental. The PCA (Photon Counting Array), which was used for these observations, can produce local irregular displacements in the wavelength and spatial direction, because of dislocations in the fiber boule that images the back of the intensifier on to the CCD. As a check, the lines in the comparison spectrum that have wavelengths near those of the $H\alpha$and [NII]$\lambda\lambda$ 6548,6584 lines from NGC 6438A were examined for this kind of structure. The result shows that deviations from the reference wavelengths did not exceed 10 km s^{-1}. I conclude that velocity deviations at the $\sim$30 km s^{-1} level or larger are real.

The overall velocity map is shown in Fig. 6.2.2, superimposed on a B-image. Where multiple peaks occur, the velocities were averaged with intensity weightings to give single values. The velocity pattern generally rises from east to west –suggestive of some level of rotational motions– but is otherwise chaotic and asymmetric. The nucleus clearly does not define the center of symmetry for the irregular's kinematics. Nevertheless it is interesting to note that the maximum velocity gradient lies along the *minor* axis of the irregular galaxy but still roughly parallel to the *major* axis of the inner disk. This suggests that much of the ordered motion observed may be residual rotation from the original spiral system. The southern arm seems to have a rather homogeneous velocity distribution.

The distribution of the $H\alpha$spectral emission is roughly similar to that of the visual images. In some regions, however, the $H\alpha$ emission is not detected although all spectra except PA=140° have comparable exposure times. Note also the extent of the $H\alpha$ emission at PA=95°, which reaches to within $\sim$1.5 kpc from its center.

6.3 Radio Observations

6.3.1 HI Observation

We observed AM 1806–852 in HI with the Compact Array of the Australia Telescope. The HI spectrum of AM 1806–852 integrated over all channels is presented in Fig. 6.12. With a peak at about 2460 km s^{-1}, it shows an asymmetric profile with a tail toward higher velocities. The systemic velocity at 20% level is V_{20}=2563 km s^{-1} with a width W_{20}=335 km s^{-1}.

The overall distribution of HI, mapped using a 3.5σ clipping, is shown in Fig. 6.13. The crosses correspond to the nucleus of the irregular component in the east and to the nucleus of the spheroidal in the west. The beam size is shown in the top right corner of each frame and the greyscale is in Jansky/beam.

The distribution of HI is concentrated around the irregular component and its

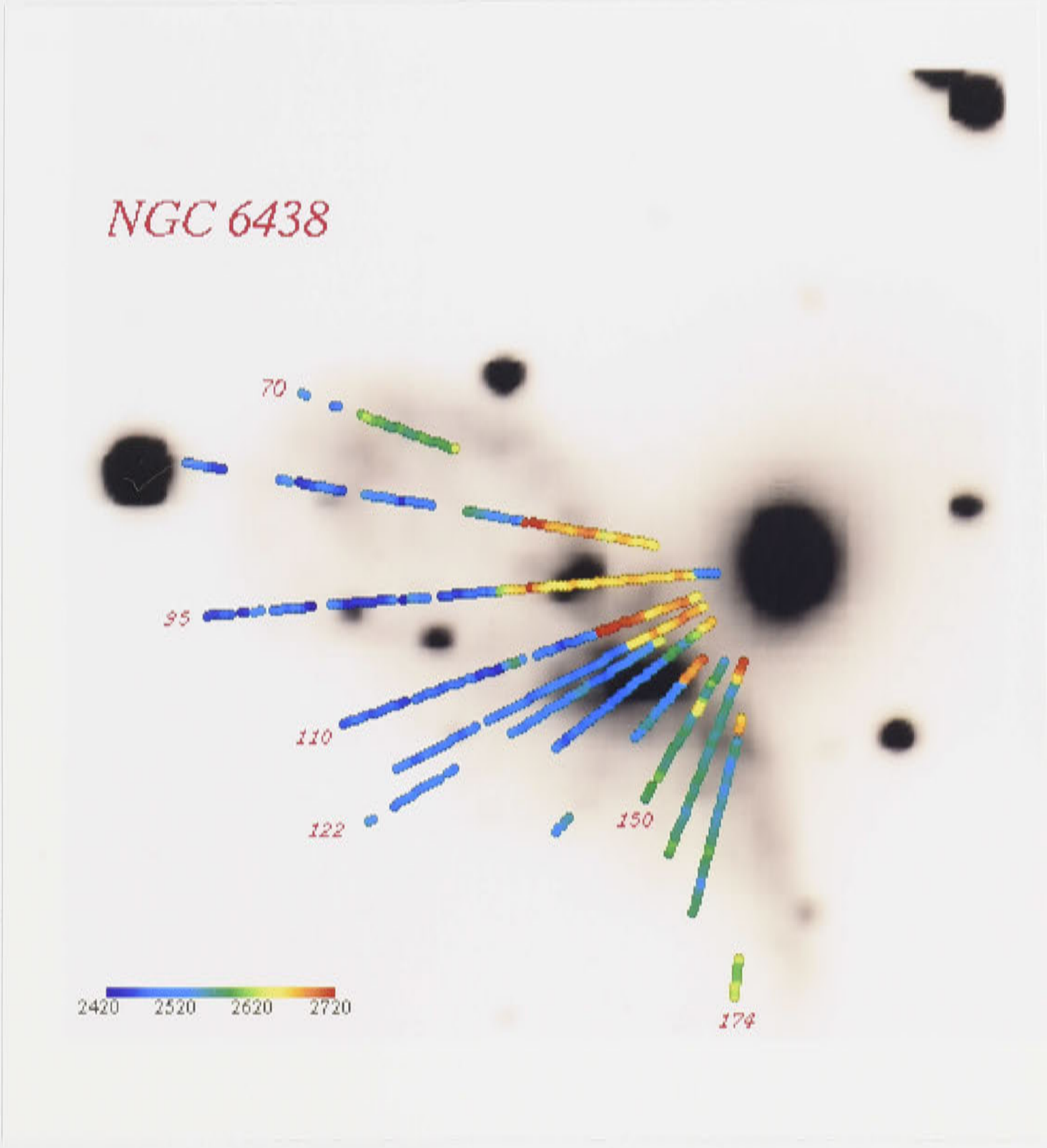

Figure 6.11: Longslit velocity maps superimposed on a B-image of AM 1806–852 .

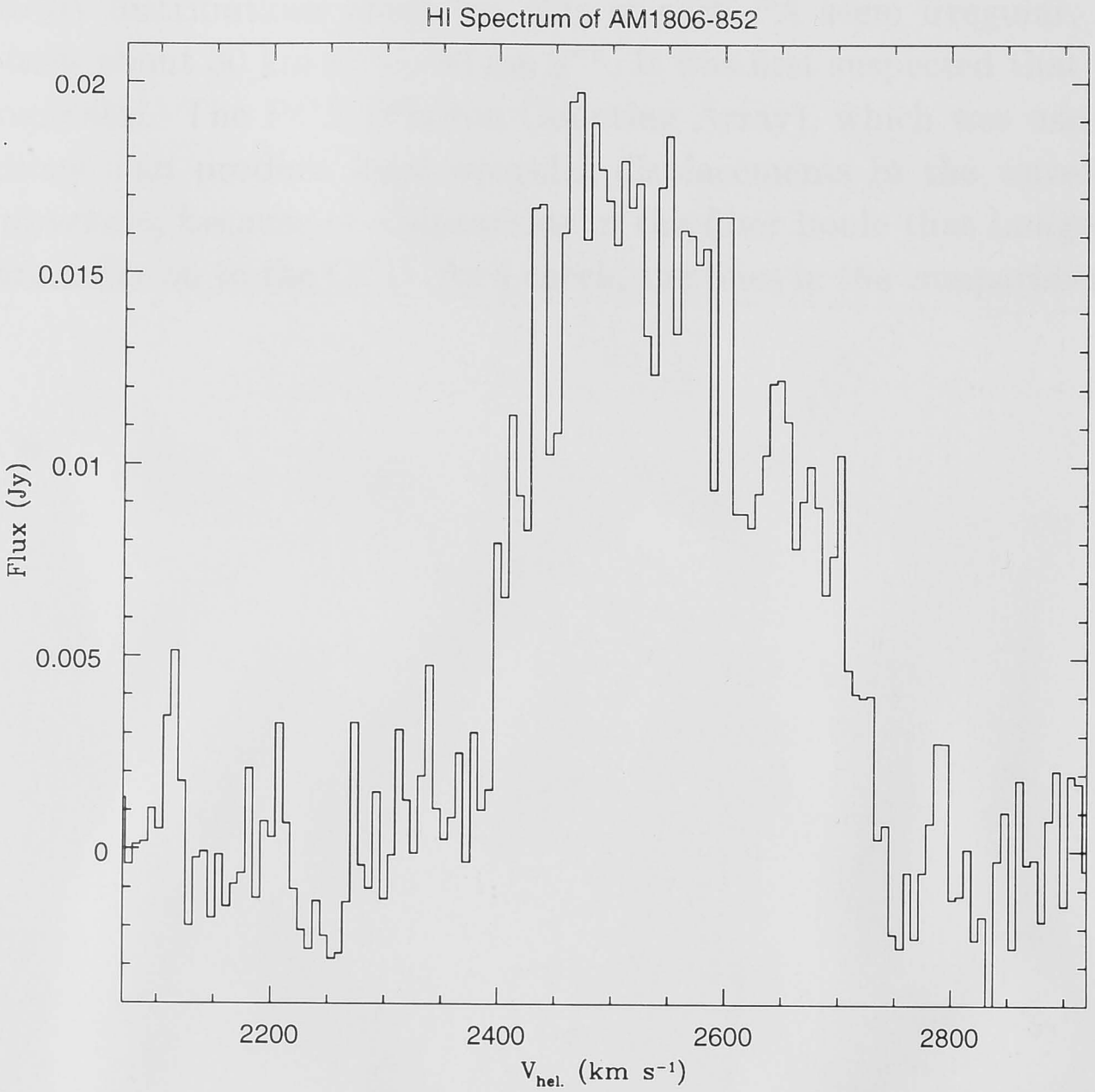

Figure 6.12: HI spectrum of AM 1806–852

orientation agrees well with that observed in the optical: elongated from NE to SW, although the extent of HI is larger than in the optical, especially in the west. The (optical) spheroidal component lies just at the edge of the HI distribution. The strongest concentration of HI is seen between and rather south of the two components. This does not seem to correspond to any structures in the optical or $H\alpha$ image. Similar, though to a lesser degree, are the HI peaks in the eastern region. The HI distribution also suggests a faint arc running from northeast to the west encircling both components. This might be related to the finding of Rampazzo & Sulentic (1992) of two partial-shell structures –ripples– on the west side of the early–type component.

Fig. 6.14 and 6.15 shows channel maps of AM 1806–852 overlaid on its zeroth moment. These were binned over 6 channels, which gives a resolution of 19.8 km s^{-1} for each frame. The numbers on the top left corners are the starting velocity of each cube. The lack of information at V_{hel} =2623 km s^{-1} is due to an externali source of interference that has been filtered out at 1410 MHz.

The lower velocity HI is seen roughly in the eastern part of the irregular, with velocities increasing towards the west. At the nucleus of NGC 6438A, the HI ve-

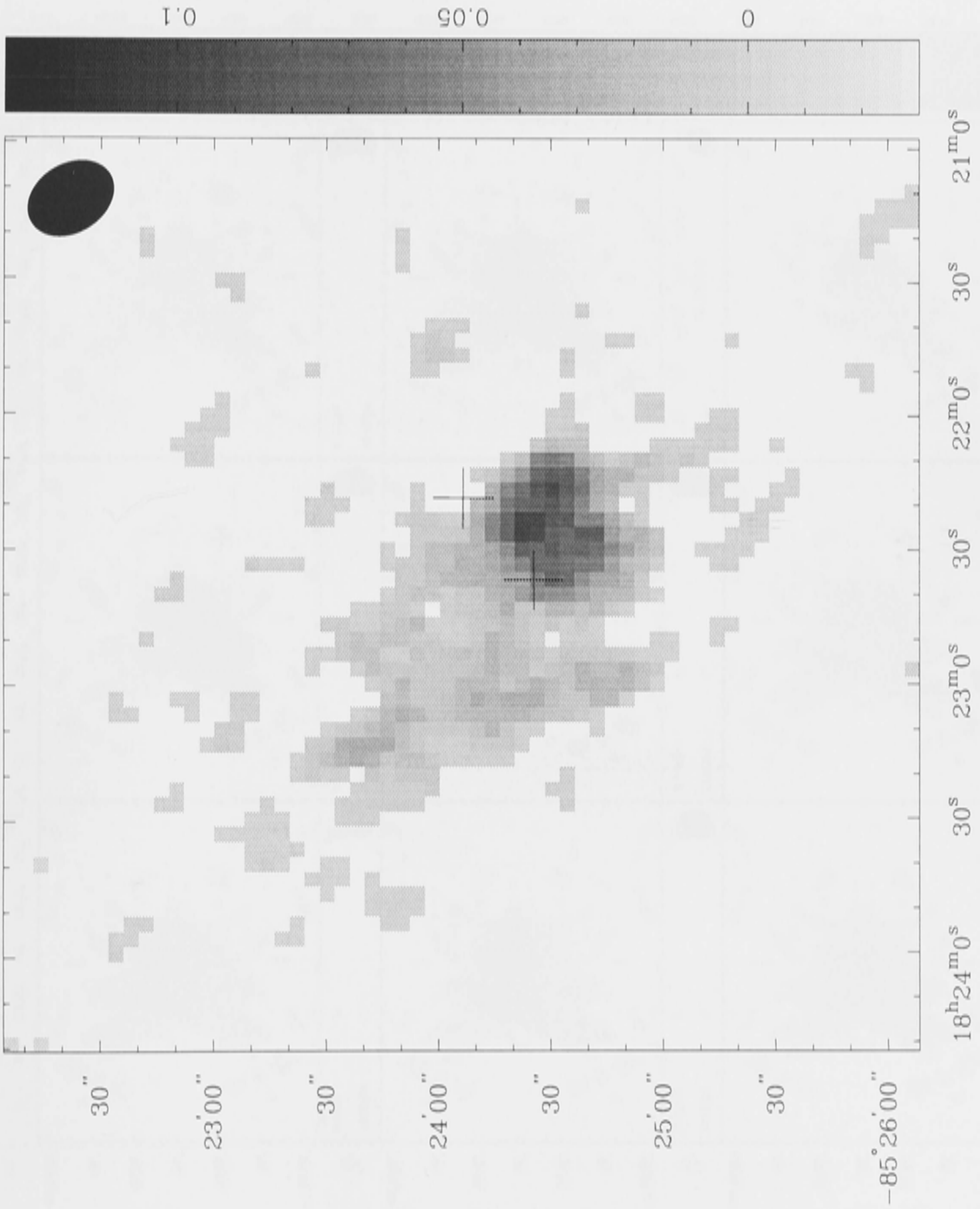

Figure 6.13: HI distribution in AM 1806–852 .

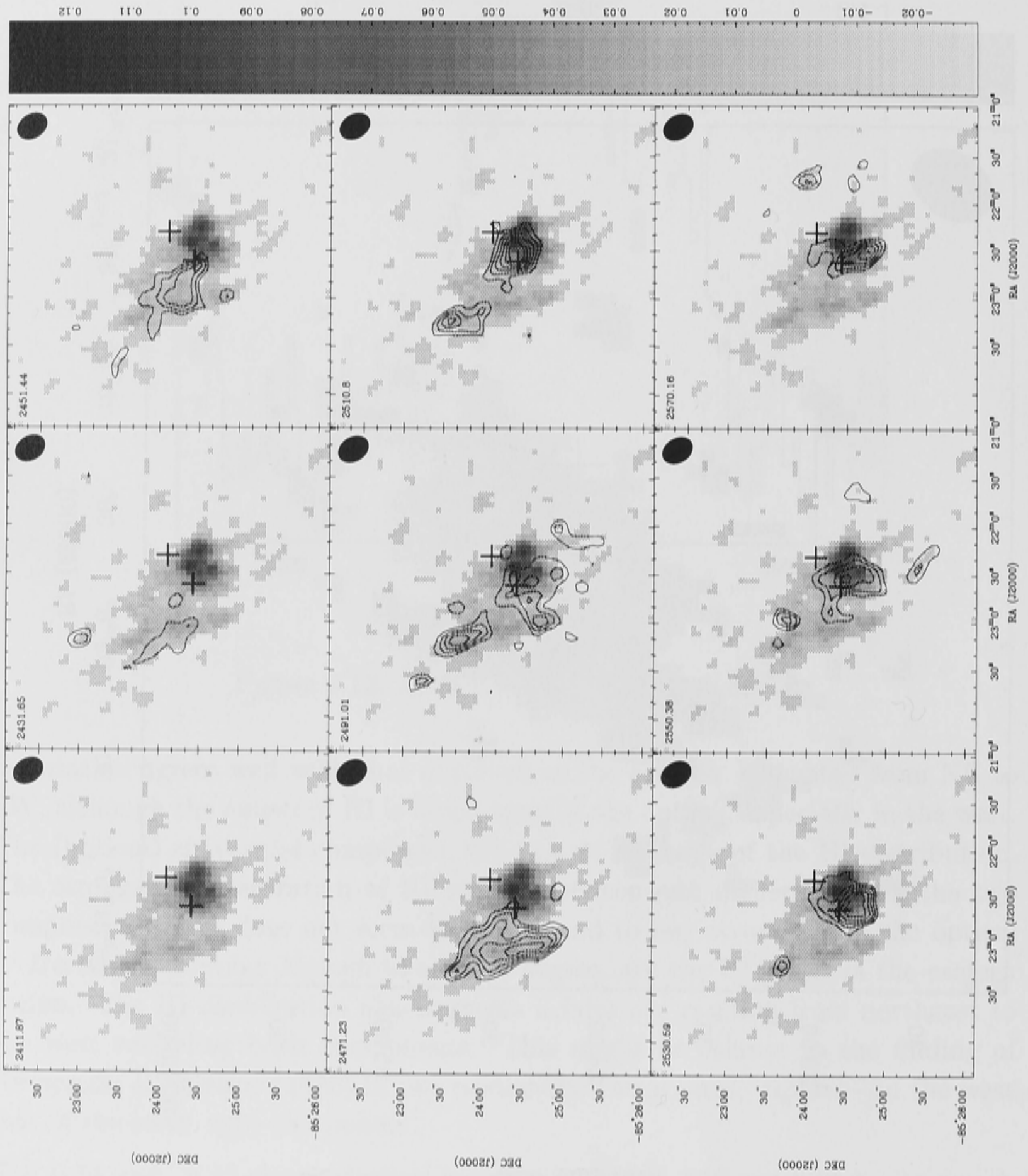

Figure 6.14: Channel maps of AM 1806–852

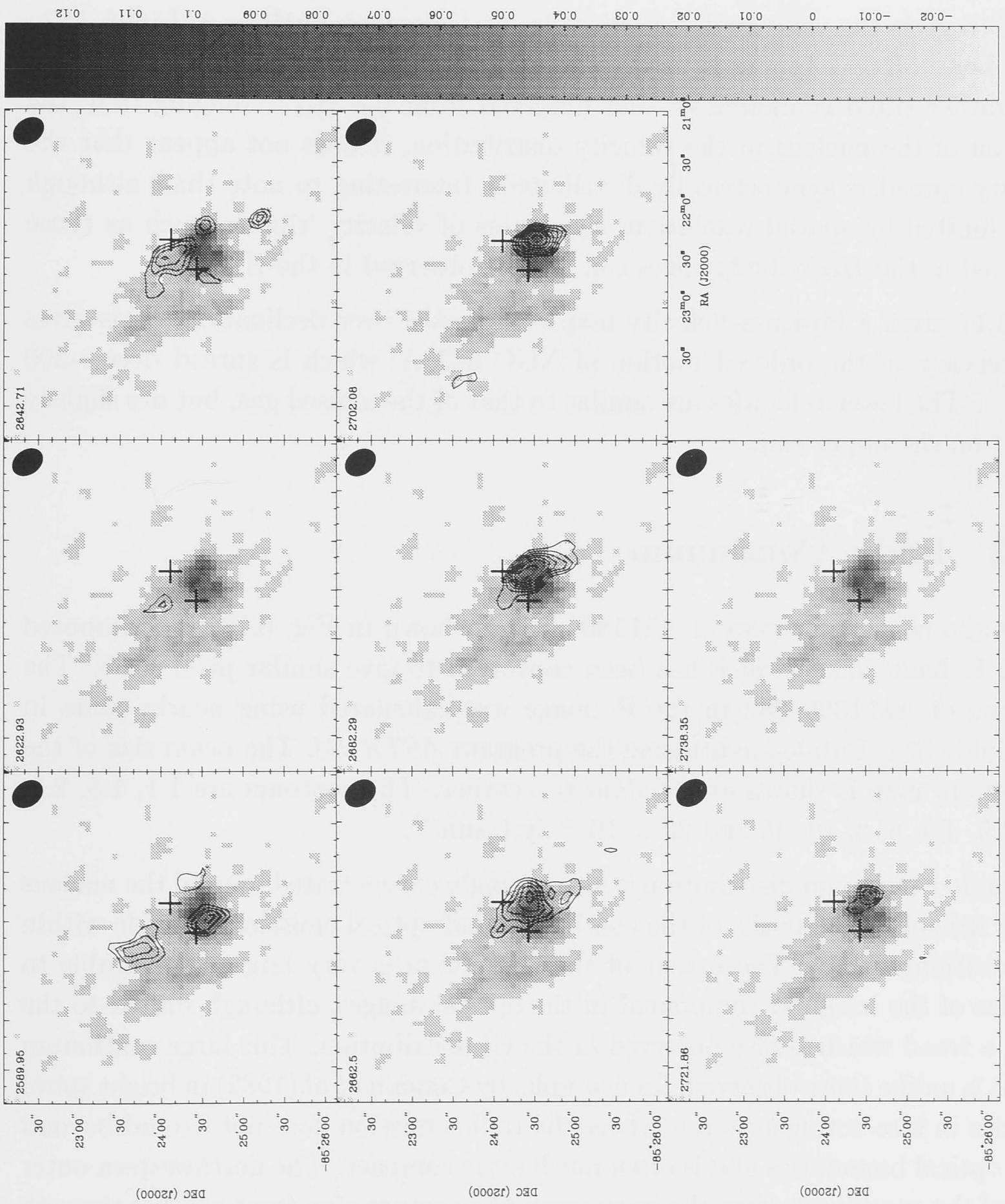

Figure 6.15: Channel maps of AM 1806–852

locity is about 2550 km s^{-1}. Past this nucleus, the HI distribution becomes more compact and is dominated by HI with higher velocities. The 'arc' around both components tends to have lower velocities, typically around 2440–2570 km s^{-1}; unfortunately this is not obvious in the figures due to the smoothing of the velocities in the maps presented.

Fig. 6.16 gives the velocity distribution, ie. first moment, of HI in AM 1806–852 ; again here a 3.5σ clipping is used. The neutral gas rotates roughly from NE to SW, rather tilted compared to that observed from the $H\alpha$. Judging from the position of the nucleus in the velocity distribution, it does not appear that the velocity spread is symmetrically distributed. Interesting to note that, although more limited by spatial resolution, signatures of velocity 'ripples' such as those observed in the $H\alpha$ velocity slices can also be observed in the HI.

Fig. 6.17 gives a Position-Velocity map compressed over declination. This gives an overview of the ordered motion of NGC 6438A, which is spread over ~300 km s^{-1}. The lower velocities are similar to that of the ionised gas, but are slightly higher on the upper end.

6.3.2 Radio Continuum

The radio continuum map of AM 1806–852 is shown in Fig. 6.18, superimposed on an R–band image which has been convolved to give similar pixel scale. The position of AM 1806–852 in the R image was calculated using nearby stars in the Guide Star Catalogue utilising the program *ASTROM*. The beam size of the continuum map is shown at the right-top corner. The contours are 1.1, 1.5, 2.2, 2.5, 3.5, 4.5, 6, 8, 10, 15 and 20×10^{-4} Jy $beam^{-1}$.

The radio continuum distribution is also strongly concentrated around the nucleus of the irregular: the peaks of the continuum and optical emission coincide within the positional error. The extent of the continuum is very large, comparable to the size of the irregular component in the optical images, although shifted to the west, a trend which is also observed in the HI distribution. This large continuum extent is unlike those observed, for example, by Condon *et al.*(1982) in bright spiral galaxies in interacting systems, where the radio emission does not extend beyond their optical boundaries and is often much more compact. The northwestern outer edge of the continuum gives the impression of a compression front passing through the spheroidal component. Near the nucleus of the spheroidal component, the radio continuum contours form a spout-like structure, which is suggestive of the continuum-emitting matter being pulled into the nuclear regions of the spheroidal companion.

About 15″ north of the peak of the continuum emission, there is an extension that is almost coincidental with the northern $H\alpha$ source; however, this structure

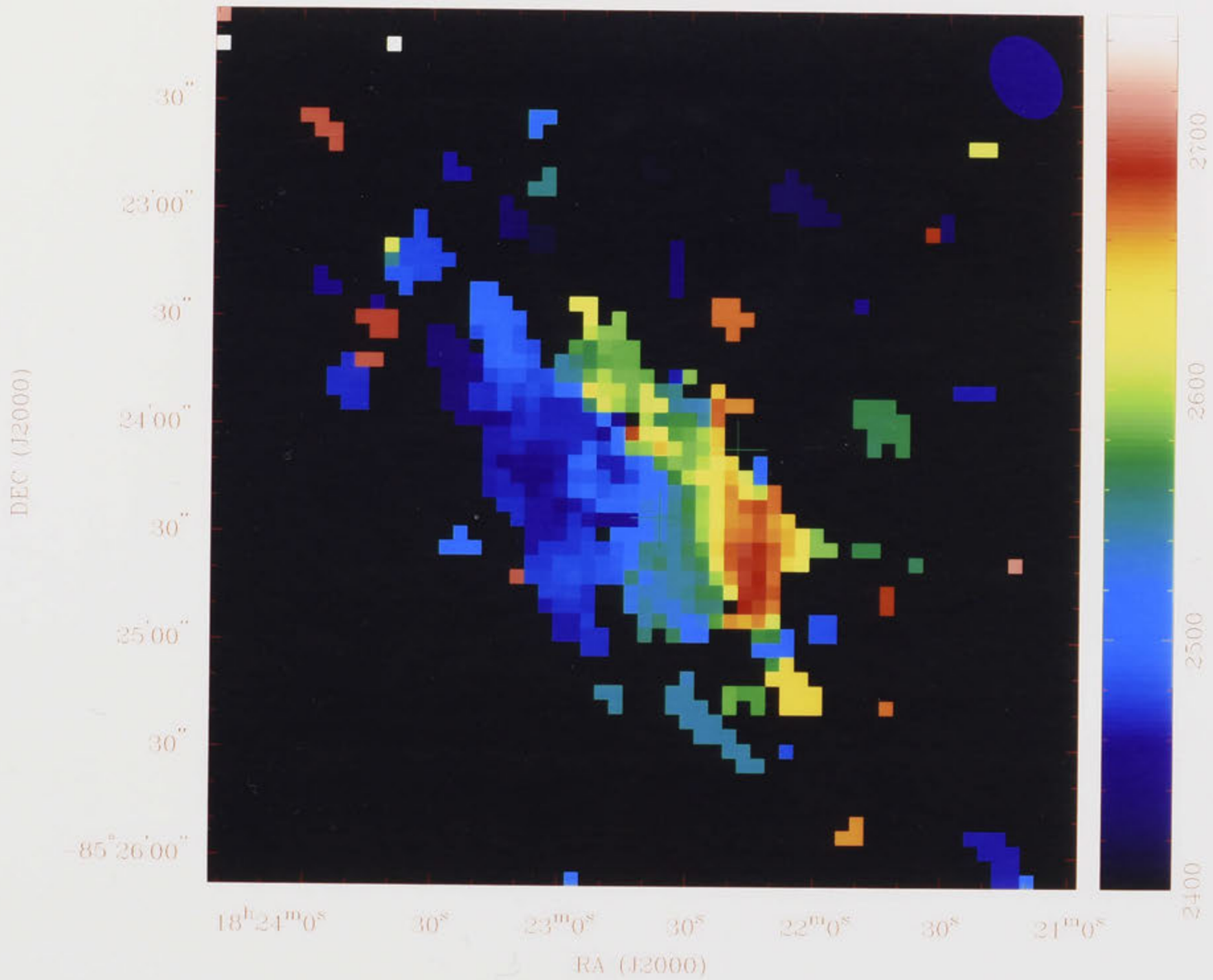
30"
23'00"
30"
24'00"
30"
25'00"
30"
-85°26'00"
DEC (J2000)
18h24m0s
30s
23m0s
30s
22m0s
30s
21m0s
RA (J2000)
2700
2600
2500
2400

Figure 6.16: HI kinematics of AM 1806–852

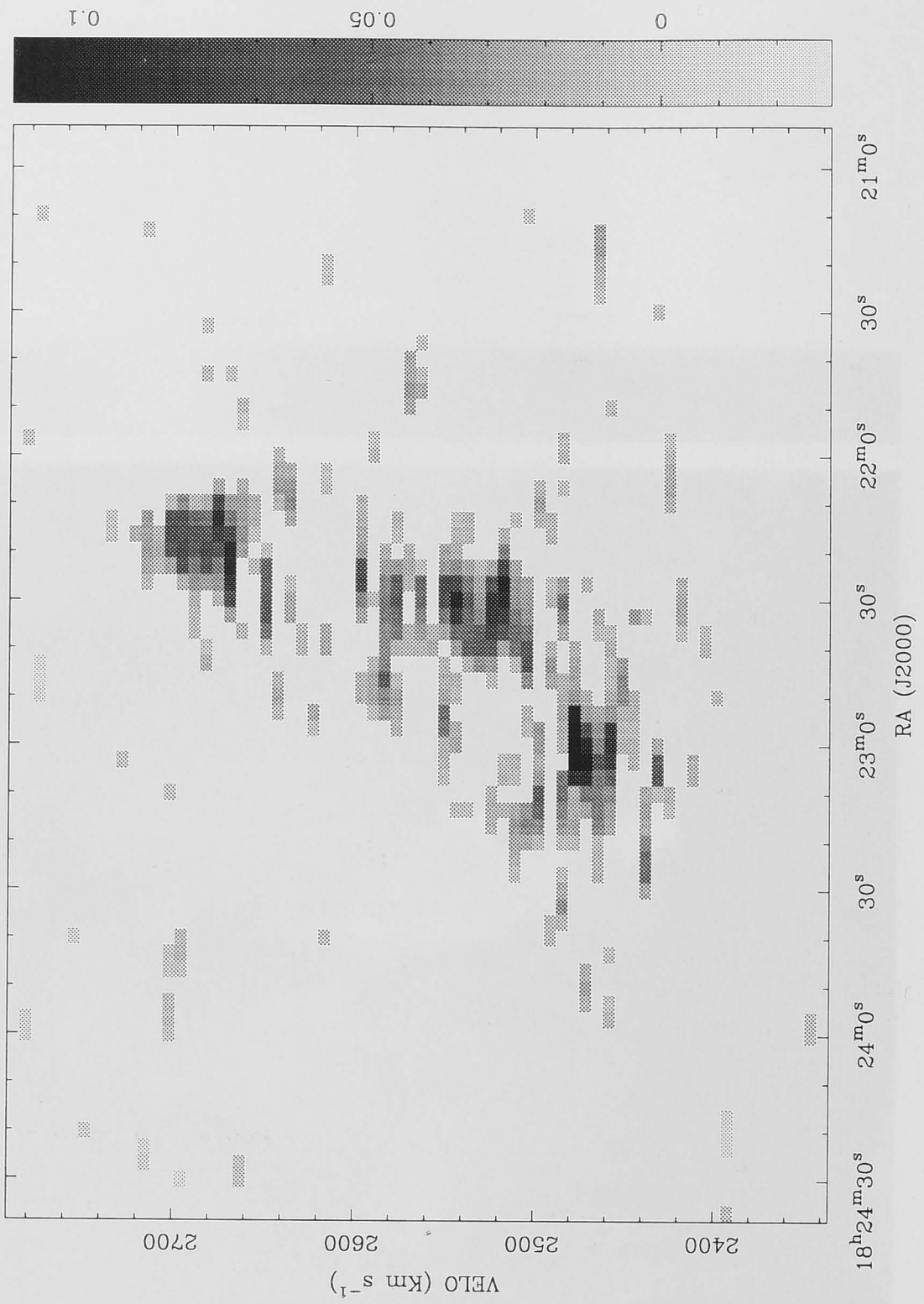

Figure 6.17: Velocity map of AM 1806–852 smoothed over declination

extends much further north, until beyond the optical extent of the irregular component. The continuum map exhibits a few local maxima, eg. the knots in the east or the extension to the west, which have no obvious optical counterparts, although the latter does coincide with one of the HII peaks.

The total radio flux is 25.5 mJy, which gives a (monochromatic) radio power of $P_{1.34GHz} = 3.1 \times 10^{21}$ W Hz^{-1}. This value gives a good fit on the far-infrared–radio correlation found by, for example, Dickey *et al.*(1988).

6.4 On the Mass

If the gas is optically thin, then the HI mass is given by:

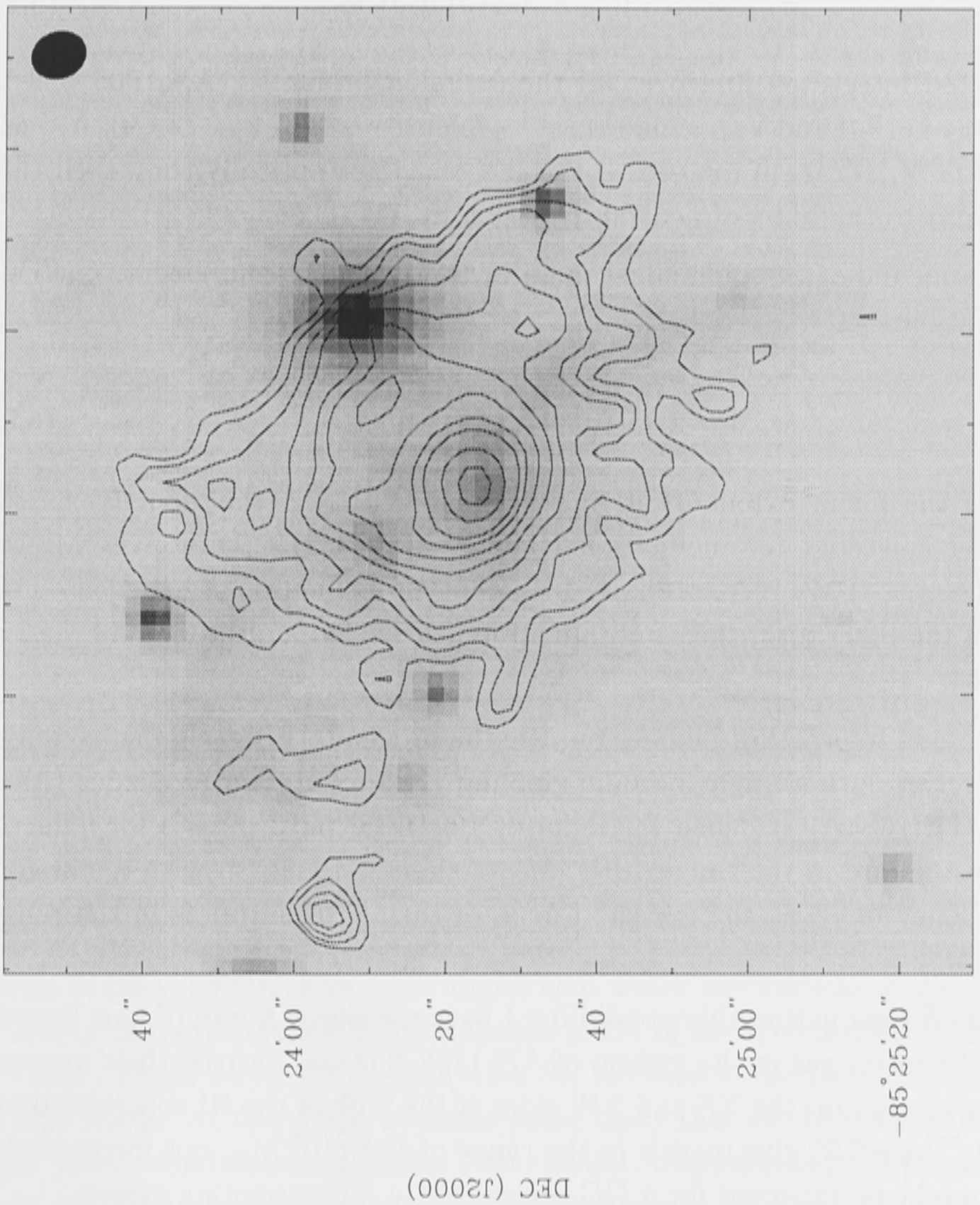

Figure 6.18: Continuum distribution of AM 1806–852

$$M_{HI} = 2.36 \times 10^5 \; D^2 \; S(v) \; d(v) \; M_\odot \tag{6.1}$$

where D is in distance in kpc, v in km s^{-1} and $S(v)$ in Jansky km s^{-1}. Since $D = V_{syst}/(100\,h)$ and h=H$_\circ$/100, then:

$$M_{HI} = 23.5 \; V_{sys}^2 \; h^{-2} \; S(v) \; d(v) \; M_\odot \tag{6.2}$$

The calculated integrated flux over all the emission profile for AM 1806–852 is 11.08±0.02 Jy km s^{-1} and V$_{sys}$=2565 km s^{-1}, which gives $M_{HI} = 1.72{\times}10^9 \; h^{-2} \; M_\odot$ or $M_{HI} = 3.06 \times 10^9 \; M_\odot$ if h=0.75. If the the gas is not optically thin, then this is a lower limit to the mass of neutral hydrogen in AM 1806–852 .

To calculate an indicative dynamical mass of the irregular component, one can use the equation:

$$M_{dyn} = 2.45 \; 10^4 \; A_\circ \; [W(0)_{20}]^2 \; M_\odot \tag{6.3}$$

where A$_\circ$ is the linear extent of HI in kpc, and W(0)$_{20}$ is the velocity spread to 20% level corrected for inclination (Reif et al., 1982). This gives M$_{dyn}$= 3.30×10^{10} (sin(i)$^{-2}$) M$_\odot$ if A$_\circ$=12 kpc. If I adopt an inclination of ∼40° based on the shape of the inner disk, then I obtain an indicative dynamical mass of M$_{dyn}$= 8.0×10^{10} M$_\odot$.

Gas fragments in interacting galaxies may be the progenitors of stellar subsytems, which in later evolution might become globular clusters or dwarf galaxies (Ashman, 1989; Fritze-v.Alvensleben & Gerhard, 1994). Typical masses for galactic globular clusters are in the range $10^{4-6} \; M_\odot$ (Ashman, 1989), so with a star formation efficiency of ∼1%, the expected mass of their progenitors is in the range of $\times \; 10^{6-8} \; M_\odot$.

In the spirit ofinvestigating this possibility, I have measured fluxes of four largest fragments of neutral gas in the system of AM 1806–852 and derived their masses. These fragments are on the NE and NW sides of the bulk of the HI concentration. The results (Table 6.2) give masses in the range of 1–2×10^7 M$_\odot$, not inconsistent with what might be expected for a GC progenitor in an interacting system.

6.5 Discussion

6.5.1 On the Morphology and Kinematics

The northeastern loop and the southern arm in NGC 6438A emerge from two different regions: from the blue knots in the north, and the irregular's nucleus in

Knot	Mass $\times 10^7 M_\odot$
1	1.11
2	1.71
3	1.16
4	1.60

Table 6.2: Masses of largest HI fragments in N6438A

the south. The blue knots have a distinctively different velocity than that of the nucleus. These two major observations draw D&E to conclude that the irregular might consist of two very distorted disk galaxies.

The blue knots, as can be seen from the images, are embedded insided diffuse matter which is suggestive of a (disturbed) disk. The same can be said about the nucleus. Both regions are strong sources of $H\alpha$, both are blue, and both, although to very different levels, are radio continuum sources. My spectra show that the blue knots, as well as the nucleus but to a much higher degreee, also display optical continuum emission indicative of an underlying stellar population. Additionally, both regions also show [NII]/$H\alpha$ values typical of HII regions. The kinematics of the ionised gas in NGC 6438A do not indicate that the nucleus is the center of the $H\alpha$ kinematics. The HI kinematics, however, show that the nucleus is closer to the center of the HI distribution, although the density peaks of the neutral gas lie elsewhere.

The evidence so far does not contradict the notion that the blue knots region might be a third galaxy. If this is so, then why should this third galaxy have a double nucleus (ie. the blue knots)? Some galaxies are indeed observed to have multiple nuclei, eg. M51 or Mrk 231, although these are usually active galaxies; the spectra of NGC 6438A show no evidence that either the nucleus or the blue knots are active. A more detailed high resolution study of the $H\alpha$kinematics around the blue knots would be useful to determine the motions in the immediate vicinity of the blue knots. At this stage, it seems more likely that the blue knots are simply bright young condensations within NGC 6438A, comparable in luminosity to the bright young star clusters seen in blue compact galaxies like NGC 1705 (Meurer *et al.*, 1992).

6.5.2 On the Star-Forming Activities

The overall HI content inside the irregular component of AM 1806–852 is similar to that observed in isolated spiral galaxies (see, for example, Zasov & Sulentic, 1994, and references herein). This means that, despite the strong interaction with the

spheroidal companion, the neutral gas has not experienced a significant depletion. One of the mechanisms for this is via a phase change, that is, conversion into molecular clouds or shock heating. An observation in CO will certainly either confirm or deny this. Nevertheless, the HI does experience dynamical stripping –which is another HI depletion mechanism– due to its interaction with the spheroidal. This results in an HI arc encircling both components, where the clumps that build this structure are candidates for globular clusters, or, if they are graviationally detached from the parent galaxy, for dwarf galaxies.

Another mechanism for HI depletion is intensive star formation associated with the interaction. Using the definition for FIR luminosities for IRAS sources described in Woltenscroft *et al.* (1987), I have calculated the FIR luminosity for NGC 6438A to be $\sim 6{\times}10^9\ L_\odot$. This value is on the lower end for interacting galaxies, about 100× less luminous than, for example, the ultraluminous and usually interacting IRAS galaxies (Sanders *et al.*, 1987). Nevertheless the radio and FIR fluxes of the irregular lie on the tight correlation found in many types of star-forming galaxies. This implies that the star formation and FIR reradiation processes, and the radio continuum emission processes, in NGC 6438 are probably similar to those in more normal galaxies (although these processes are still not fully understood).

The distribution of the radio continuum is rather smooth inside and around the immediate vicinity of the inner disk, but it becomes clumpier outward. This can be understood by a smoothing effect of the synchroton radiation by cosmic ray transport of SNRs, which can travel as far as ∼3 kpc in $2{\times}10^7$ yr (Condon, 1992). This might also explain why the blue knots region, despite emitting strong $H\alpha$and are very blue, has a rather weak peak in the continuum.

In addition to its low FIR flux, NGC 6438A also has a low $f_{60\mu m}/f_{100\mu m}$ (∼0.6), which suggests cool dust temperature (de Jong *et al.*, 1984), and mediocre L_{FIR}/L_B (∼0.6), which implies that FIR reradiations is not dominant. It is thus indicative that the irregular component of AM 1806–852 has little content of dust, despite the fact that it is heavily interacting.

6.6 Conclusion

It has been shown that the structures as well as the kinematics of AM 1806–852 are characteristic of heavy interactions taking place between both components. The colors inside the irregular component are very blue, implying underlying young stellar population. The spheroidal component, although does not exhibit severe morphological disturbances, appears suffer from interactions as well, as the detection of [NII]λ 6583 implies.

The HI distribution exhibits tidal stripping resulting in a clumpy arclike structure

around both components. The extent of the radio continuum and the $H\alpha$ narrow band image imply that starforming activities are taking place in the irregular component, and that continuum sources are being accreted by the spheroidal component. In spite of the interaction and star forming activities, little dust is contained inside the irregular component; this is unlike that observed from the spheroidal companion (Rampazzo & Sulentic, 1992).

The morphology and kinematics of NGC 6438A are suggestive of it being composed of two disk galaxies. More detailed and high resolution spectroscopic and photometry observations, including in CO, are needed to reach a more solid conclusion.

6.7 The Jet Nearby

About 12 minutes west from AM 1806–852 , an extended radio continuum source was serendipitiously discovered. This structure is about 5 arcmin. long in total, running roughly north-south, and its compact core with a bipolar feature is suggestive of a Faranoff-Riley class 1 (FR I) object (Fig. 6.19). At the north edge there is a 30″ gap in the emission which then reappears more diffusely a little to the west, while in the south it bends sharply to the east. The total observed luminosity is 34.2 mJy at 1.34 GHz.

In the Palomar Sky Survey atlas, the corresponding object appears rather compact with B_J=17.51 mag. In the PMN (Parkes-Molonglo-NRAO) survey the closest object to the continuum source is designated as PMN J1813-8522 (Griffith, 1993), having a flux of 33±5 mJy at 4.85 GHz; the positional uncertainty is about 1.5 arcmin. for this observation. However, based on known positions of nearby stars and using the package COSMOS, the exact position of the optical galaxy is calculated to be 18:11:59.8 -84:21:35 (J2000.0).

The jet was imaged in the I band and a spectrum was acquired to derive its redshift. The I images were taken with the 40 ″ telescope at Siding Spring Observatory; because the object is so far south, tracking problems were experienced, resulting in point sources being quite elongated. The radio continuum contours are shown overlaid on the I-band image of the galaxy in Fig. 6.19.

The spectrum of the host galaxy was observed with the longslit DBS (Double Beam Spectograph) at the 2.3m telescope at Siding Spring Observatory. The 300 G mm^{-1} grating was used in the blue and the 158 G mm^{-1} grating in the red: these give a dispersion of 2.2 Å pix^{-1} and 4.1 Å pix^{-1} for the blue and red respectively. The final spectrum covers the wavelength range from 4000 to 6400 Å in the blue and from 5600 to 10600 Å in the red.

The spectrum of the early-type host galaxy shows the G-band and the MgI b and

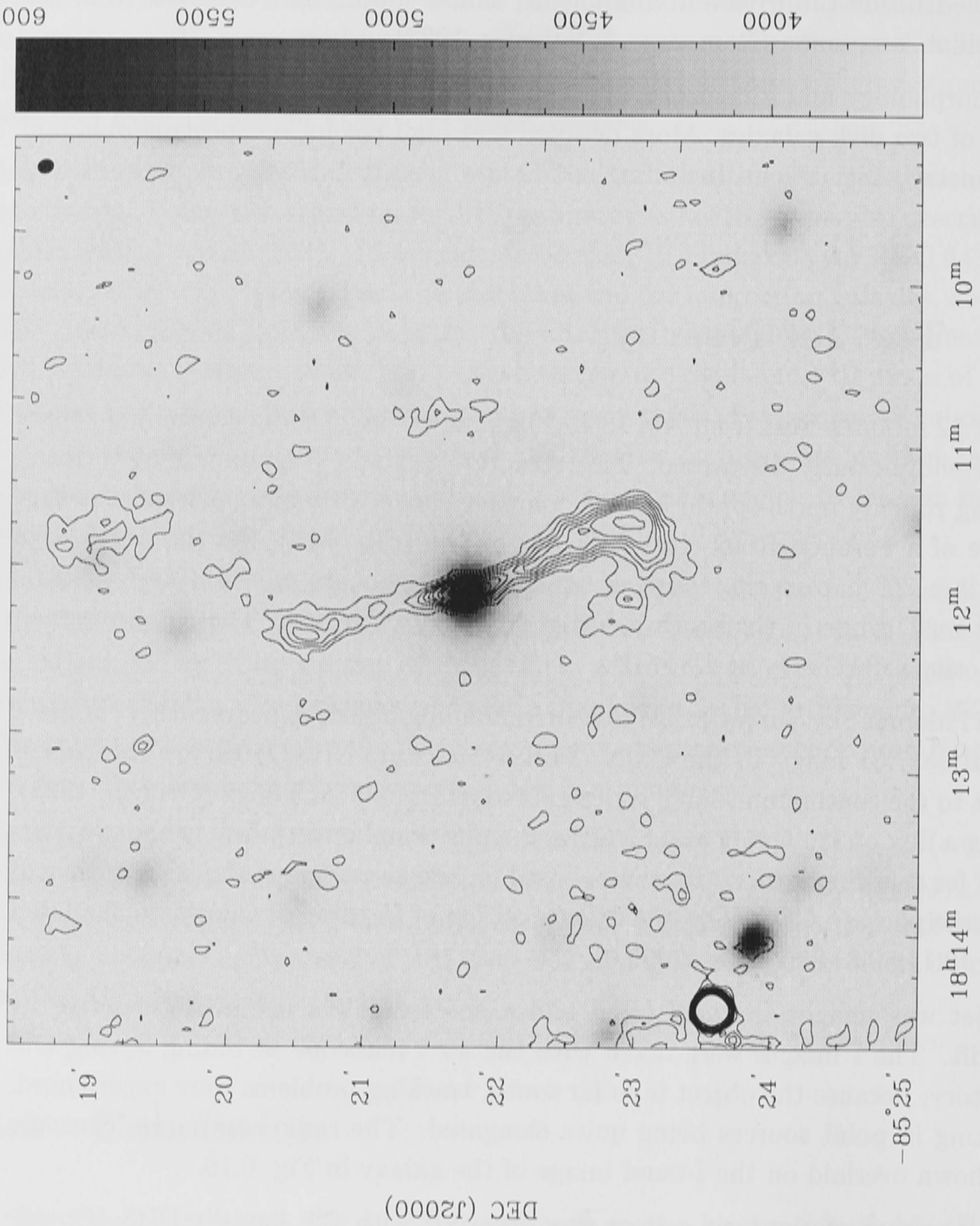

Figure 6.19: Radio continuum map of the jet near AM 1806–852

NaI D lines in absorption. There is possible a weak $H\alpha$emission but unfortunately it lies near a strong nightsky emission line. Based on the G-band, and the MgIb and NaID lines the deduced redshift is z=0.102, which correspond to a distance of 408 Mpc ($H_\circ$=75 km s^{-1} Mpc^{-1}). At this distance the jet's extent reaches about 600 kpc from north to south, which is not an unusual size for jets in radio galaxies. The (monochromatic) radio power is then 64.3×10^{22} W Hz^{-1} at 1.34 GHz, which is a typical value for FR I objects.

6.8 References

Ashman, K.M. 1989, PhD. thesis, University of London

Burbidge, E.M. & Burbidge, G.R. 1972, Ap.J. 171, 253

Buta, R. & Williams, K.L. 1995, Ap.J. 109, 543

Condon, J.J., Condon, M., Gisler, G. and Puschell, J.J. 1982, Ap.J. 252, 102

Condon, J.J. 1992, ARA&A 30, 575

Dickey, J.M., Garwood, R.W. and Helou, G. 1988, in Star Formation in Galaxies p.575, NASA, Washington

Donzelli, C.J. & Espíndola, M. 1996, A&A 111, 1057

Fritze-v.Alvensleben, U. & Gerhard, O.E. 1994, A&A 285, 751

Garcia, A.M. 1993, A&AS 100, 47

Griffith, 1993, AJ 105, 1666

Helou, G., Soifer, B.T. and Rowan-Robinson, M. 1985, Ap.J. 298, L7

Meurer, G.R., Freeman, K.C. and Dopita, M.A. 1992, A.J. 103, 60

Rampazzo, K. and Sulentic, J.W. 1992 A&A 259

Sadler, E.M. and Sharp, N.A. 1984, A.J. 89, 23

Sekiguchi, K. and Wolstencroft, R.D. 1992, MNRAS 255, 43

Sersíc, J.L. 1966, ZfA, 64, 202

Wolstencroft, R.D., Unger, S.W., Pedlar, A., Heasley, J.N., Parker, Q.A., Menzies, J.W., Savage, A. and MacGillivray, H.T., 1988, in Lecture Notes in Physics: Comets to Cosmology, Proc. of the Third IRAS Conference, ed. A. Lawrence, p. 202, Springer-Verlag

Zasov, A.V. and Sulentic, J.W. 1994, Ap.J. 430, 179

Chapter 7

Conclusion

I have presented results from investigations of six galaxy pairs in which one component is an SO or elliptical and the other component is a highly distorted irregular system. The study concentrates on the morphology and (ionised–gas) kinematics of the irregular components but attention has been paid to any observed evolutionary changes in the spheroidal components as well.

7.1 On the Morphology

Except for Arp 142, all irregular components in these interacting pairs exhibit significant morphological changes, ie. the classical extended spiral structures have disappeared from the global picture. Nevertheless, in Arp 144 and AM 1806–852 , what appears to be remnants of these spiral arms can still be observed as asymmetric structures: one extended and 'looping' arm accompanied by a rather straight arm structure in the opposite direction, both of which roughly emerge from an inner disk. The extent of this tidal distortion in NGC 6438A stretches to $\simeq 11$ kpc while it is about 8 kpc in NGC 7828. Additionally, smaller scale (more symmetric) arm structures are observed in the irregular components of these systems, Arp 118 and possibly Arp 147. Here these arms are contained inside an inner disk. With the exception of AM 1806–852 , which has three blue spiral ar the (inner) spiral structures are stellar, ie. best defined in the K–band images. It is not clear, however, whether these stellar arms are products of interactions, or remnants of pre–collision spiral structures. As noted by Noguchi (1987), inner spiral structures can develop in a disk due to a close encounter with another galaxy. However, in their sample of (non–interacting) spiral galaxies, Block *et al.* (1994) discovered that bisymmetric arms –in addition to single arms, lopsidedness, and bars– are dominating the old stellar disk as shown by their 2.2μm images.

In addition to these underlying stellar structures, blue features are observed in the irregular components. All late–type members exhibit the blue, knotty structures

on which these interacting pairs were selected. These knots are usually distributed around a common center in the irregular component, which, from the K–band image if not already evident from the shorter wavelength images, turns out to be the nucleus. An exception is Arp 147, where the nucleus is buried between two knots.

NGC 1144 and NGC 2936, are observed to have a low neutral gas to stellar mass ratio (M_{HI}/M_*) of not more than 4%. I do not have any information on the stellar mass of NGC 6438A, but if I adopt the averaged M_K/L_B value of $\simeq$1.5 as obtained in this study, then the implied gas content in this galaxy is also low, about 5%. (M_K here is mass derived from the K–band image and L_B is the blue luminosity according to RC3 (de Vaucouleurs et al., 1991).) On the other hand, IC 298, NGC 275 and NGC 7828 are found to have M_{HI}/M_* values of, respectively, 12%, 29% and $\gtrsim$19%. As Shlosman & Noguchi (1993) have indicated, a higher mass content of gas (more than 10%) inside a disk will result in gas clumps arising from local gravitational instabilities. These clumps are stable for about 1–2 rotational period but suffer dynamical friction which results in gas inflow into the nuclear region and cluster within 0.6 of the radius. These last three galaxies are indeed observed to be knotty and the condensations are much better defined in the nuclear neighbourhood.

Rings are observed in Arp 147, Arp 118, and Arp 144. In Arp 147 and Arp 118 this construction is knotty and extensive; the large extent observed in the irregular components of these systems indicates head–on collisions that occurred some time in the past and had expanded in the meantime. In Arp 144 the ring is small ($\lesssim$3.5 kpc in diameter); the highly asymmetric morphology of the regions external to the ring does not support a head–on collision scenario. In models by Gerber *et al.* (1996), a second ring can appear $\simeq$ 100 Myr after the closest passage. However, it is a stellar ring that is being produced; in NGC 7828 the ring is not observed in the K–band. All rings observed in these systems show blue colors indicating young stellar populations; in Arp 147 this is especially so. Kinematically, they show non–rotational motions in addition to ordered rotational motion.

It appears that bars –gaseous and especially stellar– are not a common feature in the interacting pairs studied here. Although the sample is not large, if stable, long-lasting bars are indeed produced in strong interactions, then one might expected that they would be more commonly observed in these interacting pairs. Only in Arp 140 has an apparent blue bar formed across the minor axis of the irregular component; this weak bar–like stuctures becomes an oval in longer wavelengths. There are signatures that the velocity spread inside the bar does not exceed $\simeq$ 50 km s^{-1} along the major axis. As observed by Elmegreen & Elmegreen (1982), the occurrence of bars is enhanced in binary galaxies, about 80% as compared to $\simeq$60%

in isolated spirals. Numerically, this phenomenon has also been predicted – and explained – by Noguchi (1988). However, as noted by Athanassoula (1990), strong interactions as apparently experienced by the pairs in my sample can temporarily decrease the bar amplitude if the bar lags behind the companion at perigalacticum.

Faint shell structures are observed in the outer regions of Arp 118, Arp 142 and AM 1806–852 as remnants of interactions. In Arp 142 these are accompanied by bipolar structures at the outer ends of the irregular components. In AM 1806–852 in HI, the whole system is embedded in arc–like structures indicating gas being stripped due to interactions.

Except for NGC 1144 and NGC 2936, the inner regions ($\simeq$ 20 arcsec) of all the irregular components can be fitted with an exponential law. A bulge-like component appears to be only contributing to the innermost ($\lesssim$3–4″) regions, consistent with the small bulges seen in the morphology of these systems. The structure of NGC 1144 does not follow the usual surface brightness laws, probably because of the multiple distorted structures seen in this system. For NGC 2936, an $R^{1/4}$ law dominates the inner region.

Dust significantly affects the nuclear regions of the irregular components of Arp 147, Arp 118, Arp 142 and Arp 144, where (B–K) exceeds 5 mag around the nuclei. In Arp 144 and Arp 147 this dust obscuration is so severe as to hide completely the nuclei in shorter wavelengths. This illustrates how blue images can give a very misleading impression of the structure of such systems. These pairs exhibit high L_{FIR} values: $>1.5\times10^{10}$ $L_\odot$ compared to 2.1×10^{9} $L_\odot$ for isolated spirals (Bushouse, 1987). But these galaxies – except for Arp 118 – have L_{FIR}/L_B values comparable to those observed in isolated galaxies ($\gtrsim$0.5), which indicates that the dust is heated by the usual star formation processes. In Arp 118, this ratio is one of the highest observed in interacting pairs ($\simeq$ 3, see Appleton & Struck–Marcel, 1987) and is believed to be caused by the extremely high level of starburst activities. On the other hand, Arp 140 is observed to have low nuclear (B–K) value ($\lesssim$3.5 mag) and a low L_{FIR} compared to most interacting galaxies. These are consistent with the view that high FIR luminosities in interacting pairs are usually concentrated to their nuclear regions.

Color ages –generally deduced from (B–R) and (B–K)– of the bluest region in the irregular components usually yield stellar population age not older than 30 Myr if an instantaneous burst model is adopted (Charlot & Bruzual, 1991, and Leitherer & Heckman, 1994). At least for Arp 147 the former can be confidently applied due to the dynamical scenario established, which gives an age of $\simeq$ 6 Myr, about one-tenth of the ring's dynamic age. A scenario with a continuous star formation rate does not appear reasonable to apply due to the nature of interactions.

It is still unclear, however, at what stage in the interactions did these bursts of star formation occur. Tidal perturbations are first anticipated near or after

the first pericenter passage of an interacting pair; the subsequent enhanced star formation is expected to occur soon after this (see, eg. Olson & Kwan, 1990; Fritze-v.Alvensleben & Gerhardt, 1994). It is thus likely that all the pairs studied here have just experienced their pericenter distances. Note, however, Noguchi's result (1991) that interacting disks will suffer recurrent bursts of star formation during their dynamic course, with periods of about 10^8 yr, independent of their initial spin and orbital orientations. Since the timescale of an interaction is $\simeq 10^9$ yr, an interacting pair can then suffer several bursts of star formation before they eventually merge. This is observationally supported by Solomon & Sage (1988), where the star formation efficiency (SFE) of merging galaxies they observed exhibit a large scatter from pair to pair. It would be interesting to perform a similar investigation on various knots and structures in the irregular components here to study their population distributions, ie. whether there exist 'jumps' of population ages. This, however, will need solid knowledge of the distribution of internal extinction in the disturbed galaxies which is a major exercise and beyond the scope of this study.

Emission lines from the nuclear regions are detected in either or both components of the interacting pairs investigated here. Nuclear emission is observed in almost all the irregulars, which indicates star formation is still active in these regions possibly induced by interactions with the spheroidal companions. A Seyfert 2 nucleus appears to be embedded in the nucleus of NGC 1144, as shown by the ratio of these lines.

[NII]λ 6583 is detected in the spheroidal components of Arp 147, Arp 140, Arp 144 and NGC 6438; in all except Arp 147 this emission is weak. In IC 298B, the line ratios indicate that a LINER nucleus is embedded in the central region of the spheroidal. Phillips *et al.* (1986) observed the [NII] line in about 50% of the 203 S0 and ellipticals they studied. Additionally, detections of this line in early type galaxies was also reported by Rubin *et al.* (1991) in the Hickson groups. It is still not fully understood, however, what the ionization and excitation processes are in these galaxies: both photoionisation and shock heating have been suggested. In interacting galaxies, the nuclear gas may be of external origin: for example, gas from one component has been funnelled to the other as a consequence of the interactions, and has induced ionization and excitation via starforming activities. In Arp 144, an extensive distribution of HI around both components of the system is observed (Higdon, 1988); this might be indicative of gas being strongly accreted by the compact companion NGC 7829. In Arp 142, Arp 118 and Arp 144, the spheroidal components exhibit blue colors atypical of those observed in early–type galaxies; in the latter two, their integrated (B–R) colors are comparable with those of their irregular companions. As pointed out by Rampazzo *et al.* (1995) in their study of six mixed pairs, the early–type components in their disky pairs (S+S0) show the most dramatic evidence for possible cross–fuelling.

Morphological disturbances in the spheroidal companions are exhibted by all interacting pairs. These are in the form of isophotal misalignments which is observed in all spheroidal components, extended structures or flares (such as in IC298B of Arp 147 and NGC 7828 of Arp 144), or additional structures, eg. knots observed in the peripheral regions of NGC 1143 or the thin filamentary structure extending from NGC 275 towards NGC 274 in Arp 140. All these might be signatures of disruptions in or accretion by the early–type components due to interactions with the companions.

In most cases, the light distribution of the spheroidal components are governed by an $R^{1/4}$ law at least in their inner few arcsec. Exceptions are Arp 142 (NGC 2937), whose light distribution cannot be fitted satisfactorily by either an exponential or $R^{1/4}$ law, and Arp 140 (NGC 275) which follows an exponential law. It is interesting to note that, among all the pairs studied here, Arp 142 has the lowest interaction level, ie. least morphological disruption and largest separation.

7.2 On the Kinematics

All irregular components display (ionised) gas kinematics still strongly dominated by ordered rotational motions, independent of the level of disruption in their morphology. A similar conclusion was drawn by Rampazzo *et al.* (1995) for the mixed interacting pairs they studied, although there the spiral components have not been morphologically altered much by interactions. In all except NGC 6438A, the maximum velocity gradient associated with the rotation lies along the major axis of the galaxy. It should be noted that, in NGC 6438A, the rotational gradient is still along the major axis of the (inner) disk. (Arp 147 is excluded from this conclusion because the ring was assumed to be circular.)

¿From their two-dimensional velocity distributions, it is found that in NGC 7828, IC 298, NGC 6438A and NGC 1144 the kinematic centers are offset from the nuclei. A displacement such as this can be easily explained by a slightly off–center head–on collision, where the nucleus is knocked off from the center of the disk, ie. the center of its kinematics. Such appears to be the case for IC 298, as supported by its ring structure which is another consequence of this type of collision. A similar conclusion can possibly be made for NGC 1144, although is unlikely to explain the high internal motions exhibited by the galaxy. For NGC 7828 and NGC 6438A, however, the kinematics are so distorted that it is difficult to decide where the kinematic centers lie. Obscuration by dust and averaging the multiple velocities component provide additional uncertainties in comparing the positions of the kinematic and luminous centers of NGC 2936.

Multiple velocities are observed in all except NGC 275. In NGC 1144, NGC 2936, NGC 7828 and NGC 6438A these occur around their nuclear regions. In

NGC 2936, at least two systems of velocities are observed across the nucleus. In NGC 7828 the multiple peaks are observed also in some parts of the tidal arms, suggestive of line-of-sight structures. Likewise, the blue knots of NGC 6438A display this signature. Non–rotational motions appear to be present in the rings of IC 298, NGC 1144 and NGC 7828. In addition, velocity cuts through the gaseous systems often exhibit local structures. In NGC 1144 and NGC 2936, these correspond to the spiral arm structures of these galaxies; in NGC 275 and NGC 7828 they relate to a number of knots.

Except for NGC 6438, and Arp 147 which is likely to have formed from a head–on collision and thus might be structurally circular, the (major) kinematic axis is approximately coincidental with the minor axis of the irregular's luminous structures. This suggests that the irregular components are still disky systems. However, non-perpendicularity of the major to minor kinematic axis is observed eg. in Arp 118, Arp 147, Arp 144 and NGC 6438, which is indicative of non–circular structures. In Arp 118, the irregular's major kinematic axis changes its position angle with radius, suggestive of an oval structure as can also be seen in the images. In NGC 6438A, the kinematic of the ionised gas is decoupled from that of the neutral gas.

Interacting spirals are observed to have lower rotational velocities and lower M/L_B values compared to isolated spirals (see, eg. Rubin *et al.*, 1991). From the six irregular components of the interacting pairs studied here, three (NGC 275, IC 298 and NGC 6438A) are found to have low rotational velocity ($\lesssim$130 km s^{-1}) and consistently low M/L_B values ($\lesssim$1.5, as compared to $\simeq 3$ observed in isolated spirals). NGC 1144, as has been shown, has an enormously high internal velocity, $\simeq$1200 km s^{-1}, thus giving $M/L_B \sim 15$. A similar trend although to a lower degree is observed in NGC 2936, where $\Delta V \simeq$ 1000 km s^{-1} but due to its lower blue luminosity gives $M/L_B \sim 20$. However this galaxy becomes rather 'normal' if the high velocity spread which is contained in the inner region is discarded and the outer, flat velocity curve is used instead: $M/L{-}B \simeq 5$. Only NGC 7828 appears to exhibit comparable ΔV and M/L_B to those of isolated spirals, despite its very distorted kinematics and morphology. Note that the masses derived here are indicative masses based on the assumption that the velocity spread is associated with an equilibrium state in the disks, which is unlikely for most of these systems.

On the other hand, the values of M_K/L_B among these pairs, where M_K is mass derived from the K–band, are found to be quite similar, ranging from 0.9 for NGC 275 to 2.6 for NGC 7828, with an average of 1.6. This might indicate that the amount of old stars regulate the birth of young, blue stars, or that those contributing to the K–luminosities are actually young stellar populations. It is more likely that the latter option is the case here. It is important to be aware that M_K values for these galaxies were derived assuming mass-to-light ratio of the

solar neighbourhood, as quoted from Thronson & Greenhouse (1988), which is about 1. Population synthesis models show that, for starburst populations, young massive stars experiencing core helium burning become very luminous in the near infra–red during their first few Gyr. For these populations, the mass-to-light ratio at 2 Gyr is calculated to be about 0.4 in the K–band (see, eg. Bruzual & Charlot, 1996). In such systems, the old population masses calculated in the galaxies here are overestimated by at least a factor of $\lesssim 2.5$.

In all cases the nuclei of the irregular components are offset from their kinematic centers. In Arp 144 and Arp 147, the nuclei have been pulled closer to their spheroidal companions (compared to their kinematic centers). The same can probably be said about NGC 6438A, although here the ionised gas kinematics is so distorted and the largest velocity gradient does not pass through the nucleus that it is difficult to judge where the kinematic axis actually lies. The kinematics of its neutral hydrogen, however, appears more 'well–behaved' and the nucleus lies approximately in the center of the largest velocity gradient. On the other hand, the centers of mass in the gaseous components of Arp 140, Arp 142 and Arp 118 lie further from the companions than their kinematic centers; in the first two these have been displaced roughly orthogonally to their kinematic axis.

For Arp 118 and Arp 142, which have extreme values for the internal velocity spread in their irregular components, we can estimate for comparison the typical velocity dispersions for their spheroidal components. The Faber–Jackson relationship (1979) for ellipticals and S0s, as adopted from results by Fukugita & Turner (1991), is used for this purpose. Among our sample, the derived velocity dispersions for the spheroidal components of Arp 118 and Arp 142 have the highest values: $\simeq 210$ km s^{-1}. Such appears to be the case as well for the spheroidal component of Arp 119: the distorted, knotty spiral is observed to have an internal velocity of $\simeq 1300$ km s^{-1} , and the compact companion has a velocity dispersion $\sim$200 km s^{-1}(Marziani *et al.* , 1994); both parameters have values comparable to those observed in Arp 118 and Arp 142. This amount of velocity spread is still much smaller than those observed in their irregular neighbours and by no means can account for the kinematics of these galaxies. However, it is clear that a more luminous (thus, for early type galaxies, more massive) galaxy is more likely to give a stronger impact or disruption to its neighbour than otherwise, as is the case for these interacting pairs.

7.3 Future Work

Studies of galaxy kinematics are incomplete without the knowledge of each component's behaviour. We need to investigate the kinematics of all the components - the stars and the neutral, ionised and molecular gases - to determine the history

and fate of these interacting galaxies. Radio continuum and narrow–band photometry studies are also of importance to trace the recent star formation history in these galaxies. As observed in AM 1806–852 , the morphology of radio continuum distribution can provide evidence for accretion from the irregular by the spheroidal companion, which is not evident from other observations.

We have not been able to observe the kinematics of the SO or elliptical components of the pairs studied here, which adds to the incompleteness of this study. It would be interesting to learn whether they are dominated by rotation or are pressure-supported, and what the interactions have done to them kinematically.

The origin of the extremely high internal motions seen in Arp 118 and Arp 142 are not understood. Detailed numerical simulations of their interactions are needed, and we have not been able to contribute to this aspect of the problem in the present study. Similarly, numerical simulations are needed to explain the production of an inner ring such as that observed in NGC 7828.

7.4 References

Appleton, P.N. and Struck-Marcell, C. 1987, Ap.J. 312, 566

Athanassoula, E. 1990, IAU Coll. 124, p. 505

Barnes, J.E. 1988, Ap.J. 331, 699

Block, D.L, Bertin, G., Stocton, A., Grosbol, P., Moorwood, A.F.M. and Peletier, R.F. 1994, A&A 288, 365

Bushouse, H.A. 1987, Ap.J. 320, 49

Bruzual, G.A and Charlot, S. 1996, Ap.J., in prep.

Charlot, S. and Bruzual, G.A. 1991, Ap.J. 367, 126

de Vaucouleurs, G., de Vaucouleurs, A., Corwin, H.G.Jr., Buta, R.J., Paturel, G. and Fouquè, P. 1991, Third Reference Catalogue of Bright Galaxies (Springer-Verlag: New York) (RC3)

Elmegreen, D.B. and Elmegreen, B.G. 1982, MNRAS 201, 1021

Fritze-v.Alvensleben, U. and Gerhard, O.E. 1994, A&A 285, 751

Gerber, R.A., Lamb, S.A., Balsara, D.S. 1996, MNRAS 278, 345

Higdon, J.L. 1988, Ap.J. 326, 146

Howard, S., Keel, W.C., Byrd, G. and Burkey, J. 1993, Ap.J. 417, 502

Leitherer, C. and Heckman, T.M. 1995, Ap.J.S. 96, 173

Marziani, P., Keel, W.C., Dultzin-Hacyan, D. and Sulentic, J.W. 1994, Ap.J. 435, 668

Noguchi, M. 1987, MNRAS 228, 635

Noguchi, M. 1988, A&A 203, 259

Noguchi, M. 1991, MNRAS 251, 369

Phillips, M.M., Jenkins, C.R., Dopita, M.A., Sadler, E.M. and Binette, L. 1986, Ap.J. 91, 1062

Rampazzo, R., Reduzzi, L., Sulentic, J.W. and Madejski, R. 1995, A&ASS 110, 131

Rubin, V.C., Hunter, D.A. and Ford Jr., W.K. 1991, ApJ.S. 76, 153

Shlosman, I. 1990, IAU Coll. 124, p. 689

Shlosman, I. and Noguchi, M. 1993, Ap.J. 414, 474

Thronson, H.A. and Greenhouse, M.A. 1988, Ap. J. 327, 671